Sheet material characterisation by multi-axial experiments

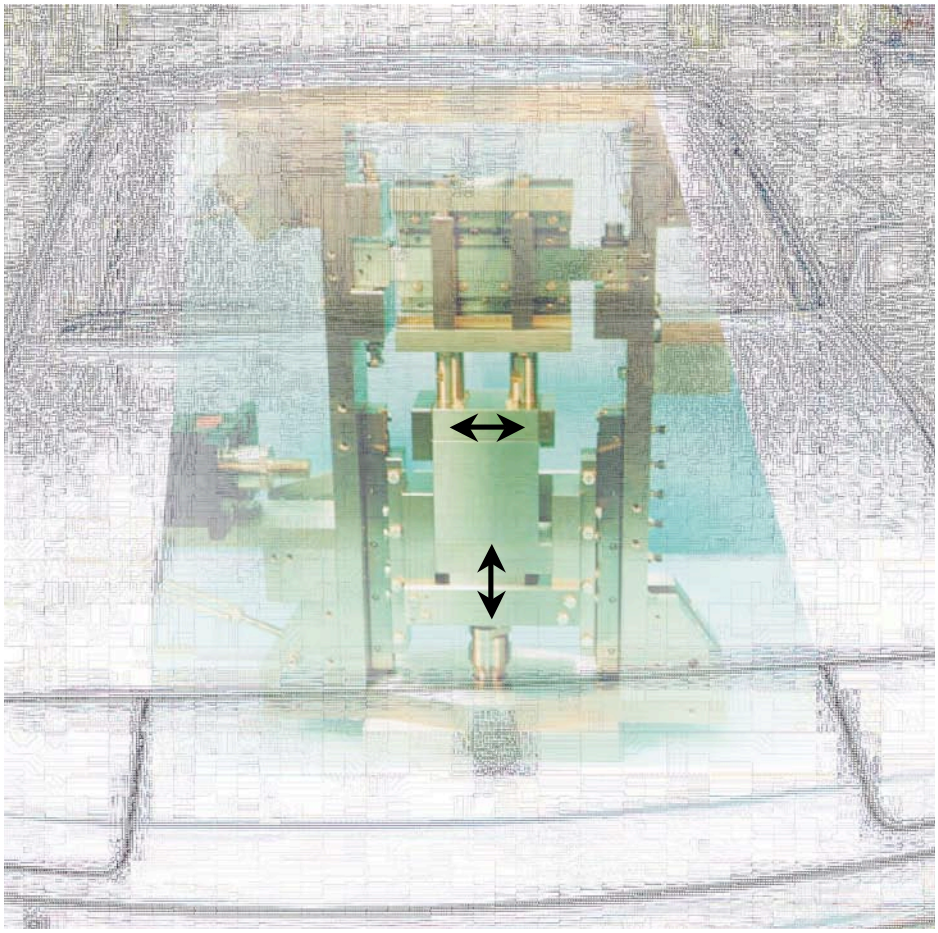

Hermen Pijlman

Sheet material characterisation by multi-axial experiments

Hermen Pijlman

This research project was sponsored by and carried out in co-operation with Corus Research, Development and Technology (Corus RD&T). The sponsoring and co-operation is gratefully acknowledged.

After the foundation of the Netherlands Institute of Metals Research (NIMR) the project was considered as a contribution to the NIMR research programme under project number 97035

De promotiecomissie:

Voorzitter en secretaris:	
Prof.dr.ir. H.J. Grootenboer	Universiteit Twente
Promotor:	
Prof.dr.ir. J. Huétink	Universiteit Twente
Assistent promotor:	
dr.ir. H. Vegter	Corus Group PLC
Leden:	
Prof.dr.ir. M.G.D. Geers	Technische Universiteit Eindhoven
Prof.dr.ir. P. van Houtte	Katholieke Universiteit Leuven
Prof.dr.ir. J. Meijer	Universiteit Twente
dr.ir. D.J. Schipper	Universiteit Twente

Title:

Sheet material characterisation by multi-axial experiments

Subject headings:

Finite element method
Vegter yield function
Bi-axial test equipment

ISBN 90-36516951

Printed by Ponsen & Looijen, Wageningen

SHEET MATERIAL CHARACTERISATION BY MULTI-AXIAL EXPERIMENTS

PROEFSCHRIFT

ter verkrijging van
de graad van doctor aan de Universiteit Twente,
op gezag van de rector magnificus,
prof.dr. F.A. van Vught,
volgens besluit van het College van Promoties
in het openbaar te verdedigen
op vrijdag 7 december 2001 te 13.15 uur.

door

Hermen Hendrik Pijlman

geboren op 23 februari 1973
te Lippenhuizen

Dit proefschrift is goedgekeurd door de promotor

Prof. dr.ir. J. Huétink

alsmede de assistent promotor

dr.ir. H. Vegter

De twee-assige tester op de omslag van dit proefschrift is ontworpen door:

ing. J. Brinkman

Summary

An advanced sheet material description is developed for finite element simulations of the deep drawing process. During deep drawing the initial flat metal sheet is plastically deformed into a desired shape. In order to obtain a product without defects or failure, the material and process conditions have to be chosen carefully. With a finite element simulation the influence of the material and process parameters can be studied before the actual process is carried out, hence a prolonged experimental trial and error process is reduced.

The yield function is the main point of focus. The yield function determines whether a stress state is elastic or plastic and is connected to the yield surface. Commonly the material parameters for the yield function are determined from uni-axial tests only. Because the results of finite element simulations appear very sensitive to variations in the yield function under multi-axial conditions, Vegter (Vegter, 1996) proposed a new yield function based on measurements of the shear (σ_{SH}), uni-axial (σ_{UN}), plane strain (σ_{PS}) and equi-bi-axial (σ_{BI}) yield stress. These measurements define the reference points of the yield surface in the principal stress space. The yield surface between the reference points is constructed with second order Bezier interpolation functions. Each Bezier interpolation function is relevant for a specified part of the principal stress space. The Vegter yield surface is illustrated in the figure on the next page.

Anisotropy is incorporated by performing the measurements in different directions of the sheet, consequently the reference points are defined for each measured direction. For intermediate directions the reference points are obtained by a Fourier interpolation technique, in this way a yield surface for any arbitrary direction is defined. Subsequently the yield function is elaborated as follows:

- The stress state is transformed into principal stresses
- The direction of the principal stresses in the sheet is determined
- The reference points of this direction are defined
- The relevant Bezier interpolation function is determined
- The yield function is derived from the principal stresses and the relevant Bezier function.

The finite element implementation of the Vegter yield function is checked and appears to be correct.

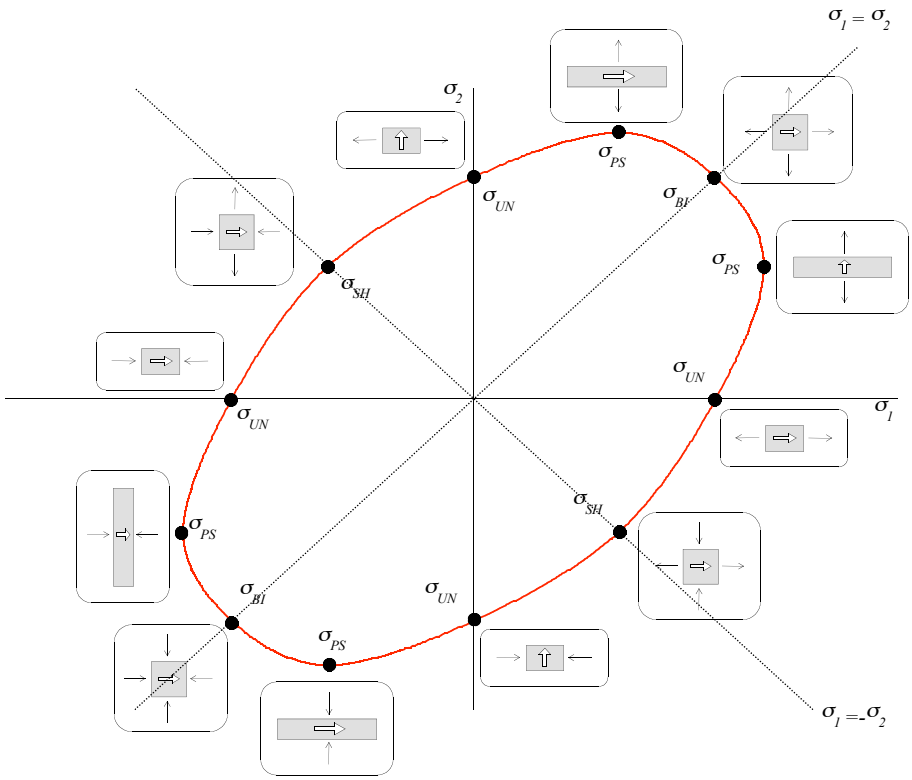

Vegter yield surface

Hardening of the material during plastic deformation is described by two models. The first hardening model is the physically based hardening model suggested by v. Liempt (v. Liempt, 1988) and Vegter (Vegter, 1991). This hardening model is able to describe the yield stress accurately for a large strain range and takes into account the influence of the deformation rate. The physically based hardening model assumes isotropic hardening behaviour, which implicates that each (multi-axial) yield stress increases with the same factor after plastic deformation. From experiments it appears that this is only valid in proportional deformation paths, hence a second hardening model is developed, taking into account the material behaviour during a cyclic deformation. This anisotropic hardening model is initially based on the theory of Vreede (Vreede, 1992). Due to the definition of the yield function in principal stresses, the model is adapted to combine it with the Vegter yield function. A start is made with extending the hardening description to general non-proportional deformations, but this extension does not give realistic results yet and needs more research.

To measure the data for the new material description, a bi-axial test equipment is developed. The test equipment is able to impose a shear deformation and a plane strain deformation. The shear deformation can be imposed in 2 directions and the plane strain deformation can be imposed in tension and compression. In this way a large variety of stress and deformation states can be investigated. In this dissertation the bi-axial test equipment is used for the next purposes:

- The determination of the shear and plane strain reference points
- The parameter determination of the anisotropic hardening model

During experiments a piece of sheet metal is fixed between two pairs of clamps. Between the clamps and at the free edges of the test piece the stress and deformation deviates from the intended values. The stress is corrected quantitatively by a finite element model of a part of the test piece. The deformation can not be predicted quantitatively with this model, hence a special deformation analysis system is purchased which directly measures the deformation from the test piece. Experiments are performed with aluminium (AA 5182) and Aluminium killed steel (AKS). It appears that the equipment can be used conveniently for the intended purposes.

The material model is validated on 3 test cases. The first test case is a bending experiment, carried out in co-operation with the University in Eindhoven. This test case is a validation of the Vegter yield function at stress states in the plane strain region. The second test case is the deep drawing of a cylindrical cup, carried out in co-operation with Corus RD&T. This test case validates the Vegter function mainly on the earing behaviour, which is known to be sensitive to differences in multi-axial yield stresses. The third test case is the deep drawing of a trapezium-shaped product. This test case validates the material model on a critical product, that means a product, which can just be manufactured without defects or material failure. It appears that in each test case the Vegter yield function gives better results than the commonly used Hill'48 yield function, hence the developed description can be considered very useful.

Finally two applications of complex deep draw products are investigated. The first is the deep drawing of a Volvo pedal box. Corus RD&T has some experience with deep drawing this product and simulations of this product can be compared with experiments at Corus. However, it appears that the process conditions can not be fixed very accurately due to wear of tools, hence the experimental results have to be interpreted with care. The second application is the deep drawing of an Audi front panel, which was used as a Benchmark at the Numisheet '99 conference. The required calculation time turns out satisfactory for this application, so it can be concluded that the developed material model can be used conveniently in real deep draw applications.

Contents

1 Scope of the research

The research in this dissertation is carried out in order to characterise sheet metal for use in finite element simulations of deep drawing processes. The deep drawing process is commonly used in the sheet metal forming for the packaging industry and the automotive industry. Examples in the packaging industry are beverage cans and pet food containers. In the automotive industry a large variety of deep drawn parts are made, for instance inner parts, stiffeners and body panels such as fenders, doors and motor hoods.

During the process of deep drawing, a sheet of metal is deformed into a desired shape by moving a punch into a die. To prevent the sheet from wrinkling, a blank holder is required. In figure 1-1 the principle of deep drawing is illustrated for a cylindrical product.

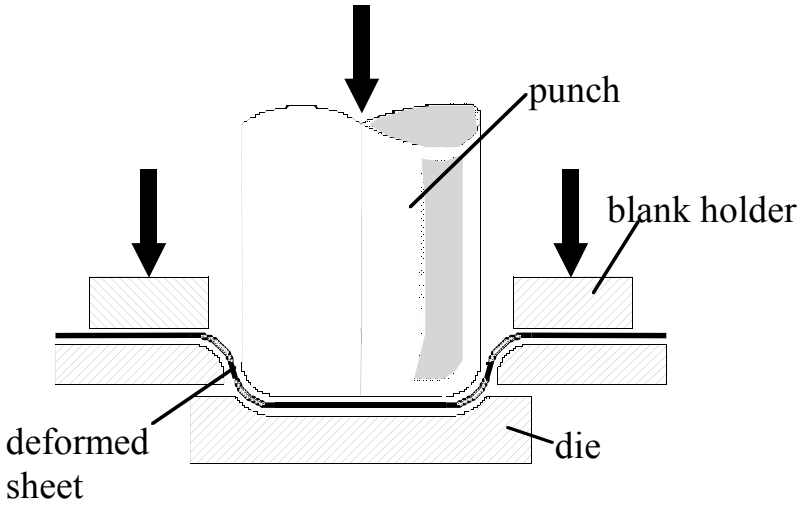

Figure 1-1 Principle of deep drawing

The shape of the punch and the die define the shape of the resulting product. During the punch displacement the material is drawn from the blank holder region into the die. The flow of material is influenced by the shape of the tools, the blank holder force, use of lubricant, the initial blank shape and the blank material.

If the process conditions and the blank are not chosen carefully, the product deviates from the intended product. Possible deviations are tears and wrinkles in the product or complete failure due to necking. Another deviation - important for outer car panels - is a non-smooth surface due to scratching and orange peel. With knowledge based on experience, many deviations can be avoided in more-or-less standard products. In order to produce a complicated part without deviations, use is made of a trial and error process. Sometimes the pre-designed tools have to be re-designed or replaced by other tools.

To reduce costs especially for tooling in the developing stage and to reduce time for new designs or concepts, use can be made of numerical simulations. With a numerical model of the deep drawing process, the influence of process parameters, blank shape and blank material can be studied before the actual process is carried out. Improvement of the quality of these simulation models will lead to further optimisation for the use of new materials such as aluminium alloys and high strength steels and new forming processes like hydroforming and rheoforming. In the scope of this research a finite element package is used as the numerical tool. The mechanics of the finite element models have achieved a high level of development (Numiform, 1998), (Numisheet, 1999) and nowadays the physics in these models have to be improved. An important item is the development of new material models in these simulation codes. The research in this dissertation focuses on the characterisation of sheet material by new mechanical tests, the derivation of the necessary equations and the implementation of these equations in a finite element code. The research is carried out in co-operation with Corus RD&T and can be considered an extension of work carried out by Vegter (Vegter, 1991) (Vegter, 1996), Vreede(Vreede, 1992) and Carleer (Carleer, 1996).

Vegter focussed on the material behaviour of sheet metal whereas Vreede developed the finite element basis for simulations of 3-dimensional sheet metal forming processes. Carleer extended the finite element basis with more sophisticated elements and an improved description of the contact between the tools and the sheet. Furthermore he made a start with the implementation of the material description of Vegter.

The research of this dissertation focuses firstly on the finite element implementation of the proposed material description of Vegter in 1996. Several material models for sheet metal are available from the literature and implemented in simulation software. Usually the material parameters for these models are determined from uni-axial tests only. However, in deep drawing all kinds of stress states occur. It is observed that the results of simulations are very sensitive to variations in the yield condition under multi-axial stress states. Therefore it is required that a material model is applied that is based on measurements under multi-axial conditions. The Vegter model has this flexibility. Besides the material parameters in the Vegter model can be chosen in such a way that most of the commonly anisotropic models are covered. For that reason the choice is made for the elaboration the Vegter material description. To carry out the required measurements for the Vegter material model, a multi-axial test equipment is developed. The improvement and application of this equipment is the second point of focus. Thirdly the Vegter yield function is extended with with 2 hardening functions. The first function is a physically based hardening function, which is based on the dissertation work of Vegter of 1991. The second function is an anisotropic hardening function, which is based on the theory of Vreede of 1992.

This dissertation starts with an introduction to sheet metal characterisation in chapter 2. Here, the modelling of sheet metal and the experimental devices for the generation of the data for the models are discussed. This chapter also provides an introduction to the finite element implementation of material models. Subsequently chapter 3 deals with the implementation of the Vegter yield function and chapter 4 discusses the implementation of the hardening functions in an implicit finite element code. In this case the functions are implemented in the code developed at the University of Twente, but the theory in these chapters can also be used conveniently for other

codes. Chapter 5 focuses on the new multi-axial test equipment. It gives a description of the equipment and explains the use of the several components. The test equipment is firstly used for determining data for the Vegter yield function. Furthermore a start is made to investigate cyclic and combined loads. In chapter 6 the implemented material description is validated on 3 test cases. The cases are simulated and carried out experimentally, so a comparison between the simulations and experiments can be made. Finally chapter 7 shows the application of the new material model in 2 simulations of complicated products.

2 Introduction to sheet material characterisation

This chapter is an introduction to sheet material characterisation. The focus will be on material modelling as well as experimental material testing. The chapter starts with some commonly used material models in finite element codes and discusses the new material model of this dissertation. The second section shows common experimental set-ups and the new set-up developed at the University of Twente (UT). Section 3 discusses the implementation of a material model in a finite element code.

2.1 Sheet material modelling

This section is an introduction to material modelling applied to sheet metal forming. In general, plastic material models are divided into two parts, one part which describes the stress states of initial yielding of the material (yield function) and a part which describes how the yield function develops after plastic deformation (hardening function). The yield function is represented by the yield surface, which is a graphical representation of yield stresses in the stress space. The hardening function describes how the yield surface changes after plastic deformation. The yield function and the hardening function are discussed separately in sections 2.1.1 and 2.1.2. Section 2.1.3 combines the yield function and the hardening function in a mathematical formulation.

2.1.1 Yield function

The yield function defines a stress state at which yielding starts. In sheet metal forming processes, the stress state is considered as plane stress. In the plane of the sheet the stresses (σ_{xx}), (σ_{yy}) and (τ_{xy}) are considered and the stresses normal to the sheet are zero. Mindlin sheet element models also take into account shear stresses (τ_{xz}) and (τ_{yz}). Appendix I shows how these stresses can be taken into consideration. In the main part of this dissertation the shear stresses (τ_{xz}) and (τ_{yz}) are omitted. The plane stress state is illustrated on a square piece of sheet metal in figure 2-1.

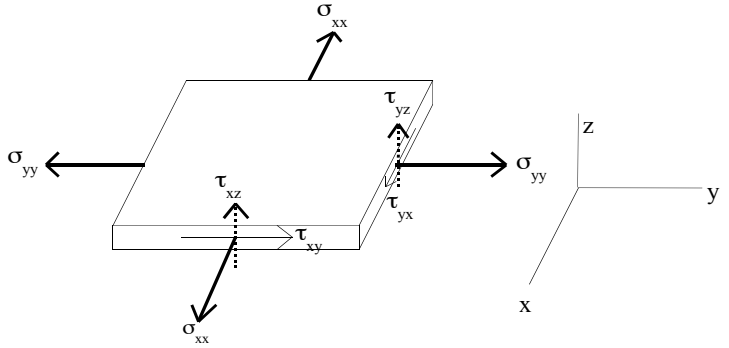

Figure 2-1 Stress state in the sheet

One of the main functions used in finite element packages is the von Mises function, which is based on the measurement of the uni-axial yield stress (σ_{un}). For a plane stress situation this function can be given by:

$$\phi = \sqrt{(\sigma_{xx} - \sigma_{yy})^2 + (\sigma_{yy})^2 + (\sigma_{xx})^2 + 6 \cdot (\tau_{xy})^2} - \sqrt{2} \cdot \sigma_{un} = 0 \qquad \textbf{2. 1}$$

The von Mises function is an isotropic yield function. No distinction is made between material behaviour normal to the sheet and in the plane of the sheet. Furthermore the yield stress states are independent of the direction in the plane of the sheet. Figure 2-3 illustrates the von Mises yield surface in the principal stress space.

Another function based on the uni-axial test is the Tresca yield function. The shape of this model is different to the von Mises model. It assumes a discontinuous gradient of the yield surface in the uni-axial yield stress. It appears that steel can be better represented by the von Mises function and that aluminium tends more towards the Tresca yield function. The Tresca yield surface is also illustrated in figure 2-3.

From uni-axial experiments it appeared that isotropic behaviour was not valid for every material. This is reflected by the measured R-values, which define the ratio between the strain in the width and thickness directions during a uni-axial tensile test, see figure 2-2.

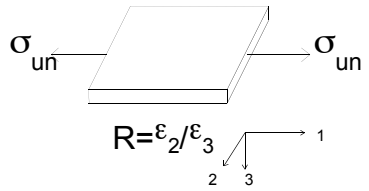

Figure 2-2 Definition of the R-value

The R-value differs from 1 in general, which means that the material behaviour in the thickness direction differs from the behaviour in the plane of the sheet. The R-value also varies for different directions in the plane of the sheet, which implies planar anisotropic material behaviour. The Hill '48 yield function incorporates this material behaviour (Hill, 1950):

$$\phi = \sqrt{\underline{\sigma} : \underline{\underline{P}} : \underline{\sigma}} - \sqrt{\frac{2}{3}(F + G + H)} \cdot \sigma_y = 0 \qquad \textbf{2. 2}$$

in which $\underline{\sigma}$ is the stress tensor and (σ_y) is the average uni-axial yield stress of the directions 0°, 45° and 90° to the rolling direction in the plane of the sheet:

$$\sigma_y = \frac{\sigma_{un}(0) + 2 \cdot \sigma_{un}(45) + \sigma_{un}(90)}{4} \qquad \textbf{2. 3}$$

The tensor $\underline{\underline{P}}$ and the factors F, G and H depend on the factors R_0, R_{45} and R_{90}, which are the R-values in the considered directions (Carleer, 1997). The Hill yield surface is shown in figure 2-3 for different R-values. In the figure no planar anisotropy is illustrated.

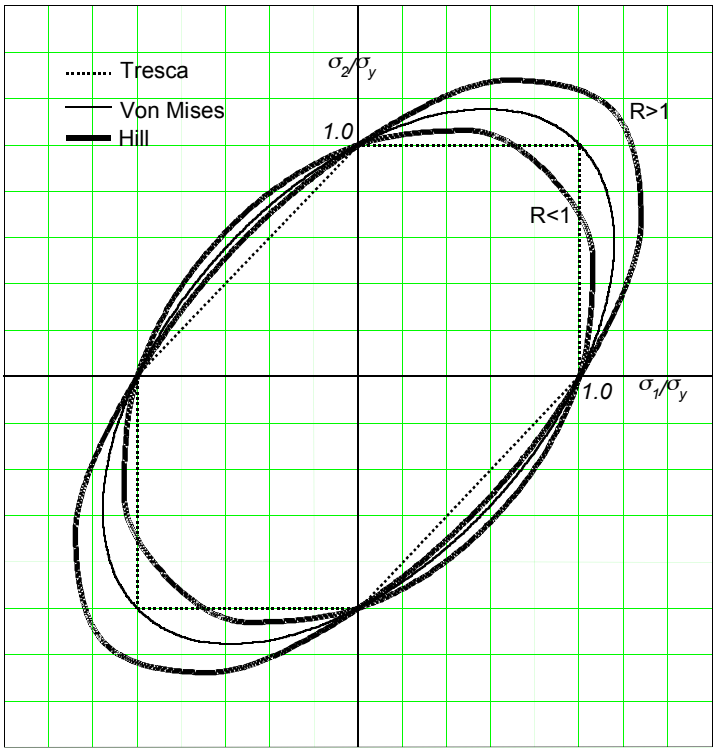

Figure 2-3 Tresca, von Mises and Hill yield surface in the principal stress space

The Hill '48 yield function is still based on uni-axial tensile tests. From several experiments it appeared that this relation is a poor approximation for some types of material. Therefore other yield functions were developed to take into account data from various multi-axial tests. An example is given by the Barlat function (Barlat, 1991). This function depends on 8 variables for a general stress situation, which can be determined from multi-axial experiments. For a plane stress situation the function depends on 5 variables (a,b,c,h,m):

$$\phi = \left|S_1 - S_2\right|^m + \left|S_1 - S_2\right|^m + \left|S_1 - S_2\right|^m = 2 \cdot \sigma_y \qquad \textbf{2. 4}$$

where S_1, S_2 and S_3 are the principal values of a symmetric matrix, which, for a plane stress situation is given by:

$$S = \begin{bmatrix} \frac{1}{3}\left(c(\sigma_{xx} - \sigma_{yy}) + b\sigma_{xx}\right) & h\tau_{xy} & 0 \\ h\tau_{xy} & \frac{1}{3}\left(a\sigma_{yy} - c(\sigma_{xx} - \sigma_{yy})\right) & 0 \\ 0 & 0 & -\frac{1}{3}\left(b\sigma_{xx} + a\sigma_{yy}\right) \end{bmatrix} \qquad \textbf{2. 5}$$

The Barlat surface is represented in figure 2-4 for 2 different values of the parameter (m). The parameters (a),(b) and (c) have the value 1 in the example, so no planar anisotropy is illustrated.

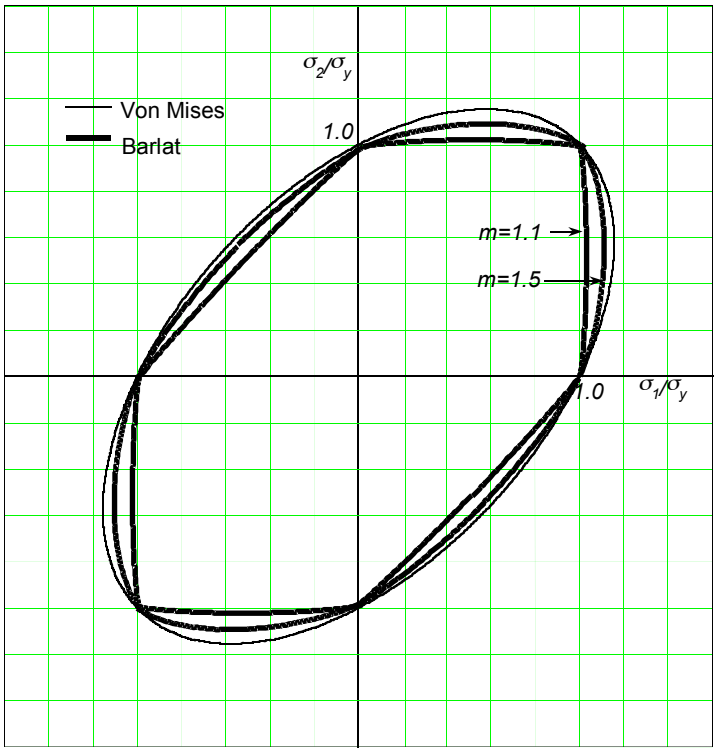

Figure 2-4 Barlat and von Mises yield surface in the principal stress space

Vegter (Vegter, 1996) proposed a new yield function which directly incorporates experimental data from multi-axial tests. The Vegter function is based on data of the shear test (σ_{SH}), the uni-axial test (σ_{UN}), the plane strain test (σ_{PS}) and the equi-bi-axial (σ_{BI}) test. The measured data can be observed in the principal stress space in figure 2-5. The points shown are called the reference points of the yield surface.

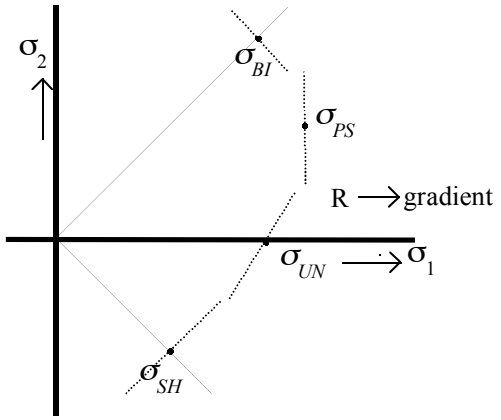

Figure 2-5 Multi-axial data in the stress-space

In order to incorporate anisotropy in the new yield function, the data are measured for different directions to the rolling direction. From experience it appears that 3 directions (0°,45° and 90°) are sufficient when 4 ears arise in deep drawing a cylindrical product.

By drawing curves through the data for different directions, surfaces for the three mentioned directions appear. Figure 2-6 illustrates the curves for the directions 0° and 45°.

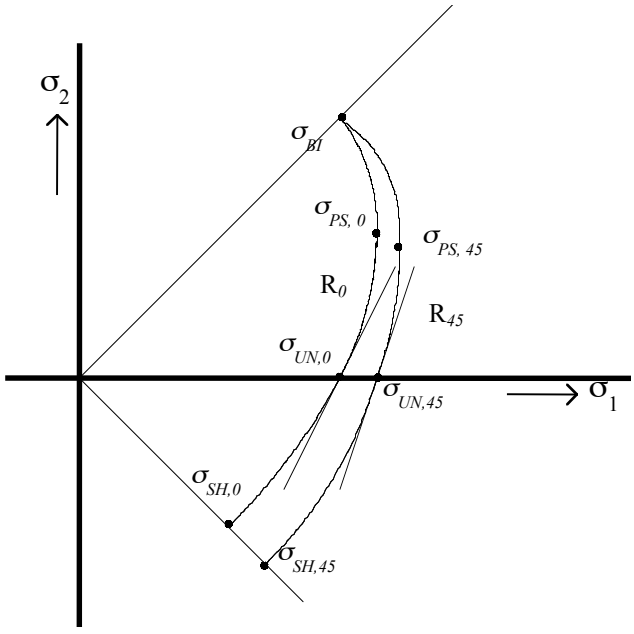

Figure 2-6 Curves through the reference points in different directions

To relate a function to the measurements, first a method to construct yield surfaces through the measured reference points must be developed. Secondly a yield surface for other angles must be defined. This is derived in detail in chapter 3.

Recently researchers put a lot of effort into microstructure based yield functions. These functions are based on the plastic behaviour of single crystals and use a homogenization scheme for the transition to polycrystals. A single crystal has a number of slip systems, depending on the type of material. A slip system consists of a slip plane in a defined direction. When the critical stress has been reached, slip occurs on the slip plane. Each crystal has an orientation in the sheet. Because sheet metal is rolled from bulk material, certain orientations develop more than others. The orientations can be measured with an X-ray diffraction technique and are commonly represented by pole figures or orientation distribution functions.

A Taylor scheme is commonly used to obtain the macroscopic behaviour of a polycrystal. In this method the deformation of each single crystal is equal to the macroscopic deformation and the macroscopic stress is determined by an average of the microstructural stresses. To comply with the macroscopic deformation, the single crystals deform by slip on the slip plane and change their orientation by rotation. A lot of research on the use of a microstructural model was carried out by van Houtte (v. Houtte, 1997).

Due to large computation times, the microstructure based functions cannot be applied directly in finite element simulations of full-scale (macroscopic) processes. An option is to calculate the yield locus on the basis of the initial orientation distribution and use this yield locus in a finite element code. For this, the Vegter yield function can be used. The reference points can be obtained by simulating the considered tests with the microstructural function.

This dissertation focuses on the Vegter yield function. This function is based on experimentally obtained multi-axial data and has the advantage of an acceptable computation time in a finite element code. Figure 2-7 illustrates the Vegter yield surface in the principal stress space together with the Hill surface. The figure illustrates that, although both surfaces have the same average uni-axial yield stress and R-value, the shape can differ to a large extent. Planar anisotropy is omitted in the example.

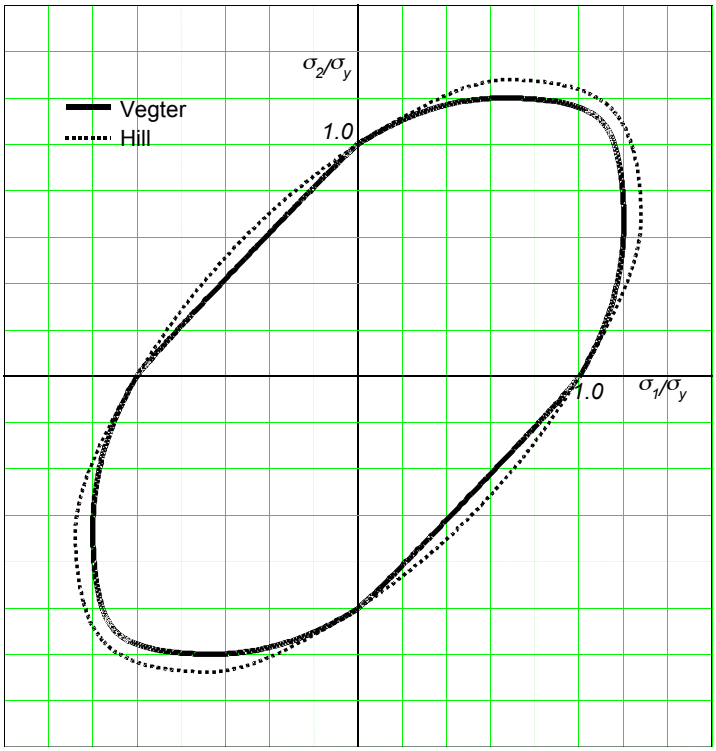

Figure 2-7 Hill and Vegter yield surface in the principal stress space

2.1.2 Hardening function

The hardening function defines the development of the yield condition after plastic deformation. In proportional deformations the hardening is commonly described by the Nadai-Ludwik function:

$$\sigma_y = C \cdot \left(\varepsilon_p + \varepsilon_0\right)^n \qquad \textbf{2. 6}$$

This function defines the yield stress (σ_y) as a function of the equivalent plastic strain (ε_p). The equivalent plastic strain is related to the plastic strain tensor by the definition of the equivalent plastic strain rate:

$$\sigma_y \dot{\varepsilon}_p = \underline{\sigma} : \underline{\dot{\varepsilon}}^p \qquad \textbf{2. 7}$$

or

$$\dot{\varepsilon}_p = \frac{\underline{\sigma}}{\sigma_y} : \underline{\dot{\varepsilon}}^p \qquad \textbf{2. 8}$$

where

is the plastic strain rate tensor

$\underline{\sigma}$ is the stress tensor

In proportional deformations, the rate form of (2. 8) can be replaced by:

2. 9

which is, for a plane stress situation:

$$\varepsilon_p = \frac{\sigma_{xx}\varepsilon_{xx}{}^p + \sigma_{yy}\varepsilon_{yy}{}^p + \tau_{xy}\gamma_{xy}{}^p}{\sigma_y} \qquad \textbf{2. 10}$$

The Nadai-Ludwik function is a phenomenological function, which does not take into account the effect of the strain rate. It does not describe the yield stress accurately for a large strain range (for instance for values till 1.0), and therefore van Liempt (v Liempt, 1988) and Vegter (Vegter, 1991) derived a hardening function based on the multiplication of dislocations with plastic deformation. This function is partly based on the theory of Bergström (Bergström, 1969). The function can describe the real hardening behaviour more accurately and takes the strain rate influence into account. In this dissertation the function is called the physically based hardening function:

$$\sigma_y = \sigma_0 + \Delta\sigma_m \cdot \left[\beta \cdot (\varepsilon_0 + \varepsilon_p) + \left\{1 - e^{-\Omega\cdot(\varepsilon_0+\varepsilon_p)}\right\}^{\frac{1}{2}}\right] + \sigma_0{}^* \cdot \left\{1 + \frac{kT}{\Delta G0} \cdot \ln\left(\frac{\dot{\varepsilon}_p}{\dot{\varepsilon}_0}\right)\right\}^{m'} \qquad \textbf{2. 11}$$

The yield stress (σ_y) is defined as a function of the equivalent strain and the equivalent strain rate. The function is discussed extensively in the first part of chapter 4 of this dissertation, where it is used in combination with the Vegter yield function.

In proportional deformations the hardening can be considered isotropic. In that case the yield surface does not translate in the stress space. Only the size of the yield surface changes after plastic deformation, see figure 2-8. The yield surface before ($\sigma_y=\sigma_0$) and after plastic deformation is illustrated by the dotted line and the solid line respectively. When the isotropic hardening function is used in a tension-compression deformation, the material starts to yield at minus the current yield stress after the load reversal, see figure 2-9.

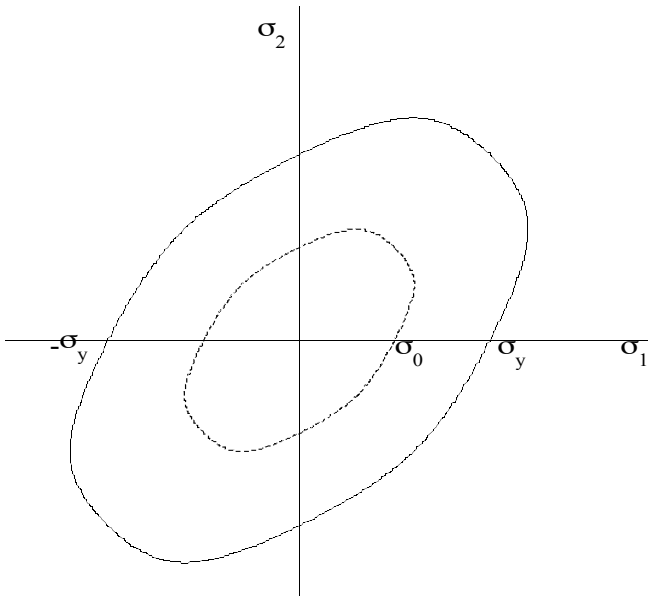

Figure 2-8 Development of the yield surface at isotropic hardening

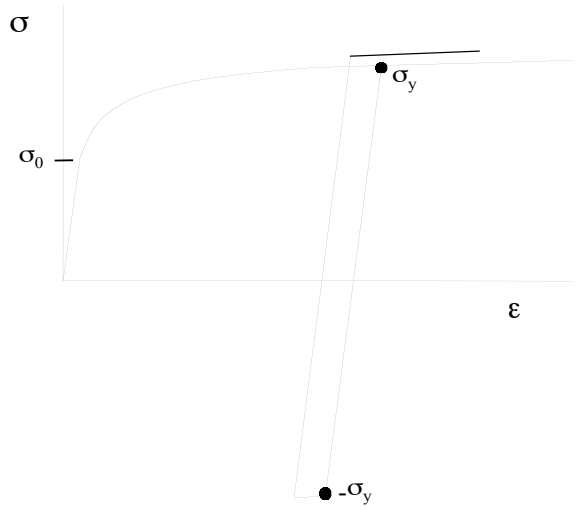

Figure 2-9 Yield behaviour after a load reversal for isotropic hardening

Another model suggests that the yield surface only translates in the stress space while its size remains constant. This type of hardening is called kinematic hardening, see figure 2-10. After a load reversal the material starts to yield at a stress change of twice the initial yield stress (σ_0), see figure 2-11.

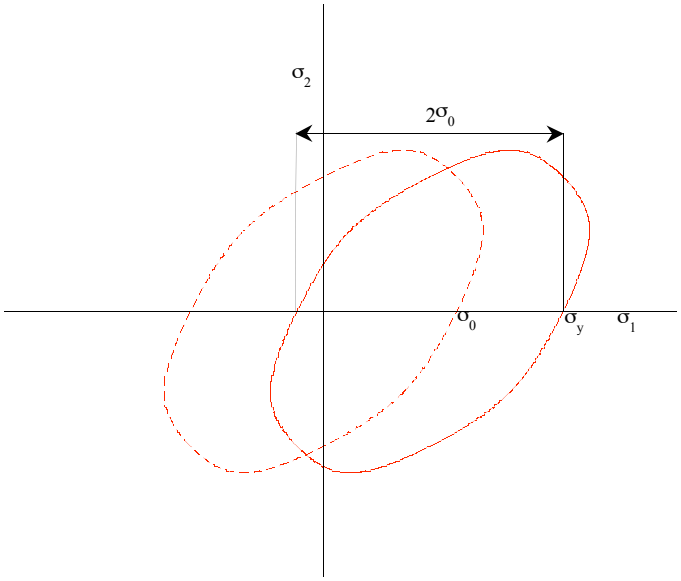

Figure 2-10 Development of the yield surface at kinematic hardening

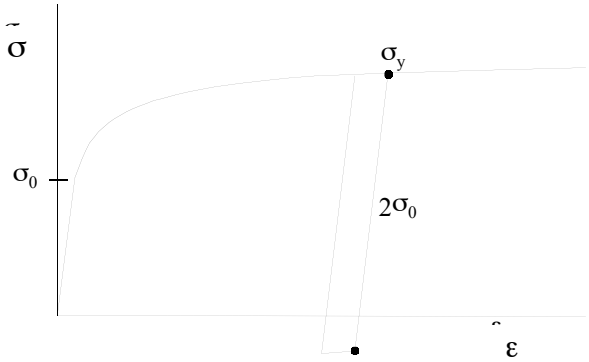

Figure 2-11 Yield behaviour after a load reversal for kinematic hardening

The real stress - strain behaviour lies somewhere in between the kinematic hardening and the isotropic hardening, illustrated by figure 2-12. It appears that after a load reversal the material starts to yield after about twice the initial yield stress. At this stress state a relatively large hardening rate is observed. After further deformation, the hardening rate tends towards the same level as before the load reversal, illustrated by the parallel dotted lines in figure 2-12. The yield point directly after a load reversal is predicted well by the kinematic hardening function and the behaviour after further plastic behaviour is predicted well by the isotropic hardening function.

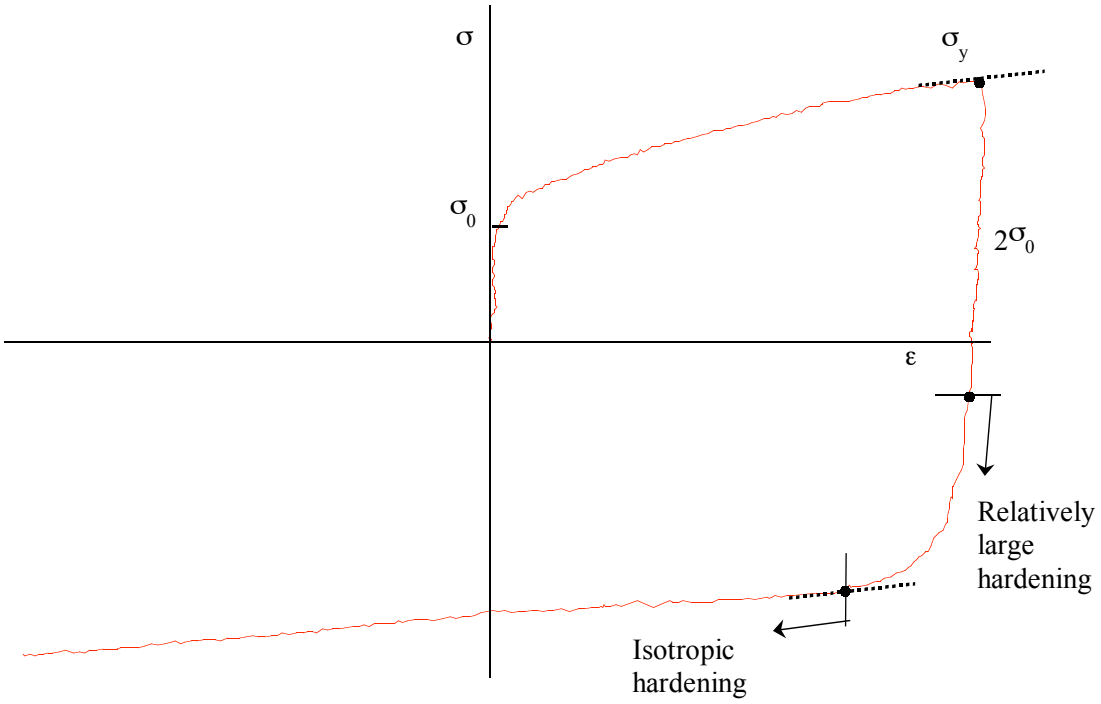

Figure 2-12 Experimental stress strain relation at a load reversal

To describe the experimental stress-strain behaviour a combination of isotropic and kinematic hardening can be used (Vreede, 1992). The model developed here makes use of 2 surfaces. One surface defines the yield condition directly after a load change and the other surface defines the hardening after further deformation. This model will be described extensively in the second part of chapter 4, where it is used in combination with the Vegter yield function.

2.1.3 Mathematical formulation

The mathematical formulation of a yield function after plastic deformation is given by:

$$\phi = \phi(\underline{\sigma}, \underline{\beta}) = 0 \qquad \textbf{2. 12}$$

where

ϕ is the yield function
$\underline{\sigma}$ is the stress tensor
$\underline{\beta}$ is the hardening tensor

This formulation captures both the yield condition and the hardening.

Expression (2. 12) defines the stress and the strain after plastic deformation. The plastic strain rate is defined, using the normality principle of Drucker, by:

$$\underline{\dot{\varepsilon}}^{p} = \dot{\lambda}\frac{\partial \phi}{\partial \underline{\sigma}} \qquad \textbf{2. 13}$$

where

is the plastic strain rate tensor

$\dot{\lambda}$ is the plastic multiplier rate, which represents the plastic deformation rate

$\frac{\partial \phi}{\partial \underline{\sigma}}$ is the normal to the yield locus

The stress in a co-rotational reference frame is defined, using Hooke's law as follows:

$$\underline{\dot{\sigma}} = \underline{\underline{E}} : \dot{\varepsilon}^{e} = \underline{\underline{E}} : \left(\underline{\dot{\varepsilon}} - \underline{\dot{\varepsilon}}^{p}\right) \qquad \textbf{2. 14}$$

where

$\underline{\dot{\sigma}}$ is the stress rate tensor
$\underline{\underline{E}}$ is the elasticity tensor
$\dot{\varepsilon}^{e}$ is the elastic strain rate tensor
$\underline{\dot{\varepsilon}}$ is the strain rate tensor
$\underline{\dot{\varepsilon}}^{p}$ is the plastic strain rate tensor

Substitution of (2. 13) into (2. 14) gives:

$$\underline{\dot{\sigma}} = \underline{\underline{E}} : \left(\underline{\dot{\varepsilon}} - \underline{\dot{\varepsilon}}^{p}\right) = \underline{\underline{E}} : \left(\underline{\dot{\varepsilon}} - \dot{\lambda}\frac{\partial \phi}{\partial \underline{\sigma}}\right) \qquad \textbf{2. 15}$$

The value of the yield function stays zero during plastic deformation:

$$\dot{\phi} = \frac{\partial \phi}{\partial \underline{\sigma}} : \underline{\dot{\sigma}} + \frac{\partial \phi}{\partial \underline{\beta}} : \underline{\dot{\beta}} = 0 \qquad \textbf{2. 16}$$

The second term is proportional to the plastic multiplier rate, so this term is written as:

$$\frac{\partial \phi}{\partial \underline{\beta}} : \underline{\dot{\beta}} = f\dot{\lambda} \qquad \textbf{2. 17}$$

and consequently

$$\dot{\phi} = \frac{\partial \phi}{\partial \underline{\sigma}} : \underline{\dot{\sigma}} + f\dot{\lambda} = 0 \qquad \textbf{2. 18}$$

Note that (f) represents the hardening rate when plastic deformation occurs. This term can represent any kind of hardening.

Substitution of (2. 15) into (2. 18) gives:

$$\dot{\phi} = \frac{\partial \phi}{\partial \underline{\sigma}} : \dot{\underline{\sigma}} + f\dot{\lambda} = \frac{\partial \phi}{\partial \underline{\sigma}} : \underline{\underline{E}} : \left(\dot{\underline{\varepsilon}} - \dot{\lambda} \frac{\partial \phi}{\partial \underline{\sigma}} \right) + f\dot{\lambda} = 0 \qquad \textbf{2. 19}$$

Hence the plastic multiplier can be written as:

$$\dot{\lambda} = \frac{\frac{\partial \phi}{\partial \underline{\sigma}} : \underline{\underline{E}} : \dot{\underline{\varepsilon}}}{\frac{\partial \phi}{\partial \underline{\sigma}} : \underline{\underline{E}} : \frac{\partial \phi}{\partial \underline{\sigma}} - f} \qquad \textbf{2. 20}$$

Now the stress rate - strain rate relation is obtained by

$$\dot{\underline{\sigma}} = \underline{\underline{E}} : \left(\dot{\underline{\varepsilon}} - \dot{\underline{\varepsilon}}^{p} \right) = \underline{\underline{E}} : \left(\dot{\underline{\varepsilon}} - \frac{\frac{\partial \phi}{\partial \underline{\sigma}} \frac{\partial \phi}{\partial \underline{\sigma}} : \underline{\underline{E}} : \dot{\underline{\varepsilon}}}{\frac{\partial \phi}{\partial \underline{\sigma}} : \underline{\underline{E}} : \frac{\partial \phi}{\partial \underline{\sigma}} - f} \right) = \left(\underline{\underline{E}} - \underline{\underline{Y}} \right) : \dot{\underline{\varepsilon}} \qquad \textbf{2. 21}$$

where

$$\underline{\underline{Y}} = \left(\frac{\underline{\underline{E}} : \frac{\partial \phi}{\partial \underline{\sigma}} \frac{\partial \phi}{\partial \underline{\sigma}} : \underline{\underline{E}}}{\frac{\partial \phi}{\partial \underline{\sigma}} : \underline{\underline{E}} : \frac{\partial \phi}{\partial \underline{\sigma}} - f} \right) \qquad \textbf{2. 22}$$

2.2 Experiments

In order to obtain data for the Vegter model, experimental data under multi-axial stress conditions are used. In this section the tests and set-ups are described. The tests are discussed in detail in section 2.2.1, in section 2.2.2 the experimental set-ups are shown.

2.2.1 Required tests

The following tests are required for the Vegter yield function (see also figure 2-5):

Shear test

This test defines the location and the gradient of the shear point of the Vegter yield surface. The data can be obtained by applying opposite loads in 2 perpendicular directions, see figure 2-13. This experiment determines the pure shear yield stress. The white arrow in the test piece denotes the rolling direction, which can be chosen as desired. The black arrows indicate the stress state.

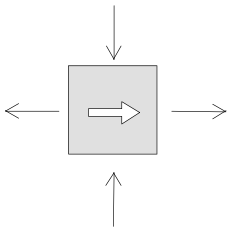

Figure 2-13 Pure shear test

It is difficult to keep both loads exactly the same during the test. Therefore the shear experiment is carried out by clamping a piece of sheet metal on two sides and prescribing one clamp in the transverse direction (figure 2-14). This test is called the simple shear test.

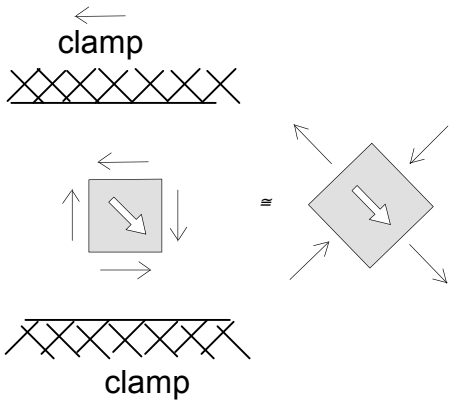

Figure 2-14 Simple shear test

Uni-axial test

The conventional uni-axial test defines the location and the gradient of the uni-axial reference point. The gradient is related to the R-value:

2. 23

Plane strain test

The plane strain test defines the location of the plane strain point in the first principal stress direction. A tensile test is performed on a piece of sheet metal with a large width compared to its length. The second principal stress is not determined because the stress in transverse direction cannot be measured. The gradient in the plane strain point is infinite due to a zero strain in the transverse direction.

Equi-bi-axial test

The equi-bi-axial test defines the position and the gradient of the equi-bi-axial point. The data can be obtained by applying the same load in 2 mutually perpendicular directions, see the left of figure 2-15.

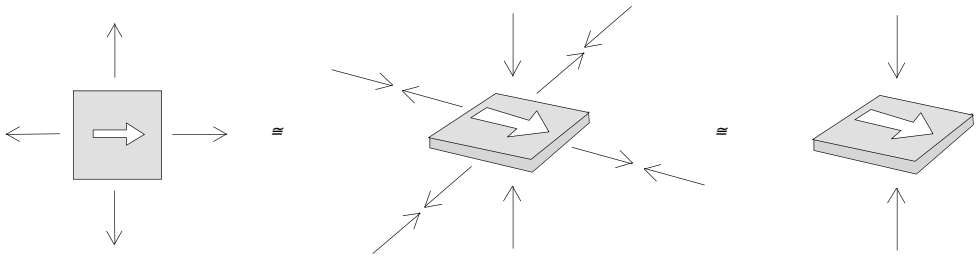

Figure 2-15 Equi-bi-axial test

It is difficult to keep both stresses exactly the same. The material is assumed to behave independently relative to a hydrostatic pressure (middle of figure 2-15). Therefore the experiment can also be performed by compressing the sheet in the normal direction, see the right of figure 2-15. The gradient is determined by the strain according to the normality principle of Drucker.

The required data for the Vegter yield function are listed in table 2-1. Figure 2-5 illustrates the data in the principal stress space.

Measurement	σ_1	σ_2	gradient
Equi-bi-axial test	σ_{BI}	= σ_{BI}	$-d\varepsilon_1/d\varepsilon_2$
Plane strain test	σ_{PS}	not measured	∞
Uni-axial test	σ_{UN}	= 0	$-d\varepsilon_1/d\varepsilon_2$
Shear test	σ_{SH}	= $-\sigma_{SH}$	$-d\varepsilon_1/d\varepsilon_2$

Table 2-1 Data for the Vegter yield function

2.2.2 Experimental set-ups

Several experimental set-ups have been developed for specific purposes. For instance, Miyauchi (Miyauchi, 1987) developed a shear test to investigate material behaviour in a shear deformation. Recently some set-ups have been developed which can impose more than one type of deformation. These set-ups have the advantage that combinations of deformations can be imposed on the same test piece. Some can impose different deformations in succession without detaching the test piece from the necessary equipment. This section focuses on a few recent developments.

A well known experimental technique is the Nakazima test. This test is often used to determine the forming limit curves of materials. The test deforms a piece of sheet metal with a hemispherical punch, a cylindrical die and a blank holder with draw beads. The blank holder and draw beads are applied to restrict the material from flowing into a cylindrical die. Grease and a polymer disk are used to reduce the friction between the punch and the test piece. The experimental set-up is shown in figure 2-16. By varying the width (W) of the test pieces, the stresses range from uni-axial to equi-bi-axial. A narrow test piece will show a uni-axial stress whereas a ‘square’ shape of the test piece will show stresses in the equi-bi-axial region. This set-up cannot impose different deformations to the same test piece, nor can a successive pattern of deformations be applied. Moreover a complete control of the strain path is not guaranteed.

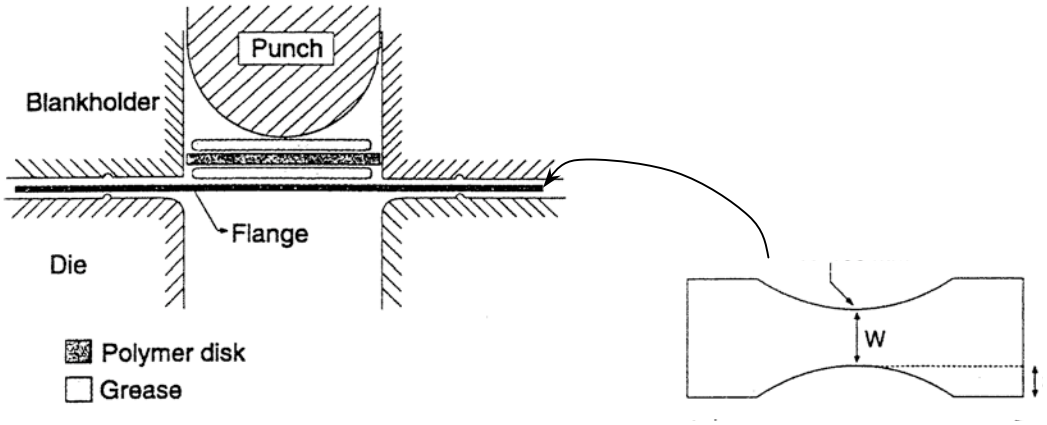

Figure 2-16 Nakazima experiment principle (Knockaert, 2001)

Another multi-axial test set-up was developed at Inpro (Inpro, 1989). Inpro uses a cross test set-up, which deforms a square piece of sheet metal in two perpendicular directions. The two directions can be controlled separately. The forces applied on the test piece are transmitted through clamping arms. Multiple arms are applied to ensure that a tensile force in one direction does not effect the forces in the perpendicular direction. This test has been used by several researchers, see for instance (Hoverlin, 1998). The test set-up is illustrated in figure 2-17.

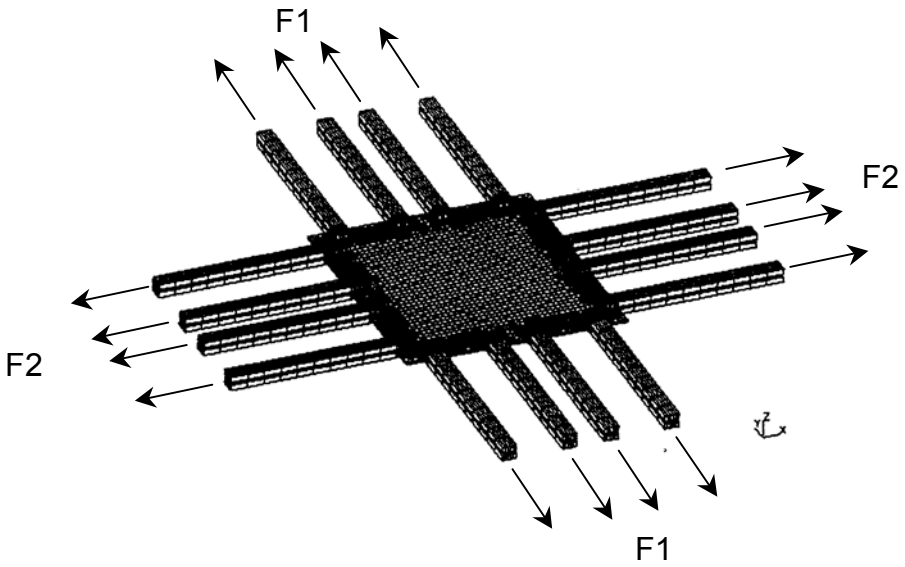

Figure 2-17 Cross test principle (Hoverlin, 1998)

By altering the ratio of the forces in the two directions (F1 and F2), the stresses range from uni-axial to equi-bi-axial. A tensile force in one direction will show a uni-axial stress whereas two equal tensile forces will impose an equi-bi-axial stress. This set-up can impose different deformations to the same test piece. A successive pattern of deformations can also be applied. The set-up does not permit a compression load in either direction.

At the university of Twente a bi-axial test equipment has been designed which is capable of combining a plane strain deformation together with a shear deformation on a piece of sheet metal. The shear deformation can be imposed in 2 directions and the plane strain deformation can be imposed in tension and compression. The principle of the equipment is illustrated in figure 2-18.

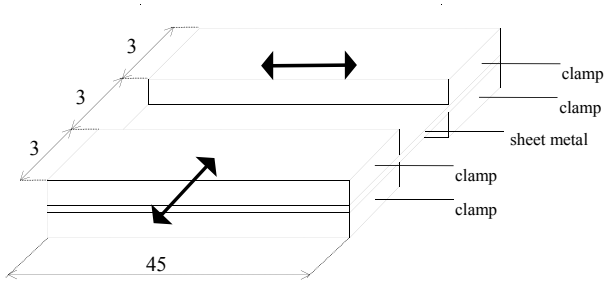

Figure 2-18 Bi-axial equipment principle

A piece of sheet metal is clamped between two pairs of clamps. The first pair can be moved in the tensile direction, which imposes a plane strain stress. The second pair can be moved in a transverse direction, which imposes a shear stress. The equipment allows for a cyclic pattern of the same deformations as well as a successive pattern of different deformations. Currently the equipment can be considered a prototype and is being improved. The bi-axial test equipment is discussed in chapter 5 of this dissertation.

For the sake of completeness it is mentioned that also the Snecma division in France uses a similar principle to test the material behaviour of elastomers (Paulus, 1999). The principle is illustrated in figure 2-19.

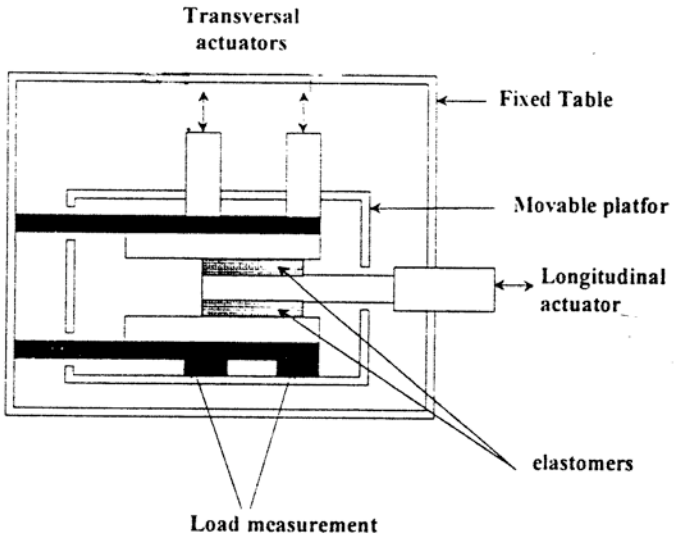

Figure 2-19 Snecma principle

2.3 Finite elements

Within the framework of the current project, the Vegter yield function and the hardening models described earlier are implemented in a finite element code. In this section the finite element implementation is introduced.

The Finite Element Method is used for calculating data of complicated products, which cannot be obtained analytically. The finite element method divides the total product with a complicated shape into discrete parts, called elements, with a simple shape. By connecting the elements, the behaviour of the complete product is obtained. Because the shape of the elements can never describe the real shape of the product, the calculated data of the product are always an approximation.

In this dissertation the finite element method is used for simulations of sheet metal forming processes. As an example a sheet metal product divided in triangular elements is shown in figure 2-20. The figure zooms in at one element whose position is defined by the 3 corner nodes. The complete forming process is divided into steps, during which a part of the total deformation is imposed. The data calculated within each step are called the incremental data.

Internal element data (stresses, strains) are stored in integration points. Element and nodal properties are determined by numerical integration, using the integration point data. The integration points are defined at certain positions in the element. In this dissertation 3 integration points in the plane of the sheet and 2 to 7 through the thickness are used, see figure 2-20:

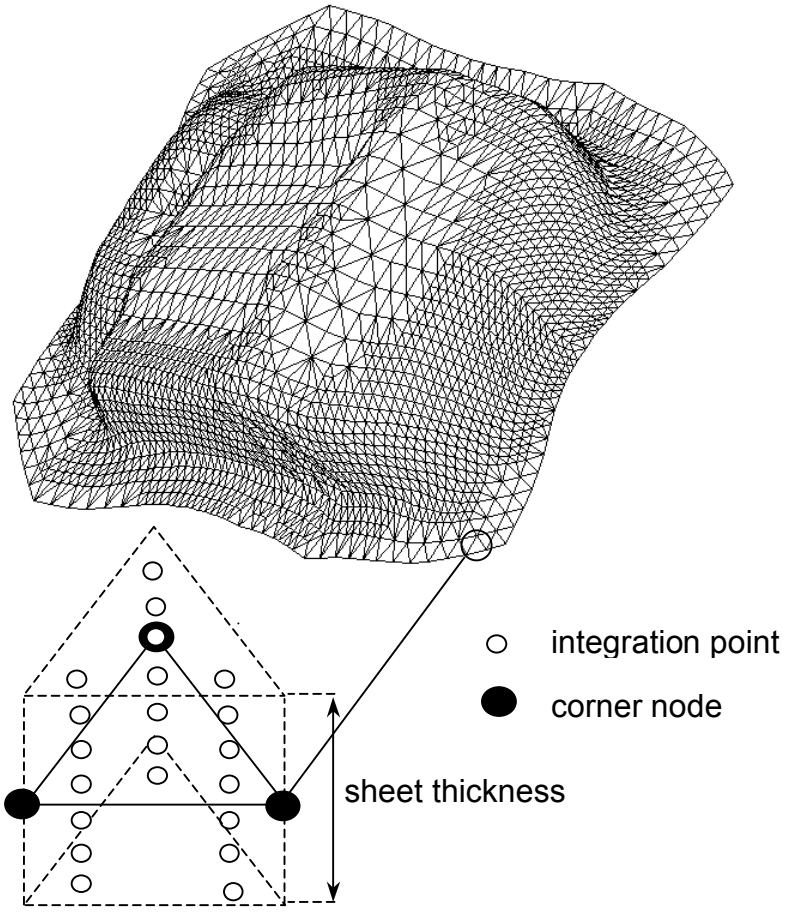

Figure 2-20 Sheet metal product divided into triangular elements with 3 integration points in the plane of the sheet and 7 through the thickness

An extensive overview of the finite element method applied to sheet metal forming is given by (Meinders, 1999). A short overview is given here, starting with the weighted force - equilibrium of a plastically deformed product:

2. 24

where

is the nodal displacement increment vector
$\{F_{\text{int}}\}$ is the nodal internal force vector
$\{F_{\text{int}}\}$ is the nodal external force vector

Equation (2. 24) is a non-linear equation. A Newton-Raphson scheme is used to solve the equation, see also figure 2-24:

$$[K\{\Delta u^i\}]\{\Delta u^{i+1}\} - \{\Delta u^i\} = \{F_{ext}\} - \{F_{\text{int}}\{\Delta u^i\}\} \qquad \textbf{2. 25}$$

with

$$[K\{\Delta u\}] = \frac{d\{F_{\text{int}}\{\Delta u\}\}}{d\{\Delta u\}}$$

The matrix [K{Δu}] is called the stiffness matrix. The Newton-Raphson process is described in the following steps:

1. The stiffness matrix is constructed with a displacement increment vector $\{\Delta u^0\}$ equal to zero:

   $$[K] = [K\{\Delta u^0\}] \qquad \textbf{2. 26}$$

2. With this stiffness matrix the displacement increment $\{\Delta u^1\}$ is calculated by (2. 25). Based on this displacement increment, the internal force vector $\{F_{\text{int}}\{\Delta u^1\}\}$, abbreviated as $\{F_{\text{int}}^1\}$ is calculated:

   $$\{F_{\text{int}}^1\} = \int_V \{B^T\}\underline{\sigma}^1 dV \qquad \textbf{2. 27}$$

   where

   $\{B^T\}$ is the vector with tensor functions which relate the strain increment to the nodal displacements

3. A new stiffness matrix is constructed :

   $$[K] = [K\{\Delta u^1\}] \qquad \textbf{2. 28}$$

4. With the new stiffness matrix solutions for $\{\Delta F_{\text{int}}^2\}$ and $\{\Delta u^2\}$ are obtained by (2. 25). The procedure is repeated until the internal force increment vector is close enough to the external force increment.

This iterative procedure is called the main iteration process in the finite element method. For the material model the iteration process has two implications. The first implication is the construction of the stiffness matrix, indicated by the tangent on the force-displacement curve in figure 2-24. The second implication is the stress determination in order to obtain the internal force vector, indicated by the vertical dotted lines in figure 2-24. The following sections discuss these processes in more detail.

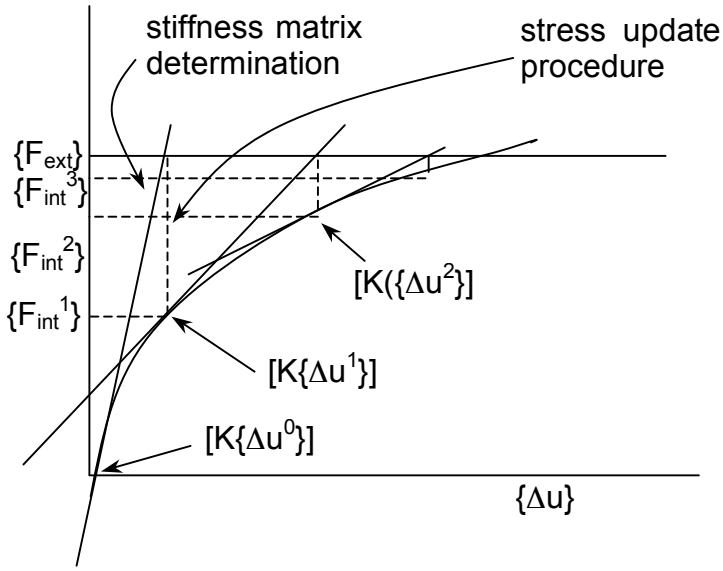

Figure 2-24 Numerical finite element solution process

2.3.1 Stiffness matrix determination

The global stiffness matrix is composed of the local element stiffness matrices. The element continuum stiffness matrix is defined by:

$$[K] = \int_V [\underline{B}]^T : \left(\underline{\underline{E}} - \underline{\underline{Y}}\right) : [\underline{B}] dV \qquad \textbf{2. 29}$$

The tensor ($\underline{\underline{Y}}$) incorporates the plastic material behaviour:

$$\underline{\underline{Y}} = \left(\frac{\underline{\underline{E}} : \frac{\partial \phi}{\partial \underline{\sigma}} \frac{\partial \phi}{\partial \underline{\sigma}} : \underline{\underline{E}}}{\frac{\partial \phi}{\partial \underline{\sigma}} : \underline{\underline{E}} : \frac{\partial \phi}{\partial \underline{\sigma}} - f} \right) \qquad \textbf{2. 30}$$

where

$\underline{\underline{E}}$ is the elasticity tensor

$\frac{\partial \phi}{\partial \underline{\sigma}}$ is the derivative of the yield function

f is the hardening parameter

Expression (2. 30) indicates that the derivative of the yield function and the hardening parameter must be determined in order to define the stiffness matrix. It is referred to in the implementation of the new material model in chapters 3 and 4.

2.3.2 Stress update procedure

The stress update starts by treating the total strain increment as elastic and calculating the corresponding stress:

$$\underline{\sigma}_t = \underline{\sigma} + \underline{\underline{E}} : \Delta\underline{\varepsilon} \qquad \textbf{2. 31}$$

where ($\underline{\sigma}_t$) is called the trial stress tensor and ($\underline{\sigma}$) is the stress at the beginning of the procedure. When the stress is inside the yield surface (ϕ<0), the deformation is elastic and the procedure stops. When the stress is outside the yield surface (ϕ>0), plastic deformation has occurred. The incremental form of (2. 15) is used to project the trial stress ($\underline{\sigma}_t$) onto the new stress ($\underline{\sigma}_n$) on the yield surface:

$$\underline{\sigma}_n = \underline{\sigma} + \underline{\underline{E}} : \left[\Delta\varepsilon - \Delta\lambda \left(\frac{\partial \phi}{\partial \underline{\sigma}} \right) \right] = \underline{\sigma}_t - \Delta\lambda \underline{\underline{E}} \cdot \left(\frac{\partial \phi}{\partial \underline{\sigma}} \right) \qquad \textbf{2. 32}$$

This stress projection is handled in detail in chapter 4 of this dissertation. The parameter ($\Delta\lambda$) is determined by the fact that the value of the yield function is zero after projection.

$$\phi\left(\underline{\sigma}_t - \Delta\lambda \underline{\underline{E}} \cdot \left(\frac{\partial \phi}{\partial \underline{\sigma}} \right), \underline{\beta} \right) = 0 \qquad \textbf{2. 33}$$

This equation is non-linear, because the yield function (ϕ) depends on the stress ($\underline{\sigma}_n$) and the hardening tensor ($\underline{\beta}$). The hardening tensor ($\underline{\beta}$) is a function of the derivative of the yield function to this tensor ($\partial\phi/\partial\underline{\beta}$), the hardening parameter (f), the plastic multiplier (λ) and the plastic multiplier rate, see (2. 17). The plastic multiplier rate is assumed to be directly related to the plastic multiplier increment ($\Delta\lambda$):

$$\underline{\beta} = \underline{\beta}\left(\frac{\partial \phi}{\partial \underline{\beta}}, f, \lambda, \Delta\lambda \right) \qquad \textbf{2. 34}$$

where

λ is the plastic multiplier
$\Delta\lambda$ is the plastic multiplier increment

A numerical procedure solves equation (2. 33):

1. The hardening tensor $\underline{\beta}$ is calculated putting $\Delta\lambda^0$ equal to 0:

$$\underline{\beta} = \underline{\beta}\left(\frac{\partial\phi}{\partial\underline{\beta}}, f, \lambda, \Delta\lambda^0\right) \qquad \textbf{2. 35}$$

2. Next a new $\Delta\lambda^1$ is calculated, satisfying:

$$\phi\left(\underline{\sigma}_t - \Delta\lambda^1 \underline{\underline{E}} \cdot \left(\frac{\partial\phi}{\partial\underline{\sigma}}\right), \underline{\beta}\right) = 0 \qquad \textbf{2. 36}$$

3. With this solution the hardening tensor $\underline{\beta}$ is calculated with the new $\Delta\lambda^1$:

$$\underline{\beta} = \underline{\beta}\left(\frac{\partial\phi}{\partial\underline{\beta}}, f, \lambda, \Delta\lambda^1\right) \qquad \textbf{2. 37}$$

4. Subsequently a new $\Delta\lambda^2$ is calculated and so on. The procedure is repeated until convergence has been reached.

In the finite element code used here the hardening parameter (f) is not updated during the increment, to keep the procedure stable. The procedure is illustrated by scheme 3-1, which indicates that the stress must be projected to the yield surface and that the hardening tensor ($\underline{\beta}$) must be determined. This scheme is referred to in the implementation of the new material model in chapters 3 and 4.

$$\underline{\sigma}_t = \underline{\sigma} + \underline{\underline{E}} \cdot \Delta\underline{\varepsilon}$$

Initialisation of i, $\Delta\lambda^i$, $\Delta\lambda^{i-1}$

While $\dfrac{\Delta\lambda^i - \Delta\lambda^{i-1}}{\Delta\lambda^{i-1}} > error$ do

$$\frac{\partial\phi}{\partial\underline{\beta}} = \frac{\partial\phi}{\partial\underline{\beta}}(\underline{\sigma}, \underline{\beta})$$

$$\underline{\beta} = \underline{\beta}\left(\frac{\partial\phi}{\partial\underline{\beta}}, f, \lambda, \Delta\lambda^i\right)$$

Determine $\Delta\lambda^{i+1}$ by

$$\underline{\sigma}_n = \underline{\sigma}_t - \Delta\lambda^{i+1}\underline{\underline{E}} \cdot \left(\frac{\partial\phi}{\partial\underline{\sigma}}\right) \quad \text{with} \quad \phi(\underline{\sigma}_n, \underline{\beta}) = 0$$

i=i+1

End while

Scheme 2-1 Stress update procedure

3 Elaboration of the Vegter yield function

3.1 General outline

In 1996 Vegter (Vegter, 1996) proposed an advanced yield function which directly uses experimental data at bi-axial stress states. The Vegter yield function is based on data of the shear test (σ_{SH}), the uni-axial test (σ_{SH}), the plane strain test (σ_{PS}) and the equi-bi-axial (σ_{BI}) test. These data define the reference points of the Vegter yield surface, see figure 3-1.

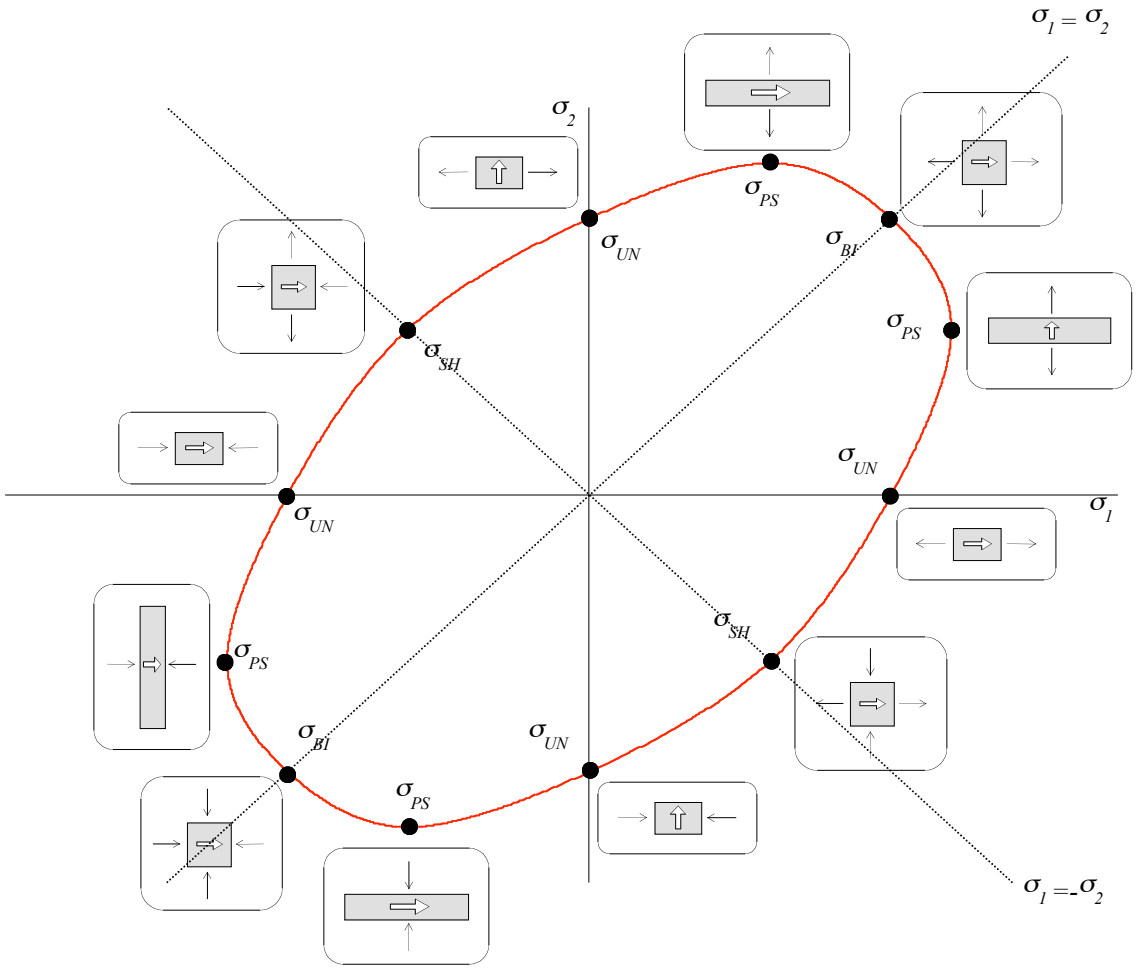

Figure 3-1 Vegter yield surface

Each reference point defines a location and a gradient of the yield surface in the principal stress space. The reference points are obtained by well known current experimental techniques. If additional experimental data can be obtained by new techniques in the future, the Vegter yield function can easily be adapted to incorporate more reference points into the description.

For isotropic material a complete yield surface is determined by 12 reference points. This number can be reduced for the following reasons:

- The principal stresses are defined in such a way that $\sigma_1 > \sigma_2$. Therefore the reference points above the line $\sigma_1 = \sigma_2$ are not required, which leads to a reduction of the number of points to 7.
- Initially it is assumed that the material yields at the same absolute stress under a compression load and under a tension load. Therefore the reference points under the line $\sigma_1 = -\sigma_2$ are related to the reference points above this line by symmetry conditions (section 3.2.3). This reduces the number of points to 4.

This chapter provides the implementation of the Vegter yield function in the stiffness matrix and the stress update algorithm in a finite element code. The basis is the mathematical description of the yield locus, which is elaborated in section 3.2. The actual implementation is described in sections 3.3 and 3.4.

3.2 Yield function definition

In this section the yield function of the Vegter yield locus is derived. Section 3.2.1 starts with the interpolation technique of the yield locus between the reference points. Section 3.2.2 discusses the extension to anisotropic behaviour. Together with symmetry conditions in section 3.2.3, the yield function is elaborated in 3.2.4.

3.2.1 Yield locus interpolation

The yield locus is constructed by a quadratic Bezier interpolation function. This interpolation function uses 2 reference points and a hinge point, see figure 3-2. The hinge point is determined by the intersection of the gradient of the yield locus in the reference points.

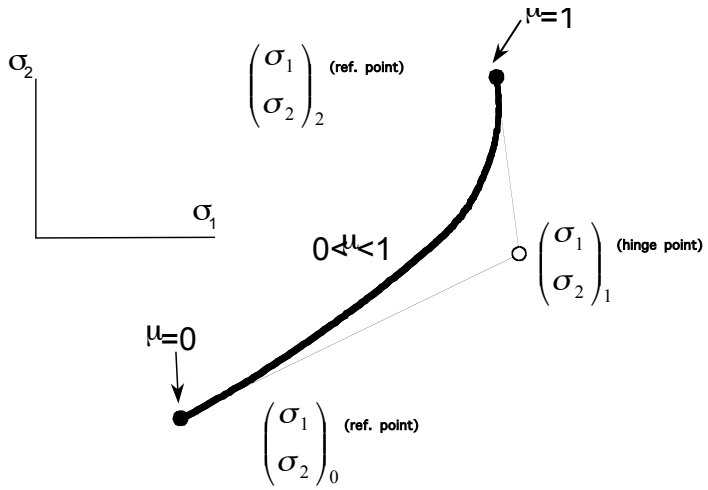

Figure 3-2 Bezier interpolation curve

The mathematical description of the Bezier interpolation is given by:

$$\begin{pmatrix}\sigma_1\\ \sigma_2\end{pmatrix} = \begin{pmatrix}\sigma_1\\ \sigma_2\end{pmatrix}_0 + 2\mu\cdot\left(\begin{pmatrix}\sigma_1\\ \sigma_2\end{pmatrix}_1 - \begin{pmatrix}\sigma_1\\ \sigma_2\end{pmatrix}_0\right) + \mu^2\cdot\left(\begin{pmatrix}\sigma_1\\ \sigma_2\end{pmatrix}_2 + \begin{pmatrix}\sigma_1\\ \sigma_2\end{pmatrix}_0 - 2\begin{pmatrix}\sigma_1\\ \sigma_2\end{pmatrix}_1\right) \qquad \textbf{3. 1}$$

where:

$\begin{pmatrix}\sigma_1\\ \sigma_2\end{pmatrix}_0$ is the first reference point

$\begin{pmatrix}\sigma_1\\ \sigma_2\end{pmatrix}_1$ is the hinge point

$\begin{pmatrix}\sigma_1\\ \sigma_2\end{pmatrix}_2$ is the second reference point

μ is a parameter which determines the location on the curve ($0\leq \mu \leq 1$).

A yield surface under the line ($\sigma_1=\sigma_2$) is described by 6 Bezier functions, see figure 3-6. On account of the use of Bezier interpolation functions, the yield surface is smooth and has a continuous gradient in the reference points. The Bezier functions also permit the definition of a smooth yield function. For an overview of 2D interpolation techniques the reader is referred to (Salmon, 1987), (Dewey, 1988).

3.2.2 Anisotropy

The yield locus in figure 3-1 shows the reference points of experiments for which the first principal stress coincides with the rolling direction in the sheet metal. The reference points can also be determined for other angles to the rolling direction (planar angle). When it appears that the reference points do not vary significantly with the planar angle, the material behaves planar isotropically. In this case the yield surface is independent of the planar angle. When the reference points vary with the angle, the material behaves anisotropically and the yield surface depends on the angle.

Anisotropic material behaviour is incorporated in the yield surface interpolation by the extension of (3. 1) to (3. 2):

$$\begin{pmatrix}\sigma_1\\ \sigma_2\end{pmatrix} = \begin{pmatrix}\sigma_1\\ \sigma_2\end{pmatrix}_0(\theta) + 2\mu\cdot\left(\begin{pmatrix}\sigma_1\\ \sigma_2\end{pmatrix}_1(\theta) - \begin{pmatrix}\sigma_1\\ \sigma_2\end{pmatrix}_0(\theta)\right) + \mu^2\cdot\left(\begin{pmatrix}\sigma_1\\ \sigma_2\end{pmatrix}_2(\theta) + \begin{pmatrix}\sigma_1\\ \sigma_2\end{pmatrix}_0(\theta) - 2\begin{pmatrix}\sigma_1\\ \sigma_2\end{pmatrix}_1(\theta)\right) \qquad \textbf{3. 2}$$

where:

$\begin{pmatrix}\sigma_1\\ \sigma_2\end{pmatrix}_i(\theta)$ are the positions of reference or hinge points for the planar angle θ (i=0,1 or 2)

The reference points are determined for a limited number of planar angles. The points for intermediate angles are interpolated between the measured points, illustrated for a quarter of the yield surface in figure 3-3.

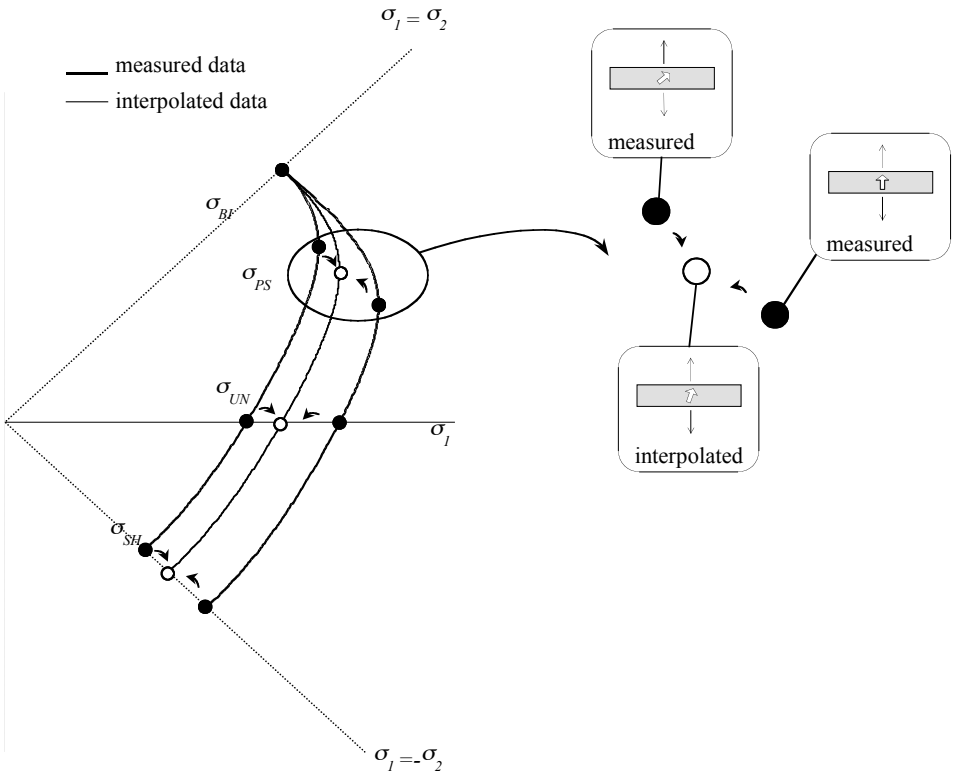

Figure 3-3 Interpolation of measured data

A Fourier series is used to interpolate the reference points. It is assumed that the planar angles 0° and 90° are symmetry angles, which leads to the following series:

$$\begin{pmatrix}\sigma_1\\ \sigma_2\end{pmatrix}_i(\theta) = \sum_{j=0}^{\infty}\begin{pmatrix}\sigma fac_1\\ \sigma fac_2\end{pmatrix}_{i,j} \cdot \cos(2 \cdot j \cdot \theta) \qquad \textbf{3. 3}$$

$$g_i(\theta) = \sum_{j=0}^{\infty} gfac_{i,j} \cdot \cos(2 \cdot j \cdot \theta)$$

where:

$\begin{pmatrix}\sigma_1\\ \sigma_2\end{pmatrix}_i(\theta)$ are the positions of reference points for the planar angle θ (i=0 or 2)

$g_i(\theta)$ are the gradients dependent on the planar angle θ

$\begin{pmatrix}\sigma fac_1\\ \sigma fac_2\end{pmatrix}_{i,j}$ are vectors dependent on measured positions of reference points

$gfac_{i,j}$ are factors dependent on measured gradients of reference points

Note that the positions of the hinge points for an angle (θ) are determined by first interpolating the positions of reference points and the gradients. Subsequently the intersection of the interpolated gradients in the reference points define the interpolated hinge point (figure 3-2).

Generally the reference points are determined for the planar angles 0°, 45° and 90°. Then the Fourier series reduces to a series of three terms:

$$\begin{pmatrix}\sigma_1\\ \sigma_2\end{pmatrix}_i(\theta) = \left[\frac{\begin{pmatrix}\sigma_1\\ \sigma_2\end{pmatrix}_i(0) + \begin{pmatrix}\sigma_1\\ \sigma_2\end{pmatrix}_i(90)}{4} + \frac{\begin{pmatrix}\sigma_1\\ \sigma_2\end{pmatrix}_i(45)}{2}\right] + \left[\frac{\begin{pmatrix}\sigma_1\\ \sigma_2\end{pmatrix}_i(0) - \begin{pmatrix}\sigma_1\\ \sigma_2\end{pmatrix}_i(90)}{2}\right]\cdot\cos(2\cdot\theta) + \left[\frac{\begin{pmatrix}\sigma_1\\ \sigma_2\end{pmatrix}_i(0) + \begin{pmatrix}\sigma_1\\ \sigma_2\end{pmatrix}_i(90)}{4} - \frac{\begin{pmatrix}\sigma_1\\ \sigma_2\end{pmatrix}_i(45)}{2}\right]\cdot\cos(4\cdot\theta) \qquad \textbf{3. 4}$$

$$g_i(\theta) = \left[\frac{g_i(0)+g_i(90)}{4} + \frac{g_i(45)}{2}\right] + \left[\frac{g_i(0)-g_i(90)}{2}\right]\cdot\cos(2\cdot\theta) + \left[\frac{g_i(0)+g_i(90)}{4} - \frac{g_i(45)}{2}\right]\cdot\cos(4\cdot\theta)$$

3.2.3 Symmetry conditions

With symmetry conditions the reference points under the line $\sigma_1 = -\sigma_2$ (denoted by the second part of the yield surface) are determined. Compared to the points above this line (first part of the yield surface), these points can be defined by the same measurements with the rolling direction rotated through 90°. This is illustrated by figure 3-4.

A stress state on the first part of the yield surface is represented at the bottom of figure 3-4. When the transition is made to the second part, the principal stresses (σ_1) and (σ_2) are interchanged by ($-\sigma_2$) and ($-\sigma_1$) respectively. The second part can be represented by the 3 situations of the upper part of 3-4. The left and the middle situation of the upper part assume the same yield behaviour in tension and compression, which is valid for isotropic material behaviour. The middle and right situation represent the same situations, only rotated rigidly through 90°. When the latter situation is compared to the situation in the first part of the yield surface, the rolling direction is rotated through 90°.

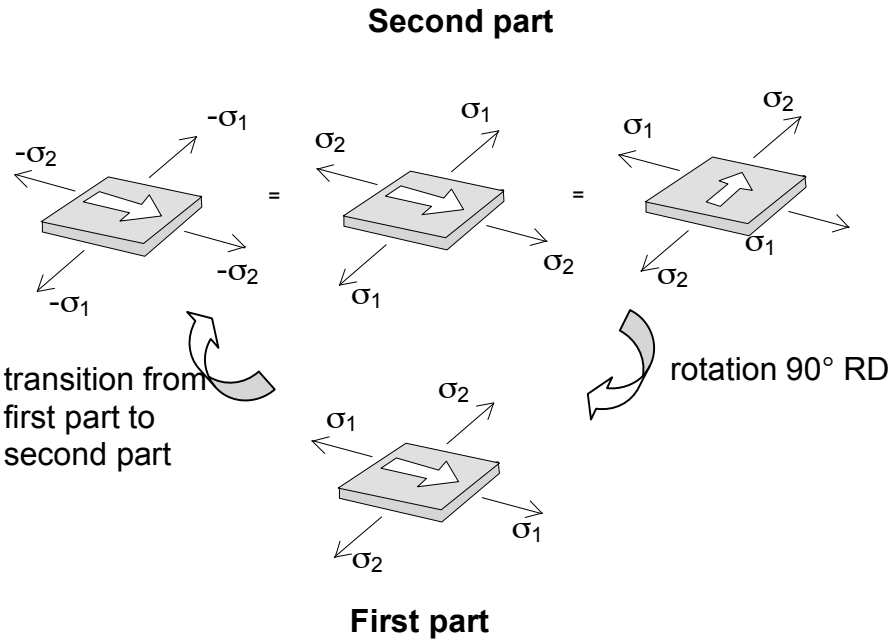

Figure 3-4 Rotation of rolling direction (RD) through 90° for the second part

Symmetry conditions are also used to determine the reference point data of the first part which are not obtained by measurements (see also table 2-1):

- The height of the plane strain point is assumed to be at a fixed distance between the hinge points on both sides. This distance is given by the factor (α_{ps}), see point (σ_{PS}) in figure 3-5:

$$\alpha_{ps} = \frac{\alpha_1}{\alpha_2} \qquad \textbf{\textit{3. 5}}$$

- The gradient of the surface at the shear point is assumed to be parallel to the line through the uni-axial points, see the slope through point (σ_{SH}) in figure 3-5. The reason that the gradient is not related to the experimental strain is explained in section 5.4.1.

The symmetry conditions are illustrated in figure 3-5. For convenience the angle for the first part of the yield surface is 0°, so the measurements for this part are performed in the rolling direction. The second part can be obtained by the same measurements for 90° to the rolling direction. The rolling directions are indicated by the white arrows in the figure.

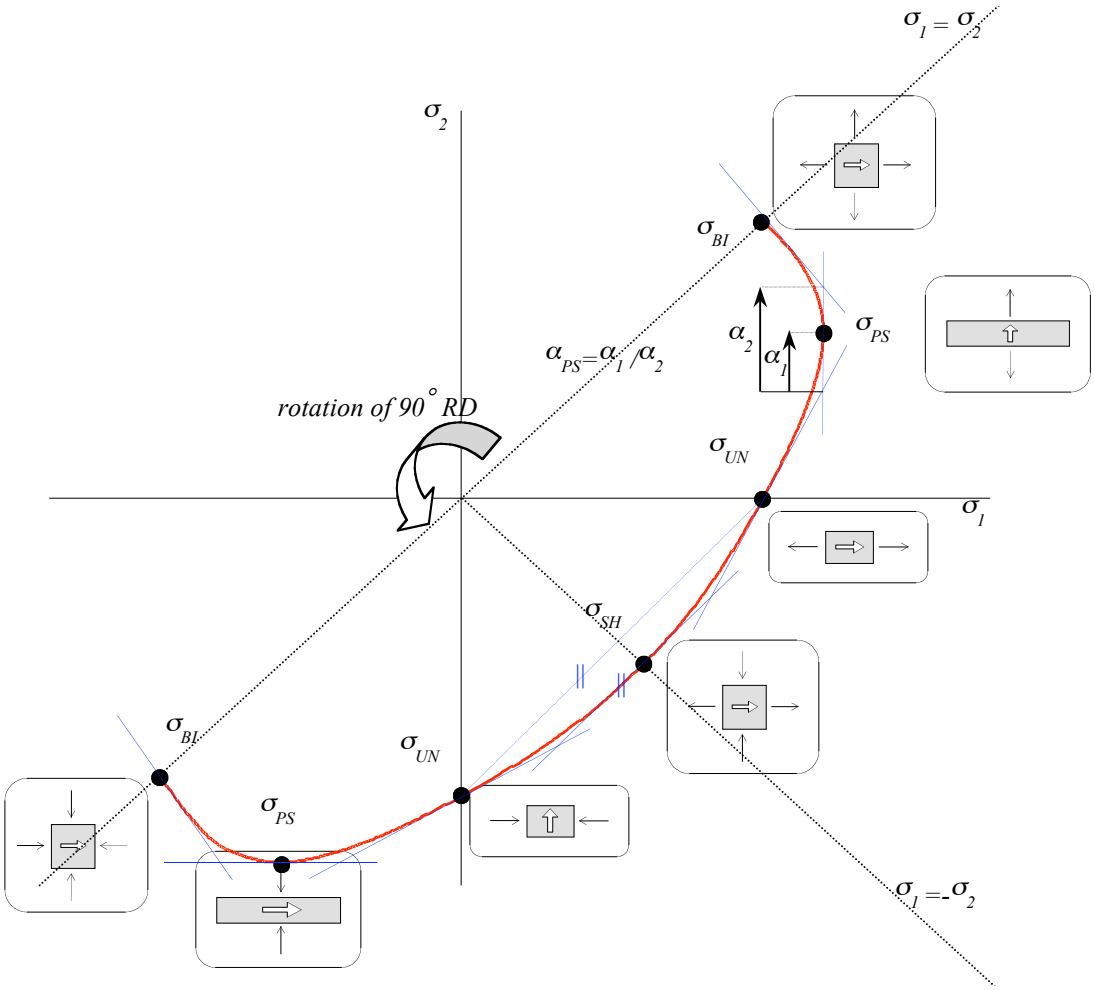

Figure 3-5 Symmetry conditions in the yield surface

3.2.4 Yield function elaboration

The yield function definition with isotropic hardening is taken as a starting point:

$$\phi = \phi(\underline{\sigma}, \sigma_y) \qquad \textbf{3. 6}$$

which for a plane stress situation is:

$$\phi = \phi(\sigma_{xx}, \sigma_{yy}, \tau_{xy}, \sigma_y) \qquad \textbf{3. 7}$$

Here (σ_y) is the average uni-axial yield stress and (σ_{xx}), (σ_{yy}), (τ_{xy}) are the stress components in the plane of the sheet. The average uni-axial yield stress is referred to as the yield stress in the rest of this dissertation. Since the Vegter yield function is based on reference points in the principal stress space, the yield function is rewritten as:

$$\phi = \phi(\sigma_1, \sigma_2, \theta, \sigma_y) \qquad \textbf{3. 8}$$

The principal stresses and the planar angle θ are defined by the rules of tensor transformation (Gere, 1991):

$$\begin{aligned}
\sigma_1 &= \frac{\sigma_{xx} + \sigma_{yy}}{2} + \sqrt{\left(\frac{\sigma_{xx} - \sigma_{yy}}{2}\right)^2 + \tau_{xy}{}^2} \\
\sigma_2 &= \frac{\sigma_{xx} + \sigma_{yy}}{2} - \sqrt{\left(\frac{\sigma_{xx} - \sigma_{yy}}{2}\right)^2 + \tau_{xy}{}^2} \\
\cos 2\theta &= \frac{\frac{\sigma_{xx} - \sigma_{yy}}{2}}{\sqrt{\left(\frac{\sigma_{xx} - \sigma_{yy}}{2}\right)^2 + \tau_{xy}{}^2}}
\end{aligned} \qquad \textbf{3. 9}$$

When the stress is on the yield surface the yield function is equal to zero. When a fictive stress is outside or inside the yield surface, the yield function has to be positive or negative respectively. Therefore an equivalent stress (σ_{eq}) is defined:

$$\phi = \sigma_{eq}(\sigma_1, \sigma_2, \theta) - \sigma_y \qquad \textbf{3. 10}$$

The equivalent stress defines a fictive yield surface through the fictive stress state, see figure 3-6. The fictive yield surface has the same shape as the yield surface but differs in size. Here the equivalent stress (σ_{eq}) is defined as follows.

With the equivalent stress (σ_{eq}), the fictive yield surface can be described similarly to equation (3. 2):

$$\begin{pmatrix}\sigma_1\\ \sigma_2\end{pmatrix} = \frac{\sigma_{eq}}{\sigma_y}\cdot\left[\begin{pmatrix}\sigma_1\\ \sigma_2\end{pmatrix}_0(\theta) + 2\mu\cdot\left(\begin{pmatrix}\sigma_1\\ \sigma_2\end{pmatrix}_1(\theta) - \begin{pmatrix}\sigma_1\\ \sigma_2\end{pmatrix}_0(\theta)\right) + \mu^2\cdot\left(\begin{pmatrix}\sigma_1\\ \sigma_2\end{pmatrix}_2(\theta) + \begin{pmatrix}\sigma_1\\ \sigma_2\end{pmatrix}_0(\theta) - 2\begin{pmatrix}\sigma_1\\ \sigma_2\end{pmatrix}_1(\theta)\right)\right] \qquad \textbf{3. 11}$$

where:

σ_y is the yield stress, which represents the size of the yield surface

σ_{eq} is the equivalent stress, which represents the size of the fictive yield surface

The term between brackets in (3. 11) is the Bezier interpolation function. Half of the yield locus consists of 6 Bezier interpolation functions. Hence the relevant Bezier function is selected by the ratio of the principal stresses (σ_1/σ_2). This is illustrated by Figure 3-6. It shows the 6 Bezier interpolation functions BI(1) till BI(6). The fictive stress is represented by the large black dot. This fictive stress lies between the line from the origin trough the uni-axial point and the line from the origin through the shear point. The first line represents a ratio of 0 and the second a ratio of –1. In this case the Bezier curve between the shear and the uni-axial point is relevant. The remaining dotted lines represent other ratios.

Equation (3. 11) is simplified by defining the normalised first (f1) and second (f2) components of the Bezier interpolation function:

$$\begin{aligned}\sigma_1 &= \sigma_{eq}\cdot f1(\mu,\theta)\\ \sigma_2 &= \sigma_{eq}\cdot f2(\mu,\theta)\end{aligned} \qquad \textbf{3. 12}$$

where:

$$\begin{aligned}f1(\mu,\theta) &= \frac{\sigma_{10}(\theta) + 2\mu\cdot\left(\sigma_{11}(\theta) - \sigma_{10}(\theta)\right) + \mu^2\cdot\left(\sigma_{12}(\theta) + \sigma_{10}(\theta) - 2\sigma_{11}(\theta)\right)}{\sigma_y}\\ f2(\mu,\theta) &= \frac{\sigma_{20}(\theta) + 2\mu\cdot\left(\sigma_{21}(\theta) - \sigma_{20}(\theta)\right) + \mu^2\cdot\left(\sigma_{22}(\theta) + \sigma_{20}(\theta) - 2\sigma_{21}(\theta)\right)}{\sigma_y}\end{aligned} \qquad \textbf{3. 13}$$

In this way 2 equations for σ_{eq} are obtained:

$$\begin{aligned}\sigma_{eq} &= \frac{\sigma_1}{f1(\mu,\theta)}\\ \sigma_{eq} &= \frac{\sigma_2}{f2(\mu,\theta)}\end{aligned} \qquad \textbf{3. 14}$$

Equating the first and second of (3. 14) gives an expression for (μ), which has two solutions. One of the solutions is a value between 0 and 1. This value is substituted into (3. 14) to obtain a solution for (σ_{eq}). Consequently the value of the yield function is determined by substitution of (σ_{eq}) in (3. 10).

In finite element applications the yield function is determined as follows:

1. The stress state $\sigma_{xx},\sigma_{yy},\tau_{xy}$ is transformed into a principal stress state σ_1 and σ_2 (equation 3. 9)
2. The planar angle θ is determined (equation 3. 9)
3. The measured reference points are interpolated in order to obtain the reference points for the angle θ (equation 3. 4)
4. From the 7 reference points, the 2 relevant reference points and the related Bezier function are chosen on the basis of the ratio of the principal stresses (figure 3-6).
5. The yield function is determined according to (3. 10), (3. 13) and (3. 14)

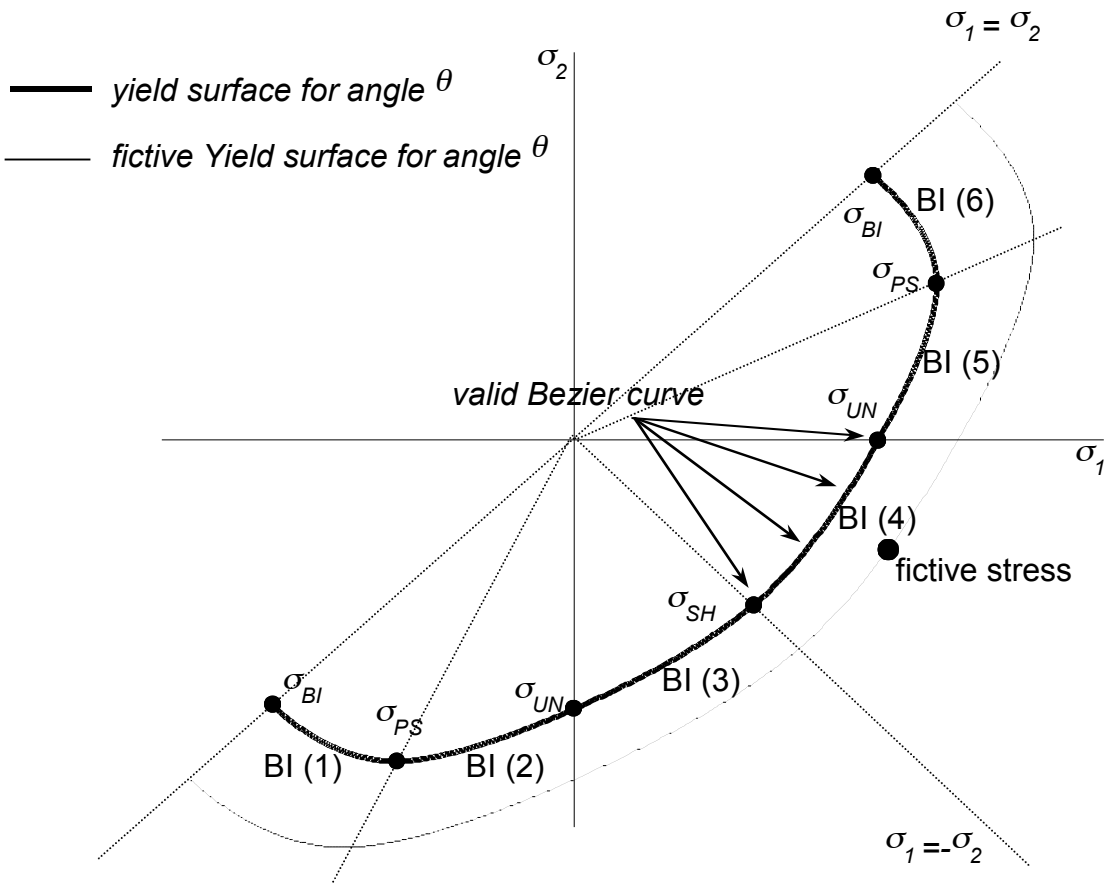

Figure 3-6 Half of a yield surface and fictive yield surface defined by 6 Bezier interpolation functions

3.3 Stiffness matrix implementation

To implement the Vegter yield function in the stiffness matrix the derivative of the yield function must be determined (section 2.3.1).

The derivative of the yield function to the stress tensor is given by:

$$\frac{\partial \phi(\underline{\sigma}, \sigma_y)}{\partial \underline{\sigma}} \qquad \textbf{3. 15}$$

This expression is written in vector format for a plane stress situation. The normal must be related to Bezier functions in the principal stress space. Therefore the normal is expressed in the principal stresses and the planar angle:

$$\begin{pmatrix} \frac{\partial \phi}{\partial \sigma_{xx}} \\ \frac{\partial \phi}{\partial \sigma_{yy}} \\ \frac{\partial \phi}{\partial \tau_{xy}} \end{pmatrix} = \frac{\partial \phi}{\partial \sigma_1} \begin{pmatrix} \frac{\partial \sigma_1}{\partial \sigma_{xx}} \\ \frac{\partial \sigma_1}{\partial \sigma_{yy}} \\ \frac{\partial \sigma_1}{\partial \tau_{xy}} \end{pmatrix} + \frac{\partial \phi}{\partial \sigma_2} \begin{pmatrix} \frac{\partial \sigma_2}{\partial \sigma_{xx}} \\ \frac{\partial \sigma_2}{\partial \sigma_{yy}} \\ \frac{\partial \sigma_2}{\partial \tau_{xy}} \end{pmatrix} + \frac{\partial \phi}{\partial \theta} \begin{pmatrix} \frac{\partial \theta}{\partial \sigma_{xx}} \\ \frac{\partial \theta}{\partial \sigma_{yy}} \\ \frac{\partial \theta}{\partial \tau_{xy}} \end{pmatrix} \qquad \textbf{3. 16}$$

The reference points for the yield function are found by interpolation using a Fourier series, consisting of terms with (cos2θ) and (cos4θ) see equation (3. 4). Therefore it is convenient to rewrite the last term of expression (3. 16) as a function of (cos2θ):

$$\begin{pmatrix} \frac{\partial \phi}{\partial \sigma_{xx}} \\ \frac{\partial \phi}{\partial \sigma_{yy}} \\ \frac{\partial \phi}{\partial \tau_{xy}} \end{pmatrix} = \frac{\partial \phi}{\partial \sigma_1} \begin{pmatrix} \frac{\partial \sigma_1}{\partial \sigma_{xx}} \\ \frac{\partial \sigma_1}{\partial \sigma_{yy}} \\ \frac{\partial \sigma_1}{\partial \tau_{xy}} \end{pmatrix} + \frac{\partial \phi}{\partial \sigma_2} \begin{pmatrix} \frac{\partial \sigma_2}{\partial \sigma_{xx}} \\ \frac{\partial \sigma_2}{\partial \sigma_{yy}} \\ \frac{\partial \sigma_2}{\partial \tau_{xy}} \end{pmatrix} + \frac{\partial \phi}{\partial \cos 2\theta} \begin{pmatrix} \frac{\partial \cos 2\theta}{\partial \sigma_{xx}} \\ \frac{\partial \cos 2\theta}{\partial \sigma_{yy}} \\ \frac{\partial \cos 2\theta}{\partial \tau_{xy}} \end{pmatrix} \qquad \textbf{3. 17}$$

a1 b1 a2 b2 c d

The expression for the normal (3. 17) is divided into 6 parts (a1, a2, b1, b2, c and d):

a1, a2: The derivatives of the yield function with respect to the principal stresses. Figure 3-7 illustrates these derivatives in the principal stress space

b1, b2: The derivatives of the principal stresses with respect to general stress components

c: The derivative of the yield function with respect to the cosine of twice the angle to the rolling direction (appendix C)

d: The derivative of the cosine of twice the planar angle with respect to the stress

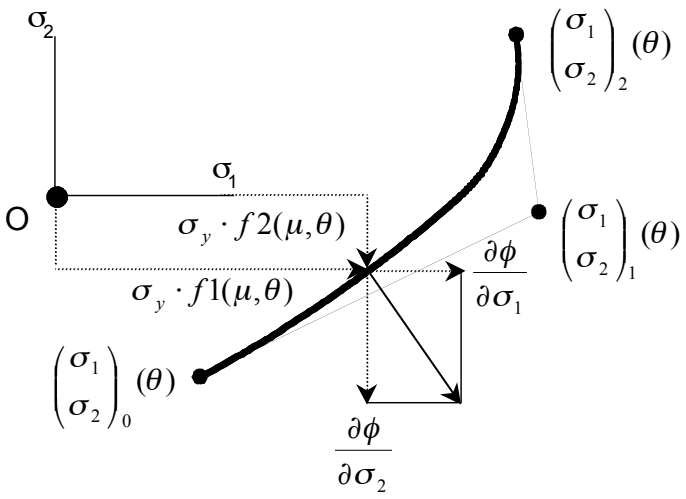

Figure 3-7 Derivative components in the principal stress space

The full elaboration of the normal to the yield surface is given in appendix A. In finite element applications the normal to the yield surface is determined as follows:

1. The stress state $\sigma_{xx},\sigma_{yy},\tau_{xy}$ is transformed into a principal stress state σ_1 and σ_2 (equation 3. 9)
2. The planar angle θ is determined (equation 3. 9)
3. The measured reference points are interpolated in order to obtain the reference points for the angle θ (equation 3. 4)
4. From the 7 reference points the 2 relevant reference points and the related Bezier function are chosen on the basis of the ratio of the principal stresses (figure 3-6)
5. The derivatives of the yield function with respect to the principal stresses are defined (a1,a2)
6. The derivatives of the principal stresses with respect to general stress components are determined (b1, b2)
7. The derivative of the cosine of twice the planar angle with respect to the stress components is determined (d)
8. The derivative of the yield function with respect to the cosine of twice the planar angle is determined (c)
9. The normal is constructed by expression (3. 17)

3.4 Stress update algorithm implementation

To implement the Vegter yield function in the stress update algorithm, the stress must be projected to the yield locus (section 2.3.2). When isotropic hardening is assumed, the tensor ($\underline{\beta}$) can be replaced by the yield stress (σ_y).

A variety of stress projection procedures is available, see for instance (Borst, 1989.). The procedures differ in the definition of the derivative of the yield function, which effects the stability of the procedure. The unconditionally stable Euler Backward procedure is applied, which uses the derivative of the projected stress:

$$\underline{\sigma}_n = \underline{\sigma}_t - \Delta\lambda \underline{\underline{E}} \cdot \left(\frac{\partial \phi}{\partial \underline{\sigma}} \right)_n \qquad \textbf{3. 18}$$

with

$$\phi(\underline{\sigma}_n, \sigma_y) = 0 \qquad \textbf{3. 19}$$

Here $\underline{\sigma}_t$ is the trial stress and $\underline{\sigma}_n$ is the projected stress. Note the addition of the subscript ‘n’ in the normal to the yield surface, compared to 2.32. Expression (3. 18) is rewritten in a vector-matrix format for a plane stress situation:

$$\begin{pmatrix} \sigma_{xx} \\ \sigma_{yy} \\ \tau_{xy} \end{pmatrix}_n = \begin{pmatrix} \sigma_{xx} \\ \sigma_{yy} \\ \tau_{xy} \end{pmatrix}_t - \Delta\lambda \begin{bmatrix} \frac{E}{1-\nu^2} & \nu \cdot \frac{E}{1-\nu^2} & 0 \\ \nu \cdot \frac{E}{1-\nu^2} & \frac{E}{1-\nu^2} & 0 \\ 0 & 0 & \frac{E}{2(1+\nu)} \end{bmatrix} \cdot \begin{pmatrix} \frac{\partial \phi}{\partial \sigma_{xx}} \\ \frac{\partial \phi}{\partial \sigma_{yy}} \\ \frac{\partial \phi}{\partial \tau_{xy}} \end{pmatrix}_n \qquad \textbf{3. 20}$$

which, in principal stresses (appendix B), is as follows:

$$\begin{pmatrix}\sigma_{xx}\\ \sigma_{yy}\\ \tau_{xy}\end{pmatrix}_n = A(\mu,\Delta\lambda)^{-1}\cdot\begin{pmatrix}\sigma_{xx}\\ \sigma_{yy}\\ \tau_{xy}\end{pmatrix}_t -$$

$$A(\mu,\Delta\lambda)^{-1}\cdot\Delta\lambda\begin{bmatrix}\frac{E}{1-\nu^2} & \nu\cdot\frac{E}{1-\nu^2} & 0\\ \nu\cdot\frac{E}{1-\nu^2} & \frac{E}{1-\nu^2} & 0\\ 0 & 0 & \frac{E}{2(1+\nu)}\end{bmatrix}\cdot\frac{\left[\frac{\partial f2(\mu,\theta)}{\partial\mu}-\frac{\partial f1(\mu,\theta)}{\partial\mu}\right]_n}{\left[\frac{\partial f2(\mu,\theta)}{\partial\mu}\cdot f1(\mu,\theta)-\frac{\partial f1(\mu,\theta)}{\partial\mu}\cdot f2(\mu,\theta)\right]_n}\begin{pmatrix}\frac{1}{2}\\ \frac{1}{2}\\ 0\end{pmatrix} - \qquad \textbf{3. 21}$$

$$A(\mu,\Delta\lambda)^{-1}\cdot\Delta\lambda\begin{bmatrix}\frac{E}{1-\nu^2} & \nu\cdot\frac{E}{1-\nu^2} & 0\\ \nu\cdot\frac{E}{1-\nu^2} & \frac{E}{1-\nu^2} & 0\\ 0 & 0 & \frac{E}{2(1+\nu)}\end{bmatrix}\cdot\left(\frac{\partial\phi}{\partial\cos 2\theta}\right)_n\cdot\begin{pmatrix}\frac{\partial\cos 2\theta}{\partial\sigma_{xx}}\\ \frac{\partial\cos 2\theta}{\partial\sigma_{yy}}\\ \frac{\partial\cos 2\theta}{\partial\tau_{xy}}\end{pmatrix}$$

The matrix A(μ,$\Delta\lambda$) depends on μ and $\Delta\lambda$. The parameters f1(μ,θ) and f2(μ,θ) are the normalised components of the Bezier interpolation function, defined by (3. 14).

Expression (3. 19) can also be rewritten in vector format for a plane stress situation with the help of equations (3. 10) and (3. 14):

$$\frac{(\sigma_1)_n}{f1(\mu,\theta)_n}-\sigma_y=0$$
$$\frac{(\sigma_2)_n}{f2(\mu,\theta)_n}-\sigma_y=0 \qquad \textbf{3. 22}$$

The principal stresses and the planar angle of the projected situation are determined by the rules of tensor transformation (equations 3. 9).

There are in all eight unknown parameters in the stress projection ($(\sigma_{xx})_n$, $(\sigma_{yy})_n$, $(\tau_{xy})_n$, $(\sigma1)_n$,$(\sigma2)_n$, μ, $\Delta\lambda$, θ), and there are eight equations available (3 from 3. 21, 2 from 3. 22 and 3 from 3. 9). Appendix B shows that an expression for $\Delta\lambda$ and μ can be derived, from which the other unknowns can be determined.

However, in the derivation 2 problems occur. In the first place it appears that the expressions become very complicated. The expression of the normal (appendix A) is very extensive and therefore hard to implement in a stress projection procedure. In order to obtain more simple expressions, the use of alternative reference points with constant slopes has been researched. In this case only positions have to be interpolated and not the gradients. This option is elaborated in appendix E. It provides a simplification of the normal, but the relation with measured data is less straightforward.

A second problem is that the valid Bezier curve cannot be determined in advance by the ratio of the principal stresses. This is because the planar angle is not known before the projection procedure. Figure 3-8 illustrates this for a trial stress state in the vicinity of the plane strain reference point. If the planar angle after projection is equal to 45°, the relevant Bezier curve is the curve between the plane strain point and the equi-bi-axial point. If the angle after projection is equal to 90°, the relevant Bezier curve is the curve between the uni-axial point and the plane strain point. Hence it is quite difficult to predict a Bezier curve for an arbitrary planar angle.

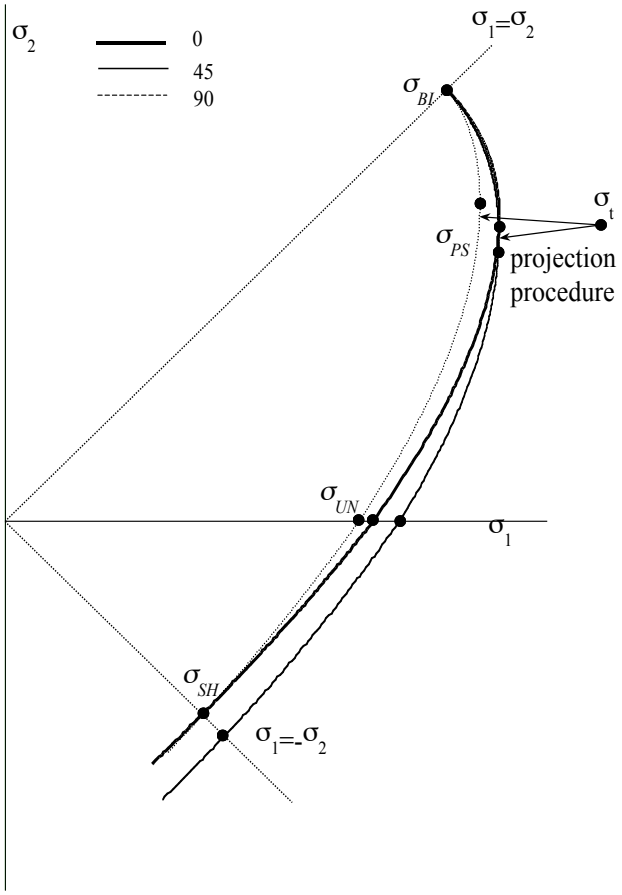

Figure 3-8 Dependence of relevant Bezier curve on the projected planar angle

A numerical procedure is developed, based upon the projection with a constant planar angle. This projection is placed into an iteration process in which the angle is updated. In this way the relevant Bezier function can be determined in a straightforward way by the ratio of the principal stresses. Appendix B provides a complete mathematical elaboration. The procedure is explained shortly as follows.

1. The procedure first neglects the third term on the right hand of (3. 21), which means that the planar angle stays equal to the planar angle of the trial stress. This is known as the Euler-backward procedure with a constant planar angle (appendix B)
2. Based on the solution with the constant planar angle a first guess of the neglected term is made. By rewriting expression (3. 21), this term can be seen as a deviation from the trial stress:

$$\begin{pmatrix}\sigma_{xx}\\ \sigma_{yy}\\ \tau_{xy}\end{pmatrix}_n = A(\mu,\Delta\lambda)^{-1}\cdot\left(\begin{pmatrix}\sigma_{xx}\\ \sigma_{yy}\\ \tau_{xy}\end{pmatrix}_t - \Delta\lambda\begin{bmatrix}\frac{E}{1-\nu^2} & \nu\cdot\frac{E}{1-\nu^2} & 0\\ \nu\cdot\frac{E}{1-\nu^2} & \frac{E}{1-\nu^2} & 0\\ 0 & 0 & \frac{E}{2(1+\nu)}\end{bmatrix}\cdot\left(\frac{\partial\phi}{\partial\cos 2\theta}\right)_n\cdot\begin{pmatrix}\frac{\partial\cos 2\theta}{\partial\sigma_{xx}}\\ \frac{\partial\cos 2\theta}{\partial\sigma_{yy}}\\ \frac{\partial\cos 2\theta}{\partial\tau_{xy}}\end{pmatrix}_n\right) -$$

$$A(\mu,\Delta\lambda)^{-1}\cdot\Delta\lambda\begin{bmatrix}\frac{E}{1-\nu^2} & \nu\cdot\frac{E}{1-\nu^2} & 0\\ \nu\cdot\frac{E}{1-\nu^2} & \frac{E}{1-\nu^2} & 0\\ 0 & 0 & \frac{E}{2(1+\nu)}\end{bmatrix}\cdot\frac{\left[\frac{\partial f2(\mu,\theta)}{\partial\mu}-\frac{\partial f1(\mu,\theta)}{\partial\mu}\right]_n}{\left[\frac{\partial f2(\mu,\theta)}{\partial\mu}\cdot f1(\mu,\theta)-\frac{\partial f1(\mu,\theta)}{\partial\mu}\cdot f2(\mu,\theta)\right]_n}\begin{pmatrix}\frac{1}{2}\\ 1\\ \frac{1}{2}\\ 0\end{pmatrix} \qquad \textbf{3. 23}$$

3. Consequently a new projection procedure is started, with the adapted trial stress as a starting point
4. The procedure is repeated until convergence has been reached. Convergence is checked upon the back scaled stress situation adapted with the last term of (3. 21)

Scheme 3-1 illustrates the procedure.

$$\begin{pmatrix}\sigma_{xx}\\ \sigma_{yy}\\ \tau_{xy}\end{pmatrix}_t$$

Stress Projection with constant planar angle (appendix B)

$$\begin{pmatrix}\sigma_{xx}\\ \sigma_{yy}\\ \tau_{xy}\end{pmatrix}_n^0$$ i=0

$(\sigma_1)_n^0$
$(\sigma_2)_n^0$
θ^0
μ^0
$\Delta\lambda^0$

While $\phi((\sigma_1)_n,(\sigma_2)_n,\theta_n,\sigma_y) > threshold$ do

i=i+1

$$\begin{pmatrix}\sigma_{xx}\\ \sigma_{yy}\\ \tau_{xy}\end{pmatrix}_t = \begin{pmatrix}\sigma_{xx}\\ \sigma_{yy}\\ \tau_{xy}\end{pmatrix}_t - \Delta\lambda^{i-1}\left(\frac{\partial\phi}{\partial\cos 2\theta}\right)_n^{i-1}[E]\cdot\begin{pmatrix}\frac{\partial\cos 2\theta}{\partial\sigma_{xx}}\\ \frac{\partial\cos 2\theta}{\partial\sigma_{yy}}\\ \frac{\partial\cos 2\theta}{\partial\tau_{xy}}\end{pmatrix}_n^{i-1}$$ (adaptation of trial stress)

Stress Projection with constant planar angle (appendix B)

$$\begin{pmatrix}\sigma_{xx}\\ \sigma_{yy}\\ \tau_{xy}\end{pmatrix}_n^i$$

$(\sigma_1)_n^i$
$(\sigma_2)_n^i$
θ^i
μ^i
$\Delta\lambda^i$

$$\begin{pmatrix}\sigma_{xx}\\ \sigma_{yy}\\ \tau_{xy}\end{pmatrix}_n = \begin{pmatrix}\sigma_{xx}\\ \sigma_{yy}\\ \tau_{xy}\end{pmatrix}_n^i - A(\mu^i,\Delta\lambda^i)^{-1}\cdot\Delta\lambda^i\left(\frac{\partial\phi}{\partial\cos 2\theta}\right)_n^i[E]\cdot\begin{pmatrix}\frac{\partial\cos 2\theta}{\partial\sigma_{xx}}\\ \frac{\partial\cos 2\theta}{\partial\sigma_{yy}}\\ \frac{\partial\cos 2\theta}{\partial\tau_{xy}}\end{pmatrix}$$ (adaptation of projected stress)

$(\sigma_1)_n$
$(\sigma_2)_n$
θ
μ
$\Delta\lambda$

End While

Scheme 3-1 Numerical stress projection procedure

3.5 Validation of numerical implementation

The definition of the yield function based on the reference points makes it possible to approximate the Hill '48 function, which is widely used in finite element codes. By a comparison of the fitted Vegter function and the Hill '48 function, the numerical implementation of the Vegter function is validated. The yield function is first used in a simple 'four-element' tensile test. Secondly the deep drawing of a cylindrical cup is treated.

The material data are given in tables 3-2 to 3-4. The first table shows the R-values of the Hill yield function. The second table provides the first components of the Vegter reference points normalised with the average uni-axial yield stress (σ_y). The parameter (α_{ps}) defines the second component of the plane strain point (figure 3-5). The last parameter is the gradient in the equi-bi-axial point for different directions. The hardening relation is according to Nadai-Ludwik. The third table shows the parameters for this hardening relation.

Hill:	0°	45°	90°
R	2.04	1.27	2.19

Table 3-2 Hill function data

Vegter :	0°	45°	90°
σ_{SH}/σ_y	0.503	0.611	0.503
σ_{UN}/σ_y	0.916	1.079	0.927
σ_{PS}/σ_y	1.247	1.301	1.262
σ_{BI}/σ_y	1.149	1.149	1.149
R	2.07	1.27	2.19
α_{ps}	0.348	0.449	0.348
gradient equi-bi-axial	-1.01	-1.00	-0.99

Table 3-3 Vegter function data

Nadai-Ludwik:		
σ_y (N/mm^2)	C	n
184.8	539	0.202

Table 3-4 Nadai-Ludwik hardening data

3.5.1 Four-element test

The test is carried out for a planar angle other than 0° or 90° on a 1 mm square piece of sheet metal. The angles of 0° and 90° are symmetry directions, hence a tensile test would not show any shear deformation. In particular this shear effect at planar anisotropic behaviour is sensitive to the material description. Therefore the test is carried out for a planar angle of 22.5°. The test is illustrated by figure 3-9. The deformed configuration is represented by the dotted lines.

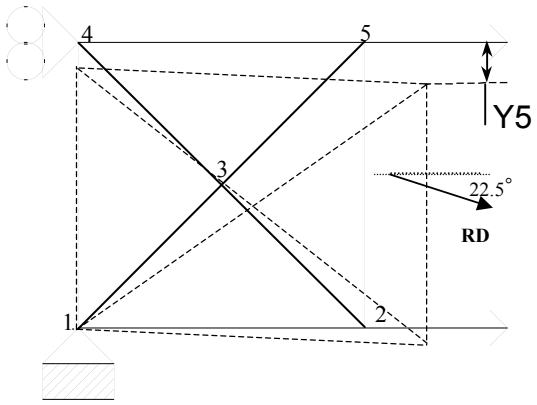

Figure 3-9 Four-element validation case

The displacements of nodes 2 and 5 are prescribed as 0.001 mm per step. In total 100 steps are used which provides a total displacement of 0.1 mm. The unbalance criterion is set on 0.1 percent. The Vegter and the Hill yield functions both show the same deformation pattern.

Results of the stresses, strains and displacement Y5 (figure 3-9) after deformation are given in table 3-5. In the table the x-direction is considered the rolling direction (RD).

	Hill yield function	Vegter yield function
σ_y (Mpa)	338	338
σ_{xx} (Mpa)	287	285
σ_{yy} (Mpa)	54	53
τ_{xy} (Mpa)	124	123
ε_{eq}	0.094	0.094
ε_{xx}	0.082	0.082
ε_{yy}	-0.046	-0.046
γ_{xy}	0.088	0.087
Y5 (mm)	-0.0876	-0.0878

Table 3-5 Stress and strain data after tensile deformation

Only small differences occur in the results, which is attributed to the small difference between the fitted Vegter and the Hill function. This is inherent to the fact that the Vegter yield function is constructed with Bezier interpolation functions and Hill with a quadratic function.

3.5.2 Deep drawing of a cylindrical cup

The set-up of the deep drawing of a cylindrical cup is shown in figure 3-10. Due to planar anisotropy the shape of the flange will not remain circular during the forming process. The visual check of the flange deformation of a partly drawn cup is taken as a second validation of the numerical implementation.

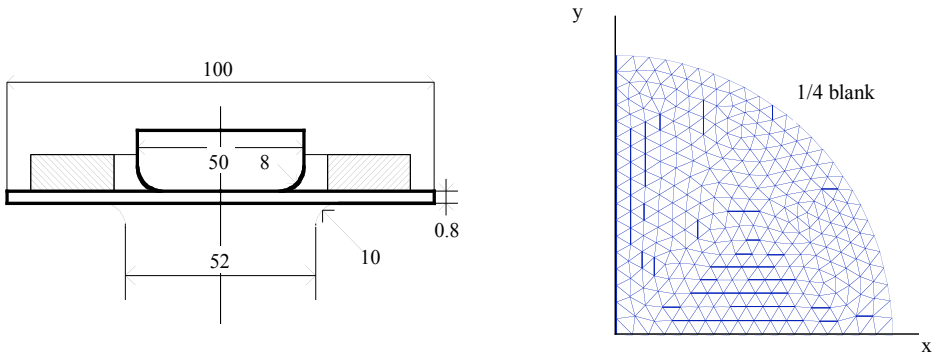

Figure 3-10 Set-up for deep drawing of a cylindrical cup

Only a quarter of the blank is simulated because of symmetry. The blank holder force decreases linearly with the punch displacement from 6 to 5 kN. The process conditions are given by table 3-6:

Process parameters	
blank holder force [kN]	6→5
friction coefficient	0.16
punch displacement [mm]	31

Table 3-6 Process parameters

The footprint of the simulations of the deep drawn cup are illustrated in figure 3-11.

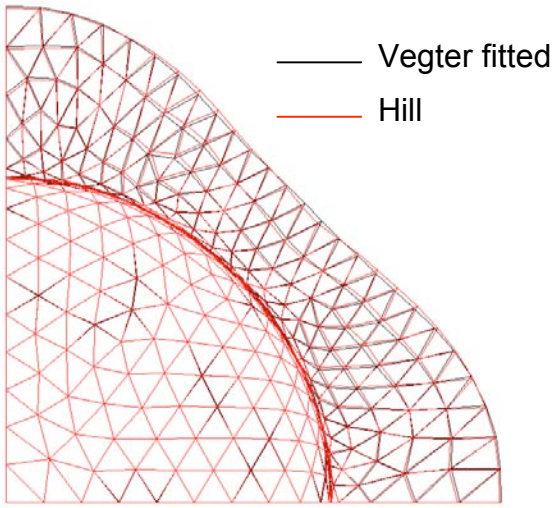

Figure 3-11 Deformed meshes of fitted Vegter criterion and the Hill criterion

The flange deformation shows very small differences. It indicates a proper numerical implementation of the Vegter yield function.

3.6 Alternative description of the Vegter yield function

The Vegter yield function is related to reference point data in the principal stress space. Hence the stress state is expressed in principal stresses and a planar angle. Because of this the definition of the derivative of the yield function is rather extensive and the stress projection procedure turns out to be quite complicated (appendix B).

To avoid complicated procedures, the possibility of defining the yield function directly in general stress components is investigated. In this case no intervention of principal stresses and the planar angle are involved. Such a definition can be obtained by using 3D interpolation functions to define the yield function between the measurements. Figure 3-12 illustrates this for the same measurements as for the current Vegter yield function.

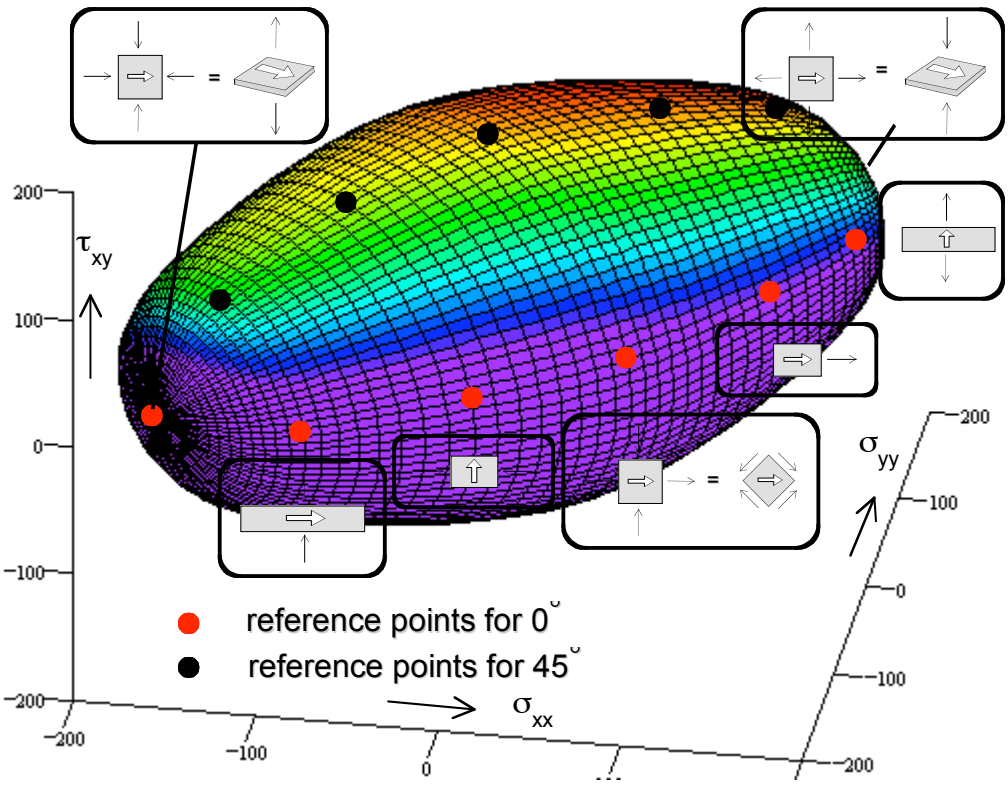

Figure 3-12 Yield surface in the σ_{xx}, σ_{yy} and τ_{xy} space

The red dots indicate the reference points for 0° to the rolling direction. The black dots give the reference points based on measurements performed for a planar angle of 45°. The measurements for 90° are on the back side of the surface.

Figure 3-13 explains the uni-axial reference point for 45°. The uni-axial stress for a planar angle of 45° is equivalent to an equi-bi-axial stress and a shear stress at the same time at 45°, on condition that the absolute values of both stress states are equal to half the uni-axial stress ($\sigma=\tau=1/2\sigma_{un}(45°)$). This is illustrated by the transition of the upper white box to the two boxes below in figure 3-13. The equi-bi-axial stress can also be represented by the same stress, rotated through 45°. The shear stress can be replaced by two opposite normal stresses, rotated through 45°. These situations are shown in the following white boxes. By using the principle of superposition, both stress states together make up the stress in the lower white box. This stress state defines the situation in the stress space represented by the black dot on the upper side of the surface. The other reference points are derived in a similar way.

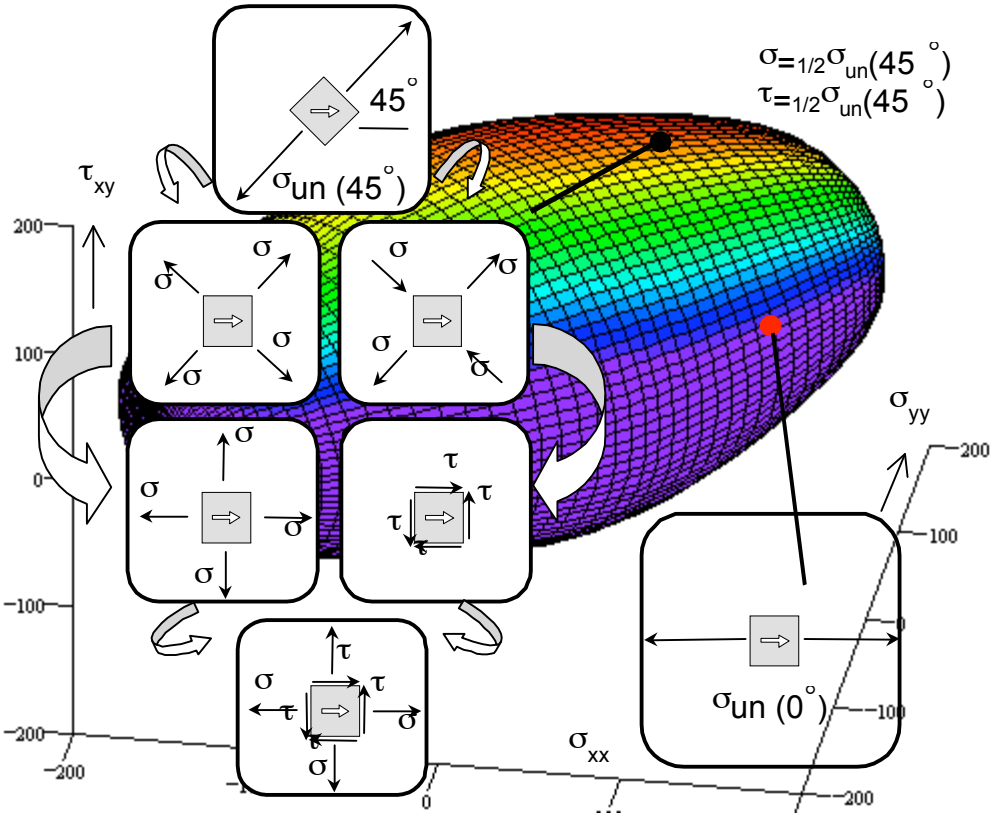

Figure 3-13 Uni-axial point for different angles in the σ_{xx}, σ_{yy} and τ_{xy} space

As in the 2D Vegter representation, the reference points define a location and a gradient in the stress space. A suitable 3D surface interpolation technique has to be found to interpolate the reference points. A number of surface descriptions are available, commonly used in computer graphics and CAD-CAM software (Salmon, 1987), (Dewey, 1988). Many descriptions are able to describe the yield surface and can provide continuity of the normal. The Bezier patch catches the eye, because this interpolation technique is an extension of the 2D Bezier interpolation function to 3 dimensions. It uses the available information of the measurements (location and gradient) and captures exactly the current 2D Bezier interpolation technique.

The advantage of the 3D surface interpolation technique is that it directly defines the yield function in general stress terms (σ_{xx}), (σ_{yy}) and (τ_{xy}). The disadvantage is that the interpolation itself is more complicated. Also the choice of the relevant part of the surface, now defined by the ratio of principal stress components (compare figure 3-6) will be more complicated. Future research has to be carried out to establish whether a 3D surface could be viable.

4 Elaboration of hardening functions

To describe the yield locus after plastic deformation, the Vegter yield function is extended by two hardening models. The first model is the physically based model of chapter 2 in order to represent isotropic hardening. This model defines only the size of the yield surface (figure 2-8). The second model is an extension to isotropic hardening models to include cyclic hardening behaviour in a reverse loading path (Vreede, 1992). The model is a combination of isotropic and kinematic hardening (figures 2-8 and 2-10).

This chapter describes the numerical implementation of the hardening models in a finite element code. Section 4.1 starts with the physically based model. Subsequently section 4.2 discusses the anisotropic hardening model.

4.1 Physically based isotropic hardening model

4.1.1 General outline

At isotropic hardening the size of the yield surface increases with plastic deformation (chapter 2). The size is given by the average uni-axial yield stress (σ_y), in this dissertation called simply the yield stress:

$$\sigma_y = \frac{\sigma_{UN}(0^\circ) + 2\sigma_{UN}(45^\circ) + \sigma_{UN}(90^\circ)}{4} \qquad \textbf{4. 1}$$

where $\sigma_{UN}(\theta)$ is the first component of the uni-axial reference point for the planar angle (θ)

To increase the size of the Vegter yield locus, the reference point location must be linked to the yield stress. This is achieved by normalising the reference points:

$$\begin{pmatrix}\sigma_1\\ \sigma_2\end{pmatrix}_{i_n}(\theta) = \frac{\begin{pmatrix}\sigma_1\\ \sigma_2\end{pmatrix}_i(\theta)}{\sigma_y} \qquad \textbf{4. 2}$$

where

$\begin{pmatrix}\sigma_1\\ \sigma_2\end{pmatrix}_i(\theta)$ are the reference and hinge points positions in the stress space (i=0,1,2)

$\begin{pmatrix}\sigma_1\\ \sigma_2\end{pmatrix}_{i\,n}(\theta)$ are the normalised position of the reference and hinge points (i=0,1,2)

Consequently each reference point is defined by its normalised format multiplied by the yield stress:

$$\begin{pmatrix}\sigma_1\\ \sigma_2\end{pmatrix}_i(\theta)=\begin{pmatrix}\sigma_1\\ \sigma_2\end{pmatrix}_{i\ n}(\theta)\cdot\sigma_y \qquad \textbf{4. 3}$$

In this way the distance from each reference point to the origin is increased by the same factor when the yield stress increases with plastic deformation. The Vegter yield surface before and after plastic deformation is illustrated in figure 4-1.

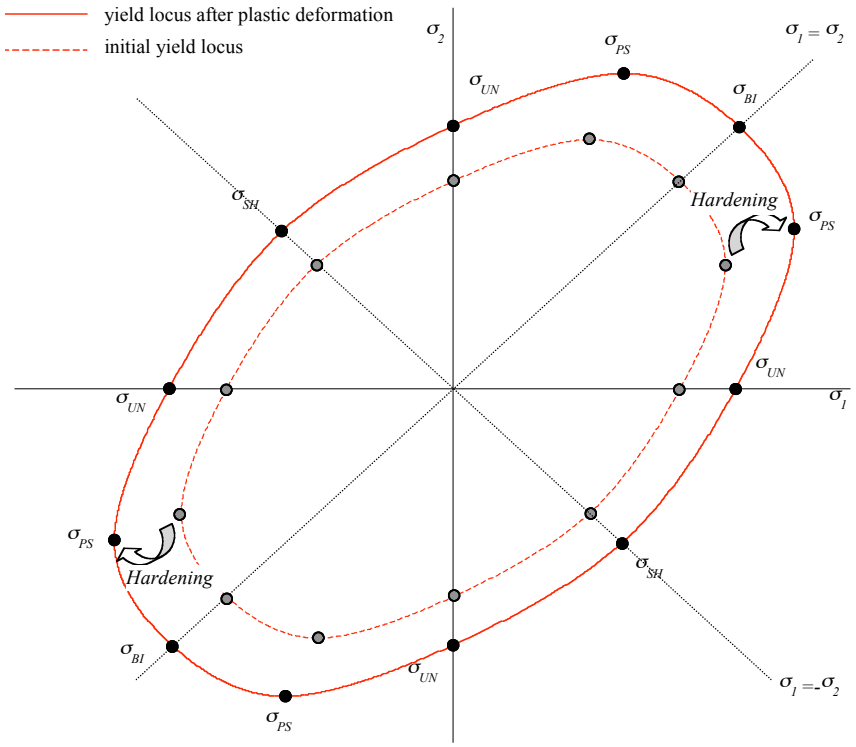

Figure 4-1 Vegter yield surface before (initial) and after plastic deformation at isotropic hardening for an arbitrary planar angle θ

The physically based hardening description from Bergström (Bergström, 1969), van Liempt (v Liempt, 1988) and Vegter (Vegter, 1991) is considered. Bergström derived a general hardening description based on the multiplication of dislocations with plastic deformation. Van Liempt and Vegter adapted the description for larger deformations.

The description is given by:

$$\sigma_y = \sigma_{y0} + \Delta\sigma_m \cdot \left[\beta \cdot (\varepsilon_0 + \varepsilon_p) + \left\{ 1 - e^{-\Omega \cdot (\varepsilon_0 + \varepsilon_p)} \right\}^{n'} \right] \qquad \textbf{4. 4}$$

where

σ_y is the yield stress
σ_{y0} is the initial yield stress, which depends on strain rate and temperature
ε_p is the equivalent plastic strain
ε_0 is the initial strain parameter
$\Delta\sigma_m$ is a stress increase constant for strain hardening, micro-structure related
β is a constant, micro-structure related
Ω is a constant, micro-structure related
n' is a strain hardening exponent, micro-structure related

The parameters $\Delta\sigma_m$, β, Ω and n' are micro-structure related, but in practice taken from mechanical measurements.

Vegter added the strain rate influence to the parameter σ_{y0} :

$$\sigma_{y0} = \sigma_0 + \sigma^* \qquad \textbf{4. 5}$$

where

σ_0 is the static yield stress
σ^* is the dynamic part of the yield stress

Here the dynamic part is given by:

$$\sigma^* = \sigma_0^* \cdot \left\{ 1 + \frac{kT}{\Delta G_0} \cdot \ln\left(\frac{\dot{\varepsilon}_p}{\dot{\varepsilon}_0} \right) \right\}^{m'} \qquad \textbf{4. 6}$$

where

k is the Boltzman number, $8.617 \cdot 10^{-5}$ eV
T is the temperature
$\dot{\varepsilon}_p$ is the equivalent strain rate
$\dot{\varepsilon}_0$ is the limit strain rate (Vegter, 1991)
σ^*_0 is the limit dynamic flow stress
m' is the exponent for the dynamic stress
ΔG_0 is the maximum activation enthalpy

The parameter σ^*_0 is fitted from mechanical measurements. The dynamic part (4. 6) has 2 restraints:

1. To avoid a negative strain rate influence, the term between brackets must be positive:

$$1 + \frac{kT}{\Delta G0} \cdot \ln\left(\frac{\dot{\varepsilon}_p}{\dot{\varepsilon}_0}\right) > 0 \qquad \textbf{4. 7}$$

   When the term is less than 0, the strain rate influence is considered zero.

2. To have a decreasing strain rate influence at higher temperatures, the strain rate has to be smaller than the limit strain rate:

$$\dot{\varepsilon}_p < \dot{\varepsilon}_0 \qquad \textbf{4. 8}$$

   Otherwise the strain rate influence is considered maximum and equal to σ_0^*.

The combination of (4. 4), (4. 5) and (4. 6) provides the total relation for the yield stress as a function of the equivalent plastic strain:

$$\sigma_y = \sigma_0 + \Delta\sigma_m \cdot \left[\beta \cdot (\varepsilon_0 + \varepsilon_p) + \left\{1 - e^{-\Omega\cdot(\varepsilon_0+\varepsilon_p)}\right\}^{r'}\right] + \sigma_0^* \cdot \left\{1 + \frac{kT}{\Delta G0} \cdot \ln\left(\frac{\dot{\varepsilon}_p}{\dot{\varepsilon}_0}\right)\right\}^{m'} \qquad \textbf{4. 9}$$

In the rest of this dissertation the first term is called the work hardening term (σ_{wh}) and the last term is called the dynamic term (σ_{dyn}):

$$\sigma_y = \sigma_{wh}(\varepsilon_p) + \sigma_{dyn}(\dot{\varepsilon}_p) \qquad \textbf{4. 10}$$

4.1.2 Stiffness matrix implementation

To implement the physically based hardening function in the stiffness matrix, the hardening parameter (f) must be determined (section 2.3.1). At isotropic hardening the hardening parameter is equal to the slope on the hardening curve, see appendix D:

$$f = -\frac{d\sigma_y}{d\varepsilon_p} = -\left(\frac{\partial\sigma_y}{\partial\varepsilon_p} + \frac{\partial\sigma_y}{\partial\dot{\varepsilon}_p}\frac{\partial\dot{\varepsilon}_p}{\partial\varepsilon_p}\right) = \qquad \textbf{4. 11}$$

$$-\frac{\partial\left[\Delta\sigma_m \cdot \left[\beta \cdot (\varepsilon_0 + \varepsilon_p) + \left\{1 - e^{-\Omega\cdot(\varepsilon_0+\varepsilon_p)}\right\}^{r'}\right]\right]}{\partial\varepsilon_p} - \frac{\partial\left[\sigma_0^* \cdot \left\{1 + \frac{kT}{\Delta G0} \cdot \ln\left(\frac{\dot{\varepsilon}_p}{\dot{\varepsilon}_0}\right)\right\}^{m'}\right]}{\partial\dot{\varepsilon}_p}\frac{\partial\dot{\varepsilon}_p}{\partial\varepsilon_p}$$

In an incremental analysis the equivalent plastic strain rate is defined by the equivalent plastic strain increment:

$$\dot{\varepsilon}_p = \frac{\Delta\varepsilon_p}{\Delta t} \qquad \textbf{4. 12}$$

where

$\Delta\varepsilon_p$ is the equivalent plastic strain increment in a finite element step
Δt is the time increment of the finite element step, which is an input parameter in a finite element simulation.

Now the total relation for the hardening is given by:

$$\begin{aligned} f = &-\Delta\sigma_m \cdot \left[\beta + n' \left\{1 - e^{-\Omega\cdot(\varepsilon_0+\varepsilon_p)}\right\}^{n'-1} \cdot \Omega \cdot e^{-\Omega\cdot(\varepsilon_0+\varepsilon_p)}\right] \\ &- \sigma_0^* \cdot m' \cdot \left\{1 + \frac{kT}{\Delta G0} \cdot \ln\left(\frac{\dot{\varepsilon}_p}{\dot{\varepsilon}_0}\right)\right\}^{m'-1} \cdot \frac{kT}{\Delta G0} \cdot \frac{1}{\dot{\varepsilon}_p} \frac{1}{\Delta t} = \\ &- \Delta\sigma_m \cdot \left[\beta + n' \left\{1 - e^{-\Omega\cdot(\varepsilon_0+\varepsilon_p)}\right\}^{n'-1} \cdot \Omega \cdot e^{-\Omega\cdot(\varepsilon_0+\varepsilon_p)}\right] \\ &- \sigma_0^* \cdot m' \cdot \left\{1 + \frac{kT}{\Delta G0} \cdot \ln\left(\frac{\varepsilon_p / \Delta t}{\dot{\varepsilon}_0}\right)\right\}^{m'-1} \cdot \frac{kT}{\Delta G0} \cdot \frac{1}{\varepsilon_p} \end{aligned} \qquad \textbf{4. 13}$$

When the term between brackets on the right hand side is smaller than 0 or larger than 1, the strain rate influence on the hardening parameter is considered zero, see equations (4. 7) and (4. 8). The consequence is that the hardening is discontinuous at the transition to these situations.

4.1.3 Stress update algorithm implementation

To implement the physically based hardening function in the stress update algorithm, the hardening tensor ($\underline{\beta}$) must be determined (section 2.3.2).

At isotropic hardening the tensor ($\underline{\beta}$) can be replaced by the yield stress (σ_y). The yield stress is a function of the total equivalent plastic strain and the equivalent plastic strain rate (expression 4. 10):

$$\sigma_y = \sigma_{wh}(\varepsilon_p) + \sigma_{dyn}(\dot{\varepsilon}_p) \qquad \textbf{4. 14}$$

In an incremental analysis the equivalent plastic strain rate is defined by the equivalent plastic strain increment (equation 4. 12).

Consequently the hardening tensor ($\underline{\beta}$) - in general a function of the derivative of the yield function to this tensor ($\partial\phi/\partial\underline{\beta}$), the hardening parameter (f), the plastic multiplier (λ) and the plastic multiplier increment ($\Delta\lambda$) – is replaced by the yield stress (σ_y), which is a function of the equivalent plastic strain (ε^p) and the equivalent plastic strain increment ($\Delta\varepsilon^p$):

$$\underline{\beta}\left(\frac{\partial\phi}{\partial\underline{\beta}}, f, \lambda, \Delta\lambda\right) \rightarrow \sigma_{wh}\left(\varepsilon_p + \Delta\varepsilon_p\right) + \sigma_{dyn}\left(\Delta\varepsilon_p\right) \qquad \textbf{4. 15}$$

The plastic multiplier (λ) and the equivalent plastic strain (ε_p) are defined by the values at the start of a finite element step and the incremental values ($\Delta\lambda$ and $\Delta\varepsilon_p$ respectively). The initial values remain fixed during the stress update, so (4. 15) is rewritten as:

$$\underline{\beta}\left(\frac{\partial\phi}{\partial\underline{\beta}}, f, \Delta\lambda\right) \rightarrow \sigma_{wh}\left(\Delta\varepsilon_p\right) + \sigma_{dyn}\left(\Delta\varepsilon_p\right) \qquad \textbf{4. 16}$$

The relation between the plastic multiplier increment ($\Delta\lambda$) and the equivalent strain increment ($\Delta\varepsilon_p$) is derived as follows. The equivalent plastic strain increment is defined by the incremental format of equation (2.7):

$$\sigma_y \Delta\varepsilon_p = \underline{\sigma} : \Delta\underline{\varepsilon}^p$$

or

$$\Delta\varepsilon_p = \frac{\underline{\sigma}}{\sigma_y} : \Delta\underline{\varepsilon}^p \qquad \textbf{4. 17}$$

where

$\underline{\sigma}$ is the stress tensor
$\Delta\underline{\varepsilon}^p$ is the plastic strain increment tensor

The plastic strain increment tensor is related to the plastic multiplier increment ($\Delta\lambda$) by the normality principle of Drucker (equation 2.13):

$$\Delta\underline{\varepsilon}^p = \Delta\lambda \frac{\partial\phi}{\partial\underline{\sigma}} \qquad \textbf{4. 18}$$

With relations (4. 16), (4. 17) and (4. 18), the numerical procedure of scheme 2-1 is rewritten to scheme 4-1:

$\underline{\sigma}_t = \underline{\sigma} + \underline{\underline{E}} \cdot \Delta\underline{\varepsilon}$

Initialisation of i,$\Delta\lambda^i$,$\Delta\lambda^{i-1}$, $\Delta\varepsilon^p$

While $\dfrac{\Delta\lambda^i - \Delta\lambda^{i-1}}{\Delta\lambda^{i-1}} > threshold$ do

$\sigma_y = \sigma_{wh}\left(\Delta\varepsilon^p\right) + \sigma_{dyn}\left(\Delta\varepsilon^p\right)$

Determine $\Delta\lambda^{i+1}$ by

$\underline{\sigma}_n = \underline{\sigma}_t - \Delta\lambda^{i+1}\,\underline{\underline{E}} \cdot \left(\dfrac{\partial\phi}{\partial\underline{\sigma}}\right)$ with $\phi\left(\underline{\sigma}_n, \sigma_y\right) = 0$

$\Delta\underline{\varepsilon}^p = \Delta\lambda^{i+1}\dfrac{\partial\phi}{\partial\underline{\sigma}}$

$\Delta\varepsilon_p = \dfrac{\underline{\sigma}_n}{\sigma_y} : \Delta\underline{\varepsilon}^p$

i=i+1

End while

Scheme 4-1 Stress update procedure for isotropic hardening material

Due to the restraints in the dynamic part of the hardening function, the numerical procedure of scheme 4-1 is not stable. When the plastic strain increment in the procedure is so low that equation (4. 7) is violated, the dynamic part vanishes. When the plastic strain increment in the procedure is as large that (4. 8) is violated, the dynamic part is maximal. The effect of restraint (4. 7) is shown in figure 4-2, which illustrates a projection of the yield stress (σ_y) as a function of the plastic strain increment tensor ($\Delta\underline{\varepsilon}^p$). The thick solid curve represents the yield stress - strain increment tensor relation with the dynamic part and the dotted curve the relation without the dynamic part. Due to restraint (4. 7) the dynamic part is zero below the strain increment $\Delta\underline{\varepsilon}^{p*}$.

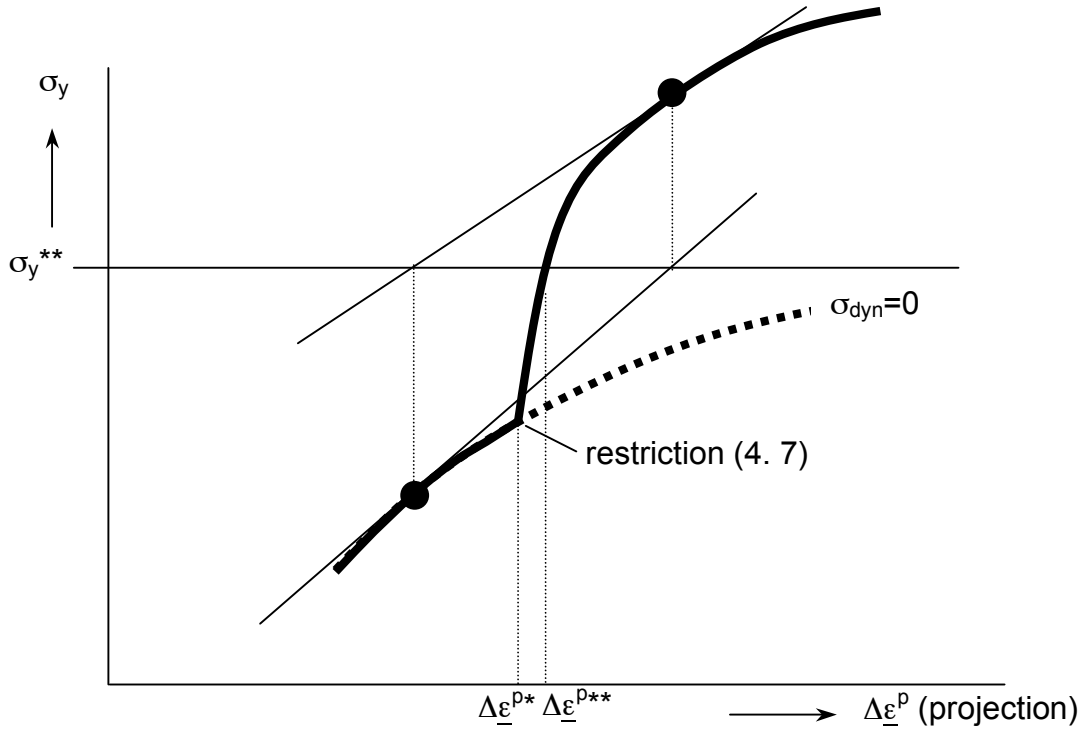

Figure 4-2 Effect of restraint (4. 7) on numerical solution process

Suppose the solution process of scheme 2-1 can be represented by a Newton-Raphson process and the correct solution is given by the yield stress (σ_y**) and strain increment tensor ($\Delta\underline{\varepsilon}^{p**}$). When the first guess is represented by the lower black dot, the second guess will be the upper black dot. If the tangents on the curve are as in figure 4-2, the third guess will be exactly equal to the first guess. So the procedure can be unstable by 'swapping' between two solutions. To avoid this problem, a new numerical procedure has been developed, in which the dynamic part is updated independently of the work hardening part. The work hardening part is updated by the procedure of 4-1. The dynamic part is updated by the average value of the new equivalent plastic strain increment of scheme 4-1 and the former equivalent plastic strain increment. In this way the 'swapping' problem is avoided and the procedure appears stable. The procedure is described by scheme 4-2.

$\underline{\sigma}_t = \underline{\sigma} + \underline{\underline{E}} \cdot \Delta\underline{\varepsilon}$

Initialisation of j,σ_{dyn}^{j}, σ_{dyn}^{j-1},$(\Delta\varepsilon^p)^j$,$(\Delta\varepsilon^p)^{j-1}$

While $\dfrac{\sigma_{dyn}{}^{j} - \sigma_{dyn}{}^{j-1}}{\sigma_{dyn}{}^{j-1}} > treshold2$ do

Initialisation of i,$\Delta\lambda^i\Delta\lambda^{i-1}$

While $\dfrac{\Delta\lambda^i - \Delta\lambda^{i-1}}{\Delta\lambda^{i-1}} > treshold1$ do

$\sigma_y = \sigma_{wh}\left(\Delta\varepsilon^p\right)^j + \sigma_{dyn}{}^{j}$

Determine $\Delta\lambda^{i+1}$ by

$\underline{\sigma}_n = \underline{\sigma}_t - \Delta\lambda^{i+1}\underline{\underline{E}} \cdot \left(\dfrac{\partial\phi}{\partial\underline{\sigma}}\right)$ with $\phi\left(\underline{\sigma}_n, \sigma_y\right) = 0$

$\Delta\underline{\varepsilon}^p = \Delta\lambda^{i+1}\dfrac{\partial\phi}{\partial\underline{\sigma}}$

$\left(\Delta\varepsilon^p\right)^j = \dfrac{\underline{\sigma}_n}{\sigma_y} : \Delta\underline{\varepsilon}^p$

i=i+1

End while

$\sigma_{dyn}{}^{j+1} = \sigma_{dyn}\left(\dfrac{\left(\Delta\varepsilon^p\right)^j + \left(\Delta\varepsilon^p\right)^{j-1}}{2}\right)$

j=j+1

End While

Scheme 4-1

Scheme 4-2 Stress update procedure for physically based hardening function

The hardening function is used in combination with the Vegter yield function. In this case the definition of the equivalent strain increment (4. 17) is elaborated in a special way. Expression (4. 17) is rewritten for a plane stress situation:

$$\Delta\varepsilon_p = \frac{\sigma_{xx}\Delta\varepsilon_{xx} + \sigma_{yy}\Delta\varepsilon_{yy} + \tau_{xy}\Delta\gamma_{xy}}{\sigma_y} = \frac{\sigma_1\Delta\varepsilon_1^* + \sigma_2\Delta\varepsilon_2^*}{\sigma_y} = f1(\mu,\theta)\cdot\Delta\varepsilon_1^* + f2(\mu,\theta)\cdot\Delta\varepsilon_2^* \qquad \textbf{4. 19}$$

where

μ	is determined by (3.14)
θ	is determined by the rules of tensor transformation (3.9)
f1(μ,θ) and f2(μ,θ)	is defined by (3.13).
$\Delta\varepsilon_1$* and $\Delta\varepsilon_2$*	are the normal strain increment components in the directions of the first and second principal stresses respectively.

In finite element applications the equivalent plastic strain increment is determined as follows:

1. The stress state σ_{xx},σ_{yy},τ_{xy} is transformed into a principal stress state $\sigma_1$and σ_2 (equation 3.9)
2. The planar angle θ is determined (equation 3.9)
3. The measured reference points are interpolated to obtain the reference points for the angle θ (equation 3.4)
4. From the 7 reference points the 2 relevant reference points and the related Bezier function are chosen on the basis of the ratio of the principal stresses (figure 3-6)
5. The normal components of the strain increment in the direction of the principal stresses $\Delta\varepsilon_1$* and $\Delta\varepsilon_2$* are determined
6. The parameter μ is determined by (3.14)
7. f1(μ,θ) and f2(μ,θ) are defined by (3.13)
8. The equivalent plastic strain increment is determined by (4. 19)

4.2 Extension to cyclic hardening behaviour

4.2.1 General outline

The extension of istropic to cyclic hardening behaviour was first attempted by the two yield surface model of (Vreede, 1992). Compared to isotropic hardening, this model consists of an adapted yield function and an extended hardening function. The yield function is described by the kinematic yield surface and the hardening function is defined by both the isotropic surface and the kinematic surface, see section 2.1.2.

The situation of the kinematic surface is denoted by the back stress tensor $\underline{\alpha}$, which defines the centre of this surface. In an incremental analysis the back stress is defined by the back stress increment (Vreede, 1992):

$$\Delta\underline{\alpha} = (\underline{\sigma} - \underline{\alpha}) \frac{\frac{\partial \phi(\underline{\sigma} - \underline{\alpha})}{\partial \underline{\sigma}} : (\underline{\underline{E}} - \underline{\underline{Y}}) : \Delta\underline{\varepsilon}}{\frac{\partial \phi(\underline{\sigma} - \underline{\alpha})}{\partial \underline{\sigma}} : (\underline{\sigma} - \underline{\alpha})} \qquad \textbf{4. 20}$$

Vreede defined the hardening on the normalised distance (D) between the kinematic and the isotropic yield surfaces:

$$f = f_{ini} + (1 - D)^q (f_{iso} - f_{ini}) \qquad \textbf{4. 21}$$

Here (f_{iso}) represents the isotropic hardening rate and (f_{ini}) the initial hardening rate at a reverse loading test. The anisotropic parameter (q) is fit on experimental results. Figure 5-5 illustrates the kinematic and isotropic surfaces and the construction of the distance (D).

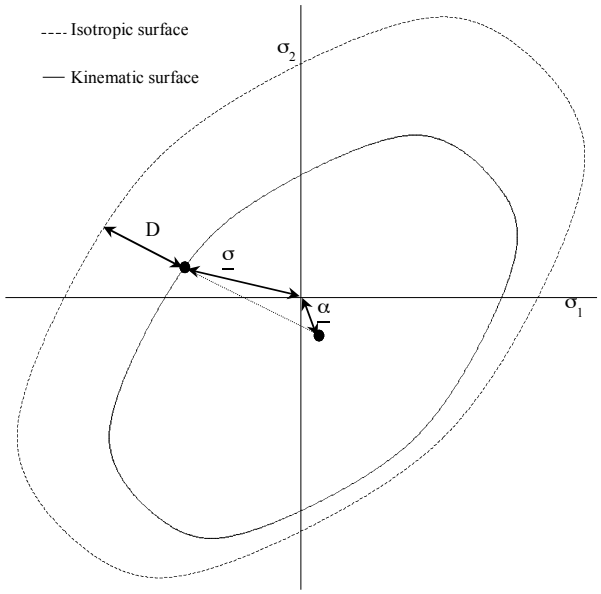

Figure 5-5 Kinematic and isotropic yield surfaces

The distance (D) is defined by the points of intersection of the line through the stress ($\underline{\sigma}$) and back stress ($\underline{\alpha}$) with the isotropic yield surface:

$$\phi(\underline{\alpha} + a(\underline{\sigma} - \underline{\alpha}), \sigma_y) = 0 \qquad \textbf{4. 22}$$

Formula (4. 22) gives two solutions for a: a1 and a2. The distance (D) is determined by:

$$D = \frac{a1 - 1}{a1 - a2 - 2} \qquad \textbf{4. 23}$$

In this way (D) always has a value between 0 and 1, irrespective of the size of the isotropic yield surface.

To apply the approach of Vreede in combination with the Vegter yield function, equation (4. 22) is considered. To solve this equation, the Vegter yield function must be elaborated with the stress tensor $\underline{\sigma}$ in equation (3.6) replaced by the tensor ($\underline{\alpha}$+a($\underline{\sigma}$-$\underline{\alpha}$)). The elaboration requires the transformation of this tensor to principal data and a planar angle. In this case the planar angle (θ*) can be obtained by rerwiting equation (3.9) to:

$$\cos 2\theta^* = \frac{\frac{\left[\alpha_{xx} + a(\sigma_{xx} - \alpha_{xx})\right] - \left[\alpha_{yy} + a(\sigma_{yy} - \alpha_{yy})\right]}{2}}{\sqrt{\left(\frac{\left[\alpha_{xx} + a(\sigma_{xx} - \alpha_{xx})\right] - \left[\alpha_{yy} + a(\sigma_{yy} - \alpha_{yy})\right]}{2}\right)^2 + \left(\tau_{xy} - \alpha_{xy}\right)^2}} \qquad \textbf{4. 24}$$

Here (α_{xx}), (α_{yy}) and (α_{xy}) are the components of the back stress tensor in a plane stress situation. If the principal stresses have the same angle to the rolling direction as the principal back stresses, the planar angle (θ*) is equal to the planar angle (θ) of the stress. In general this is not the case, so the planar angle θ* depends on the solution of (a). Because the planar angle is variable, the relevant Bezier curve can not be chosen in advance. This resembles the problem in the Euler-backward method, see section 3.4. To avoid an extensive numerical procedure, the anisotropic hardening description is modified.

The new description is discussed in the following sections. In section 4.2.2 new surfaces are defined which provide the basis for the description. Section 4.2.3 explains how the hardening function is defined with the new surfaces. Subsequently section 4.2.4 investigates the extension from cyclic to an arbitrary deformation path. The new description also involves an adaptation of the Vegter yield function, which is discussed in section 4.2.5. The implementation in a finite element code is described in sections 4.2.6 and 4.2.7.

4.2.2 Introduction of new surfaces

The new anisotropic hardening description uses 3 surfaces. The yield function is still defined by the familiar kinematic yield surface:

$$\phi = \phi(\underline{\sigma} - \underline{\alpha}, \sigma_0) \qquad \textbf{4. 25}$$

or

$$\phi = \phi(\underline{\sigma}^*, \sigma_0) \qquad \textbf{4. 26}$$

with ($\underline{\sigma}$) the stress tensor, ($\underline{\alpha}$) the back stress tensor and (σ^*) the effective stress tensor. The term (σ_0) is the initial yield stress. The planar angle in the yield function (θ_{σ^*}) is defined by the angle of the principal directions of the effective stress tensor to the rolling direction:

$$\cos 2\theta_{\sigma^*} = \frac{\frac{\sigma^*_{xx} - \sigma^*_{yy}}{2}}{\sqrt{\left(\frac{\sigma^*_{xx} - \sigma^*_{yy}}{2}\right)^2 + \tau^{*2}_{xy}}} \qquad \textbf{4. 27}$$

The new hardening function is determined by 2 new surfaces, defined by the back stress tensor ($\underline{\alpha}$). Hence the planar angle in the hardening function is defined by the angle (θ_α) of the principal back stresses to the rolling direction:

$$\cos 2\theta_{\alpha} = \frac{\frac{\alpha_{xx} - \alpha_{yy}}{2}}{\sqrt{\left(\frac{\alpha_{xx} - \alpha_{yy}}{2}\right)^2 + \alpha^2_{xy}}}$$

Note that this planar angle differs from the planar angle of the stress (equation 3.9) and from the planar angle of the effective stress (equation 4. 27). It will turn out in the following that this is not a problem as the different planar angles are used in different mathematical formulations

The first new surface is called the equivalent shift surface and the second is called the limit shift surface. The equivalent shift surface is defined by the back stress tensor. The size of this surface is given by the equivalent back stress (α_{eq}), which is is defined by:

$$\begin{pmatrix}\alpha_1\\ \alpha_2\end{pmatrix} = \frac{\alpha_{eq}}{\sigma_y}\cdot\left[\begin{pmatrix}\sigma_1\\ \sigma_2\end{pmatrix}_0(\theta_\alpha) + 2\mu\cdot\left(\begin{pmatrix}\sigma_1\\ \sigma_2\end{pmatrix}_1(\theta_\alpha) - \begin{pmatrix}\sigma_1\\ \sigma_2\end{pmatrix}_0(\theta_\alpha)\right) + \mu^2\cdot\left(\begin{pmatrix}\sigma_1\\ \sigma_2\end{pmatrix}_2(\theta_\alpha) + \begin{pmatrix}\sigma_1\\ \sigma_2\end{pmatrix}_0(\theta_\alpha) - 2\begin{pmatrix}\sigma_1\\ \sigma_2\end{pmatrix}_1(\theta_\alpha)\right)\right] \qquad \textbf{4. 28}$$

where

σ_y is the yield stress

α_{eq} is the equivalent back stress, which represents the size of the equivalent shift surface

θ_α is the planar angle of the back stress

α_1 is the first principal back stress

α_2 is the second principal back stress

The part between brackets is the Bezier interpolation function, defined by the ratio (α_1/α_2). Expression (4. 28) is derived from the expression for the equivalent stress in section 3.2.4.

The second surface is called the limit shift surface. This surface describes the maximum equivalent shift surface. The surfaces are illustrated in figures 4-4 to 4-11 during a uni-axial tension-compression deformation. In this example the yield function is assumed planar isotropic, hence all surfaces have the same shape and the kinematic yield surface can be represented in the principal stress space.

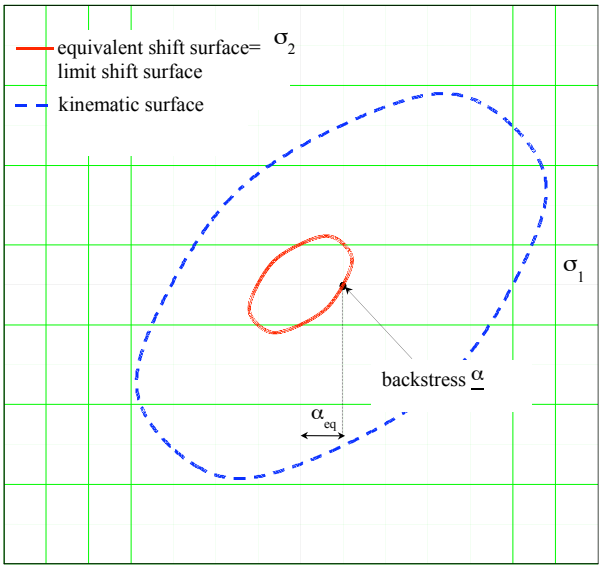

Figure 4-4 Surfaces at initial tension

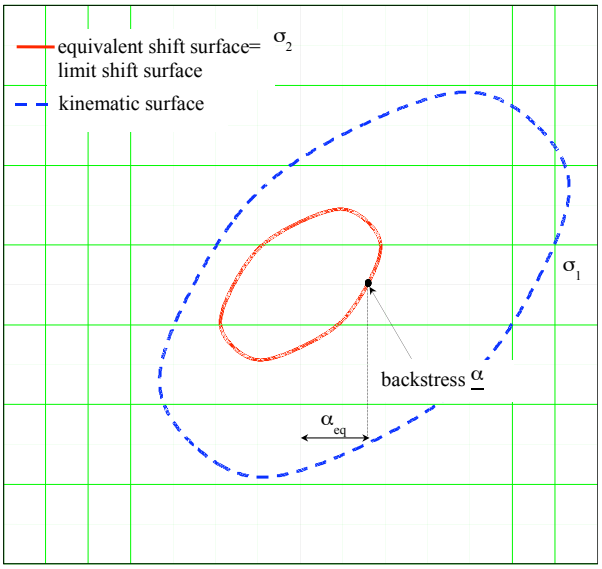

Figure 4-5 Surfaces at larger tension

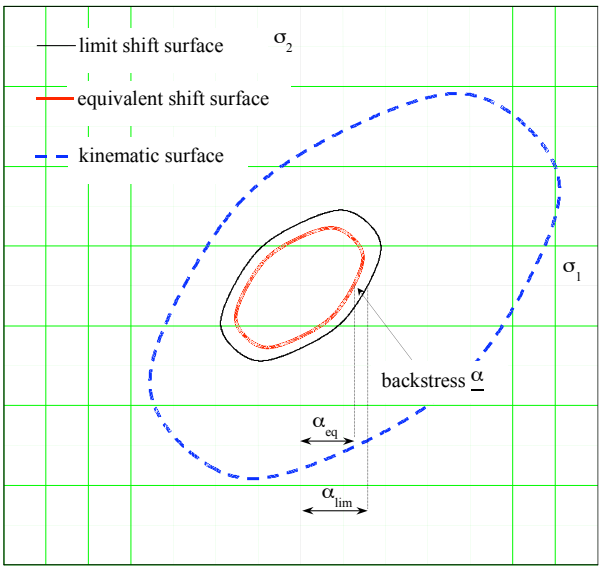

Figure 4-6 Surfaces at initial compression

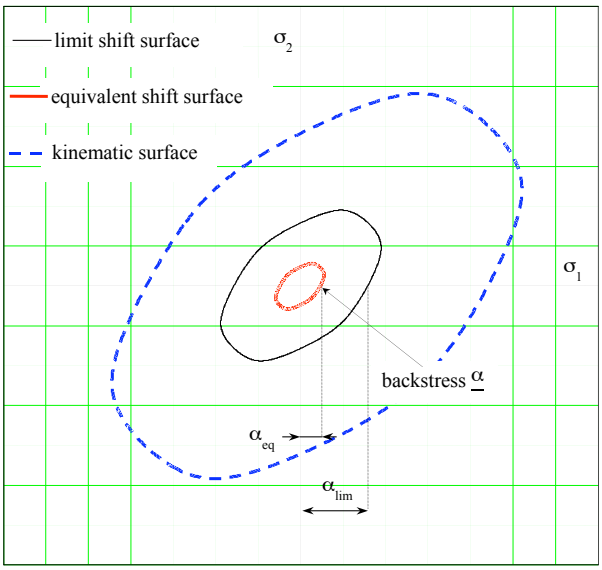

Figure 4-7 Surfaces at larger compression (1)

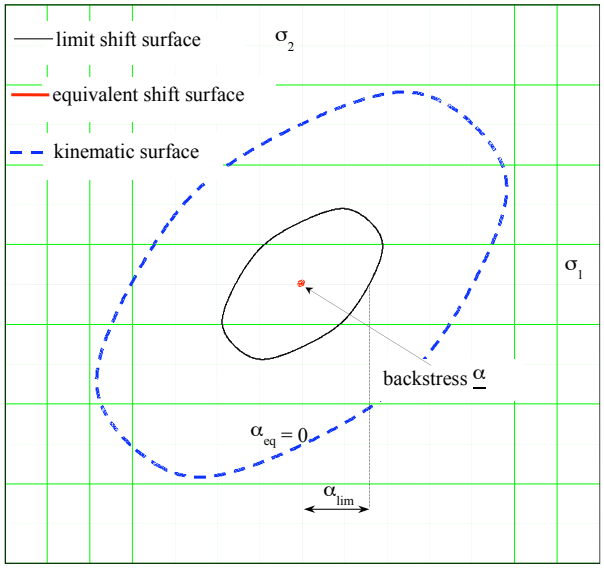

Figure 4-8 Surfaces at larger compression (2)

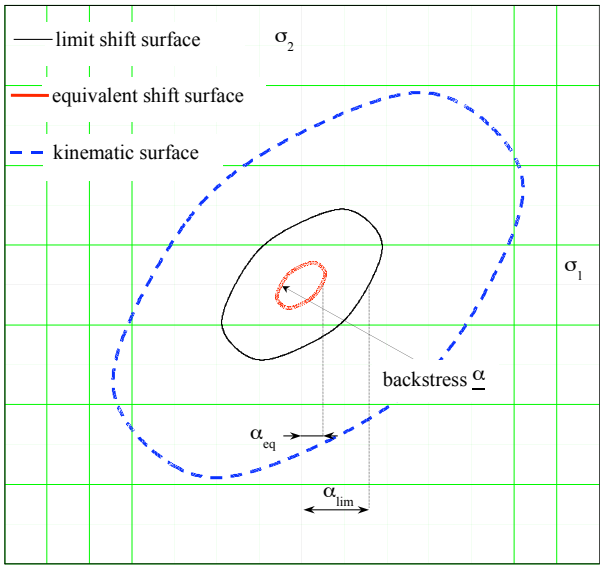

Figure 4-9 Surfaces at larger compression (3)

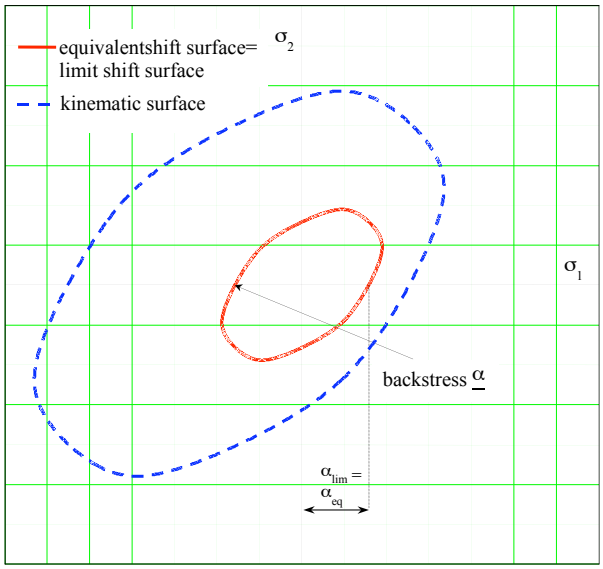

Figure 4-10 Surfaces at larger compression (4)

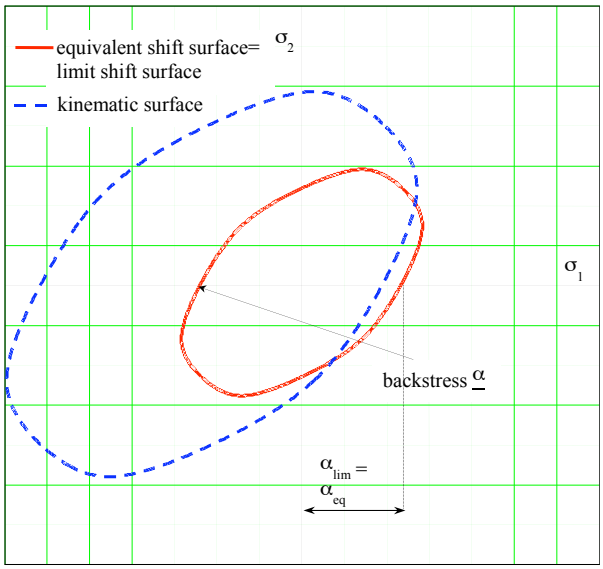

Figure 4-11 Surfaces at larger compression (5)

In the initial situation the kinematic yield surface is at the centre of the stress space. When the material deforms plastically in uni-axial tension, the kinematic surface translates in the uni-axial direction, see figure 4-4. The equivalent shift surface is defined in such a way that the back stress is on this surface. The size is denoted by the equivalent back stress (α_{eq}). The limit surface represents the maximum equivalent shift surface, hence it is equal to the equivalent shift surface at initial tension. When plastic deformation proceeds, the kinematic surface translates further in the same direction and the equivalent and limit shift surfaces grow, see figure 4-5.

When the material is plastically compressed after tension, the kinematic surface translates in the negative uni-axial direction. Because the back stress is on the shift surface, this surface decreases in size, see figure 4-6. The limit-shift surface represents the maximum equivalent shift surface, hence it remains the same size just after the tension deformation. The size of the limit shift surface is denoted by the maximum equivalent back stress (α_{lim}). When the compression deformation proceeds, the kinematic surface translates further in the negative uni-axial direction and the equivalent shift surface decreases in size, see figure 4-7. This continues until the kinematic surface is at its original position and the size of the equivalent shift surface is zero, see figure 4-8. After this the equivalent shift surface increases again in size, see figures 4-9 and 4-10. When the size of the equivalent shift surface has reached the size of the limit surface, the size of the limit surface increases together with the equivalent shift surface, see figure 4-11.

4.2.3 Hardening definition

To obtain a mathematical relation for the hardening, the slopes on a realistic hardening curve are considered, see figure 4-12.

Figure 4-12 illustrates the different hardening stages. Parts (b) and (f) represent proportional hardening. In these parts the equivalent shift and limit shift surfaces are equal ($\alpha_{eq}=\alpha_{lim}$). Parts (d) and (e) represent the anisotropic parts of the hardening curve. In these parts the equivalent shift surface is smaller than the limit shift surface ($\alpha_{eq}<\alpha_{lim}$). At the start of part (d) and at the end of part (e) the equivalent shift surface is equal to the limit shift surface ($\alpha_{eq}=\alpha_{lim}$). These situations coincide with figures 4-5 and 4-10 at uni-axial tension. At the transition from (d) to (e) the size of the equivalent shift surface is zero ($\alpha_{eq}=0$). This situation coincides with figure 4-8. In parts (d) and (e) the values of (α_{eq}) can be the same, but the hardening is different. To consider different hardening behaviour in parts (d) and (e), the change in the value of (α_{eq}) is taken into account. In part (d) the value decreases and in part (e) the value increases. When the value decreases, the hardening is larger than when the value increases.

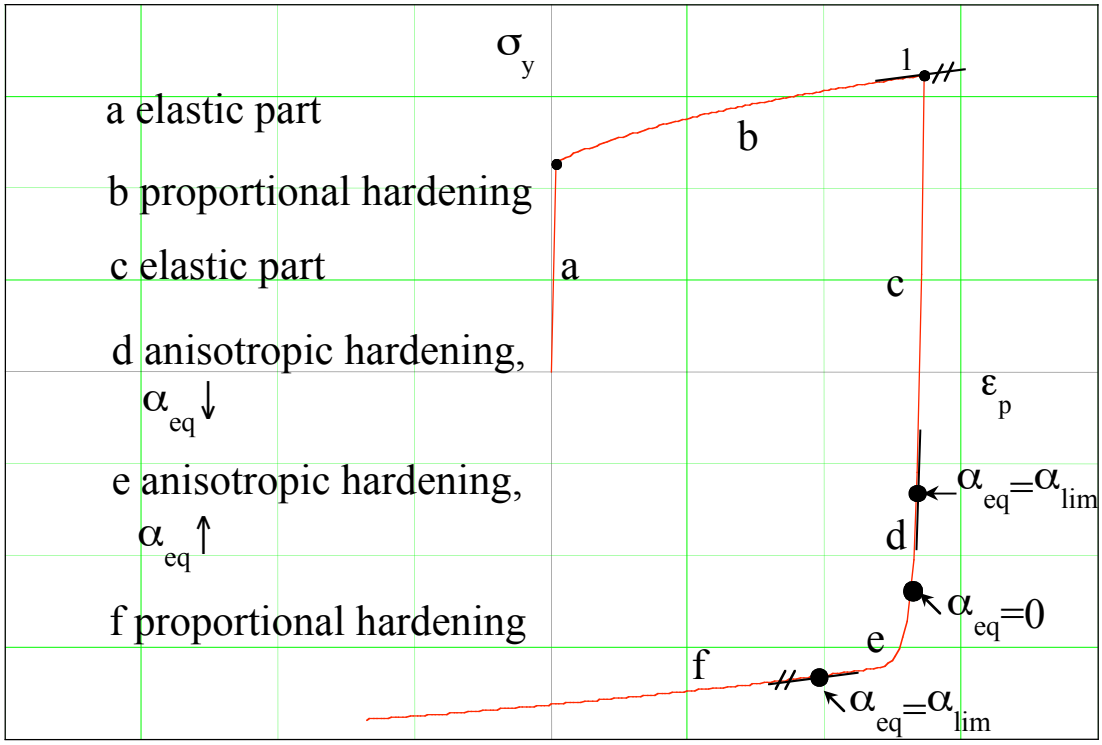

Figure 4-12 Realistic hardening curve

To relate the hardening behaviour of figure 4-12 to the definitions of the equivalent and limit shift surfaces, the original anisotropic hardening relation of Vreede (4. 21) is modified by replacing the distance (D) by a function of the surface definitions:

$$f = f_{ini} + \left[1 - \left(\frac{1}{2} + \frac{1}{2} \cdot \frac{\alpha_{eq}}{\alpha_{\lim}}\right)\right]^{q} \cdot \left(f_{iso} - f_{ini}\right) \qquad \textbf{4. 29}$$

when the value of (α_{eq}) decreases (i.e. stage (d) of the hardening curve), and

$$f = f_{ini} + \left[1 - \left(\frac{1}{2} - \frac{1}{2} \cdot \frac{\alpha_{eq}}{\alpha_{\lim}}\right)\right]^{q} \cdot \left(f_{iso} - f_{ini}\right) \qquad \textbf{4. 30}$$

when the value of (α_{eq}) increases (i.e. stage (e) of the hardening curve)

where

f_{ini} is the initial hardening rate in a load reversal
f_{iso} is the hardening rate at isotropic yielding
α_{eq} is the equivalent back stress
α_{lim} is the maximum equivalent back stress
q is the anisotropic hardening parameter (to be fit from experimental results)

4.2.4 Extension to arbitrary deformations

For arbitrary deformations the new hardening function has to be adapted to obtain a continuous hardening behaviour. For instance suppose that after a uni-axial tensile deformation a shear deformation occurs. During the shear deformation the kinematic yield surface will translate along the dotted line in figure 4-13. As in the cyclic loading case, at a certain point the value of (α_{eq}) will change from decreasing to increasing. The difference with the cyclic case, however, is that the ratio is not equal to 0 at this moment. This means that the hardening suddenly changes from a value

$$f = f_{ini} + \left[1 - \left(\frac{1}{2} + \frac{1}{2} \cdot \frac{\alpha_{eq}}{\alpha_{\lim}}\right)\right]^{q} \cdot \left(f_{iso} - f_{ini}\right)$$

to

$$f = f_{ini} + \left[1 - \left(\frac{1}{2} - \frac{1}{2} \cdot \frac{\alpha_{eq}}{\alpha_{\lim}}\right)\right]^{q} \cdot \left(f_{iso} - f_{ini}\right)$$

Hence the consequence is that the hardening is not continously defined in this case. This is not physical and can give problems in the numerical implementation in a finite element code.

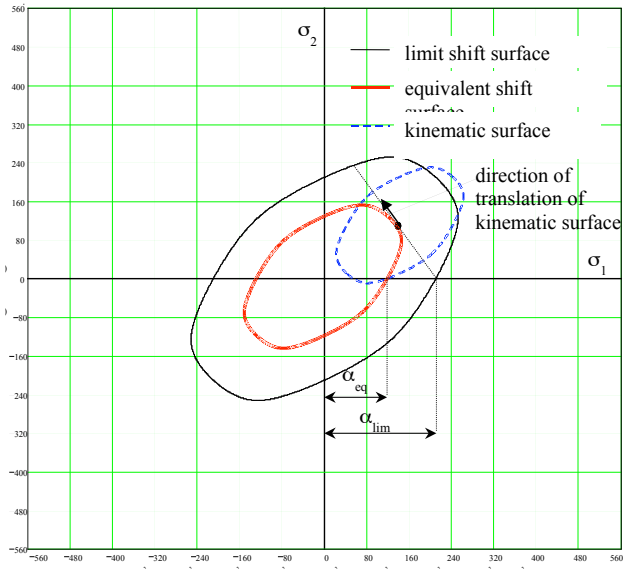

Figure 4-13 Situation at which the value of (α_{eq}) changes from decreasing to increasing

The discontinuity in the hardening during a non-proportional test can be solved by adapting the hardening definition to

$$f = fini + \left[1 - \left(\frac{1}{2} - \frac{1}{2} \cdot \frac{\alpha_{eq}}{\alpha_{\lim}} \cdot \cos\alpha\right)\right]^{nan} \cdot (fiso - fini) \qquad \textbf{4. 31}$$

with

$$\cos\alpha = \frac{\Delta\underline{\alpha} \cdot \underline{\alpha}}{|\Delta\underline{\alpha}||\underline{\alpha}|}$$

Here the term ($\cos\alpha$) describes the cosine of the angle between the current back stress ($\underline{\alpha}$) (i.e. the current situation of the centre of the kinematic yield surface) and the back stress increment ($\Delta\underline{\alpha}$) (i.e the translation increment of the centre of the kinematic surface. The term can have the following values:

- It has the value 1 when the increment ($\Delta\underline{\alpha}$) and ($\underline{\alpha}$) are in the same direction. This is the case in a proportional deformation.
- It has the value –1 when the increment ($\Delta\underline{\alpha}$) and ($\underline{\alpha}$) are in opposite directions. This is the case in the beginning of a reverse loading deformation. However, when the stress has travelled through the origin of the stress space, the value changes into +1. So in a cyclic loading case the result is exactly the same as without the term.
- It has the value 0 when the increment ($\Delta\underline{\alpha}$) and ($\underline{\alpha}$) are in perpendicular directions. For instance this is the case at the beginning of a shear deformation just after a plane strain deformation state. After successive shear deformation the term will approach 1 again.

Recapitulating, for a proportional or cyclic loading path the hardening description remains unaffected. For a non-proportional loading deformation the adapted description takes care of a continuous hardening behaviour. For the time being the adaptation is only utilized to prevent numerical instabilities and is not based on experimental data. In chapter 5 the adaptation is examined with a non-proportional deformation.

4.2.5 Yield function adaptation

At anistropic hardening the kinematic yield surface defines the yield condition. Compared to isotropic hardening, the yield function is changed from:

$$\phi = \phi(\underline{\sigma}, \sigma_y)$$

to

$$\phi = \phi(\underline{\sigma} - \underline{\alpha}, \sigma_0) \qquad \textbf{4. 32}$$

or

$$\phi = \phi(\underline{\sigma}^*, \sigma_0) \qquad \textbf{4. 33}$$

where ($\underline{\sigma}$) is the stress tensor, ($\underline{\alpha}$) is the back stress and (σ^*) is the effective stress tensor. The term (σ_y) represents the isotropic yield stress and (σ_0) is the initial yield stress. So no change in the yield criterion itself is made, only the stress tensor is replaced by the effective stress tensor and the isotropic yield stress is replaced by the initial yield stress.

In finite element applications the yield function is determined by the following steps:

1. The stress state $\sigma_{xx},\sigma_{yy},\tau_{xy}$ is adapted with the back stress $\alpha_{xx},\alpha_{yy},\alpha_{xy}$ to $\sigma^*_{xx},\sigma^*_{yy},\tau^*_{xy}$
2. The effective stress state is transformed into a principal stress state σ^*_1,σ^*_2 (equation 3.9)
3. The planar angle θ_{σ^*} of the effective stress is determined (equation 3.9)
4. The measured reference points are interpolated to obtain the reference points for the angle θ_{σ^*} (equation 3.4)
5. From the 7 reference points the 2 relevant reference points and the related Bezier function are chosen on the basis of the ratio of the effective principal stresses (figure 3-6)
6. The yield function is determined according to 3.10, 3.13 and 3.14

4.2.6 Stiffness matrix implementation

To implement the new hardening description in the stiffness matrix, the derivative of the yield function and the hardening parameter (f) must be determined (section 2.3.1).

Derivative of the yield function

The derivative of the yield function to the stress tensor can also be written as a function of the derivative to the effective stress tensor, assuming an independent back stress tensor:

$$\frac{\partial \phi(\underline{\sigma}-\underline{\alpha},\sigma_0)}{\partial \underline{\sigma}} = \frac{\partial \phi(\underline{\sigma}-\underline{\alpha},\sigma_0)}{\partial (\underline{\sigma}-\underline{\alpha})} \cdot \frac{\partial (\underline{\sigma}-\underline{\alpha})}{\partial \underline{\sigma}} = \frac{\partial \phi(\underline{\sigma}-\underline{\alpha},\sigma_0)}{\partial (\underline{\sigma}-\underline{\alpha})} \qquad \textbf{4. 34}$$

This expression is elaborated in a way similar to the procedure in section 4.3.1, with the stress ($\underline{\sigma}$) replaced by the effective stress ($\underline{\sigma}^*$) and the isotropic yield stress (σ_y) replaced by the initial yield stress (σ_0). In a finite element code the derivative is determined by the next steps:

1. The stress state $\sigma_{xx},\sigma_{yy},\tau_{xy}$ is adapted with the back stress $\alpha_{xx},\alpha_{yy},\alpha_{xy}$ to $\sigma^*_{xx},\sigma^*_{yy},\tau^*_{xy}$
2. The effective stress state is transformed into a principal stress state σ^*_1,σ^*_2 (equation 3.9)
3. The planar angle θ_{σ^*} of the effective stress is determined (equation 3.9)
4. The measured reference points are interpolated to obtain the reference points for the angle θ_{σ^*} (equation 3.4)
5. From the 7 reference points the 2 relevant reference points and the related Bezier function are chosen on the basis of the ratio of the effective principal stresses (figure 3-6)
6. The derivatives of the yield function to the principal stresses are defined (a1,a2 of equation 3.17)
7. The derivatives of the principal stresses to general stress components are determined (b1, b2 of equation 3.17)
8. The derivative of the cosine of twice the planar angle to the stress components is determined (d of equation 3.17)
9. The derivative of the yield function to the cosine of twice the planar angle is defined (c of equation 3.17)
10. The derivative is constructed by expression (4. 34)

Hardening parameter (anisotropic hardening)

The hardening definition is handled extensively in the former sections. The basis for the finite element implementation is equation (4. 31). This equation is elaborated as follows:

1. The back stress is transformed into a principal back stress α_1,α_2 (equation 3.9)
2. The planar angle θ_α of the back stress is determined (equation 3.9)
3. The measured reference points are interpolated to obtain the reference points for the angle θ_α (equation 3.4)
4. From the 7 reference points the 2 relevant reference points and the related Bezier function are chosen on the basis of the ratio of the principal back stresses (figure 3-6)
5. The size of the equivalent shift surface is determined by α_{eq} (equation 4. 28)
6. The size of the limit shift surface is determined. If the size of the current limit shift surface is larger than the shift surface of the former step, the limit surface is updated
7. The term $\cos\alpha$ is determined by the current back stress $\underline{\alpha}$ and the back stress increment $\Delta\underline{\alpha}$ (equation 4. 31)
8. The hardening f is determined according to (4. 31)

4.2.7 Stress update algorithm implementation

To implement the new hardening function in the stress update procedure, the stress must be projected to the kinematic yield surface and the hardening tensor ($\underline{\beta}$) must be determined (section 2.3.2).

Stress projection procedure

Compared to isotropic hardening, the equations for the stress projection procedure change from (3.18) and (3.19) to (4. 35) and (4. 36):

$$\underline{\sigma}_n = \underline{\sigma}_t - \Delta\lambda \underline{\underline{E}} \cdot \left(\frac{\partial \phi}{\partial \underline{\sigma}} \right)_n \qquad \textbf{4. 35}$$

where

$$\phi(\underline{\sigma}_n - \underline{\alpha}, \sigma_0) = 0 \qquad \textbf{4. 36}$$

By substracting ($\underline{\alpha}$) from both sides of equation (4. 35) and rewriting the normal with (4. 34), equation (4. 35) is modified to:

$$(\underline{\sigma}_n - \underline{\alpha}) = (\underline{\sigma}_t - \underline{\alpha}) - \Delta\lambda \underline{\underline{E}} \cdot \left(\frac{\partial \phi}{\partial (\underline{\sigma}_n - \underline{\alpha})} \right) \qquad \textbf{4. 37}$$

So the stress projection procedure remains identical to the procedure of section 3.4, with the stress ($\underline{\sigma}$) replaced by the effective stress ($\underline{\sigma}^*$) and the isotropic yield stress (σ_y) replaced by the initial yield stress (σ_0). In a finite element code the stress is projected by the next steps:

1. The stress state $\sigma_{xx},\sigma_{yy},\tau_{xy}$ is adapted with the back stress $\alpha_{xx},\alpha_{yy},\alpha_{xy}$ to $\sigma^*_{xx},\sigma^*_{yy},\tau^*_{xy}$
2. The stress projection takes place according to the steps in section 3.4, with the isotropic yield stress (σ_y) replaced by the initial yield stress (σ_0)

Determination of hardening tensor

At anisotropic hardening the tensor ($\underline{\beta}$) can be replaced by the back stress tensor ($\underline{\alpha}$). The back stress is defined by (4. 20). Substitution of the incremental format of (2.21) and (4. 34) results in:

$$\Delta\underline{\alpha} = (\underline{\sigma}-\underline{\alpha})\frac{\frac{\partial\phi(\underline{\sigma}-\underline{\alpha})}{\partial\underline{\sigma}} : (\underline{\underline{E}}-\underline{\underline{Y}}) : \Delta\underline{\varepsilon}}{\frac{\partial\phi(\underline{\sigma}-\underline{\alpha})}{\partial\underline{\sigma}} : (\underline{\sigma}-\underline{\alpha})} = (\underline{\sigma}-\underline{\alpha})\frac{\frac{\partial\phi(\underline{\sigma}-\underline{\alpha})}{\partial\underline{\sigma}} : \Delta\underline{\sigma}}{\frac{\partial\phi(\underline{\sigma}-\underline{\alpha})}{\partial\underline{\sigma}} : (\underline{\sigma}-\underline{\alpha})} = \quad \textbf{4. 38}$$

$$(\underline{\sigma}^*)\frac{\frac{\partial\phi(\underline{\sigma}^*)}{\partial\underline{\sigma}^*} : \Delta\underline{\sigma}}{\frac{\partial\phi(\underline{\sigma}^*)}{\partial\underline{\sigma}^*} : (\underline{\sigma}^*)}$$

Consequently the hardening tensor ($\underline{\beta}$) - in general a function of the derivative of the yield function to this tensor ($\partial\phi/\partial\underline{\beta}$), the hardening parameter (f), the plastic multiplier (λ) and the plastic multiplier increment ($\Delta\lambda$) – is replaced by the back stress ($\underline{\alpha}$), which is a function of the effective stress tensor ($\underline{\sigma}^*$) and the stress increment tensor($\Delta\underline{\sigma}$):

$$\underline{\beta}\left(\frac{\partial\phi}{\partial\underline{\beta}}, f, \Delta\lambda\right) \rightarrow \underline{\alpha}(\underline{\sigma}^*, \Delta\underline{\sigma}) \qquad \textbf{4. 39}$$

The stress increment is defined by the projected stress minus the stress at the start of the procedure:

$$\Delta\underline{\sigma} = \underline{\sigma}_n = \underline{\sigma} \qquad \textbf{4. 40}$$

The effective stress is defined by (4. 34). With relations (4. 34), (4. 37), (4. 39) and (4. 40) the numerical procedure of scheme 2-1 is rewritten to scheme 4-3:

$\underline{\sigma}_t = \underline{\sigma} + \underline{\underline{E}} \cdot \Delta\underline{\varepsilon}$

Initialisation of i,$\Delta\lambda^i$, $\Delta\lambda^{i-1}$

While $\dfrac{\Delta\lambda^i - \Delta\lambda^{i-1}}{\Delta\lambda^{i-1}} > error$ do

$\underline{\alpha} = \underline{\alpha}\left(\underline{\sigma}^*, \Delta\underline{\sigma}\right)$

Determine $\Delta\lambda^{i+1}$ by

$\left(\underline{\sigma}_n - \underline{\alpha}\right) = \left(\underline{\sigma}_t - \underline{\alpha}\right) - \Delta\lambda^{i+1}\,\underline{\underline{E}} \cdot \left(\dfrac{\partial\phi}{\partial\left(\underline{\sigma}_n - \underline{\alpha}\right)}\right)$ with $\phi\left(\underline{\sigma}_n - \underline{\alpha}, \sigma_0\right) = 0$

$\Delta\underline{\sigma} = \underline{\sigma}_n - \underline{\sigma}$

$\underline{\sigma}^* = \underline{\sigma}_n - \underline{\alpha}$

i=i+1

End while

Scheme 4-3 Stress update procedure

4.2.8 Validation of numerical implementation

The numerical implementation is checked with a tensile-compression test on a 1 mm square piece of sheet metal. The simulations are carried out with different hardening parameters (q) to show the influence of this parameter. The real performance of the model is compared with experimental results of the bi-axial test equipment in chapter 5.

The hardening data are given in table 4-1. The first columns show the Nadai-Ludwik hardening data and the last column gives the anisotropic hardening parameter (q).

Nadai-Ludwik extended with anistropic behaviour:			
σ_y (N/mm^2)	C	n	q
181.3	727.6	0.34	0.02→ 0.5

table 4-1 Anisotropic hardening data

The test is illustrated by figure 4-14.

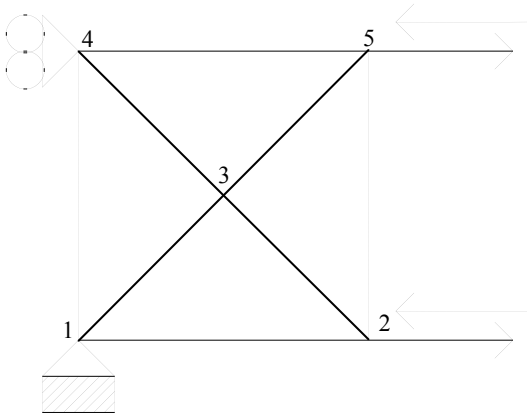

figure 5-13 Four-element validation case

The test is divided into two parts. Nodes 2 and 5 are first prescribed in the tensile direction with 0.001 mm per step. Then, 50 steps are imposed to reach a displacement of 0.05 mm. Subsequently the nodes are prescribed in the compression direction with -0.001 mm per step (second part). In this part 100 steps are applied which results in an extra displacement of –0.100 mm. The unbalance criterion is set at 0.1 percent.

Five simulations are carried out: the first with the isotropic Nadai-Ludwik model and the second til the fifth with the anisotropic hardening model with the hardening parameter (q) varying from 0.02 to 0.5. The force-displacement curves of the simulations are given in figure 4-15.

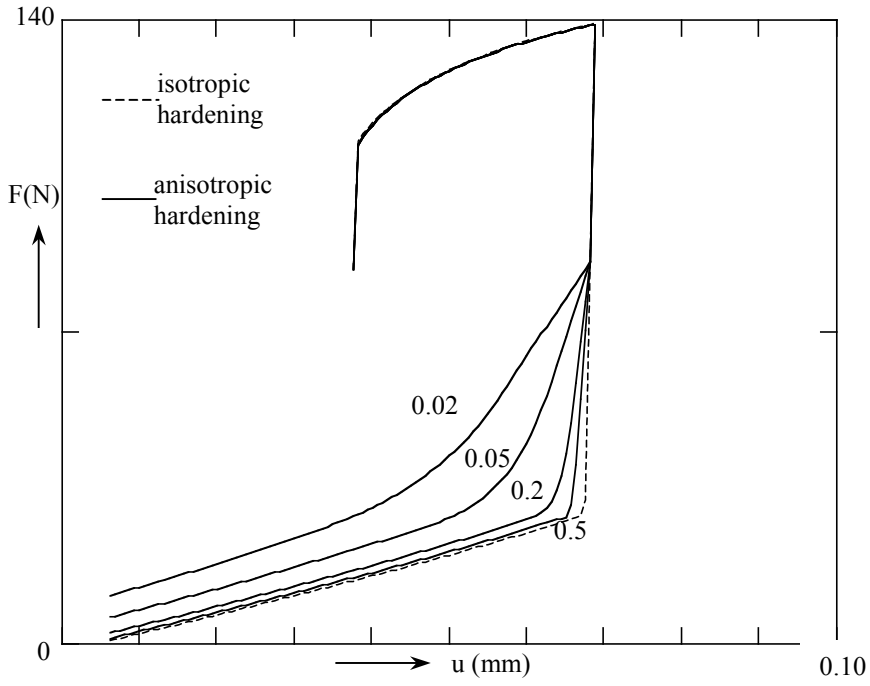

figure 5-15 Force (F) displacement (u) curves

The anisotropic hardening model shows identical force displacement curves as the isotropic Nadai-Ludwik model in the tensile part of the test. In the compression part differences are clearly observed. The influence of the parameter (q) becomes apparent: when this parameter has a larger value, the hardening rate will reach the isotropic value sooner.

5 Bi-axial test equipment

At the university of Twente a bi-axial test equipment has been designed. The general purpose of the equipment is testing sheet material behaviour under multi-axial and non proportional loads. The equipment is capable of combining a plane strain deformation together with a shear deformation on a piece of sheet metal. The shear deformation can be imposed in 2 directions and the plane strain deformation can be imposed in tension and compression. The central part of the equipment is illustrated by figure 5-1. In this figure also the position of the test piece is illustrated. The arrows indicate the directions of movement of the tester. The upper part can move in a horizontal direction. This is the movement for the shear deformation. The lower part can move in a vertical direction. This is the movement for the plane strain deformation.

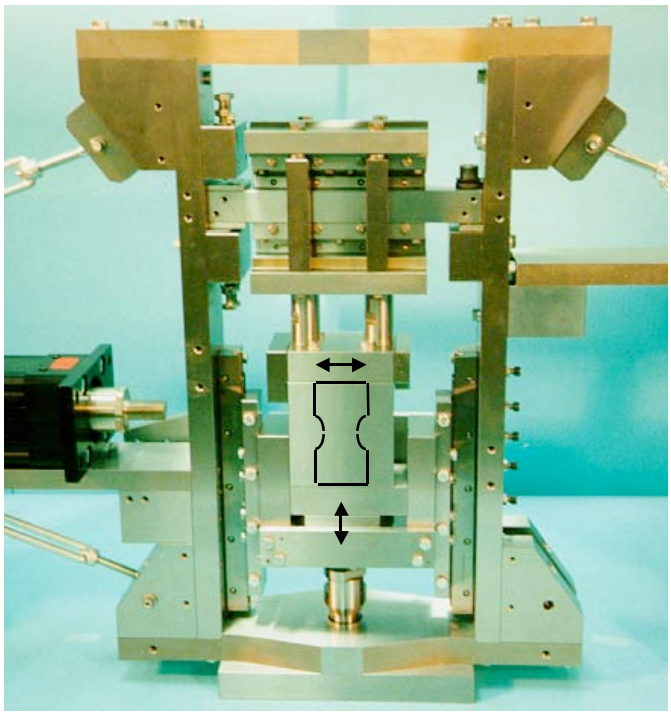

Figure 5-1 Illustration of the central part of the test equipment

Within the scope of this research the test equipment is used for the following purposes:

- Determination of the shear and plane strain reference points of the Vegter yield function
- Determination of the hardening parameter for the anisotropic hardening description (q)
- To check whether the current material description gives a reasonable approximation of the material behaviour under non-proportional loads.

This chapter describes how the equipment is used for these purposes. Section 5.1 starts with a description of the test equipment, which was designed by ing J.Brinkman. In this section the mechanical functions of the equipment are dealt with. Moreover some modifications to the equipment are shown. Section 5.2 discusses finite element simulations of the experiments. With these simulations the influence of edge effects on the stress and deformation in the test piece can be examined. These effects occur at the edges of the test piece and at the transition from the deformation zone to the clamping zone. Subsequently, section 5.3 deals with the data acquisition. In this section the 'raw' test data of plane strain and shear experiments are transformed to desired stress-strain data. Section 5.4 links the test equipment data to the Vegter yield function description. Here the plane strain and shear reference points are determined. To obtain also data for the anisotropic hardening function, section 5.5 describes cyclic experiments. Finally, the current material description is compared with results of non-proportional tests in section 5.6.

5.1 Description of the test equipment

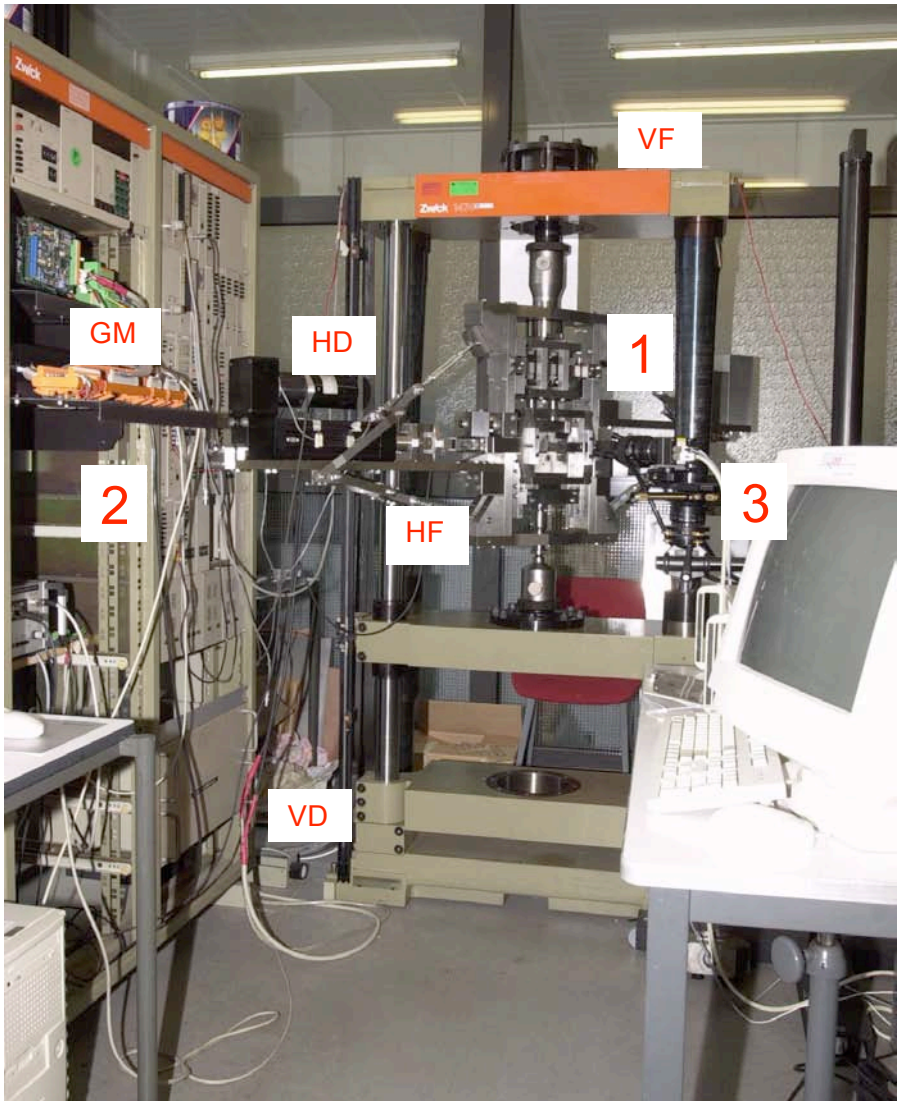

Figure 5-2 Total test equipment

The equipment is illustrated in figure 5-2. It can be divided into 3 parts:

- The main part (1) which imposes the deformation on the test piece. Figure 5-1 shows this part in more detail
- The motion control part (2), which steers and controls the motion of the clamps. This part also measures the forces and displacements on the clamps and stores these data on a computer hard disk
- The deformation analysis part (3). This part accounts for measuring the deformation in the middle of the test piece.

Each part is described briefly:

Part 1

This part is also illustrated in figure 5-1. The central part of the tester is shown, two pairs of clamps which impose the deformation on a test piece. The dimensions of the test piece are given in figure 5-3. The test piece consists of a deformation section and two clamp sections. In the deformation section the material is forced into a deformation by the clamps. In each clamp section the material is clamped between two clamps, existing of pieces of hardened steel. Four Pins are stabbed through the clamps and the sheet material to secure the sheet material to the clamps. Figure 5-4 also shows a shaded part in the middle of the test piece. This part is modelled by finite elements, which will be referred to in section 5.2.

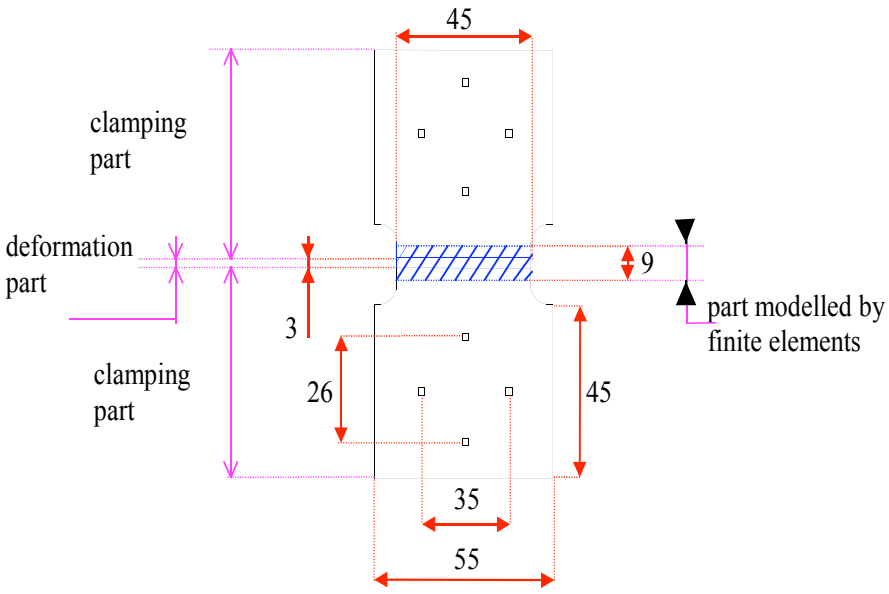

Figure 5-3 Dimensions of the test piece

A schematic representation of the deformation zone loaded in shear and plane strain is given in figure 5-4.

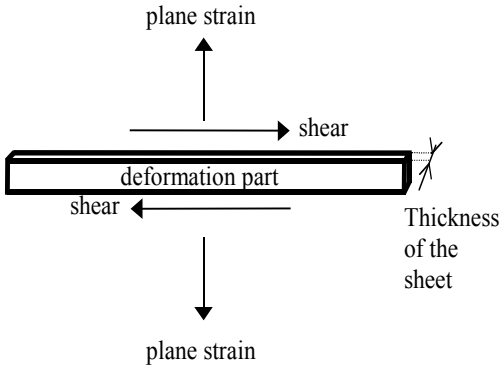

Figure 5-4 Combination of a shear load and a plane strain load on sheet metal

The width of the deformation zone of the sheet is large relative to the height, this is a requirement for the plane strain test. The height must be chosen not too large relative to the thickness, see for instance (G'Sell, 1983).

The clamp force between the clamps and the sheet is applied by tightening 4 bolts with the maximum allowed moment. The clamps were re-designed. Originally the steel sheet was clamped with pieces of files. The disadvantages of these files were:

- The files had a certain orientation. Due to this orientation, the sheet was fixed better in one direction than other directions.
- The files were not totally flat. As a result some parts of the sheet were fixed better and some less. This lead to an inhomogeneous deformation.
- One part of the clamp consisted of 6 files. Not all files had exactly the same thickness. As a result the part of the sheet under some files was fixed better than under other files. This contributed to an inhomogeneous deformation.

The new clamps consist of hardened powder metallurgy blocks, which have the following advantages:

- The blocks are symmetrical in every direction, so no orientation problems occur during the tests.
- The blocks were made of 1 piece with a spark-erosion technique. The accuracy of this technique warrants a flat clamp surface.

A diagram of the clamp blocks is shown in appendix F. Also a few other new parts were designed to improve and complete the equipment, see appendix G.

Part 2

The second part is the motion control part, see figure 5-2. This part consists of the following components:

- a Galil Motion controller (GM)
- a Zwick motor which accounts for the vertical movement of the clamps.
- a side motor which accounts for the horizontal movement of the clamps
- a Vertical Force measurement device (VF)
- a Horizontal Force measurement device (HF)
- a Vertical Displacement measurement device (VD)
- a Horizontal Displacement measurement device (HD)

The motion controller (GM) controls the motion of the test equipment. Table 5-1 shows the features of the controller.

	Max displacement	Min displacement	Min Velocity	Max velocity
Horizontal motion	5 mm left 5 mm right	0.00001 mm	0.00001 mm/s	Not known (>1 mm/s)
Vertical motion	5 mm up 5 mm down	0.01 mm	0.05 mm/s	Not known (> 1 mm/s)

Table 5-1 Features of the motions of the tester

The vertical force measurement device (VF) is a Zwick load cell, attached to the Zwick frame. The horizontal force measurement device (HF) is a Pekel load cell, attached to the frame for the horizontal movement. The properties of these load cells are listed in table 5-2.

	Max Force	Min Force	Accuracy
Horizontal motion	100000 kN	-100000 kN	50 N
Vertical motion	100000 kN	-100000 kN	20 N

Table 5-2 Features of the load cells

The vertical displacement measuring device is incorporated into the Galil motion controller. This motion controller measures the revolutions of the Zwick motor and transforms it into a displacement. The horizontal movement is measured in a similar way.

Part 3

The third part is the deformation analysis part. The deformation analysis system is based upon the recognition of objects on the sheet metal. The objects are distinguished from the sheet metal by a difference in grey value contrast (black-white). The objects can be tracked in real time and the co-ordinates are stored on a harddisk in a position array. The dot-tracker system is described extensively in the manual (DVS, 1999). The important features of the system are given by table 5-3:

	Mutual Dot distance in Pixels	Dot size in mm	Dot size in Pixels	Accuracy Theoretical	Accuracy Practical
Horizontal motion	± 60 pixels	± 0.2 mm	±12 pixels	< 1/12 pixel	0.4 pixel
Vertical motion	± 60 pixels	± 0.2 mm	±12 pixels	< 1/12 pixel	0.4 pixel

Table 5-3 features of the deformation analysis system

As can be observed in the table, the practical accuracy is less than the theoretical value. The value of the practical accuracy was obtained by tracking stationary dots and detecting the position. The difference between the theoretical and practical accuracy is probably due to light intensity variations and environmental vibrations, which result in a less distinct contrast.

Objects on the sheet metal are created by placing dots of silicon-kit in the middle of the test piece. Also dots of ink with a professional equipment and dots of ink from a simple ink-pencil were tried. It appeared that silicon-kit has a few advantages:

- It is matt black and has some volume in the direction normal to the sheet. Dots of ink are more or less flat and have a shiny appearance. Matt dots absorb more light and due to the volume the light is reflected more diffusely. Therefore the contrast between the sheet and the objects is best with kit-dots.
- It is elastic up to 100 % of deformation. The dots stay intact during almost every desired deformation. Dots of ink are elastic up to a few percent of deformation. Beyond this deformation they break into pieces which stick independently to the sheet metal. This gives significantly less contrast compared to the kit-dots.

Before the experiments are started, four dots are placed in the middle of the test piece with a mutual distance of 1 mm. The dot-tracker system recognises the dots, calculates their centre and stores the co-ordinates on the disk. The determination of the centre is a weighted function of the grey value of the pixels. The edge of a kit-dot will have a lower grey-value than the middle of the dot. Correspondingly the edge will have a smaller effect on the centre than the middle of the dot. So when due to variations in light or other external influences the edge of the dots vary slightly, this will have a minor effect on the centre position of the dots. In this way the practical accuracy (table 5-3) is kept within limits. The use of the deformation analysis system will become more clear after investigating the influence of the edge effects on the deformation.

5.2 Edge effect determination by finite element simulations

Two types of edge effects can be considered. The first effect is the deformation of the sheet material under the clamps. Due to this so-called clamp slip the resulting deformation in the middle of the test piece deviates from the intended deformation. The second effect is the deviating stress state at the free edges, which influences the resulting stress state in the middle of the test piece. A finite element model of the test equipment was constructed to investigate the influence of these two edge effects.

The finite element model represents the shaded part of the test piece and the clamp equipment in figure 5-3. The parts next to the modelled part are used for positioning the test piece. It is assumed that these parts have no influence on the deformation and stress in the deformation area. The clamping part is modelled by two moving clamps and two fixed clamps, see figure 5-5. In the actual test the lower clamps are moved vertically and the upper clamps are moved horizontally. The clamp force is related to the moment which is applied on the clamp bolts.

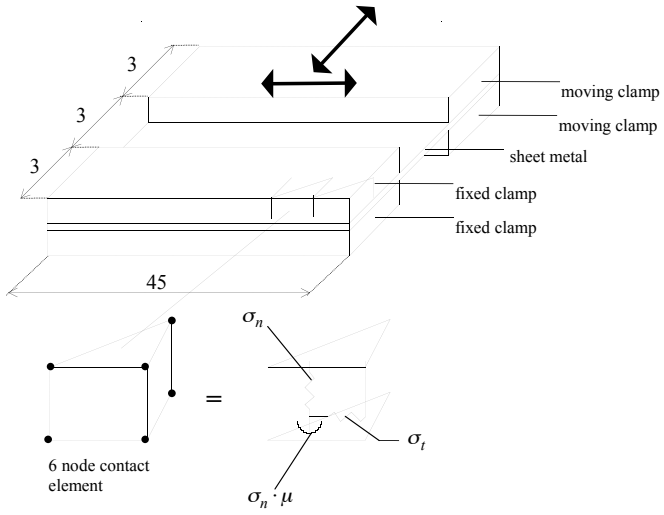

Figure 5-5 Part modelled by finite elements

The finite element mesh is illustrateded in figure 5-6. The mesh is refined in the areas with large deformations (at the free edges) and large deformation differences (near the transition of the shear deformation zone D to the clamping parts C). The piece of sheet material is modelled by sheet elements with three integration points in the plane of the sheet and two through the thickness of the sheet (see section 2.3).

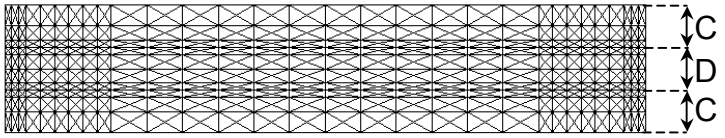

Figure 5-6 finite element mesh

The contact between the clamps and the sheet metal is modelled by contact elements, shown in figure 5-5. The material modelling of these contact elements is handled in detail in (Vreede, 1992). In short the behaviour is illustrated in figure 5-5 by the springs and the sliding contact. The stress in the normal direction is given by (σ_n). This stress is defined by the distance from the upper surface of the contact element to the lower surface in the normal direction. The stress in the tangential direction is given by (σ_t). This stress in the tangential direction is initially defined by the distance from the upper surface of the contact element to the lower surface in the tangential direction (stick). When the stress is higher than the normal stress (σ_n) multiplied by the friction coefficient (μ), this value is defined by the latter ($\sigma_t=\sigma_n \cdot \mu$) (slip). In the simulations the friction coefficient was set to 1.0, which aims on the demands that slip has to be limited. This high friction coefficient aims on the demands that slip has to be avoided. In this way the estimation of the high friction coefficient is justified. In reality the clamps consist of rough surfaces which fixes the steel sheet with sharp tips. It is realised that the modelling of the clamps does not represent reality entirely.

The simulations investigate only the edge effects in proportional deformations. The influence of edge effects during a plane strain deformation on the resulting plane strain data and the edge effects during a shear deformation on the shear data are determined. To provide a good prediction of the edge effects in non-proportional tests, also the edge effects of an imposed shear deformation on the plane strain data and vice versa should be examined. The simulations of a proportional shear and plane strain test are discussed separtely in the following sections.

5.2.1 Shear simulation

A shear simulation is performed by moving the upper clamp to the right. The result of 4 mm clamp displacement is given by figure 5-7. In this figure the yield stress after deformation is illustrated.

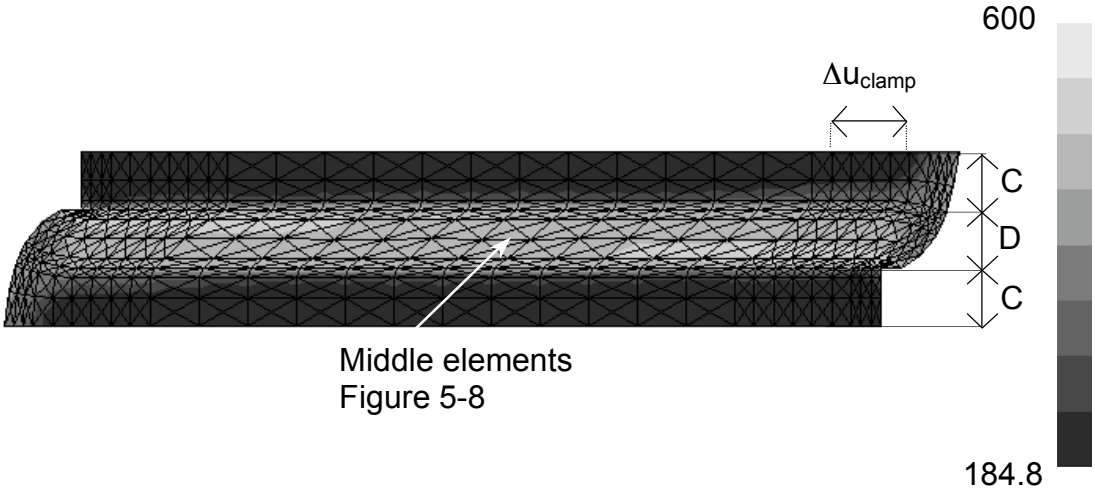

Figure 5-7 Yield stress in the deformed mesh

Figure 5-7 shows clearly the shear edge effects. Firstly the clamp slip is visible: the deformation is not limited to the deformation region (D), but spreads to the clamp zones (C). Secondly the deformation at the free edges is different from the rest of the test piece. To investigate the edge effects quantitatively, the resulting stress and strain situation in the 4 middle elements is focussed on:

Influence of clamp slip on the 4 -lement shear deformation

Without clamp slip, the deformation in the test piece is given by:

$$\gamma_{SH} = \frac{\Delta u_{clamp}}{h_D} \qquad \textbf{5. 1}$$

where

Δu_{clamp} is the clamp displacement
h_D is the height of the deformation zone

The finite element simulation predicts the deformation in the middle of the test piece, taking into account the clamp slip. Four elements in the middle of the test piece are observed, see figure 5-8:

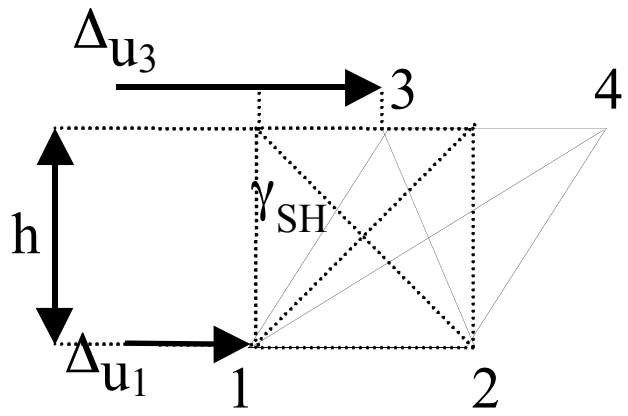

Figure 5-8 Deformed mesh of 4 middle elements

The shear deformation of the middle elements is given by the ratio of the relative displacement (Δu_3-Δu_1) of the upper nodes and the height h of the element:

$$\gamma_{SH} = \frac{\Delta u_3 - \Delta u_1}{h} \qquad \textbf{5. 2}$$

The results are observed for different clamp displacements, see table 5-4. A deformation correction factor can be defined by the ratio of (5. 2) to (5. 1). Because the clamp model does not represent reality entirely, the correction factors only give an indication.

Influence of deviating edge stress on the 4-element shear stress

Without a deviating stress state at the free edges, the shear stress is given by:

$$\sigma_{SH} = \frac{FX}{a \cdot L} \qquad \textbf{5. 3}$$

where

FX is the horizontal clamp force
a is the initial sheet thickness
L is the length of the test piece

The finite element simulation predicts the stress in the middle of the test piece, taking into account the deviating edge stress, see figure 5-8.

$$\sigma_{SH} = \sigma_{SH}(node1) \qquad \textbf{5. 4}$$

The results of (5. 3) and (5. 4) are observed for different clamp displacements, see table 5-4. A stress correction factor is defined by the ratio of (5. 4) to (5. 3). The modelling of the free edges is assumed to represent the real situation satisfactorily, so the correction factors can be used to in the data acquisition of section 5.3.

5.2.2 Plane strain simulation

A plane strain simulation was performed by moving the upper clamp upwards. The result of 1 mm clamp displacement is given by figure 5-9. In this figure the yield stress is shown.

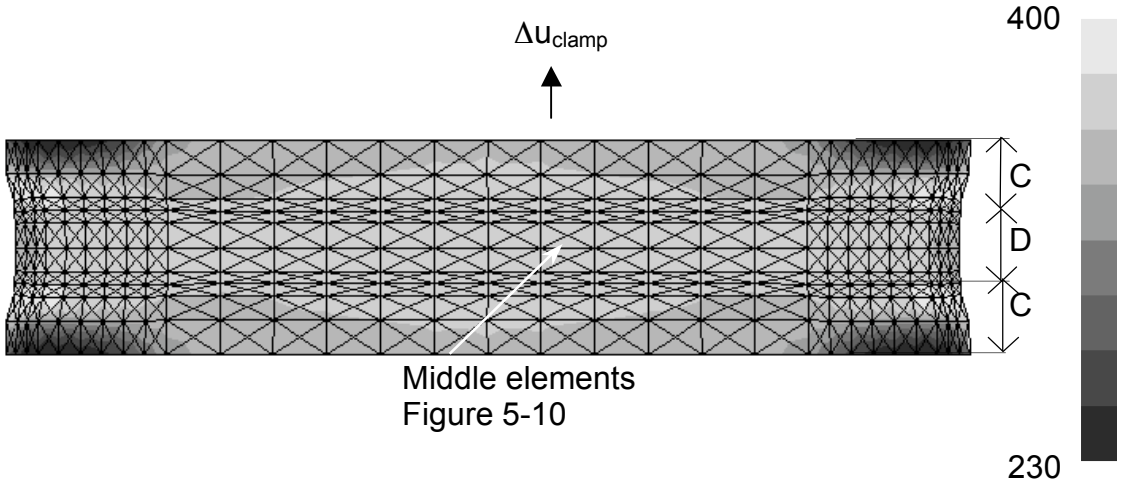

Middle elements
Figure 5-10

Figure 5-9 Yield stress in the deformed mesh

Figure 5-9 shows clearly the plane strain edge effects. Firstly the clamp slip is visible: the deformation is not limited to the deformation region (D), but it spreads into the clamp zones (C). Compared to the shear deformation this effect is more apparent, which indicates that it is quite difficult to restrict slip in a plane strain experiment. Secondly the stress at the free edges is different to that in the rest of the test piece. The stress and deformation are checked quantitatively.

Influence of clamp slip on the 4-element plane strain deformation

Without clamp slip, the plane strain deformation is given by:

$$\varepsilon_{PS} = \frac{\Delta u_{clamp}}{h_D} \qquad \textbf{5. 5}$$

where

Δu_{clamp} is the clamp displacement
h_D is the height of the deformation zone

The finite element simulation predicts the deformation in the middle of the test piece, taking into account the clamp slip. Four elements in the middle are observed, see figure 5-10.

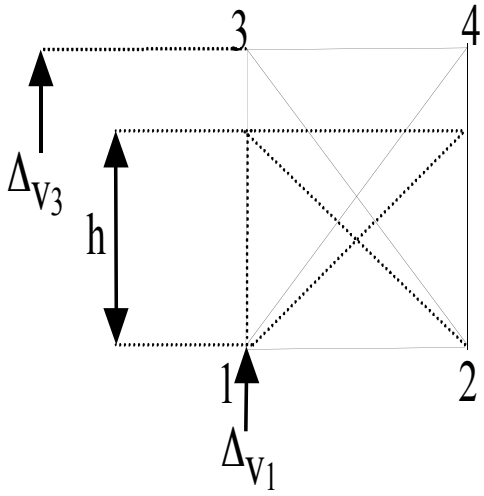

Figure 5-10 Deformed mesh of 4 middle elements

The plane strain deformation of the middle elements is given by the ratio of the relative displacement of the upper nodes (Δv_3-Δv_1) to the height (h) of the element:

$$\varepsilon_{PS} = \ln\left(\frac{h + (\Delta v_3 - \Delta v_1)}{h}\right) \qquad \textbf{5. 6}$$

The results are observed for different clamp displacements, see table 5-4. A deformation correction factor can be defined by the ratio of (5. 6) and (5. 5). Because the clamp model does not represent reality entirely, the correction factors only give an indication.

Influence of deviating edge stress on the 4-element plane strain stress

Without a deviating stress state at the free edges, the plane strain stress is given by:

$$\sigma_{PS} = \frac{FY}{a_c \cdot L} \qquad \textbf{5. 7}$$

$$a_c = a * e^{\varepsilon_{thick}} = a * e^{-\varepsilon_{PS}}$$

where

FY is the vertical clamp force
a is the initial sheet thickness
a_c is the current sheet thickness
L is the length of the test piece

The thickness is calculated by the thickness strain (ε_{thick}), which is assumed to be minus the strain (ε_{PS}) in the tensile direction.

The finite element simulation predicts the stress in the middle of the test piece, taking into account the deviating edge stress, see figure 5-10:

$$\sigma_{PS} = \sigma_{PS}(node1) \qquad \textbf{5. 8}$$

The results of (5. 7) and (5. 8) are observed for different clamp displacements, see table 5-5. A stress correction factor is defined by the ratio of (5. 8) to (5. 7). The modelling of the free edges is assumed to represent the real situation satisfactorily, so the correction factors can be used to in the data acquisition of section 5.3.

Imposed horizontal displacement	0.02	2.00	4.00
Intended shear deformation	0.02/3	2/3	4/3
Real shear deformation	**0.0064**	**0.6420**	**1.1822**
Deformation correction factor	0.964	0.963	0.887
Horizontal clamp force (N)	4699	10104	11460
Shear stress based on clamp force (Mpa)	104.4	224.5	254.6
Shear stress middle node (Mpa)	106.3	228.8	260.0
Stress correction factor	**1.018**	**1.019**	**1.021**

Table 5-4 Shear correction factors

Imposed vertical displacement	0.05	1.00	2.00
Intended plane strain deformation	0.05/3	1/3	2/3
Real plane strain deformation	**0.008**	**0.108**	**0.271**
Deformation correction factor	0.48	0.33	0.4065
Vertical clamp force (N)	12024	17126	17335
Plane strain stress based on clamp force (Mpa)	269.4	424.0	505.1
Plane strain stress middle node (Mpa)	276.7	441.3	531.9
Stress correction factor	**1.027**	**1.049**	**1.053**

Table 5-5 Plane strain correction factors

5.3 Data acquisition

During experiments data are sampled from the measuring devices and stored on a computer hard disk. The data are forces from the force measuring devices (HF and VF in figure 5-2), displacements from the displacement measuring devices (HD and VD in figure 5-2) and positions of dots from the deformation analysis system. To develop a material description from the experiments, stress and strain states are desired. This section describes how the stress and strain states are obtained from the measured data.

The finite element simulations show that the clamp slip has a significant influence on the strain state. Compared to the intended deformation, the deformation in the middle of the test piece is about 10% less at the shear test and 60 % to 70 % less at the plane strain test. The clamp model does not match the reality entirely. Therefore the deformation correction factors only give an indication of the real clamp slip. It implies that the deformation in the test piece cannot be related properly to the displacements of the clamps. For this reason the deformation analysis system is used. This system directly measures the deformation on the sheet metal, so no clamp slip has to be taken into account. Section 5.3.1 provides the transformation of the data from the deformation analysis system to strain data.

It appears that the deviating stress at the free edges has a small influence on the stress state inside the test piece. So the stress state inside the test piece can be determined from the forces on the clamps, with a correction of a few percent. Section 5.3.2 describes how the stress data is derived from the measured clamp forces.

5.3.1 Strain determination

The deformation analysis system measures coordinates of the centre of the dots in the middle of the test piece. These dots are placed within the limits of the investigated 4 elements of the former section. The determination of the strains from the four dots is discussed separately for a shear and a plane strain deformation.

Shear strain

The shear strain is determined according to figure 5-11.

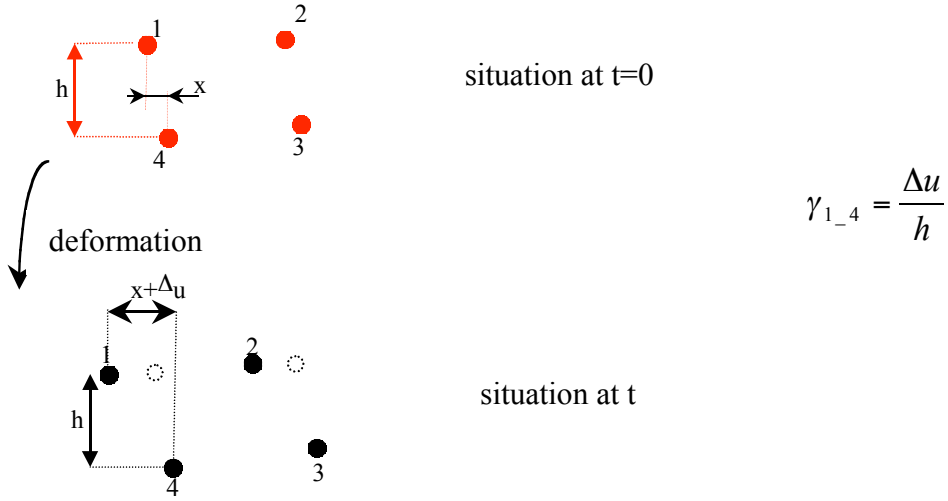

Figure 5-11 Determination of the shear strain from camera images

The figure shows the centres of the 4 dots at the start of the test (t=0) and the centres of the 4 dots at a sample time (t). The deformation of the sheet between dots 1 and 4 is given by (γ_{1_4}). The deformation between dots 2 and 3 is calculated in the same way. Figure 5-12 shows the development of (γ_{1_4}) and (γ_{2_3}) during a proportional shear test.

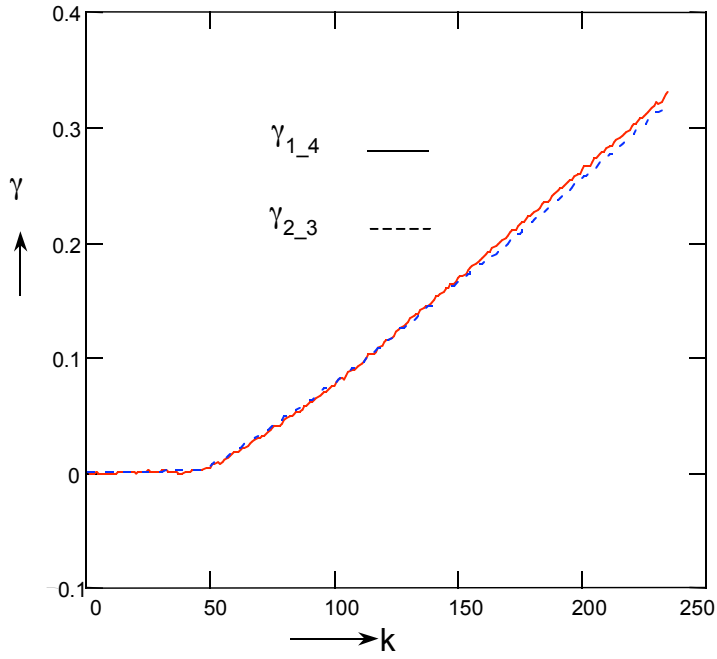

Figuer 5-12 Shear strains as a function of the number (k) of camera images

Appendix H states that the measurement of the shear strain is accurate within (γ_{SH}=0.011). The difference between the two strains remains within this accuracy, so it can be fairly assumed that the deformation is homogeneous. The resulting shear strain (γ_{SH}) in the sheet metal is assumed to be the average of the strains (γ_{1_4}) and (γ_{2_3}).

Plane strain

The strain in the tensile direction is determined according to figure 5-13. The figure shows the centres of the 4 dots at the start of the test (t =0) and the centres of the 4 dots at a sample time (t). The deformation of the sheet metal between dots 1 and 4 is given by (ε_{1_4}). The deformation of the sheet between dots 2 and 3 (ε_{2_3}) is calculated in the same way. Figure 5-14 shows the development of (ε_{1_4}) and (ε_{2_3}) during a proportional plane strain test.

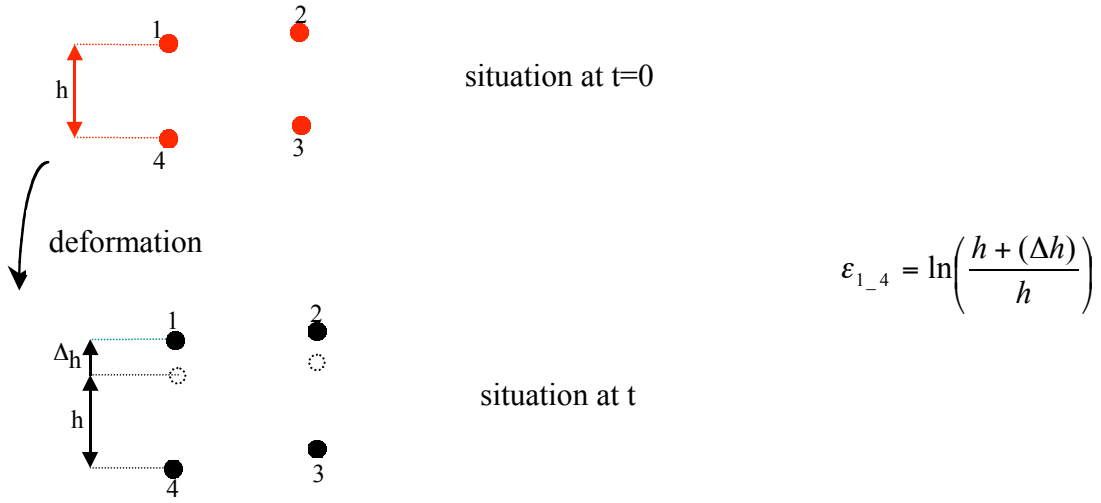

Figure 5-13 Determination of the plane strain from camera images

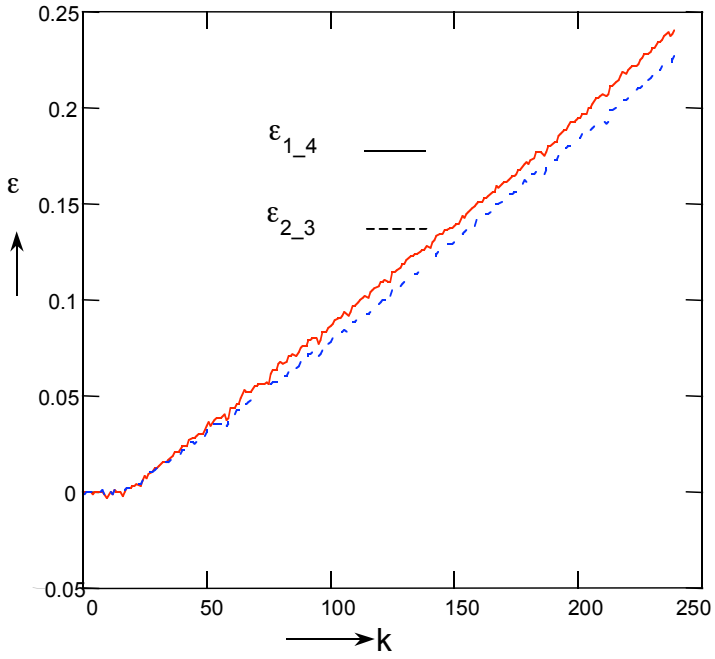

Figure 5-14 Plane strains as a function of the number (k) of camera images

Again the assumption that the deformation is homogeneous in the observed area of the test piece is checked. The strains tend to deviate as the test progresses. Appendix H states that the measurement of the plane strain is accurate within (ε_{PS}=0.016). The difference between the two strains remains within this accuracy, so it can be fairly assumed that the deformation is homogeneous. The resulting plane strain (ε_{PS}) in the sheet metal is assumed to be the average of the strains (ε_{1_4}) and (ε_{2_3}).

5.3.2 Stress determination

The stress state is determined from the sampled force data. The determination of the shear stress and of the plane strain stress is discussed separately.

Shear stress

The shear stress is defined by :

$$\sigma_{SH} = \frac{FX}{a \cdot L} \qquad \textbf{5. 9}$$

where

FX is the horizontal clamp force
a is the initial sheet thickness
L is the length of the test piece

Due to the edge effects the measured stresses have to be corrected. Table 5-4 provides the correction factors. A linear relation is assumed between the correction factor and the shear deformation:

$$\sigma_{SH} = \frac{FX}{a \cdot L} * \left(c1 + c2 \cdot \gamma\right) \qquad \textbf{5. 10}$$

with the coefficients (c1) and (c2) chosen to fit the discrete correction factors of table 5-4.

Plane strain stress

The plane strain stress is defined by:

$$\sigma_{PS} = \frac{FY}{a_c \cdot L} \qquad \textbf{5. 11}$$

$$a_c = a \cdot e^{-\varepsilon_{PS}}$$

where

FY is the vertical clamp force
a is the initial sheet thickness
a_c is the current sheet thickness
L is the length of the test piece

Similar to the shear stress determination, the measured stresses are corrected (table 5-5). A linear relationship is assumed between the correction factor and the plane strain deformation:

$$\sigma_{PS} = \frac{FY}{a \cdot e^{-\varepsilon_{PS}} \cdot L} * \left(c3 + c4 \cdot \varepsilon_{PS}\right) \qquad \textbf{5. 12}$$

with the coefficients (c3) and (c4) chosen to fit the correction factors of table 5-5.

5.4 Experimental determination of Vegter reference points

The bi-axial test equipment is used to determine the shear and plane strain reference points of the Vegter yield criterion. The shear reference point is determined by a proportional shear experiment and the plane strain point by a proportional plane strain experiment. Both experiments are carried out for 3 directions (0°, 45° and 90° to the rolling direction) in the plane of the sheet to take into account planar anisotropic material behaviour.

The shear and plane strain reference points are given by the shear factor (f_{sh}) and the plane strain factor (f_{ps}) respectively. These factors define the ratio between the shear and plane strain yield stress respectively on one hand and the average uni-axial yield stress on the other hand, see figure 5-15. The average uni-axial yield stress is given by:

$$\sigma_y = \frac{\sigma_{UN}(0) + 2 \cdot \sigma_{UN}(45) + \sigma_{UN}(90)}{4} \qquad \textbf{5. 13}$$

Figure 5-15 also illustrates the stress factor (f_{arb}) of an arbitrary stress state (σ_{arb}) on the yield surface. This factor defines the ratio between the arbitrary stress and the yield stress.

In order to determine the shear and the plane strain factors, the initial shear and plane strain yield stress can be divided by the initial average uni-axial yield stress. However, the initial yield stresses cannot be distinguished very easily from the measured data (see figures 5-20 and 5-21). Therefore use is made of the fact that hardening during a proportional deformation can be described by the isotropic hardening model. The ratio between each stress state on the yield locus and the yield stress remains constant in this case (section 2.1.2), so also the stress factors remain constant.

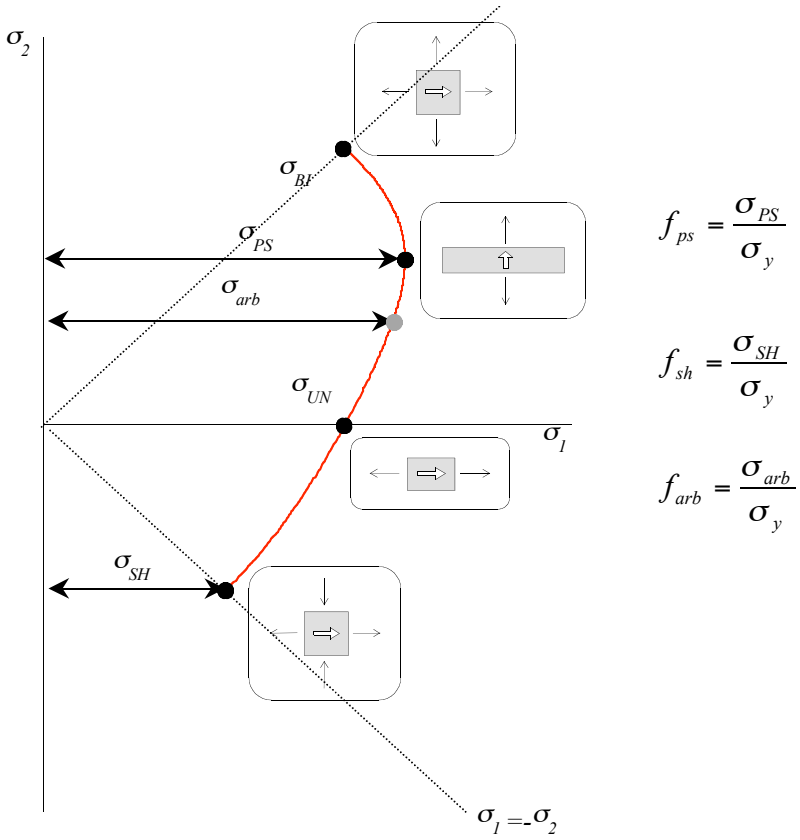

Figure 5-15 Graphical representation of the definition of the shear (f_{sh}) and plane strain (f_{ps}) factor

The stress (σ_{arb}) as a function of the strain (ε_{arb}) during a proportional deformation is given by:

$$\sigma_{arb} = f_{arb}\cdot\sigma_0 + f_{arb}\cdot\Delta\sigma_m\cdot\left[\beta\cdot(\varepsilon_0 + f_{arb}\cdot\varepsilon_{arb}) + \left\{-e^{-\Omega\cdot(\varepsilon_0+f_{arb}\cdot\varepsilon_{arb})}\right\}\right] + f_{arb}\cdot\sigma_0^{*}\cdot\left\{1+\frac{k\cdot T}{\Delta G0}\cdot\ln\left(\frac{f_{arb}\cdot\dot{\varepsilon}_{arb}}{\dot{\varepsilon}_0}\right)\right\}^{m} \qquad \textbf{5. 14}$$

where

$$\sigma_{arb} = f_{arb}\cdot\sigma_y$$

$$\varepsilon_{arb} = \frac{\sigma_y}{\sigma_{arb}}\cdot\varepsilon_{eq} = \frac{1}{f_{arb}}\cdot\varepsilon_{eq} \qquad \textbf{5. 15}$$

The deformations during a plane strain and a shear test can be considered proportional, hence the parameter (σ_{arb}) in (5. 14) is replaced by the shear stress (σ_{SH}) for the shear experiment and (σ_{PS}) for the plane strain experiment. The parameter (ε_{arb}) is replaced by (γ_{SH}) and (ε_{PS}) respectively. The shear and plane strain factors can now be obtained by a least squares fit on the measured samples of the multi-axial tester. A few remarks in the fit procedure are:

- The physically based hardening parameters of (5. 14) were supplied by Corus RD&T. So only the parameters (f_{sh}) and (f_{ps}) are fit to the measured data.

- The latter part of (5. 14) represents the strain rate influence. At every sample the strain rate could be determined by comparing two successive strain samples and divide the difference by the time between the samples. The solid line in figure 5-16 illustrates this strain rate. Due to the limited accuracy of the deformation analysis system this line is very erratic. Therefore the average strain rate (dotted line) is assumed as a constant strain rate.

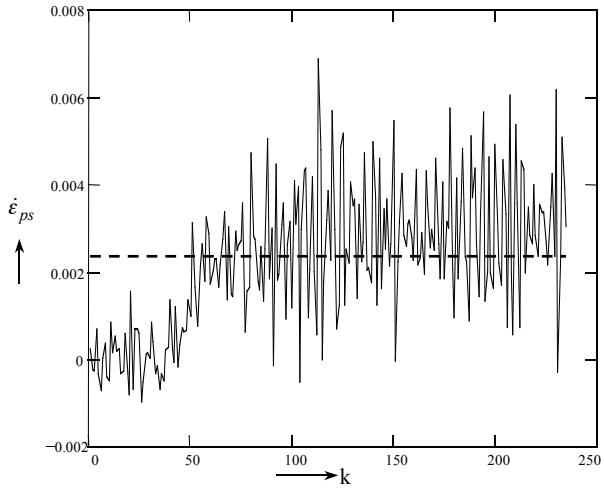

Figure 5-16 Strain rate as a function of number of samples (K)

- Only the samples with strains between 8 and 18 % are fit. These values are based on experience at Corus RD&T and the UT.

5.4.1 Shear factor determination

The shear factor is determined by the simple shear experiments. The experiments are carried out for 3 directions (0°, 45°, 90° to RD) in the plane of the sheet to incorporate planar anisotropic material behaviour. Two comments should be made on the experiments:

Comment 1

The angle of the principal stresses (planar angle) is not evident during the experiment. The finite element code in which the Vegter yield function is implemented defines a linear material rotation in the plane of the sheet:

$$\rho = -\frac{1}{2}\cdot\left(\frac{\partial u}{\partial y} - \frac{\partial v}{\partial x}\right) \qquad \textbf{5. 16}$$

Here u and v represent the displacement in the horizontal and the vertical direction respectively and x and y are the horizontal and the vertical axis respectively. In the simple shear experiment no displacement occurs in the vertical direction, so equation (5. 16) can be rewritten as:

$$\rho = -\frac{1}{2}\cdot\frac{\partial u}{\partial y} \qquad \textbf{5. 17}$$

Expression 5. 17 implies that, if the simple shear experiment were simulated with the used finite element code, a rotation of the rolling direction would occur, equal to half of the shear angle, illustrated by figure 5-18.

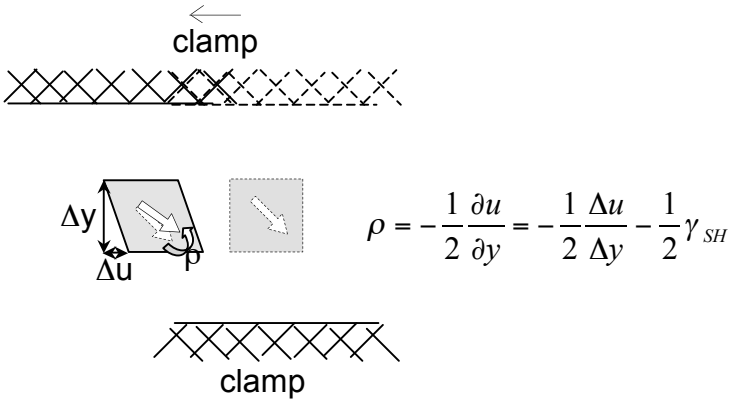

Figure 5-18 Material rotation during simple shear

The principal stresses remain in the same direction. So the angle of the principal stresses to the rolling direction (planar angle) is not constant during the simple shear experiment. In the current interpretation the material rotation is not taken into account, which is only justified when the deformation is small.

Comment 2

The clamps are fixed in the vertical direction. This allows a normal stress component in this direction, which causes a deviation from the pure shear stress ($\sigma_1 \neq \sigma_2$). Research of Huétink (Huétink, 1991) indicated that the vertical stress can be considered small during small deformations. So the experiment provides a fair approximation of the pure shear reference point. In the future this can be checked by measuring the vertical clamp force during the shear experiment.

Due to the vertically fixed clamps the deformation is restricted in the vertical direction, so the deformation is always pure shear ($\varepsilon_1 = -\varepsilon_2$). This is the reason that the gradient in the pure shear reference point is not determined from the strain state.

The tested materials are sheet steel (AKS) and aluminium (AA 5182). The steel experiments were performed 5 times for each direction. The aluminium experiments were performed 1 time for each direction due to the lack of manpower. Fortunately plane strain and shear experiments were also carried out at Corus RD&T for the same type of aluminium. So the results of Corus can are used in the rest of this dissertation. The experiments were carried out under the following conditions:

Horizontal clamp displacement:	2.5 mm
Time:	150 s
Horizontal clamp velocity:	0.05 mm/s
Number of force-samples:	250
Number of displacement samples:	250
Number of Camera samples:	8.5 per second

The shear factors are given in table 5-6 and table 5-7. If the material behaviour under tension and compression is the same, the shear factor for 0° and 90° should be equal. This is illustrated by figure 5-19. The first 2 situations on the left show a shear experiment to determine the reference point for a planar angle equal to 0°. Only if the material behaves identically under tension and compression can the second situation be replaced by the third. This situation is equal to the fourth, which is the shear experiment for 90°. Both for steel and aluminium the values for 0° and 90° are equal up to 0.01. This is within the limits of the accuracy (appendix H). In the rest of this dissertation the average value of 0° and 90° is taken for the shear factor for 0° and 90°.

Sample	1	2	3	4	5	Average	Max. abs. deviation
Angle RD							
0	0.532	0.532	0.537	0.537	0.529	0.533	0.004
45 (1)	0.570	0.574	0.577	0.567	0.570	0.5716	0.005
45 (2)	0.573	0.567	0.584	0.567	0.567	0.5716	0.012
90	0.523	0.524	0.524	0.525	0.528	0.524	0.004

Table 5-6 Shear factors of steel sheet (AKS)

Angle RD	
0	0.602
45 (1)	0.573
45(2)	0.582
90	0.591

Table 5-7 Shear factors of aluminium sheet (AA 5182)

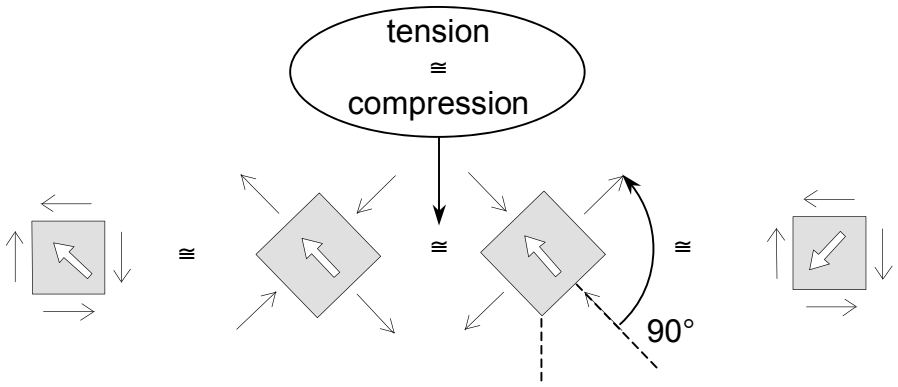

Figure 5-19 Shear experiment for 0° and 90°

The samples of a shear experiment are illustrated together with the fitted hardening function in figure 5-20.

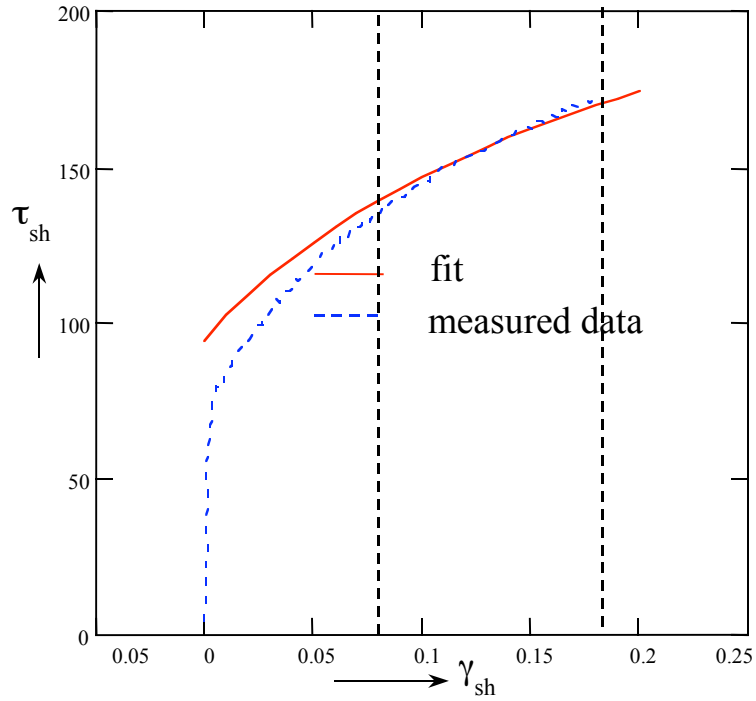

Figure 5-20 Measured data and fitted function model of the shear experiment

The shear strain range used for the fit is the area between the vertical dotted lines. It can be observed that the shape of the fitted hardening function deviates from the measured data. This is due to the fact that only the shear factor is fitted. The shape also depends on the physically based hardening data, which are supplied by Corus RD&T.

5.4.2 Plane strain factor determination

Proportional plane strain experiments were carried out on the same test pieces as in the shear experiments for sheet steel (AKS) and aluminium (AA 5182). The steel experiments were performed 5 times for each direction. The aluminium experiments were performed 1 time for each direction. The experiments were carried out under the following conditions:

Vertical clamp displacement:	1.5 mm
Time:	150 s
Vertical clamp velocity:	0.01 mm/s
Number of force samples:	250
Number of displacement samples:	250
Number of camera samples:	8.5 per second

The plane strain factors are given in table 5-8 and table 5-9.

Sample	1	2	3	4	5	Average	Max.abs. deviation
Angle RD							
0	1.245	1.245	1.238	1.239	1.234	1.240	0.006
45	1.242	1.249	1.236	1.247	1.241	1.243	0.007
90	1.240	1.250	1.247	1.256	1.257	1.25	0.01

Table 5-8 Plane strain factors for steel sheet (AKS)

Angle RD	
0	1.086
45	1.118
90	1.114

Table 5-9 Plane strain factors of aluminium sheet (AA 5182)

The samples of a plane strain experiment are illustrated together with the fitted hardening function in figure 5-21.

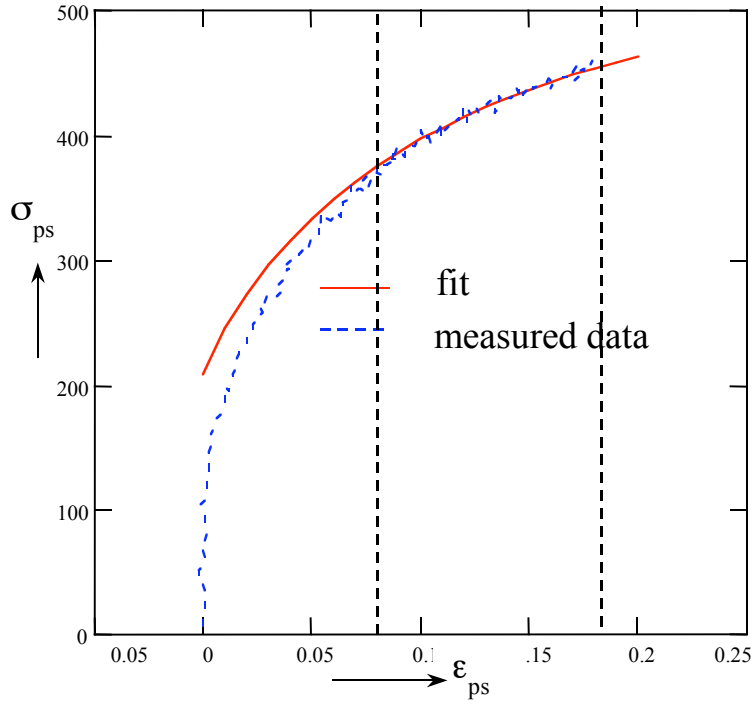

Figure 5-21 Measured data and fitted hardening function of the plane strain experiment

The plane strain range used in the fit is illustrated by the area between the vertical dotted lines. It can be observed that the shape of the fitted hardening function coincides fairly well with the measured data.

5.4.3 Vegter reference points for steel (AKS) and aluminium (AA 5182)

The shear and plane strain reference points for steel are determined by the shear and plane strain factors respectively in sections 5.4.1 and 5.4.2. The uni-axial and equi-bi-axial reference points for steel are supplied by Corus RD&T. The reference points for aluminium are all taken from Corus RD&T, because the aluminium plane strain and shear factors of sections 5.4.1 and 5.4.2 were obtained from only 1 test. These results do not differ much from the results of Corus, but it is preferable to base reliable factors on more tests. The material parameters are summarised in tables 5-10 to 5-15. The yield surfaces of steel and aluminium are illustrated in figures 5-22 to 5-27.

	0°	45°	90°
f_{sh}	0.5285	0.5716	0.5285
f_{un}	0.916	1.079	0.927
f_{ps}	1.24	1.243	1.25
f_{bi}	1.149	1.149	1.149
R	2.04	1.27	2.19
α_{ps}	0.5	0.5	0.5
gradient equi-bi-axial	-1.01	-1.00	-0.99

Table 5-10 Vegter function data for steel

σ_y (N/mm^2)	C	n
184.8	539	0.202

Table 5-11 Nadai-Ludwik hardening data for steel

σ0	Δσm	β	Ω	n	ε0	σ0dyn	m
146.8	218.5	0.462	7.753	0.75	0.005	591.1	2.2

Table 5-12 Physically based hardening data for steel

	0°	45°	90°
f_{sh}	0.596	0.579	0.556
f_{un}	0.992	1.008	0.992
f_{ps}	1.081	1.071	1.054
f_{bi}	1.026	1.026	1.026
R	0.73	0.79	0.67
α_{ps}	0.5	0.5	0.5
gradient equi-bi-axial	-1.00	-1.00	-1.00

Table 5-13 Vegter function data for aluminium

σ_y (N/mm^2)	C	n
128.0	531	0.226

Table 5-14 Nadai-Ludwik hardening data for aluminium

σ0	Δσm	β	Ω	n	ε0	σ0dyn	m
125.5	261.8	0.10	6.31	0.75	-	0.0	-

Table 5-15 Physically based hardening data for aluminium

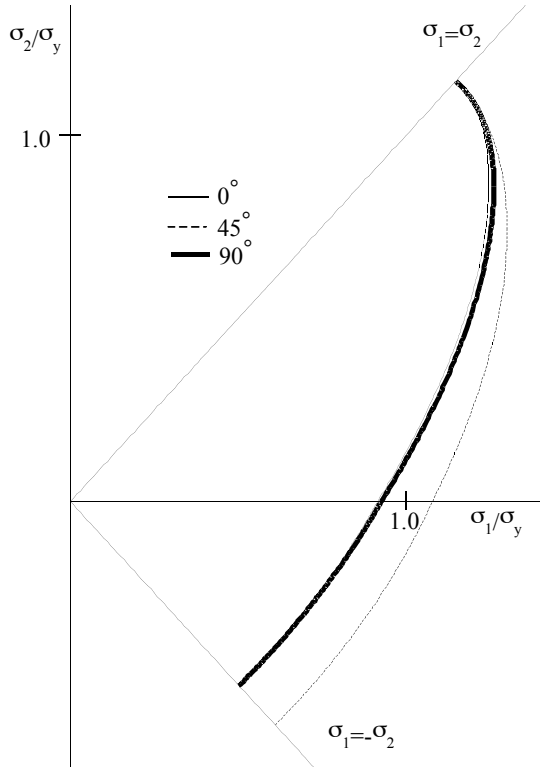

Figure 5-22 Quarter of Hill yield surfaces for 0°,45° and 90° (steel)

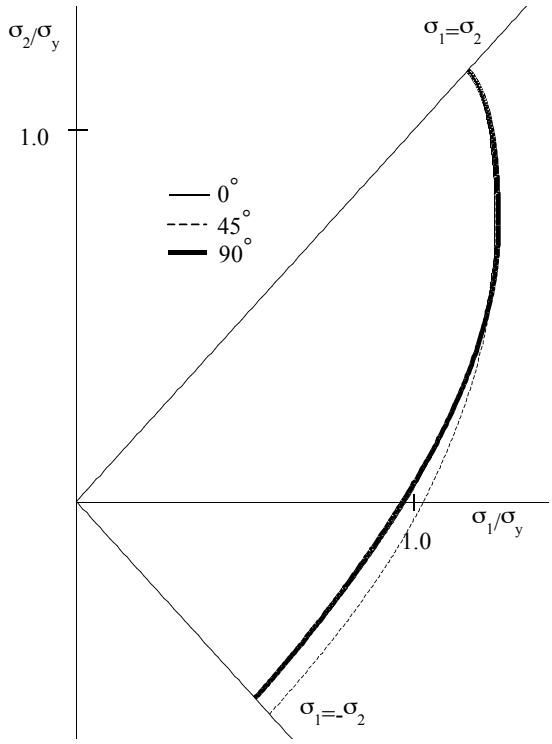

Figure 5-23 Quarter of Vegter yield surfaces for 0°,45° and 90° (steel)

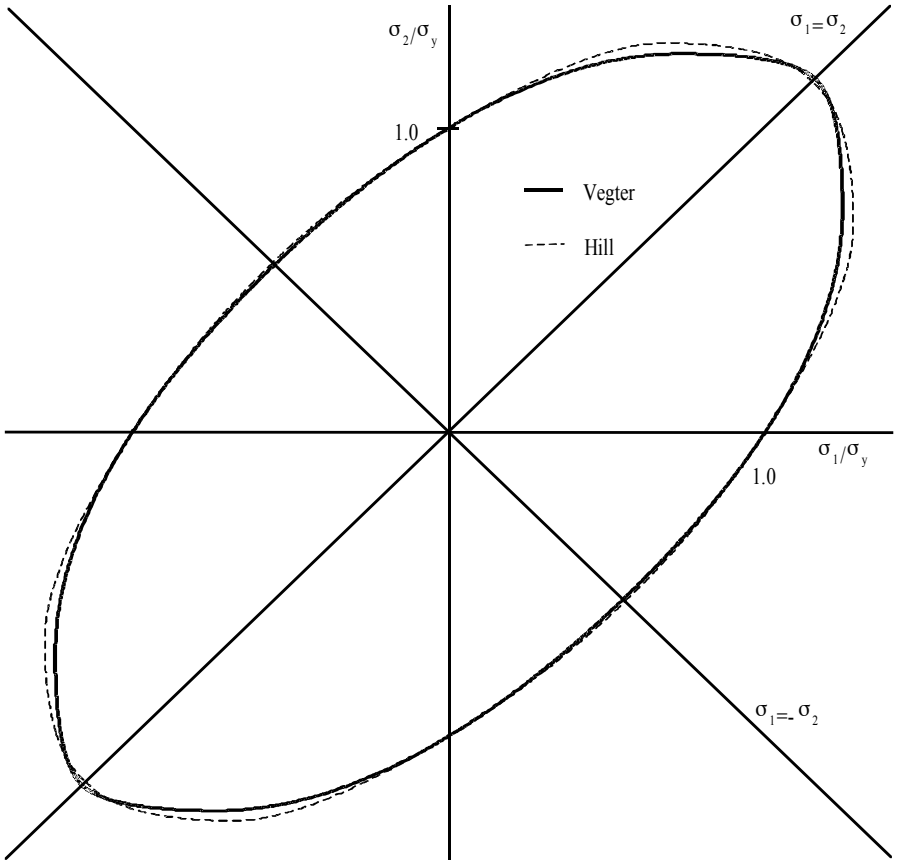

Figure 5-24 Average Vegter and Hill yield surfaces (steel)

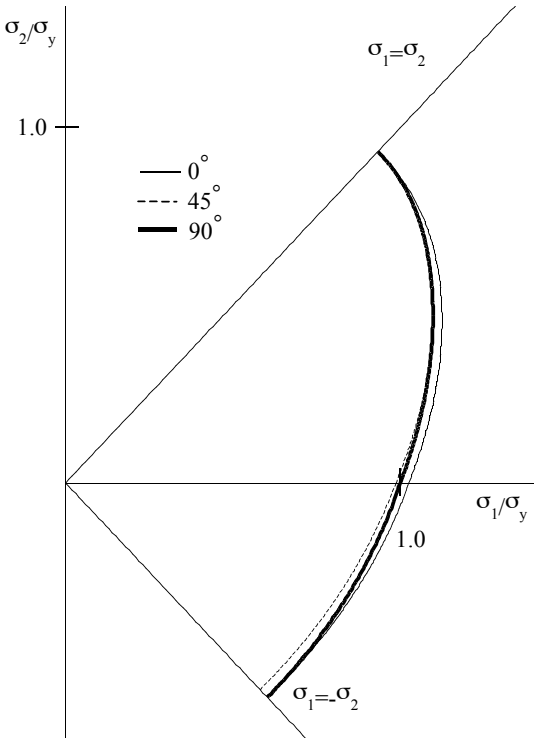

Figure 5-25 Quarter of Hill yield surfaces for 0°,45° and 90° (aluminium)

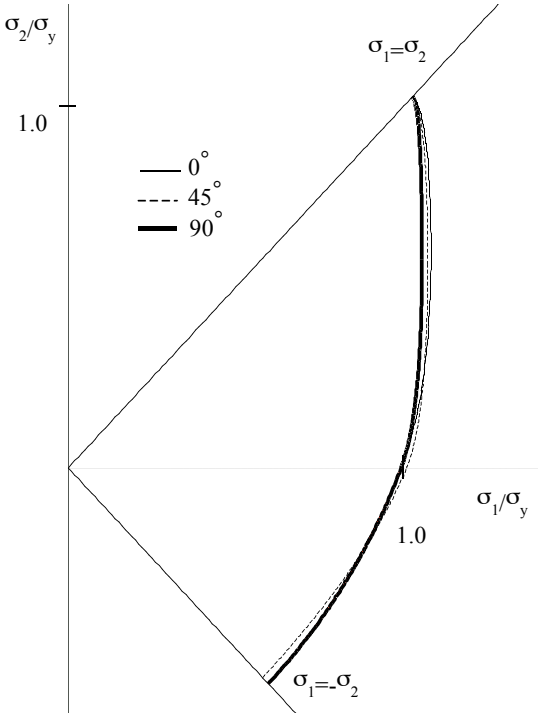

Figure 5-26 Quarter of Vegter yield surfaces for 0°,45° and 90° (aluminium)

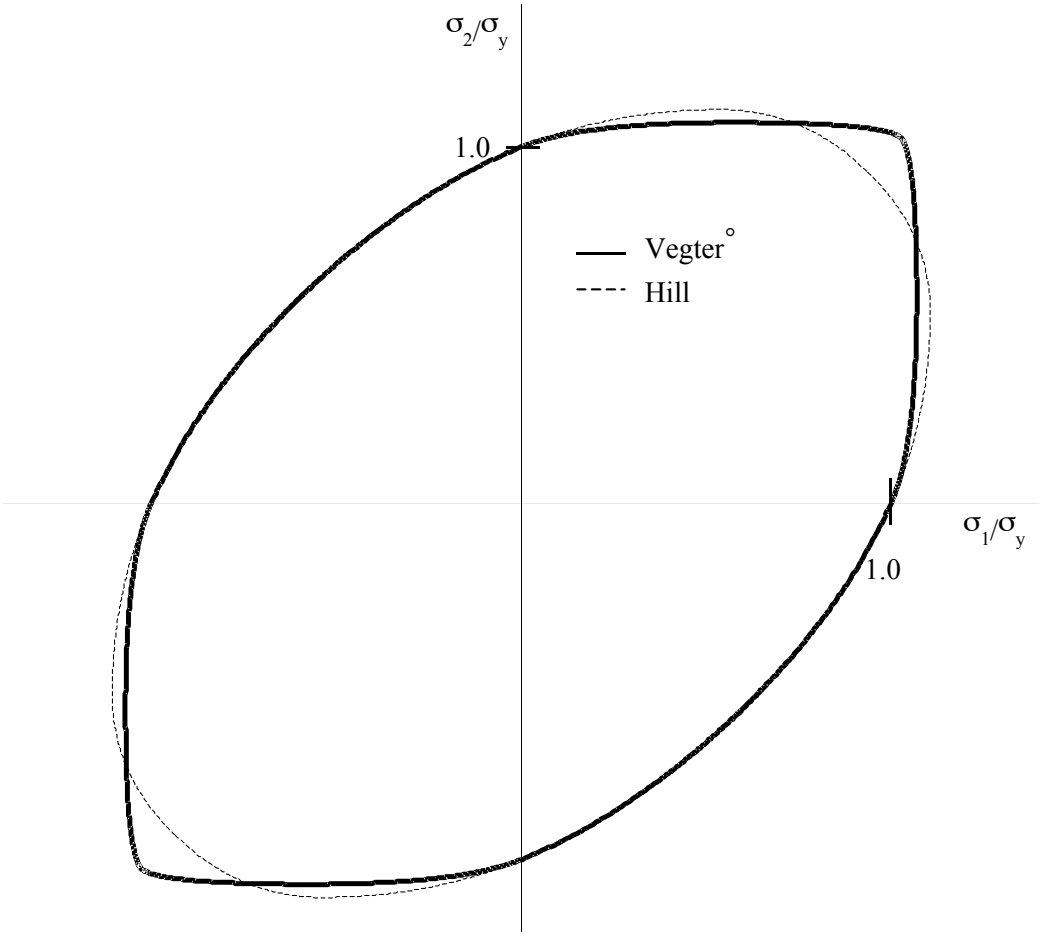

Figure 5-27 Average Vegter and Hill yield surfaces (aluminium)

5.5 Experimental determination of anisotropic hardening parameter

The bi-axial test equipment can be used to determine the anisotropic hardening parameter (q) by carrying out a cyclic deformation test. Due to insufficient clamping the test piece buckles during plane strain compression tests, hence the test case was carried out by a cyclic shear experiment. The anisotropic hardening function is given by (chapter 4):

$$f = -\frac{\partial \sigma_y}{\partial \varepsilon_{eq}} = f_{ini} + \left[1 - \left(\frac{1}{2} - \frac{1}{2} \cdot \frac{\alpha_{eq}}{\alpha_{\lim}} \cdot \cos\alpha\right)\right]^q \cdot \left(f_{iso} - f_{ini}\right) \qquad \textbf{5. 18}$$

Relation (5. 15) is expressed in shear terms:

$$\sigma_{SH} = f_{sh} \cdot \sigma_y$$

$$\gamma_{SH} = \frac{\sigma_y}{\tau_{xy}} \cdot \varepsilon_{eq} = \frac{1}{f_{sh}} \cdot \varepsilon_{eq} \qquad \textbf{5. 19}$$

The shear hardening rate in the shear stress - strain curve is defined by:

$$f_{shear} = -\frac{\partial \sigma_{SH}}{\partial \gamma_{SH}} = -\frac{\partial\left(f_{sh} \cdot \sigma_y\right)}{\partial\left(\frac{1}{f_{sh}} \cdot \varepsilon_{eq}\right)} = -{f_{sh}}^2 \frac{\partial \sigma_y}{\partial \varepsilon_{eq}} = -{f_{sh}}^2 \cdot f =$$

$$-{f_{sh}}^2 \cdot \left(f_{ini} + \left[1 - \left(\frac{1}{2} - \frac{1}{2} \cdot \frac{\alpha_{eq}}{\alpha_{\lim}} \cdot \cos\alpha\right)\right]^q \cdot \left(f_{iso} - f_{ini}\right)\right) = \qquad \textbf{5. 20}$$

$$-f_{shear,ini} + \left[1 - \left(\frac{1}{2} - \frac{1}{2} \cdot \frac{\alpha_{eq}}{\alpha_{\lim}} \cdot \cos\alpha\right)\right]^q \cdot \left(f_{shear,iso} - f_{shear,ini}\right)$$

Here (f_{shear}) is the shear hardening rate, ($f_{shear,iso}$) is the isotropic shear hardening rate and ($f_{shear,ini}$) the initial shear hardening rate at reverse loading. The parameter f_{sh} is the shear factor, which is determined from the proportional experiments of the former section. The anisotropic hardening parameter (q) can be obtained by fitting the hardening definition 5. 20 on the experimental hardening curve.

Cyclic experiments were carried out with test pieces cut out at 0°,45° and 90° to the rolling direction of steel sheet (AKS) and aluminium sheet (AA 5182). The clamp displacement reverses 5 times. Results of the fit are given in tables 5-10 and 5-11.

After the fitting procedure the experiment was simulated with both the isotropic and anisotropic hardening functions. The isotropic part was described by the Nadai-Ludwik function and the average anisotropic parameter (q) was used.

Angle	q
0	
	0.20
45	
	0.10
90	
	0.13
Average	
	0.14

Table 5-10 Anisotropic hardening parameters for steel sheet

Angle	q
0	
	0.39
45	
	0.37
90	
	0.50
Average	
	0.41

Table 5-11 Anisotropic hardening parameters for aluminium sheet

Figures 5-28 to 5-31 show the experimental data from a cyclic test for 0° together with the results of the simulations. It can be observed that the anisotropic hardening rule gives better results in the beginning of the first reverse stage and at the first reverse loading stage. At the end of the first reverse loading path also the isotropic hardening model gives a satisfactory result.

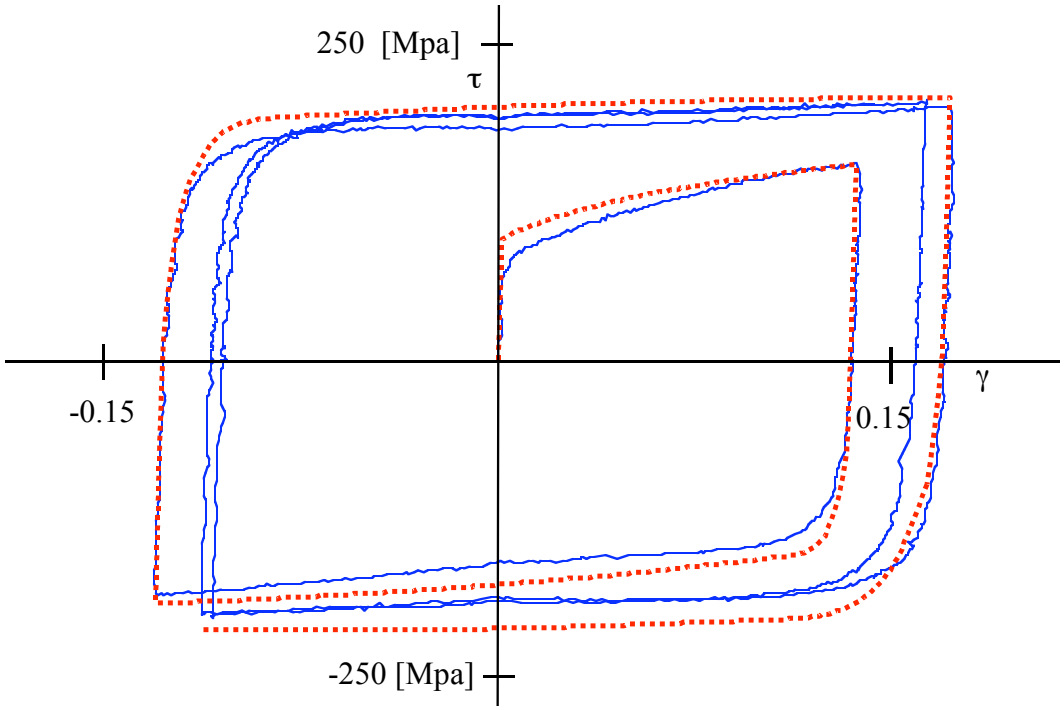

Figure 5-28 Comparison of anisotropic hardening based simulation (dotted line) with experimental results (solid line) for steel sheet

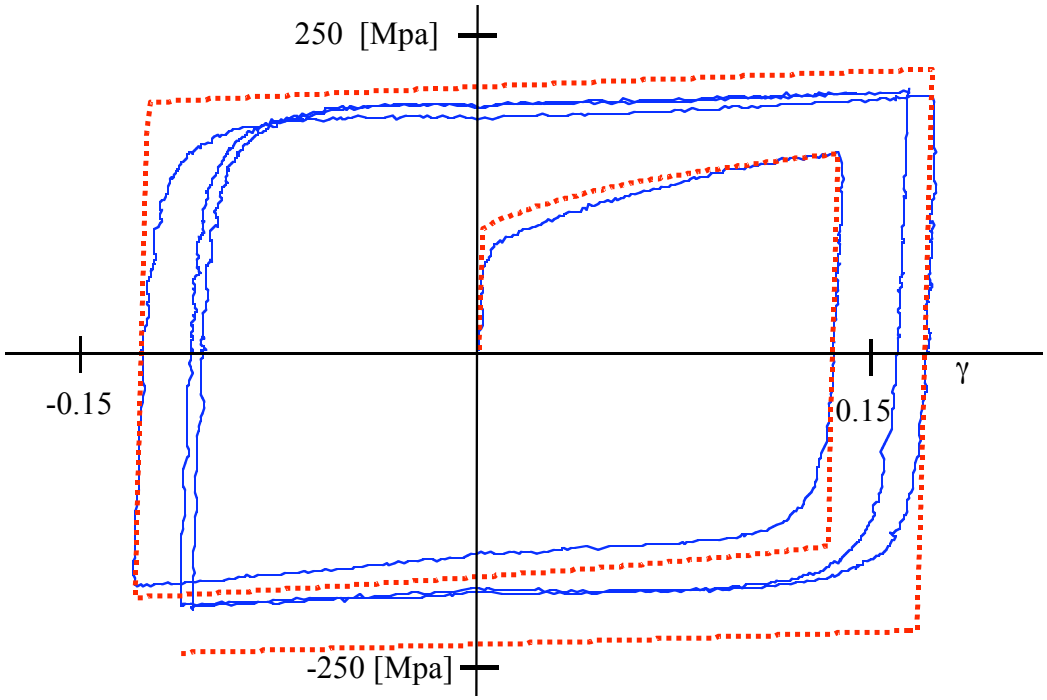

Figure 5-29 Comparison of isotropic hardening based simulation (dotted line) with experimental results (solid line) for steel sheet

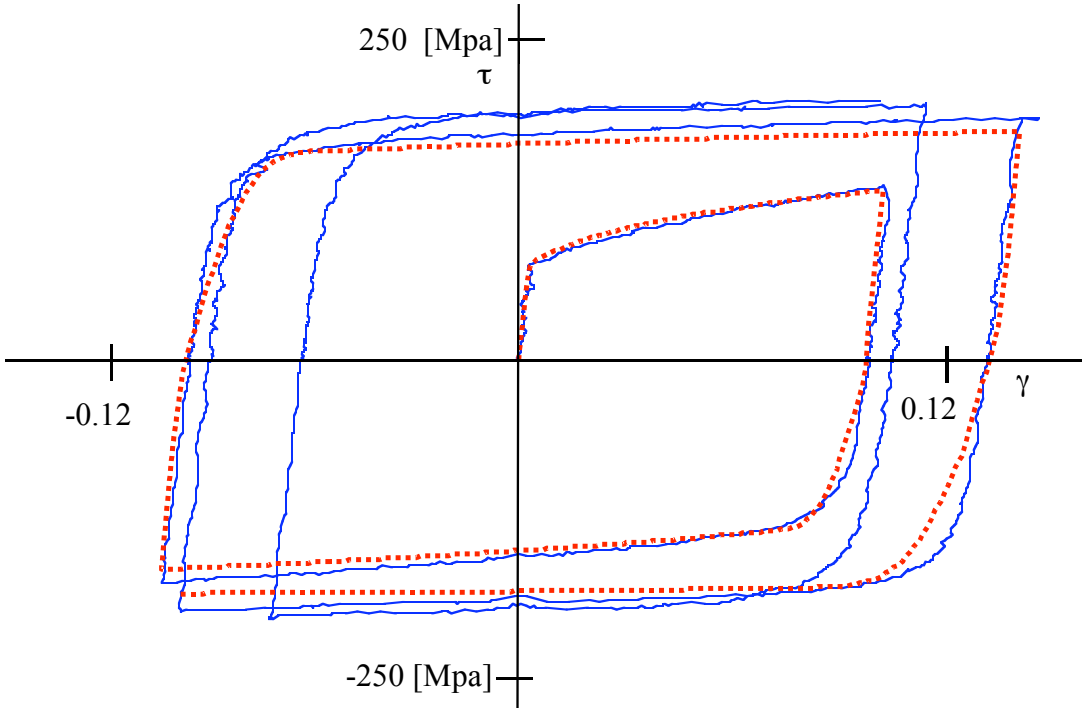

Figure 5-30 Comparison of anisotropic hardening based simulation (dotted line) with experimental results (solid line) for aluminium sheet

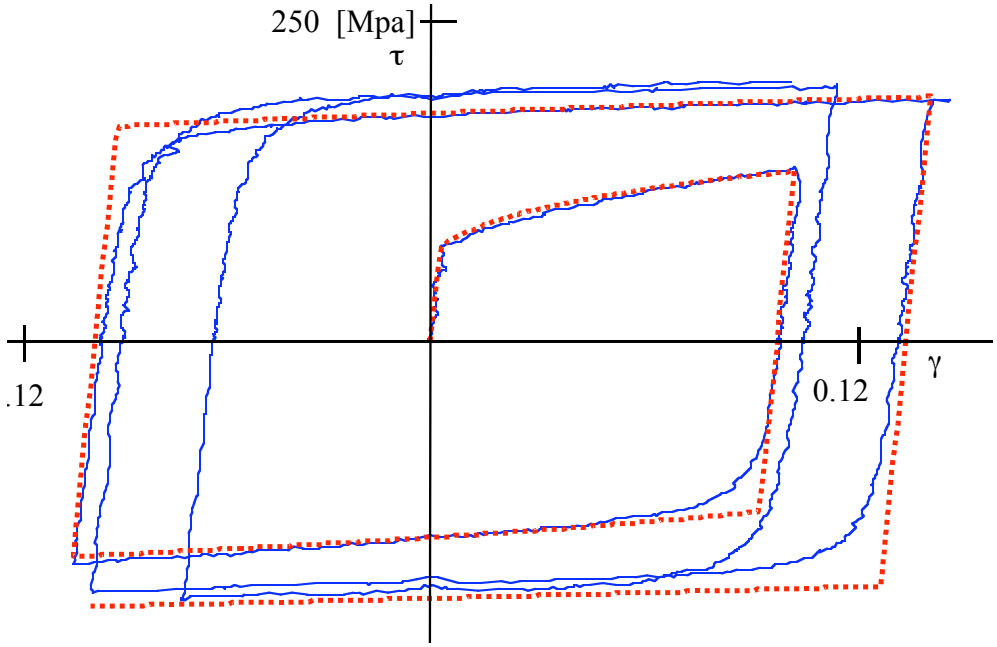

Figure 5-31 Comparison of isotropic hardening based simulation (dotted line) with experimental results (solid line) for aluminium sheet

5.6 Examination of non-proportional deformation paths

The material model of chapters 3 and 4 is examined in non-proportional deformations on shear experiments after 3%, 7% and 13% plane strain pre-deformation on steel sheet. The procedure of examining the material model is set up as follows. The shear factors for different planar angles are determined from the proportional experiments of section 5.4. Then the parameter (q) for the anisotropic hardening model is determined by the fit of the cyclic loading – reverse loading test of the former section. Subsequently the experiments are simulated with the Vegter yield function combined with both the isotropic physically based hardening model and the anisotropic hardening function. After this the simulations are compared with the experiments.

The stress-strain curves of the experiments and simulations are given by figures 5-32 and 5-33. Figure 5-32 shows the simulations with the isotropic hardening function and figure 5-33 the simulations with the anisotropic hardening function. By a comparison of experimental data and the isotropic hardening function the following conclusions can be drawn:

- A higher plane strain pre-deformation gives a larger initial shear yield stress. This is fairly well predicted by the isotropic hardening function.
- At the start a small ‘bubble’ is present in the shear stress-shear strain curve. First the hardening behaviour is larger than the isotropic hardening behaviour, then the hardening becomes smaller. After a certain maximum in the curve softening occurs. This phenomenon becomes more apparent when the pre-deformation is larger. The isotropic hardening function cannot predict this behaviour.
- As the shear test proceeds, the hardening rate tends towards the isotropic hardening rate.

Figure 5-33 shows the result of a simulation with the new anisotropic hardening relation for a non proportional test with 13 % plane strain pre deformation. It can be concluded that the anisotropic hardening model gives worse results in this non-proportional deformation path than the isotropic hardening model. The anisotropic hardening model has been adapted especially for a continuous hardening behaviour in non–proportional deformation paths in section 4.2.4. This adaptation does not provide a good basis to describe the real behaviour. A more sophisticated approach should be investigated in the future.

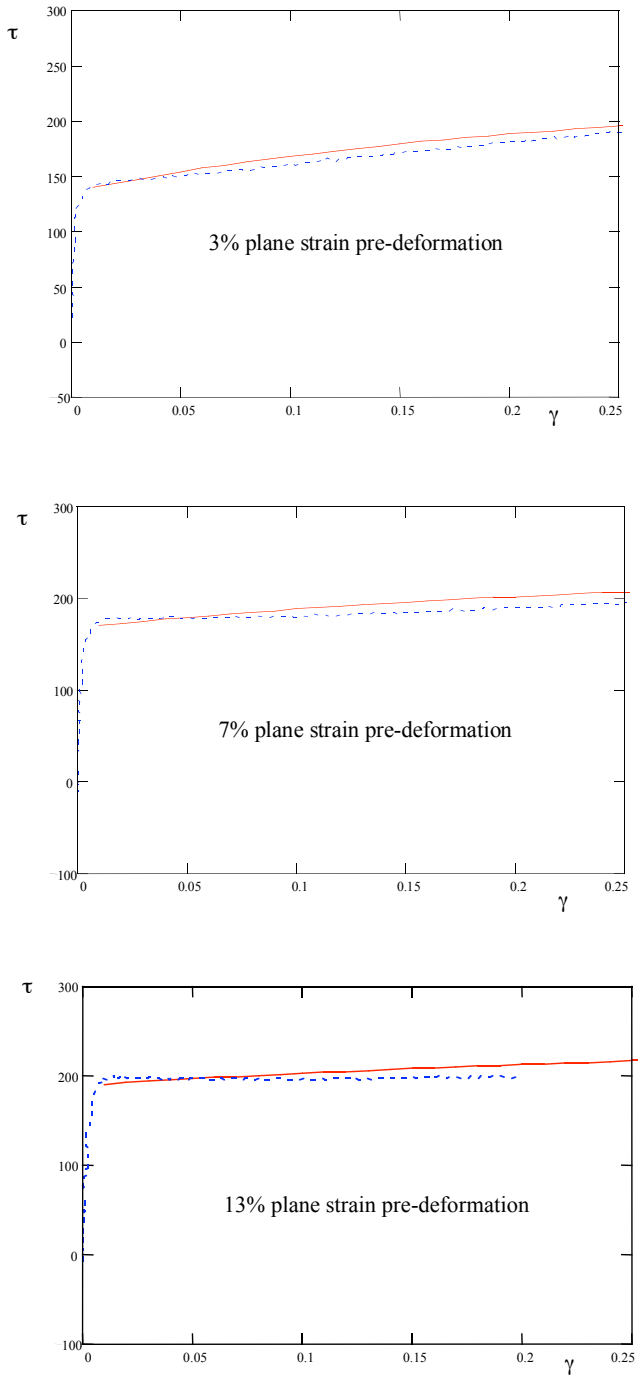

Figure 5-32 Comparison of isotropic hardening based simulations (solid line) with experiments (dotted line) of shear tests after 3, 7 and 13 % plane strain deformation

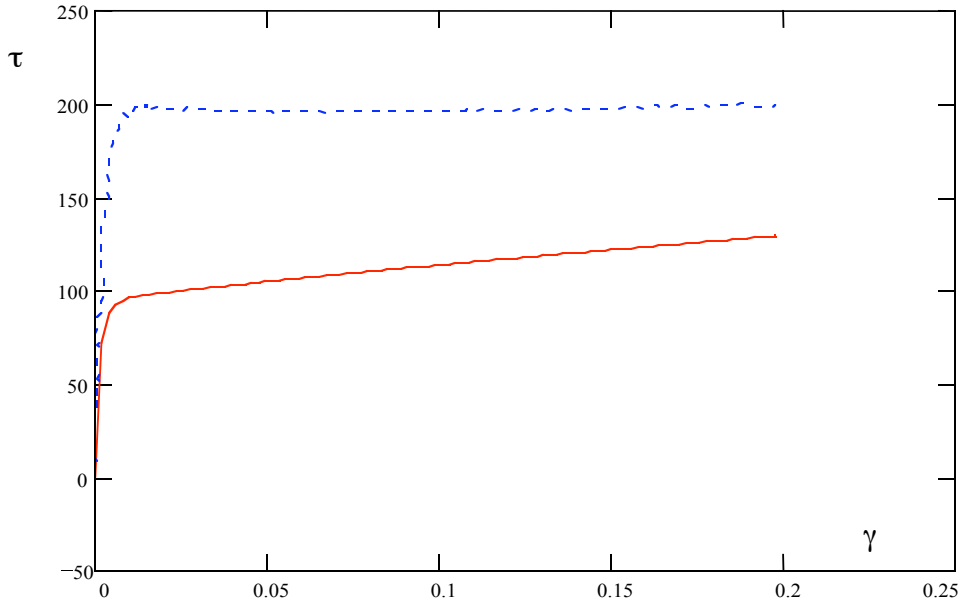

Figure 5-33 Comparison of anisotropic based hardening simulation with experimental results

5.7 Conclusions

The bi-axial equipment can be conveniently used to investigate a large variety of deformation paths. In this dissertation the equipment is used to determine the shear and plane strain reference points of the Vegter yield function. Cyclic shear experiments were carried out to determine the anisotropic hardening parameter (q) and a start was made with non-proportional experiments. In order to make the best possible use of the equipment, it has to be improved to impose a plane strain compression deformation.

6 Validation

To validate the material model 3 test cases are investigated. Each test is both carried out experimentally and simulated using the new material model. The new model is based on experimental data from the bi-axial test equipment and data from Corus RD&T, see also the data of tables 5-10 to 5-15. The first test case is a plane strain bending test which is carried out in co-operation with the University of Eindhoven (TUE). This test is a validation of the plane strain point determination and the performance of the Vegter yield function. The second test is the deep drawing of a cylindrical cup. This test is carried out in co-operation with Corus RD&T. It validates the performance of the Vegter yield function mainly on the earing behaviour. The third case is the deep drawing of a trapezium-shaped product. Here the material model is validated on the strain distribution of a critical product. In each validation case the performance of the Vegter function is compared with the Hill'48 function, which has been widely used in finite element codes. The Vegter and Hill yield functions display significantly different yield stresses in the plane strain and equi-bi-axial regions of the yield surface for the tested materials, see figures 5-22 to 5-27. Therefore improvements in the simulation results are expected when using the Vegter yield function.

This chapter is mainly a validation of the Vegter yield function. In some cases the yield function is used in combination with the Nadai-Ludwik hardening function and in other cases with the physically based hardening function. No specific cases have yet been investigated to validate the hardening function.

6.1 Bending test case

The plane strain bending test case is carried out in co-operation with the University of Eindhoven (TUE). The finite element simulation and the data acquisition of the plane strain reference point are carried out by the University of Twente and Corus RD&T. The experimental part is carried out at the TUE. With the bending test a plane strain deformation is imposed on the sheet metal. By comparing the simulations with the experiments the performance of the Vegter yield function in the plane strain region of the yield surface is validated.

The experimental set-up is shown in figure 6-1.

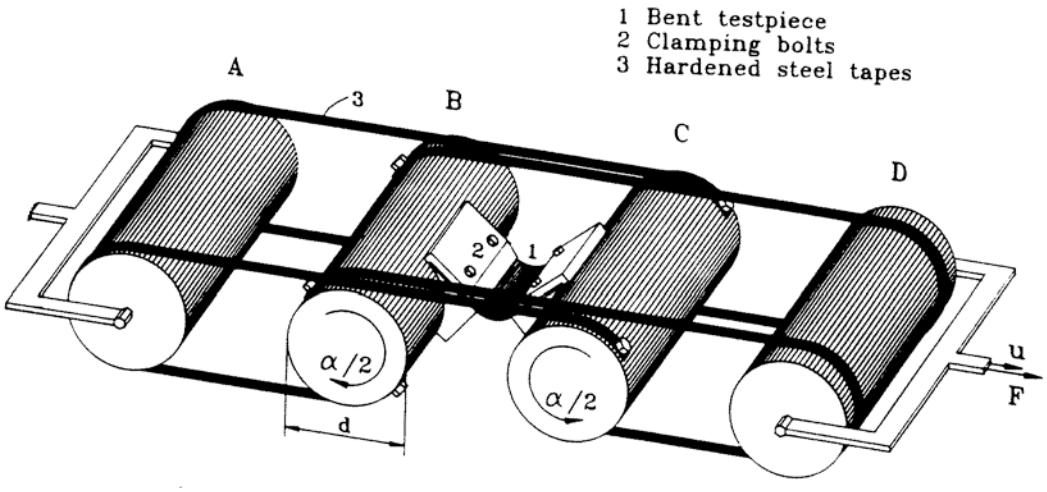

Figure 6-1 Experimental set-up (Hoogenboom, 1993)

The details of the experiment can be found in (Hoogenboom, 1993). In brief the experiment is carried out as follows. Use is made of four rolls with equal diameters (Figure 6-1). The rolls (A) and (D) are free to rotate but are prescribed in the translation direction. The rotation of rolls (B) and (C) are related to the translation of rolls (A) and (D) by steel tapes. The influence of the friction between the steel tapes and the rolls is neglected, which means that a pure bending moment is applied to the rolls (B) and (C). A test piece is clamped to rolls (B) and (C). Consequently the test piece is loaded in pure bending.

The large relative width of the sheet ensures a plane strain state in the sheet. The upper part of the sheet is loaded in a plane strain compression and the lower part in tension. In the zones near the clamps and at the free edges the deformation will differ from pure bending. A correction for these effects is made by a finite element simulation, already in use at the TUE (Hoogenboom, 1993).

The experiment is carried out with both steel (AKS) and aluminium (AA 5182) for different angles (0, 45 and 90°) to the rolling direction. These are the same materials as used in the bi-axial test equipment in chapter 5. The sheet is bent once till a radius of curvature of 2.0 mm is reached. For steel sheet this implies strains ranging from 0 inside the sheet to 18 % at the surface and for aluminium strains from 0 to 25 %. These values coincide fairly well with the imposed deformation in the bi-axial test equipment of chapter 5 (values from 0 to 18%).

With the current experimental set-up only 1 bending direction is possible. In the future also cyclic bending experiments are intended. For these experiments a new set-up is being prepared at the TUE.

The simulations are carried out with the model in figure 6-2. The model consists of 400 elements and represents half of the deformation area of the sheet in the experiment. If no edge effects are observed in the simulations, no elements need to be modeled across the width of the sheet because no deformation takes place in this direction. However, the model is also set up to investigate edge effects during a cyclic experiment in the future, which also requires the elements across the width. The number of integration points across the thickness is set to 7, which is the maximum available in the finite element code used.

The right-hand edge is prescribed a rotation and the other side is suppressed in all directions. The nodes at all the edges are suppressed in the width direction. The material is modelled with both the Vegter and the Hill‘48 yield functions in combination with the Nadai-Ludwik hardening function. The material parameters are the same as in the experiments with the bi-axial test equipment, see tables 5-10 to 5-15.

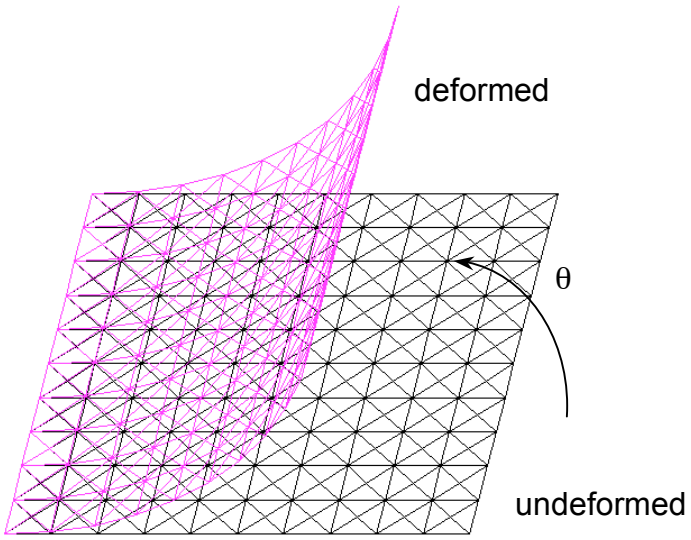

Figure 6-2 Bending simulation set-up

The results of the experiments and the simulations are illustrated in figures 6-3 to 6-8. The figures show the normalised bending moment ($M/b \cdot t^2$) as a function of the normalised curvature (t/ρ) for each planar angle. Here (M) is the bending moment in the sheet, (b) the width, (t) the thickness of the sheet and (ρ) the curvature radius. The simulation results are discussed separately for steel and aluminium.

6.1.1 Steel simulations

For each planar angle 6 bending experiments were performed. The plane strain factors in the simulations for steel are based on 5 experiments. The average experimental data and the simulation results with the average plane strain factor are represented in figures 6-3 to 6-5. Figures 6-6 to 6-8 illustrate the spread in experimental data together with the possible spread in simulation results. This spread in simulations is based on the maximum and minimum measured plane strain factors of table 5-8.

The Vegter results show a fair agreement with the experimental data. Each simulation result with the Hill '48 yield function shows a larger bending moment as a function of the curvature, which can be attributed to the larger plane strain yield stress, see also figures 5-22 and 5-23.

However, the simulations with the Vegter yield function start with a larger bending moment and end with a smaller moment compared to the experiments. The larger moment at the start can partly be attributed to the fact that the elastic deformation is larger than the exact deformation. This is explained by the situation of the integration points below the surface of the sheet metal (Carleer, 1996). Carleer also discovered that an uneven number of integration points underestimates the bending stiffness at higher deformations, which contributes to a lower moment-curvature plot. However, the effects found by Carleer were not as large as the differences in figures 6-3 to 6-5. Other reasons have to be found to explain the differences.

A first reason for the difference is that the simulations assume identical material behaviour under a compressive and a tensile load. The sheet then behaves symmetrically across the whole thickness. It is suspected that in reality the material shows different behaviour under tension and compression. This means that the sheet is not symmetrically deformed, which affects the shape of the moment-curvature plot. No research has been done within this dissertation on this effect. A plane strain compression test with the bi-axial test equipment could reveal different behaviour under compression compared to tension. However, this test cannot be performed conveniently with the current test equipment. In the future the equipment should be modified to carry out this test.

A second reason is the effect of the strain rate. The experiments are performed within a time of about 60 seconds. This effectuates a strain rate that influences the hardening behaviour significantly. The strain rate is not constant for the height of the sheet, but increases towards the edges. When the change in curvature is constant during the time of the experiment, the strain rate only affects the height of the curve. Otherwise also the shape of the curve will be influenced. Because the experimental course of the strain rate has not yet been investigated, the simulations are performed without strain rate influence. For a proper validation the experimental strain rate should be examined and taken into account in the simulations in the future. Another option is filtering out the strain rate influence by performing an experiment with a very low strain rate.

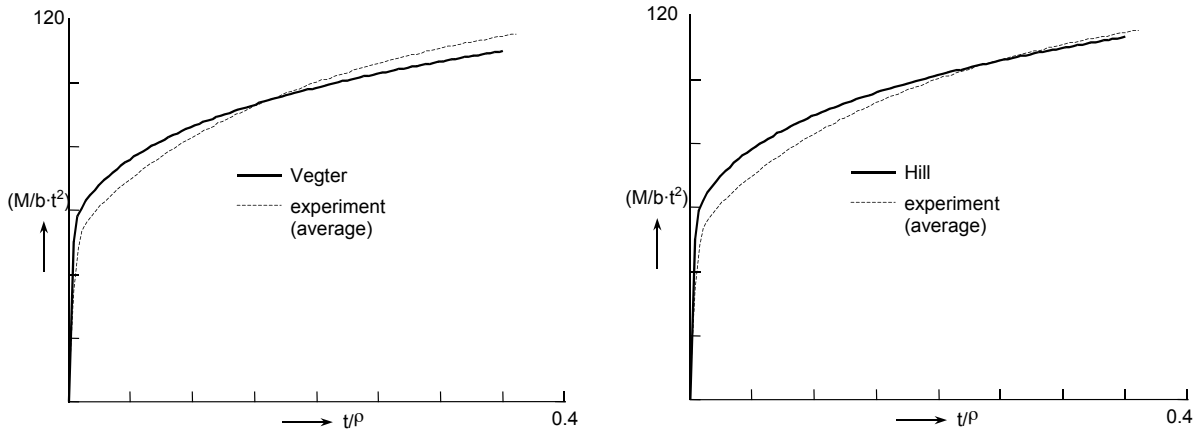

Figure 6-3 Comparison of simulation results with experimental data, 0° (steel)

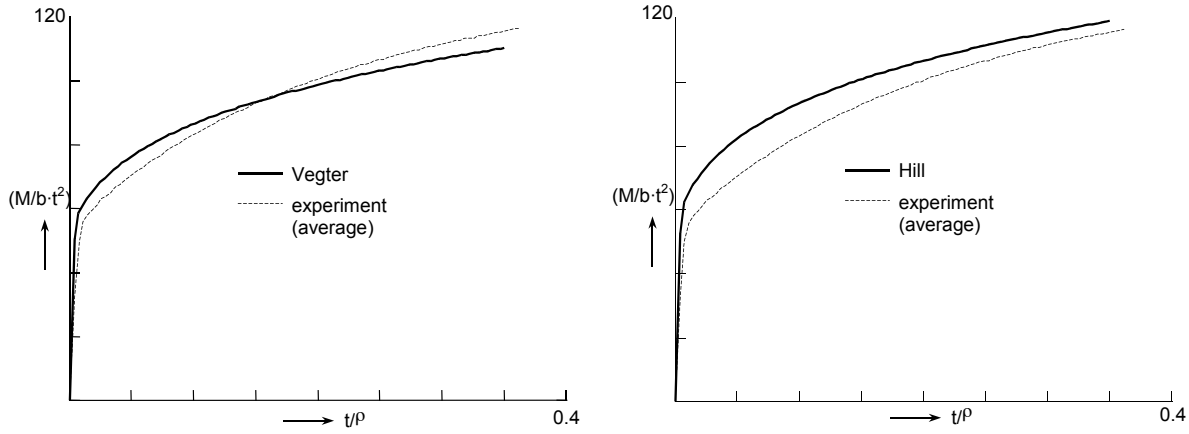

Figure 6-4 Comparison of simulation results with experimental data, 45° (steel)

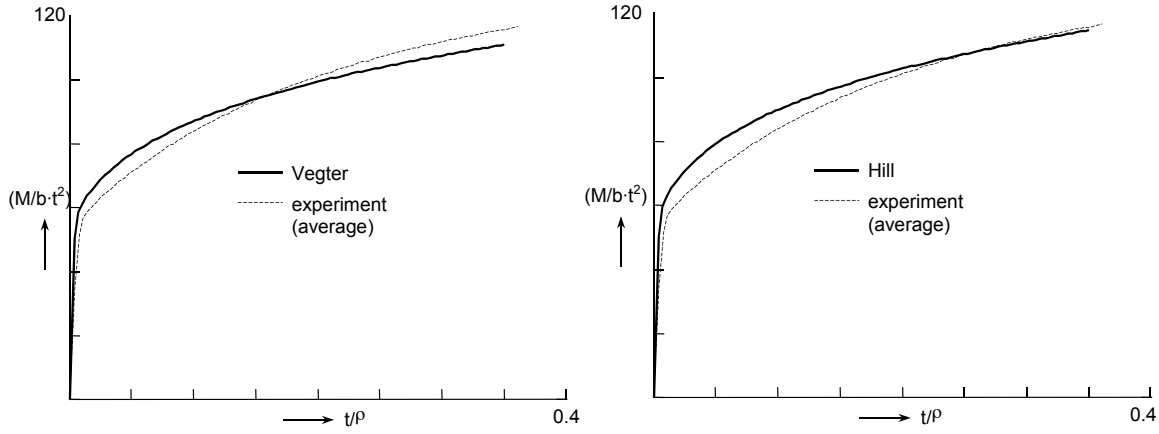

Figure 6-5 Comparison of simulation results with experimental data, 90° (steel)

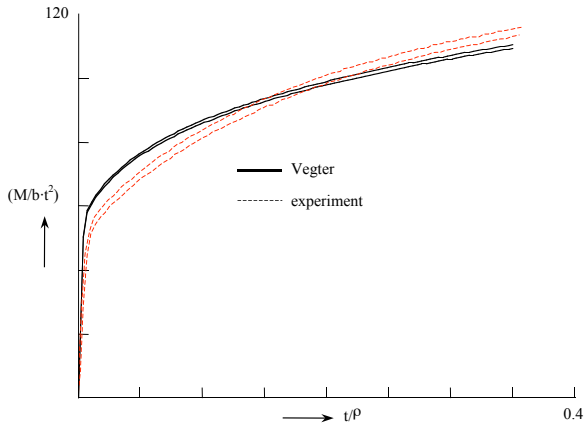

Figure 6-7 Spread in experimental data together with with simulation results for the maximum and minimum plane strain factor, 0° (steel)

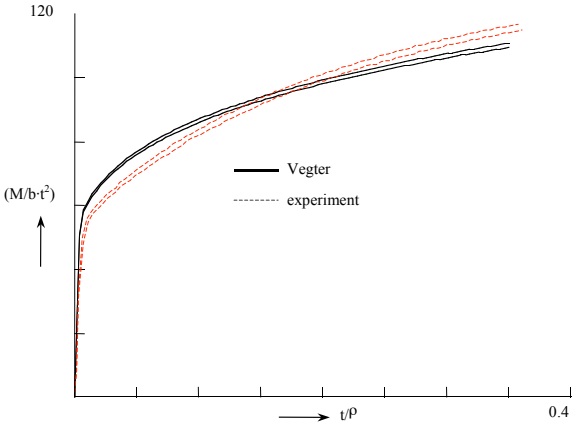

Figure 6-8 Spread in experimental data together with with simulation results for the maximum and minimum plane strain factor, 45° (steel)

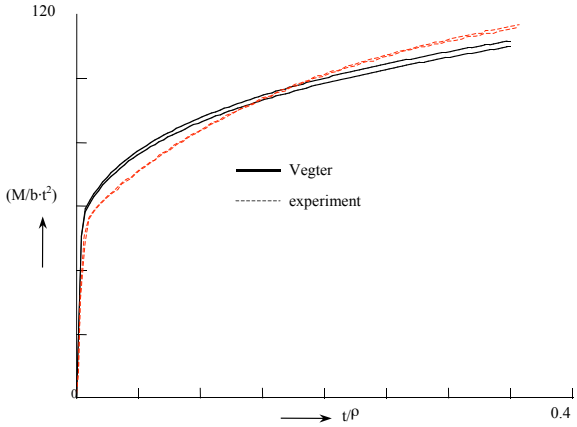

Figure 6-9 Spread in experimental data together with with simulation results for the maximum and minimum plane strain factor, 90° (steel)

6.1.2 Aluminium simulations

For each planar angle 6 bending experiments were performed. Due to the small number of plane strain experiments carried out on aluminium at the UT, the plane strain factors were provided by Corus RD&T. The average experimental data and the simulation results are represented in figures 6-10 to 6-12. The spread in experimental data can be considered similar to the data of steel. The spread in plane strain factors is not known.

With the aluminium simulations (figures 6-10 to 6-12) the difference between the Vegter and the Hill yield functions become more clear. The simulation results of the Vegter function coincide much better with the experiments than the results of the Hill '48 function. For 0° still a small difference is present but for 45° and 90° the moment-curvature plots represent the experimental data almost exactly.

Each Hill '48 simulation shows a larger bending moment as a function of the curvature. Similar to the simulations with steel this is attributed to the larger plane strain yield stress. The advantage of aluminium compared to steel is that the strain rate does not affect the hardening behaviour significantly, so this effect does not have to be examined. Also here the simulations assume similar material behaviour in tension and compression. Probably this assumption is reasonable with aluminium sheet metal.

6.1.3 Conclusion

Due to the fact that the plane strain yield stress is an input parameter of the Vegter yield locus, the yield surface shape differs significantly from the Hill yield surface in the plane strain region (figures 5-22 to 5-27). The shape of the yield surfaces explains directly the difference in the moment-curvature plots of a plane strain bending test. The results for steel need more research for a proper validation, but first results provide a fair impression. The results for aluminium are satisfying, considering the good agreement between the experimental and simulation results.

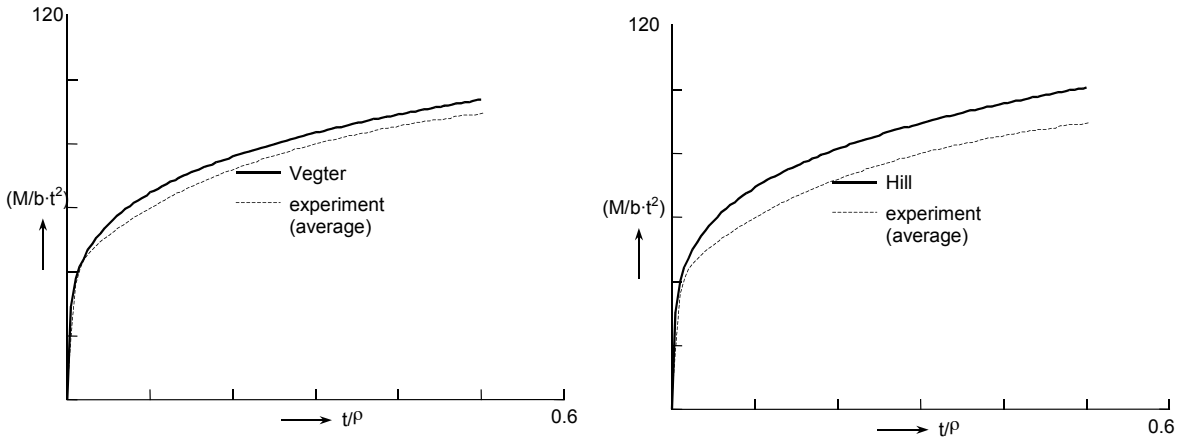

Figure 6-10 Comparison of simulation results with experimental data, 0° (Al)

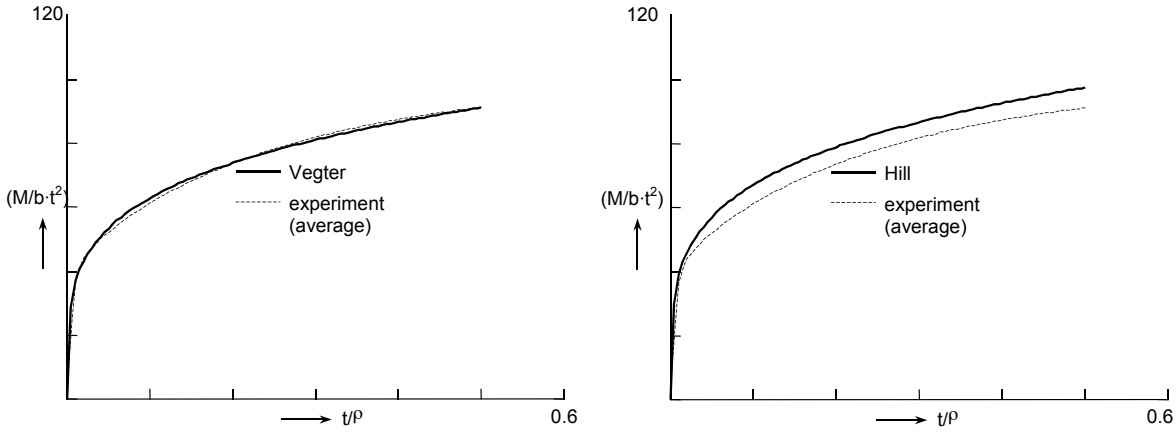

Figure 6-11 Comparison of simulation results with experimental data, 45° (Al)

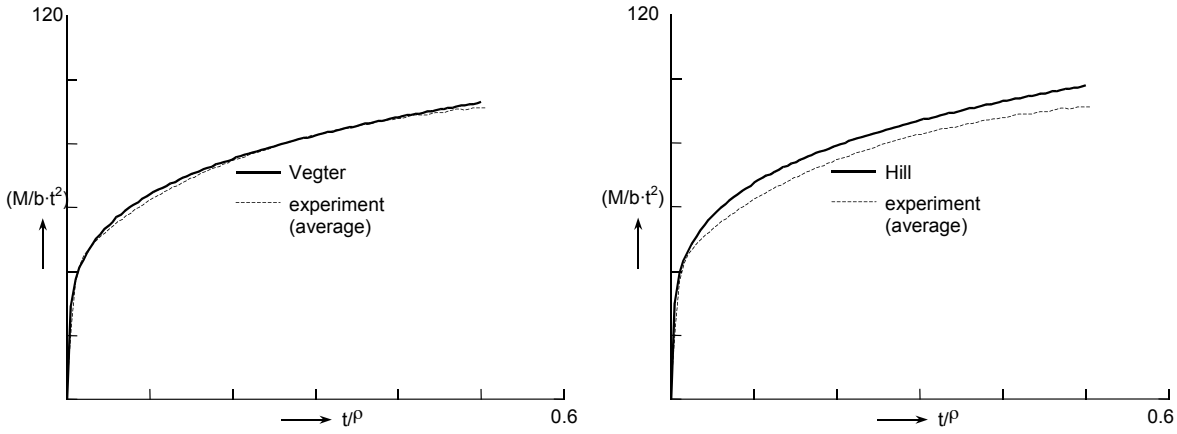

Figure 6-12 Comparison of simulation results with experimental data, 90° (Al)

6.2 Deep drawing of a cylindrical product

The deep drawing of a cylindrical product is carried out in co-operation with Corus RD&T. The experiments and simulations are carried out at Corus. The data for the Vegter function are supplied both by the UT and Corus. By comparing the simulation results with experiments the performance of the Vegter yield function on a basic deep drawn product is validated. A large effect of using different material models can be observed in the earing profile, so this will be investigated first. Furthermore the Vegter function will be validated with the strain distributions.

The experimental set-up is shown in figure 6-13.

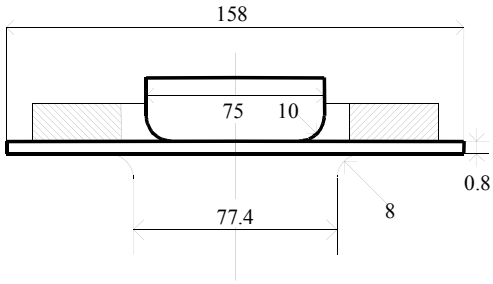

Figure 6-13 Geometrical set-up

The experiment is carried out with both steel (AKS) and Aluminium (AA 5182). These are the same materials as used in the bi-axial test equipment in chapter 5. The process parameters are listed in table 6-1.

Process parameters	
blank holder force [Kn]	20
friction coefficient	0.16
punch displacement [mm]	60

Table 6-1 Process parameters

The simulations are carried out with the model in figure 6-14, which shows the undeformed mesh. The model consists of 5250 elements and represents a quarter of the sheet of the experiment. At the time the calculations were carried out, no automatic refinement procedure was available in the used code. Therefore the elements towards the edges are refined in advance to obtain a fine discretization of the earing region.

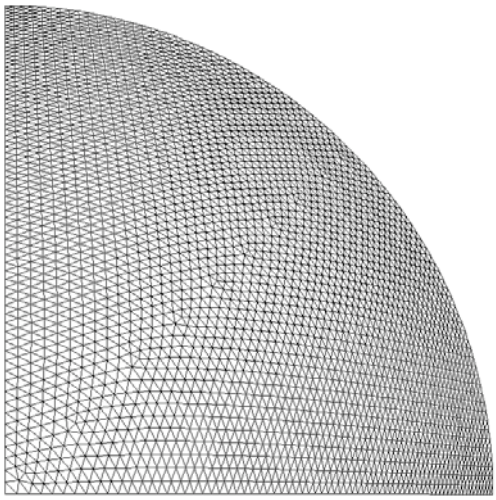

Figure 6-14 Initial cup drawing mesh

The number of integration points across the thickness is set to 5 to obtain a reasonable calculation time with an acceptable accuracy. The material is modelled with both the Vegter and the Hill'48 yield functions. The material parameters are the same as in the experiments with the bi-axial test equipment, see tables 5-10 to 5-15.

Figure 6-15 shows the final cup drawing mesh. First the earing profile is checked. This earing profile can be defined by observing the height (h) of the cup as a function of the angle (β), see figure 6-15. Subsequently the strain distributions on the thick lines in the figure are examined. The thick line in direction (l_0) coincides with the angle β=0° and the line in direction (l_{45}) coincides with the angle β=45°. The steel and aluminium simulations will be discussed separately.

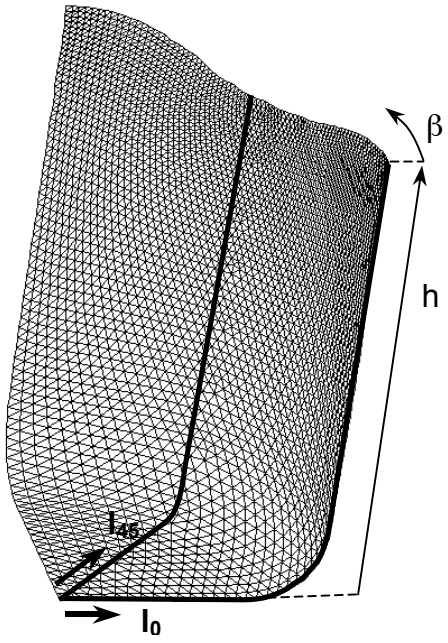

Figure 6-15 Final cup drawing mesh

6.2.1 Steel simulations

The earing profiles are given by figure 6-16. The earing profile of the Vegter function coincides better with the experimental data than the Hill'48 function. The Vegter function shows less variation in the height of the cup. This can be explained by the shape of the yield surfaces for different planar angles (figures 5-22 and 5-23). Though both yield functions have the same R-values, the Vegter yield surfaces differ less for different angles than the Hill'48 surfaces, which indicates less anisotropic material behaviour.

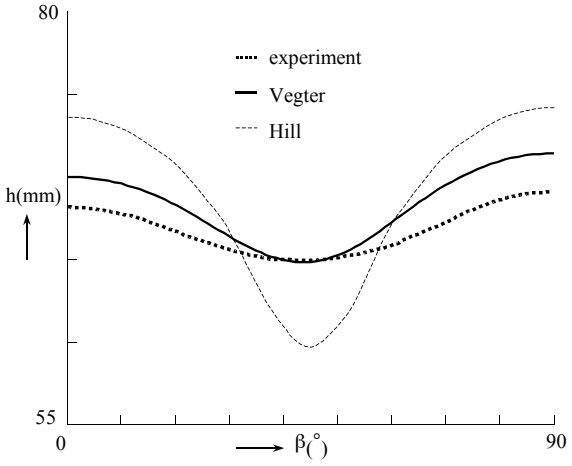

Figure 6-16 Height of the cup (h) as a function of the angle (β) for steel

Some care must be taken in the comparison of simulations with experiments. The experimental blank holder force is not known exactly because it is related to the hydraulic pressure, which is assumed constant. In reality the pressure can vary during the process. Due to the grid applied on the sheet, the friction between the tools and the die can have different values locally. This influences the results, which is illustrated in figures 6-17 and 6-18. Nevertheless the results of the Vegter yield function remain valid, considering that the blank holder force and the friction influence mainly the overall cup height and not the earing of the cup.

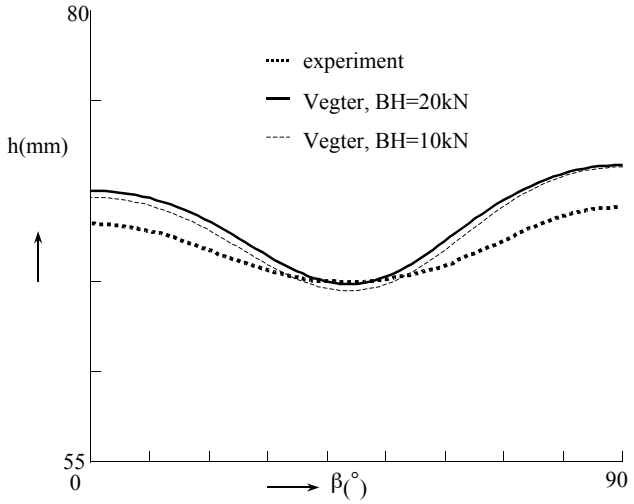

Figure 6-17 Height of the cup (h) for different blank holder forces (BH)

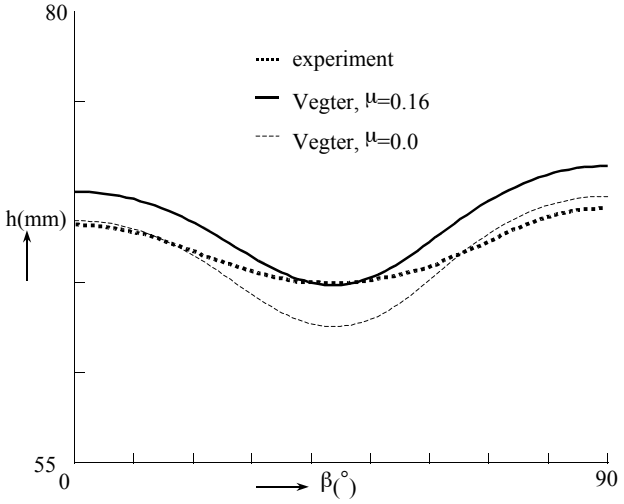

Figure 6-18 Height of the cup (h) for different friction coefficients (μ)

The first (=largest) principal strain as a function of the profile lengths (l_0) and (l_{45}) are given in figures 6-19 and 6-20. Also here the Vegter function provides a more realistic prediction of the strain distribution in the product. In the punch head area the Vegter and Hill functions show the same strain distribution. This is explained by the fact that the stress can be considered equi-bi-axial in this area. Because the equi-bi-axial yield stresses of the Vegter and Hill functions of steel are almost equal (figure 5-24), the strain distributions are also similar. In the cup wall area differences occur between the yield functions. In this area the material has drawn in from the flange into the cup wall. In the flange a shear deformation has occurred and in the cup wall a plane strain deformation. Only the yield locus around the plane strain yield stress differs between the two yield functions (figure 5-24), which explains the better performance of the Vegter function in this area.

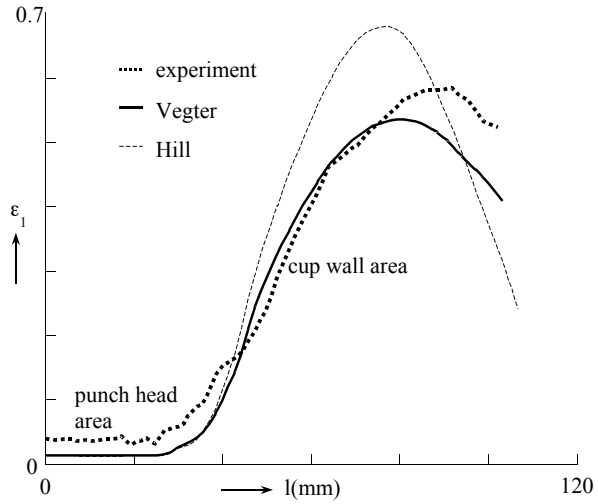

Figure 6-19 Principal strain (ε_1) as a function of the profile length (l_0), steel

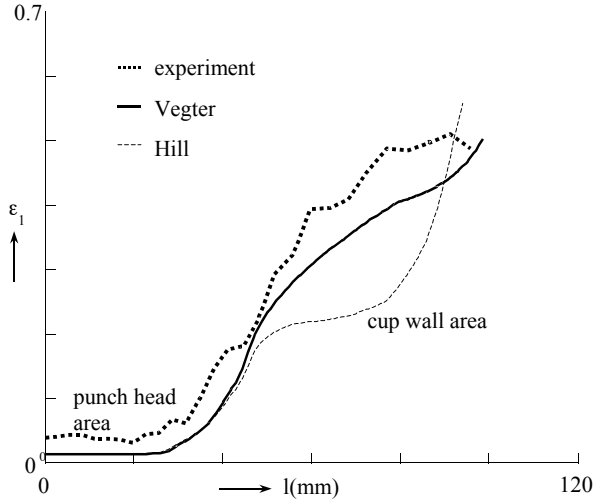

Figure 6-20 Principal strain (ε_1) as a function of the profile length (l_{45}), steel

6.2.2 Aluminium simulations

The earing profiles are given in figure 6-21. The earing profile of the Vegter function coincides better with the experimental data than the Hill'48 function, but the improvement is not as large as for steel. This can be explained by the shape of the yield surfaces. For aluminium both the Vegter and the Hill'48 yield surfaces vary only slightly for different planar angles (figures 5-25 and 5-26). This indicates a small anisotropic behaviour, which is reflected by the small earing profile for both functions. Nevertheless the Vegter function shows a small improvement.

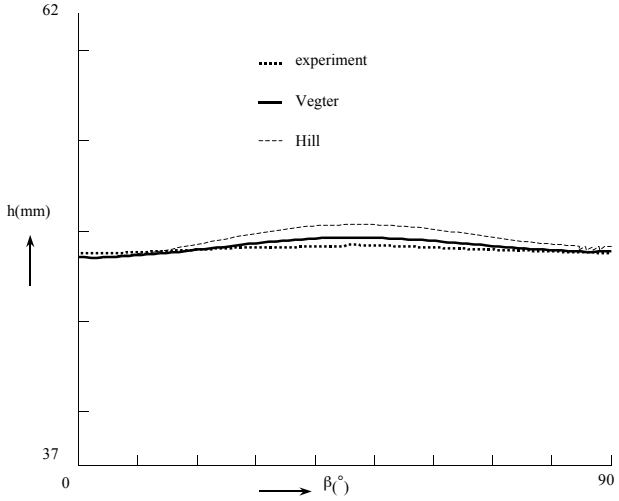

Figure 6-21 Height of the cup (h) as a function of the angle (β) for aluminium

The first principal strain as a function of the profile lengths (l_0) and (l_{45}) are given in figures 6-22 and 6-23. In the punch head area the Vegter prediction is more realistic, which can be attributed to the equi-bi-axial yield stress value. The equi-bi-axial yield stress for the Vegter function is larger than for the Hill function (figure 5-27), which results in a smaller deformation. In the cup wall area also differences occur between the yield functions, but here the differences are smaller than for steel. This is consistent with the fact that the plane strain yield stress difference is smaller for aluminium than for steel (figure 5-27).

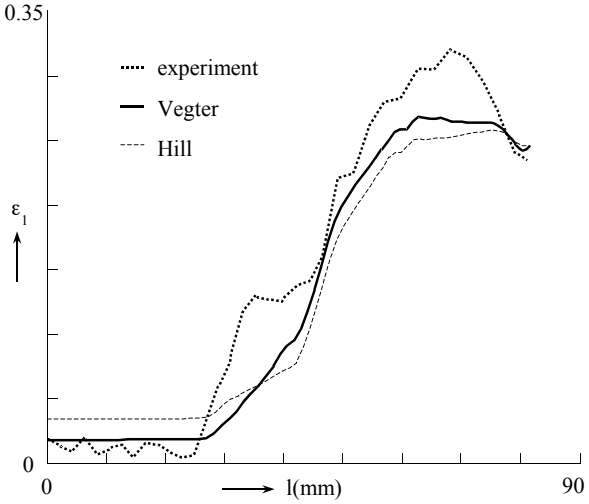

Figure 6-22 First principal strain (ε_1) as a function of the profile length (l_0)

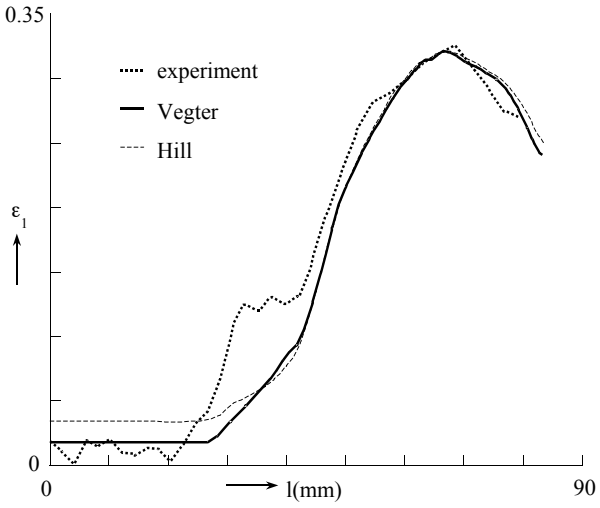

Figure 6-23 First principal strain (ε_1) as a function of the profile length (l_{45})

6.2.3 Conclusion

Due to the fact that the Vegter yield locus is based on bi-axial stress states, the yield surface shape differs significantly from the Hill yield surface although the R-values are the same, see figures 5-22 to 5-27. This results in more realistic results in the deep drawing of a cylindrical cup.

6.3 Deep drawing of a trapezium-shaped product

Experimental data on the deep drawing of a trapezium-shaped product is available from tests carried out at TNO (Kevie, 1999). The product has been developed to assess the formability of sheet metal. The test is simulated with the Vegter yield function at Corus RD&T. The material used is the same aluminium, of chapter 5 (table 5-13). The simulation was carried out with a constant planar angle in the stress remap procedure, because the procedure was not developed further at that time. It implies that anisotropic behaviour is not incorporated entirely correctly, but since the material is almost planar isotropic, the simulation is assumed to provide valuable information.

Several experiments and simulations with different process conditions (blank holder force, blank shape and punch displacement) were performed. It appears that the most striking results are obtained in a critical case, i.e. with process conditions such that the product can just be manufactured without failure of the material. In this case the punch displacement is stopped at the moment the sheet breaks up. The results of this critical case are discussed here.

Failure occurs when the strain distribution is above the forming limit curve (FLC) in the principal strain space (ε_1-ε_2). The Vegter yield function is validated on the Forming Limit Diagram (FLD) which shows the principal strain distribution together with the FLC. The results of the Hill'48 yield function are given for a comparison.

The experimental set-up of the drawing die is given in figure 6-24.

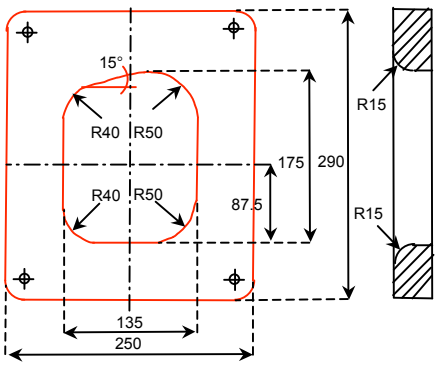

Figure 6-24 Geometrical set-up

The process parameters are given in table 6-2.

Process parameters	
blank holder force [kN]	5
friction coefficient	0.16
punch displacement [mm]	40.5

Table 6-2 Process parameters

The simulations are carried out with the model in figure 6-25, which shows the modelled tool and deformed mesh. The model consists of 1085 elements and represents the complete sheet. The number of integration points across the thickness is set to 5. In the deformed mesh the experimentally observed corner of the sheet is indicated by the thick line.

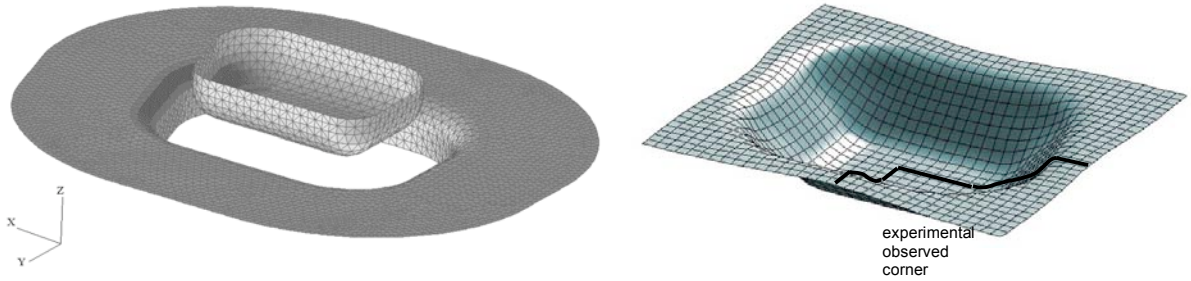

Figure 6-25 Simulation of trapezium-shaped product drawing

The strain distribution of the simulations and the experimental data of the accentuated corner are represented in figures 6-26 and 6-27. As can be observed the strain distributions are clearly different for the Hill'48 and the Vegter yield function. The strain distribution of the Vegter function is close to the FLC and compares better with the experimental data. The Hill function shows a strain distribution which tends more to the equi-bi-axial state. The different strain distributions can be explained by the yield surface shapes (figure 5-27). The equi-bi-axial stress of the Hill function is smaller than the value of the Vegter function. Therefore the simulation with the Hill function will show more deformation at the bottom of the product, where the stress state tends towards equi-bi-axial. The Vegter function will show more deformation in the wall, where the stress tends to the plane strain state. As a consequence the Vegter function predicts a critical product and the Hill function a non-critical product.

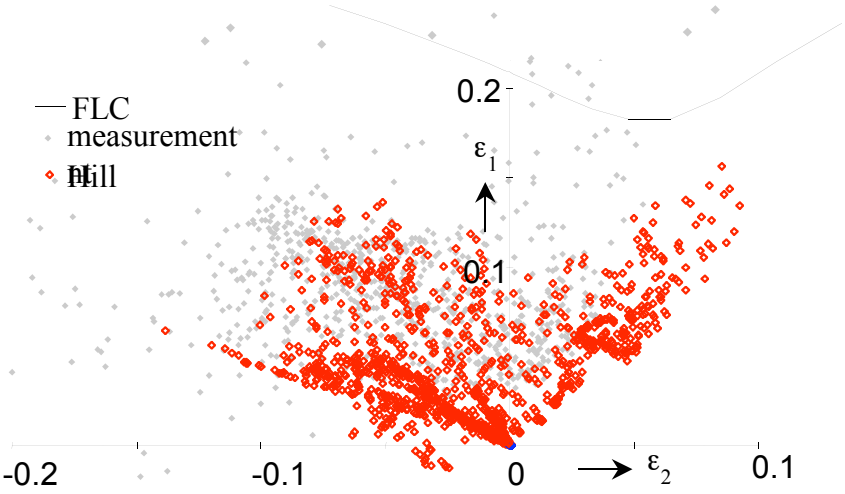

Figure 6-26 Experimental and Hill simulated FLD compared with FLC

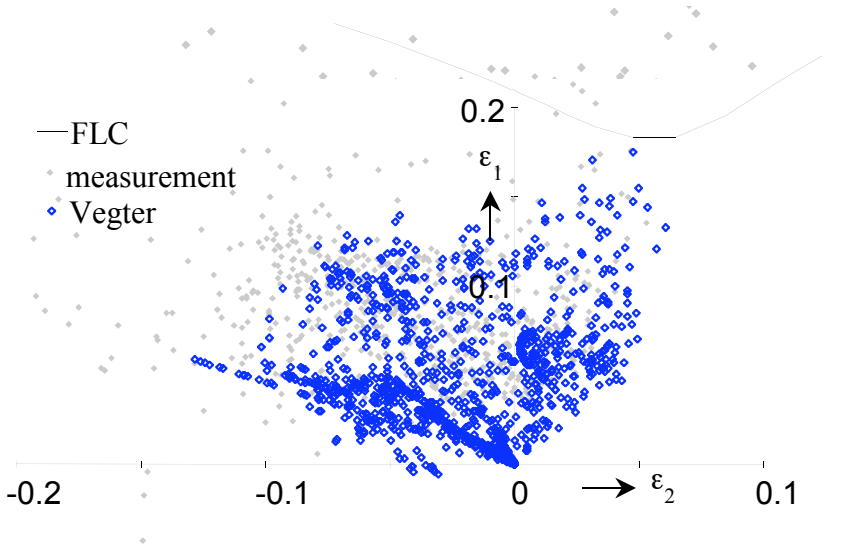

Figure 6-27 Experimental and Vegter simulated FLD compared with FLC

Nevertheless the experimental strain distribution is above the FLC, whereas the strain distribution of the Vegter yield function is below the FLC. This is explained as follows. In the experiment the exact punch displacement at failure is difficult to determine, so it is possible that the punch is stopped just before or just after the sheet breaks up. In the considered case the strain distribution is above the FLC, hence it can be assumed that the punch is stopped after failure. The influence of the extra punch displacement after failure is investigated by a simulation. The simulation is carried out with the Vegter and the Hill yield functions with a punch displacement of 45.5 mm.

Figure 6-28 shows the strain distribution of the simulations. The strain distribution of the Hill yield function is still below the FLC and consequently a non-critical product is predicted. The strain distribution of the Vegter yield function is clearly above the FLC now, which indicates that the product has broken up.

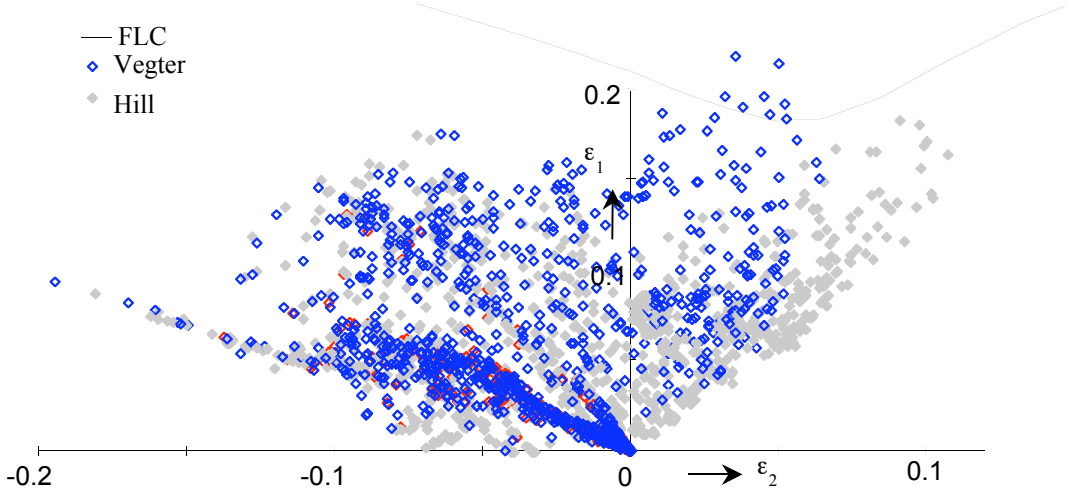

Figure 6-28 Vegter and Hill simulated FLD at 45.5 mm punch displacement

It must be noted that, similar to the cup drawing simulations, the results can vary due to variable process conditions. For instance the friction and the blank holder are not known exactly from the experiments. The friction is increased by the grid that has been applied to the sheet. The blank holder force is derived from the imposed hydraulic pressure, but can vary during the process.

6.3.1 Conclusion

In the trapezium-shaped product the plane strain and equi-bi-axial yield stress play an important role in the strain distribution under critical conditions. Because the Vegter yield surface is more accurate in the plane strain and equi-bi-axial regions, it provides a better prediction of the strain distribution.

7 Applications

The material model is applied in 2 simulations of complicated deep draw products. The first application is the deep drawing of a Volvo pedal box. The second application is the deep drawing of an Audi front panel, which was a benchmark at the Numisheet'99 conference.

7.1 Deep drawing of the Volvo pedal box

The deep drawing of the Volvo pedal box is carried out in cooperation with Corus RD&T. Simulations are performed at the University of Twente and experiments are carried out at Corus RD&T. From chapter 6 it appears that the influence of different material models becomes mainly clear in critical cases. In these cases the process conditions are chosen in such a way that the product can just be manufactured without failure of the material. Corus already acquired some experience on deep drawing the pedal box with zinc coated steel. It was expected that critical cases could be obtained with steel (AKS) and aluminium (AA 5182) after some minor modifications on the process conditions.

Initially simulations were carried out to determine the critical process conditions. The blank shape and blank holder force were tuned until a product without defects was simulated with a strain distribution just below the FLC. Subsequently experiments were performed with the same process conditions as in the simulations. It appeared that at one side the material failed and at the other side severe wrinkling occurred, so the simulations deviated a lot from the experiments. A closer look at the tool geometry revealed that an important part of the punch and die was not modeled, so this was probably the reason for the bad prediction of the simulations. Thanks to the large experience at Corus RD&T, the process conditions were easily adjusted by trial and error to obtain a satisfying product which was just critical.

Corus supplied new geometrical data of the punch and the die and subsequently simulations were carried out with the new tool data. The results of these simulations are compared with experiments.

The experimental set-up is given by figure 7-1. The upper part represents the side and front dimensions of the die and the lower part the top dimensions.

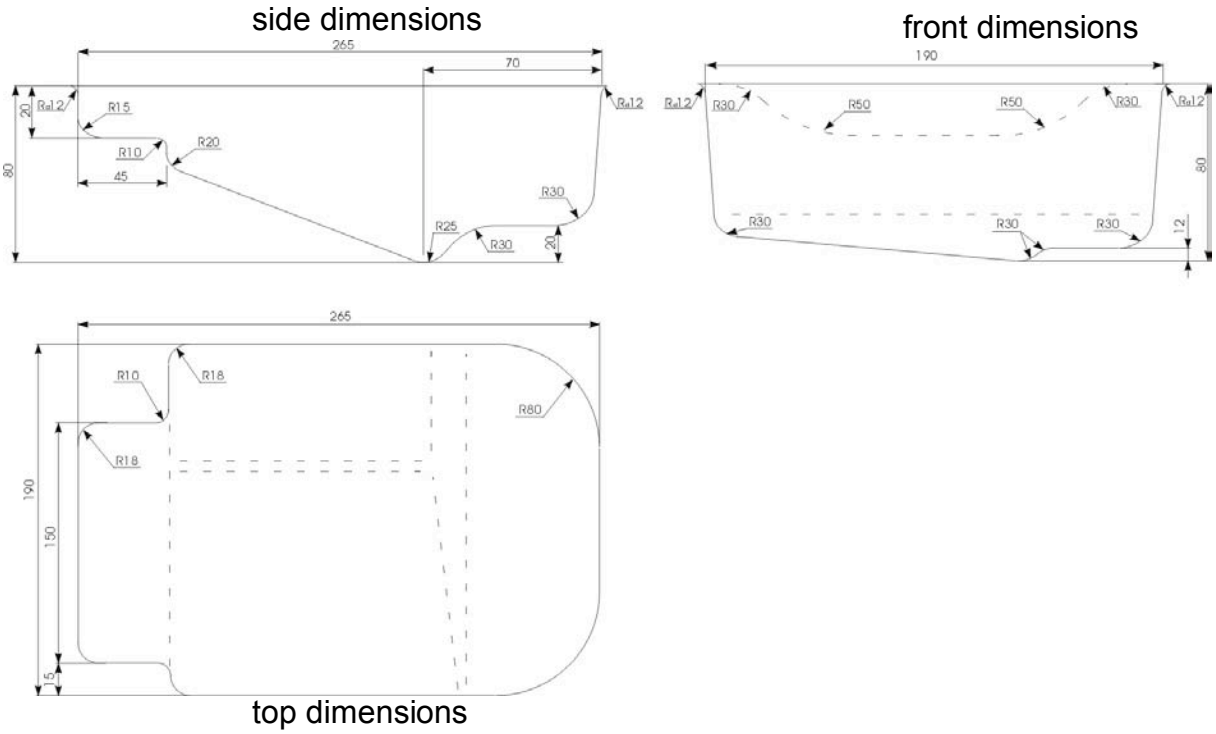

Figure 7-1 experimental set-up

A critical pedal box is realized by changing the blank shape, altering the friction between the tools and the sheet and varying the blank holder force by trial and error. On the outer side of the sheet a 2.5 mm grid is etched on half of the front side of the blank. After deep drawing this grid is measured by a 3D-measurement device Phast (Corus RD&T 2001), to obtain the strain distribution of this part of the product. To protect the grid during contact between the tools and the sheet, plastic foil is layed over the sheet. It is estimated that the friction coefficient of the foil equals 0.05, so on the outer side the friction is fixed to this value. The friction on the inner side of the sheet can be controlled by applying a lubricant or applying a foil.

The critical process conditions for steel and aluminium sheet are given by figure 7-2 and 7-3. The adaptations from the initial zinc coated blank shape are represented by the thick black lines. To obtain a critical steel product, the blank is elongated at the front side and trimmed at the back side. The oblique side at the back is shifted 4 mm towards the middle and two triangular (shaded) parts are cut of. A foil is used on the outer side and lubrication on the inner side. In order to obtain a critical aluminium product, the blank needs less adaptations compared to the initial shape. Only 4 mm shift of the oblique side and cutting of the shaded parts are necessary. In this case on both sides a plastic foil is applied.

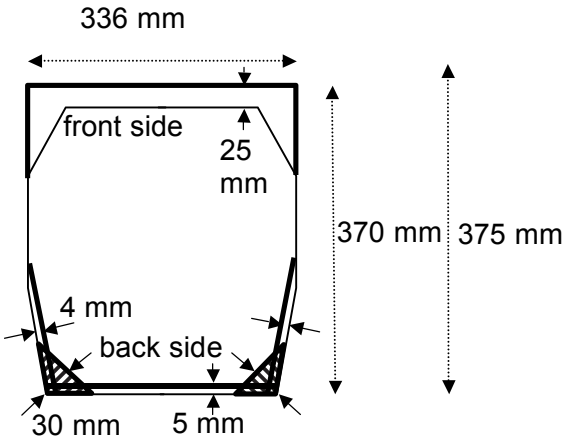

Blankholder force

400kN

Friction conditions

Outer side: foil (μ=0.05)
Inner side : lubrication (μ=0.16)

Figure 7-2 Critical pedal box process conditions and steel blank geometry

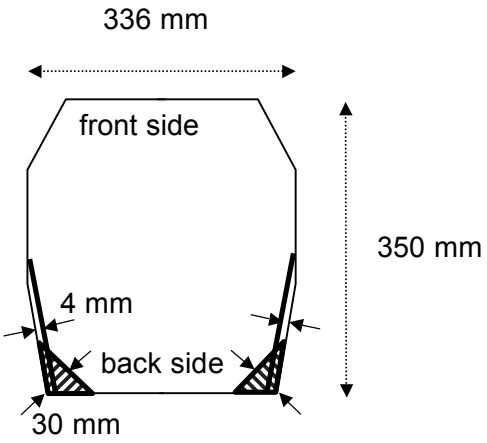

Blankholder force

325kN

Friction conditions

Outer side: foil (μ=0.05)
Inner side : foil (μ=0.05)

Figure 7-3 Critical pedal box process conditions and aluminium blank

It is worth noticing that the tools have been used in the actual production process and wear due to the use in production can be observed. For instance, when one touches the tools by hand, it can be felt clearly that the initial blank edges have been pressed in the tools. So the die and blank holder are not completely flat and consequently the process conditions are not defined exactly. For instance, when the blank shape is changed and the blank reaches beyond the initial edges, the blank holder force will not be uniform. So the experimental data must be interpreted with care.

The simulation set-up is shown in figure 7-4. The die is constructed from the 3D measurement of the outer side of a deep drawn product, represented by the black surface in figure 7-4. The fine mesh of this surface represents the measured product and the course regular mesh is added to obtain a complete die. Hence the die does not represent reality completely but it can be considered a good approximation. The punch is constructed by an offset of 1.2 mm normal to the die surface, represented by the green surface. The red surface represents the blank holder.

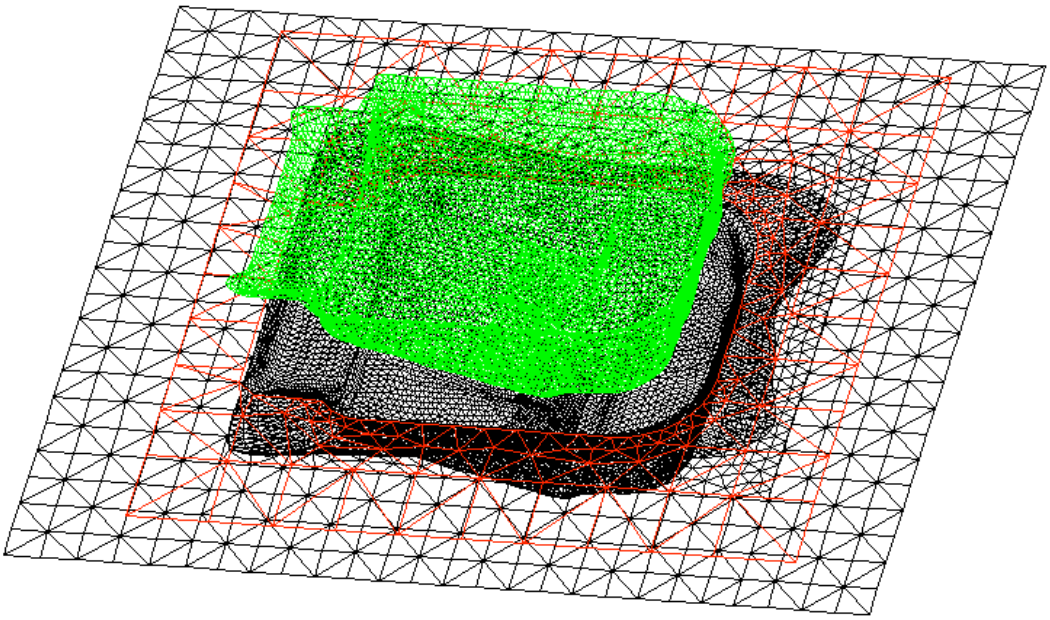

Figure 7-4 Simulation set-up

The simulations are carried out with a refinement procedure (Meinders, 2000). A sheet element is refined when a thickness error or a geometrical error is reached. The thickness error is calculated by the ratio of the actual integration point thickness in the considered element and the average thickness of surrounding elements. The geometrical error is determined by the angle between the considered element and the surrounding elements. In combination with elasto-plastic material numerical problems occurred when an element was refined more than 1 time, so only 1 element refinement is allowed. The results are discussed separately for steel and aluminium.

7.1.1 Steel simulations

The simulated product shape with the first principal strain distribution is given in figure 7-5. Compared to figure 7-4, the product geometry is shown upside down in order to show the spot with the largest strain.

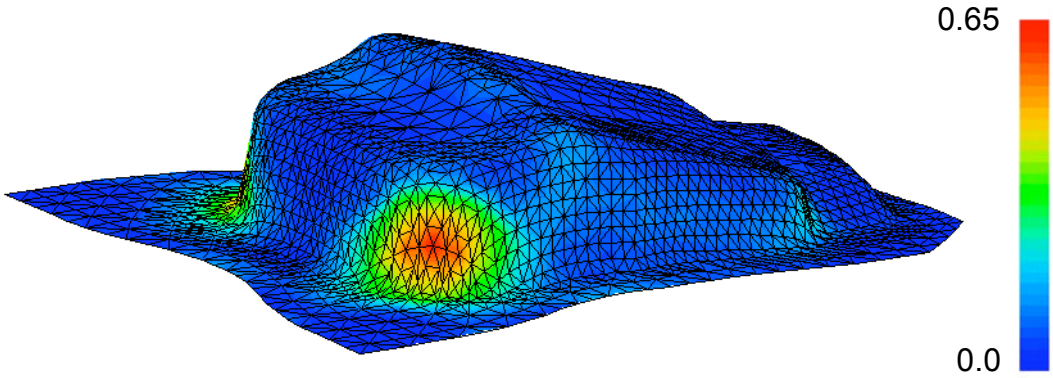

Figure 7-5 Simulated deformation with first principal strain distribution (steel)

The first and second principal strains are given by the FLD in figure 7-7. It can be observed that the strain distribution is very close to the FLC, which indicates a critical product. The strains closest to the FLC tend towards pure shear, but the maximum first principal strain (≈0.6) is slightly larger than the maximum absolute value of the second principal strain (≈0.4). This corresponds to the strain distribution of figure 7-5. The spot with the maximum first principal strain is situated in the wall of the pedal box. Here most of the deformation has taken place in the blank holder region (shear deformation) and a small amount of deformation in the wall (plane strain deformation).

The experimental first principal strain distribution of the corner is given in figure 7-6. The FLD of this part is given in figure 7-8. The experimental strain distribution deviates from the simulated strain distribution. The maximum first principal strain of the experiment is about 0.25 larger and the minimum second principal strain is 0.25 less so the difference can be considered an extra shear deformation. This can be explained by the fact that the experiment is just over critical. The exact process settings at failure of the material are difficult to determine. This is inherent to the tools, which are not perfect due to wear during the production process. Furthermore the friction is influenced locally by the foil, which breaks up at certain places. So the process conditions can deviate from the intended settings and the deformation can reach the FLC earlier than expected. When the material is deformed further after reaching the FLC, shear bands show up which effectuate an extra shear deformation. In fact these shear bands are observed by the human eye with some effort by looking from a certain angle at the corner of the product.

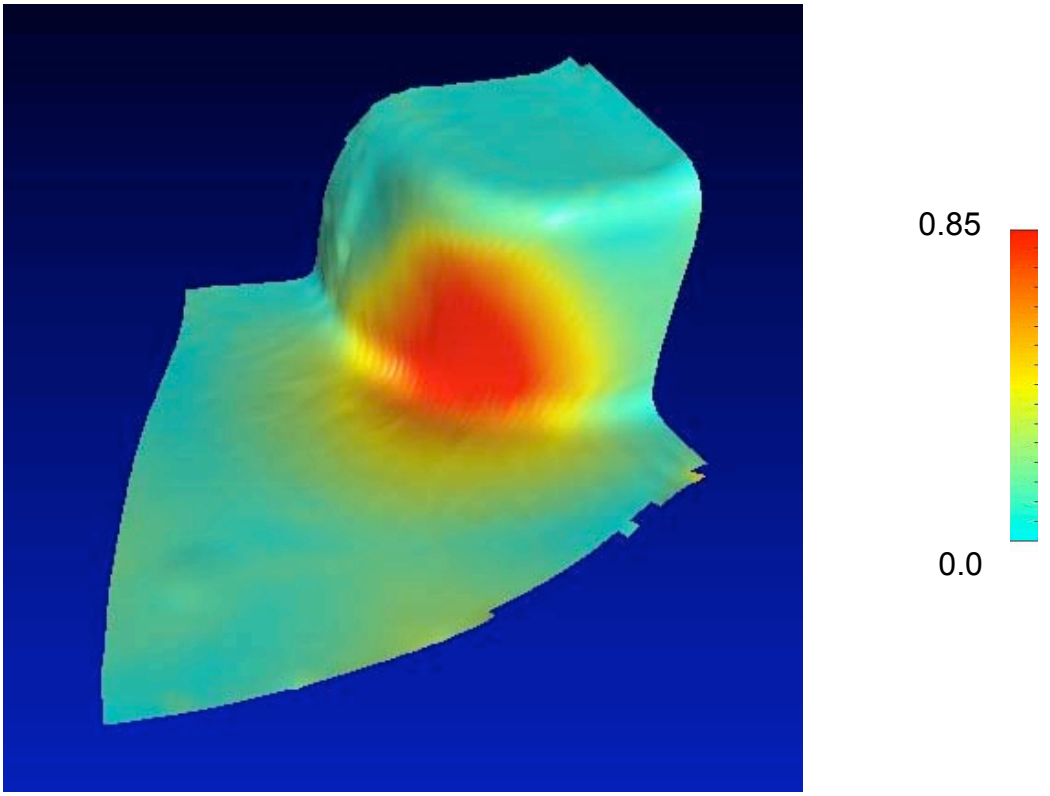

Figure 7-6 Corner with experimental first principal strain distribution (steel)

From the trapezium shaped validation case (section 6.3) it is known that an over critical situation can be simulated by adjusting the process conditions in the simulation slightly. In that case the used finite element code does not predict the shear bands, but shows a larger plane strain deformation in the wall. So the strain distribution still differs from the experimental distribution and consequently this distribution is not shown.

The simulation is also carried out with the Hill yield function. The strain distribution of this simulation is shown in figure 7-9. It appears that the Hill strain distribution is less critical than the distribution of the Vegter function but still the Hill function predicts a critical product fairly well. This indicates that the shape of the product is not influenced much by the material model but mainly geometrically determined.

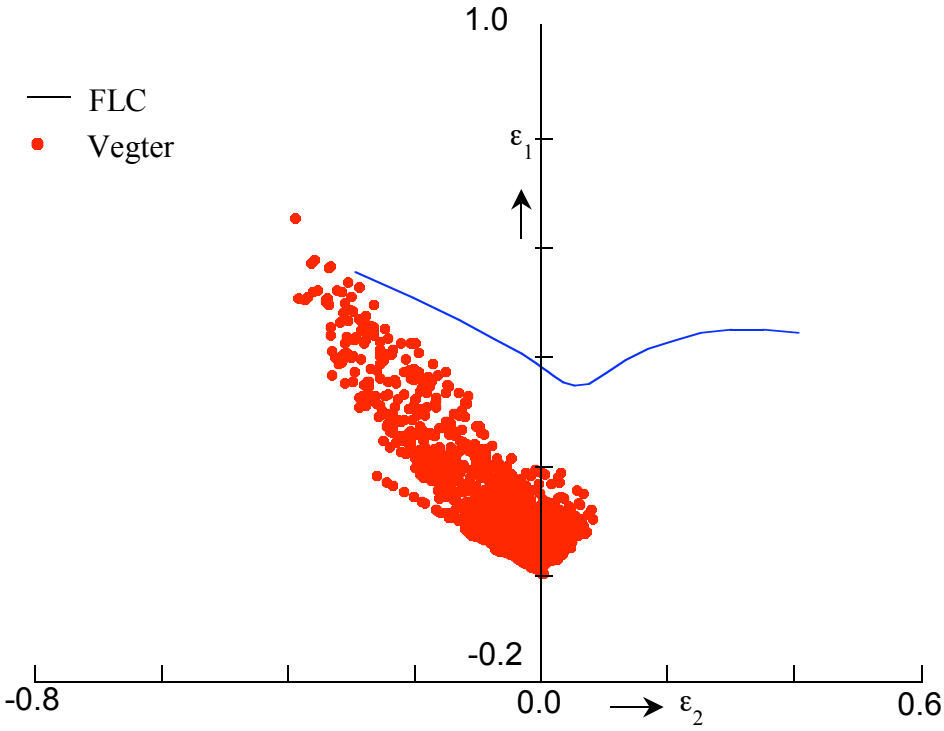

Figure 7-7 Vegter simulated FLD compared with FLC (steel)

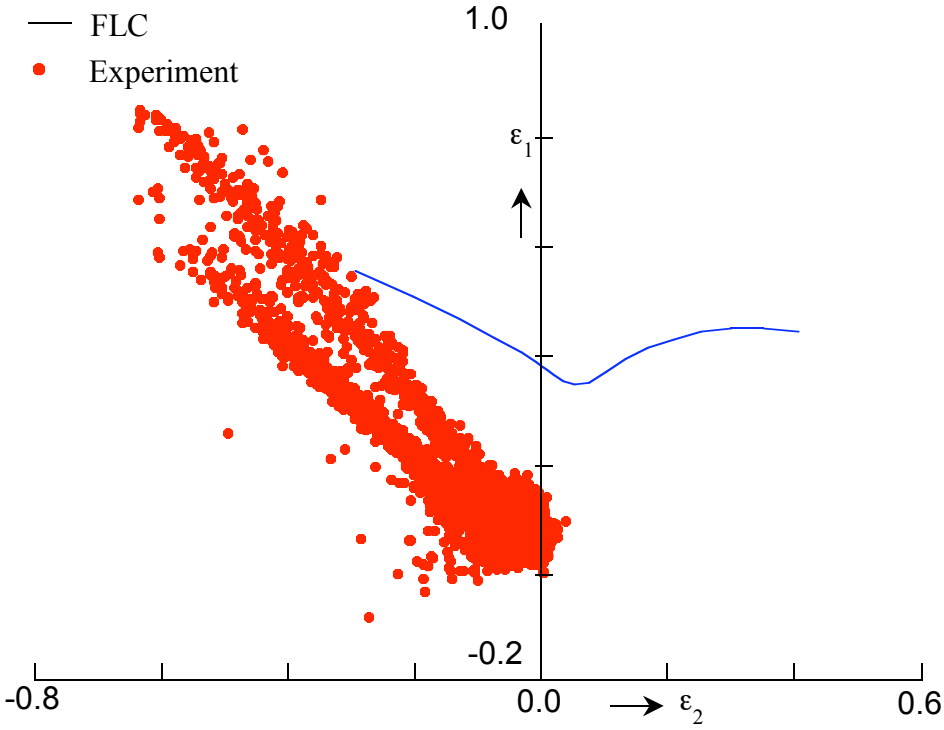

Figure 7-8 Experimental FLD compared with FLC (steel)

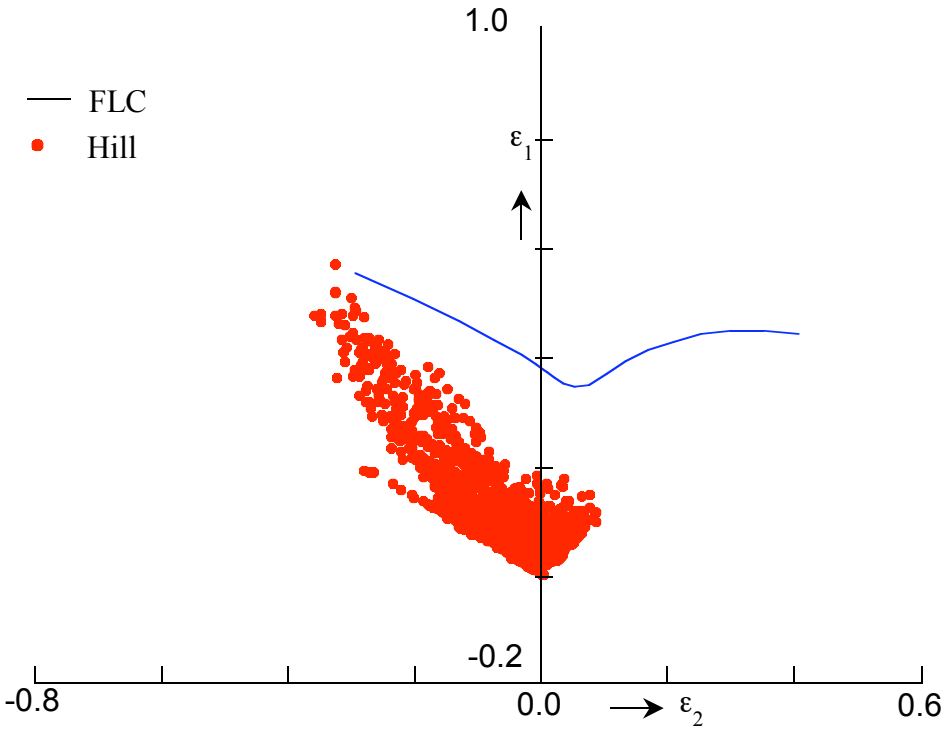

Figure 7-9 Hill simulated FLD compared with FLC (steel)

7.1.2 Aluminium simulations

The simulated product shape with the first principal strain distribution is given in figure 7-10.

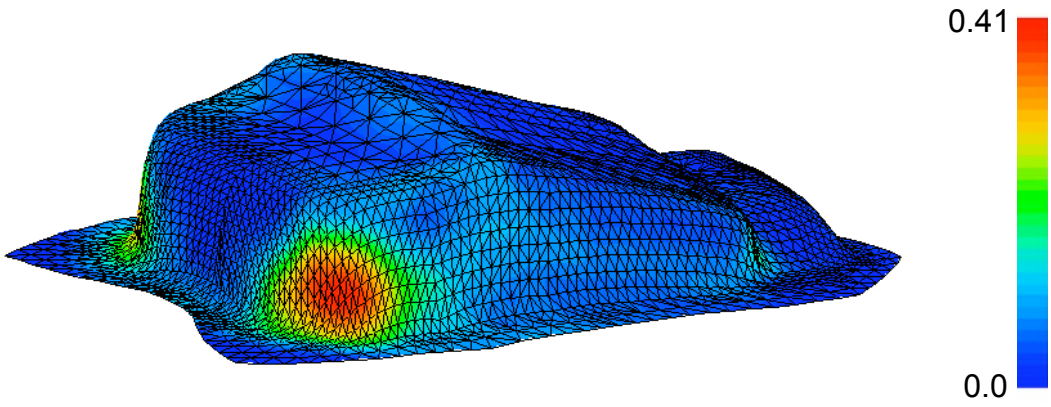

Figure 7-10 Simulated deformation with first principal strain distribution (aluminium)

The first and second principal strains are given by the FLD in figure 7-12. This strain distribution is very close to the FLC, which indicates a critical product. The strains closest to the FLC are almost pure shear. The maximum first principal strain (≈0.4) can be considered equal to the maximum absolute value of the second principal strain (≈0.4). This corresponds to the strain distribution of figure 7-10. The spot with the maximum first principal strain is situated just in the wall of the pedal box corner. Here almost all of the deformation has taken place in the blank holder region (shear deformation) and very little deformation in the wall (plane strain deformation). When the blank shape is compared with the steel blank, it is evident that the material deforms relatively more in shear. The blank has less material under the blank holder compared to the steel blank. As a consequence the material will deform easier under the blank holder.

The experimental first principal strain distribution of the corner of the product is given in figure 7-11. The FLD of this part is given in figure 7-13.

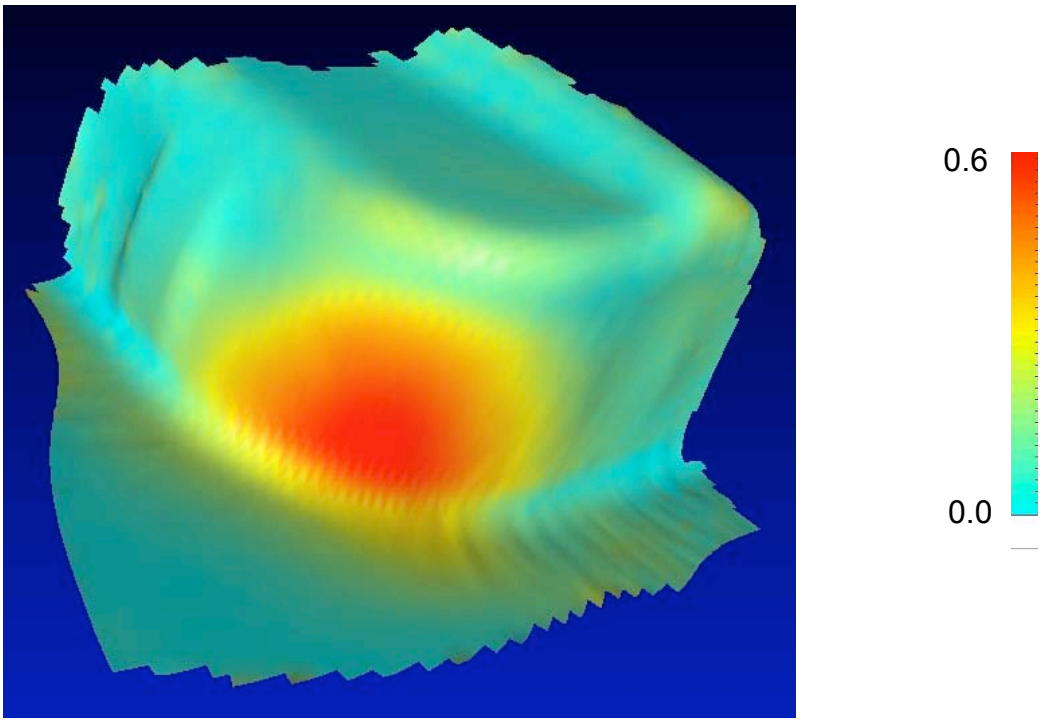

Figure 7-11 Corner with experimental first principal strain distribution (aluminium)

The experimental strain distribution deviates from the simulated strain distribution. The maximum first principal strain is about 0.20 larger and the minimum second principal strain is 0.10 smaller. Also the strains in the plane strain region are larger than in the simulation. So in this case no extra shear deformation due to shear bands is measured, compared to the simulated results. In fact these shear bands can not be observed, because some wrinkles occur in the area with the largest strains. These wrinkles are recorded with a photo-camera at the inner side of the pedal box, see figure 7-14. Also under the blank holder wrinkles are observed. The wrinkles can have a significant influence on the deformation distribution in the product. Locally the blank holder pressure will be larger, which effectuates a larger plane strain deformation in the wall and more critical strains than predicted by the simulations. When the wrinkles are smaller than the grid distance, the wrinkles can also distort the Phast measurements, which can be an additional reason that no extra shear deformation is observed in the strain distribution compared to the simulations.

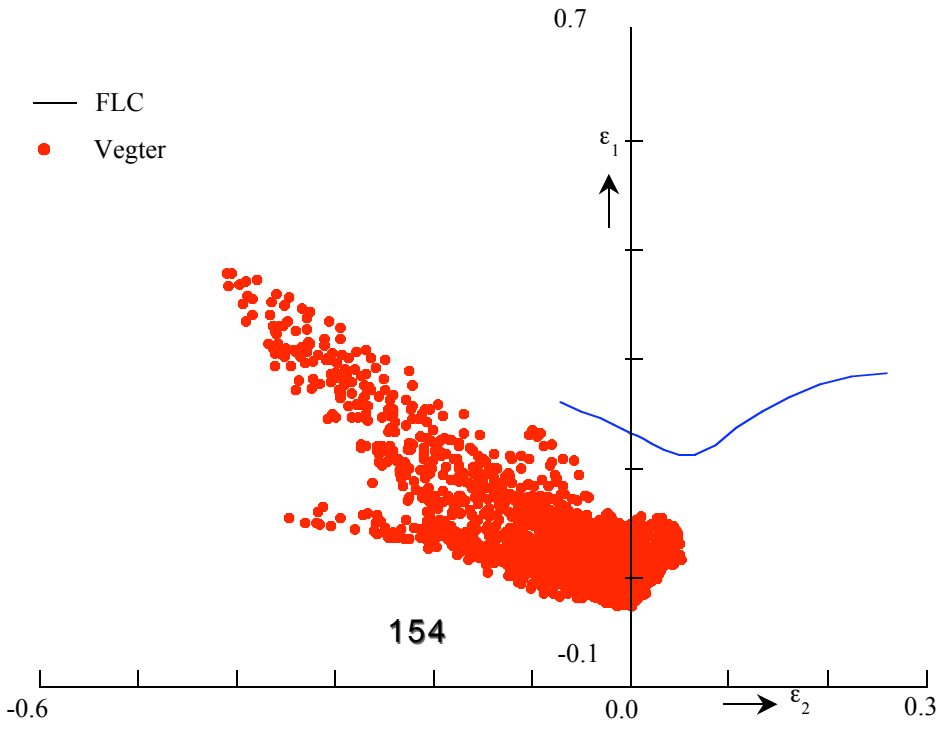

Figure 7-12 Vegter simulated FLD compared with FLC (aluminium)

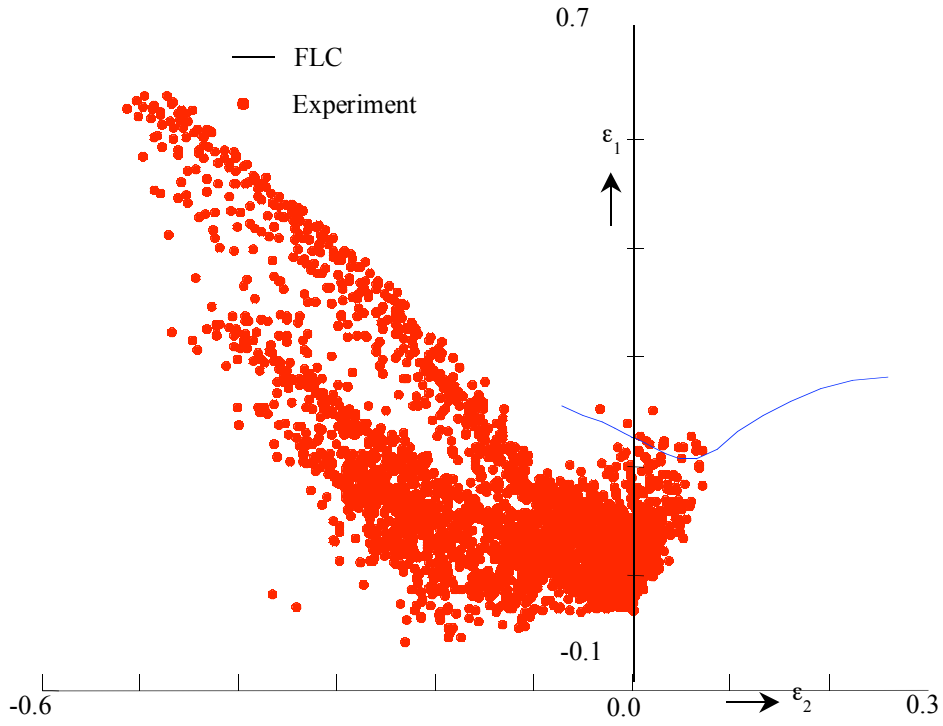

Figure 7-13 Experimental FLD compared with FLC (aluminium)

Because only one element refinement was allowed in the finite element model, the wrinkles are not observed in the simulation. One extra simulation with more refinements reveals that the geometry can be described better. The deformed geometry of this simulation is illustrated in figure 7-15 together with the first principal curvature. The result is shown with the inner side upward to show the wrinkles in the sheet. A visual comparison with the experiments reveals that the wrinkles in the sheet are described fairly accurate and that also in the corner wrinkles occur.

Figure 7-14 Wrinkles in the aluminium pedal box

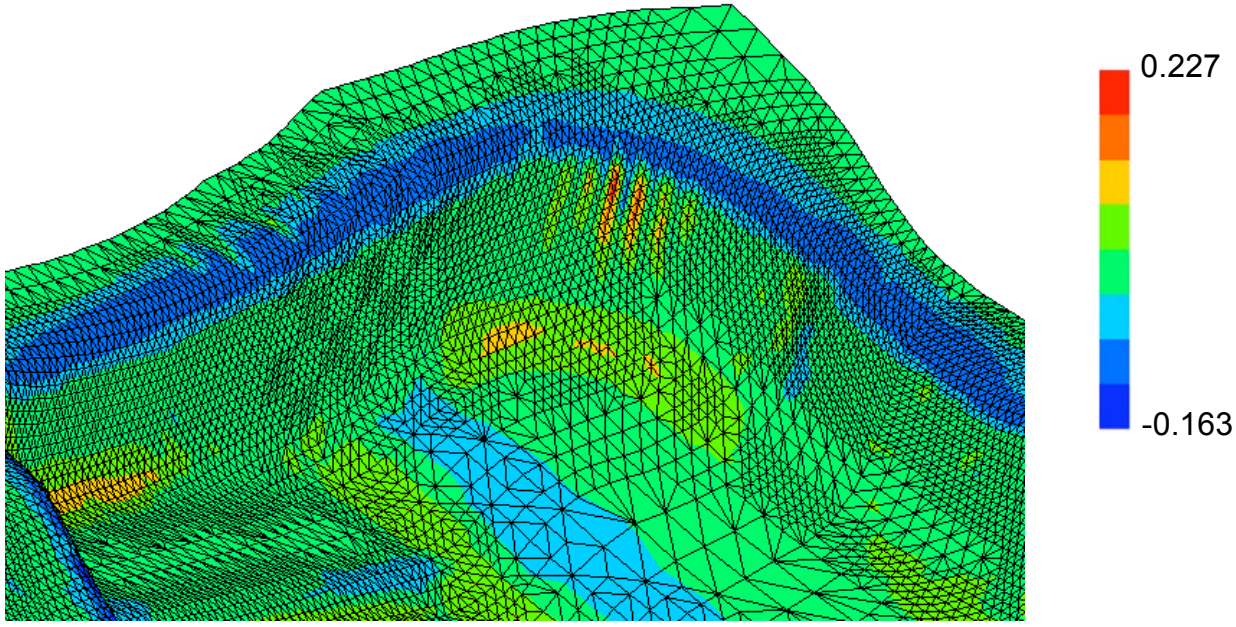

Figure 7-15 Deformed aluminium sheet with first principal curvature

7.1.3 Conclusions

The simulations predict a critical product at the same process conditions as in the experiment. However, the simulated strain distribution deviates from the experimental distribution for both steel and aluminium. Due to not perfect tools the process conditions are not defined well and consequently the product is over critical in the experiments. When steel is used as blank material, the deviating strain distribution can be explained by the occurrence of shear bands. When aluminium is used, wrinkles are observed in the wall and the blank holder region, which are not found in the simulations. These wrinkles cause more critical strains than predicted by the simulations.

7.2 Deep drawing of the Audi front door panel

The forming process of the Audi front door panel was a benchmark at the Numisheet '99 conference (Numisheet, 1999). The complete forming process of the panel includes deep drawing, cutting, flanging and spring back. This section focuses on the deep drawing part. This part is simulated with the finite element program Dieka, developed at the University of Twente. The deep drawing part of Dieka is mainly used as development code in cooperative projects with Corus RD&T.

The tool geometry is illustrated in figures 7-17 to 7-20. Draw beads are used to control the material flow under the blank holder. The simulation set-up is shown in figure 7-21. Significant differences with the pedal box simulation are the draw beads and the curved blank holder. The blank holder gives numerical instabilities when it is closed, illustrated by figure 7-16. At initial contact the blank holder generates a force on the sheet in vertical direction (FY) and horizontal direction (FX). The vertical force is resisted by the forces (FY*) and (FY**) of the die. The horizontal force is not resisted initially and results in a translation of the sheet out of the die region. In reality also this force exists, but the mass of the sheet restricts it from moving. Meinders (Meinders, 2001) has incorporated mass terms in Dieka, which appear to be stabilizing.

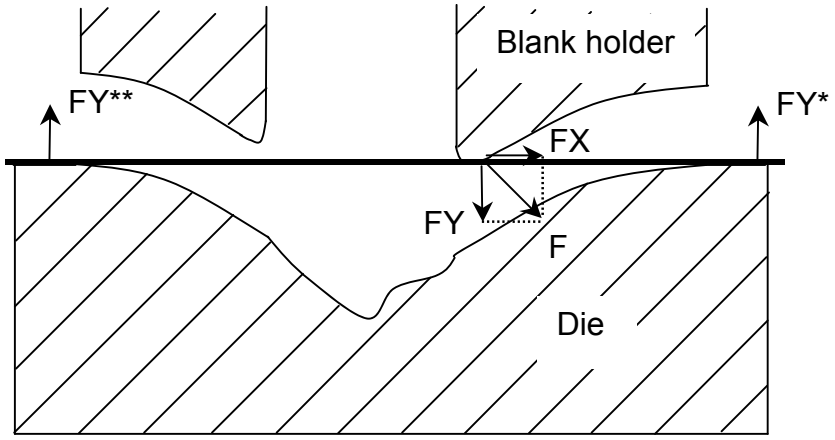

Figure 7-16 Horizontal force on the sheet at initial contact of the blank holder

The focus was at running a stabilized simulation with mass terms in combination with the new material model. Therefore the draw beads are left out and the blank shape is chosen simple. So the results can not be interpreted quantitatively but should be considered an illustration of the performance of Dieka at this moment. An extensive explanation of the simulations with the incorporation of refinement procedure and mass terms is given in (Meinders, 2001).

The simulated product shape with the thickness distribution is illustrated in figure 7-22. The required computation time for the simulation with the Vegter yield function equals 8 hours and 53 minutes on a HPJ5600 system. The simulation with the Hill yield function requires 10 hours and 25 minutes. So, although the Vegter function is a more advanced yield function, it requires less compution time. This indicates an efficient implementation in the finite element code Dieka.

7.3 Conclusions

The new material model is used in a deep draw simulation of a realistic automotive product. Compared to the Hill yield function, the Vegter yield function needs less calculation time, which indicates an efficient implementation. It can be concluded that the new material model can be used conveniently in real deep draw simulations.

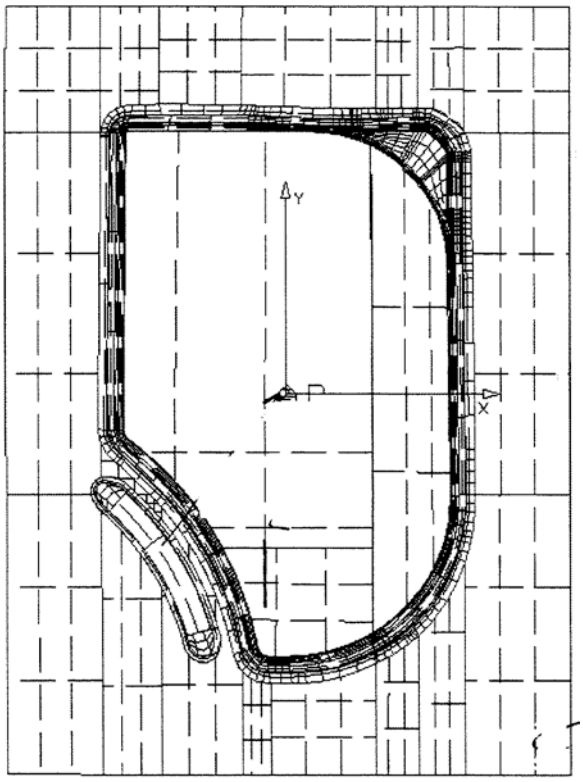

Figure 7-17 Die geometry

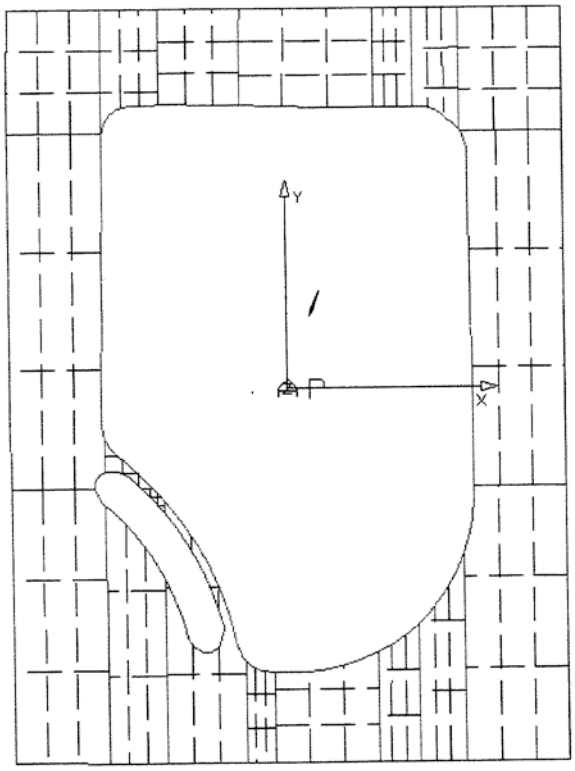

Figure 7-18 Blank holder geometry

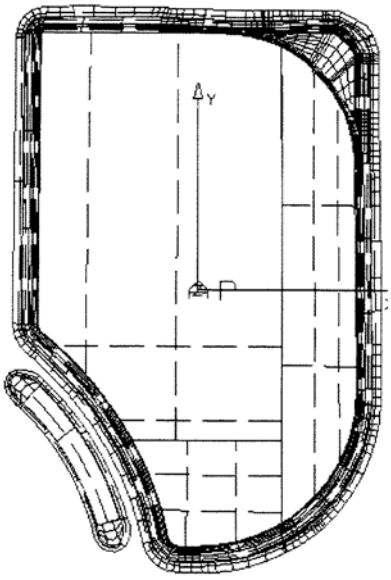

Figure 7-19 Punch geometry

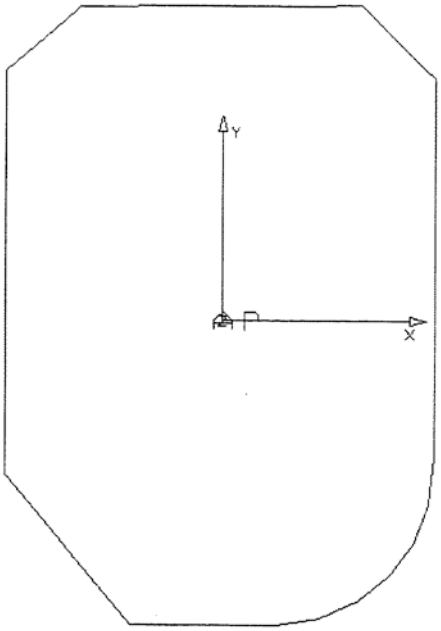

Figure 7-20 Initial blank

Audi benchmark (Numisheet 1999)

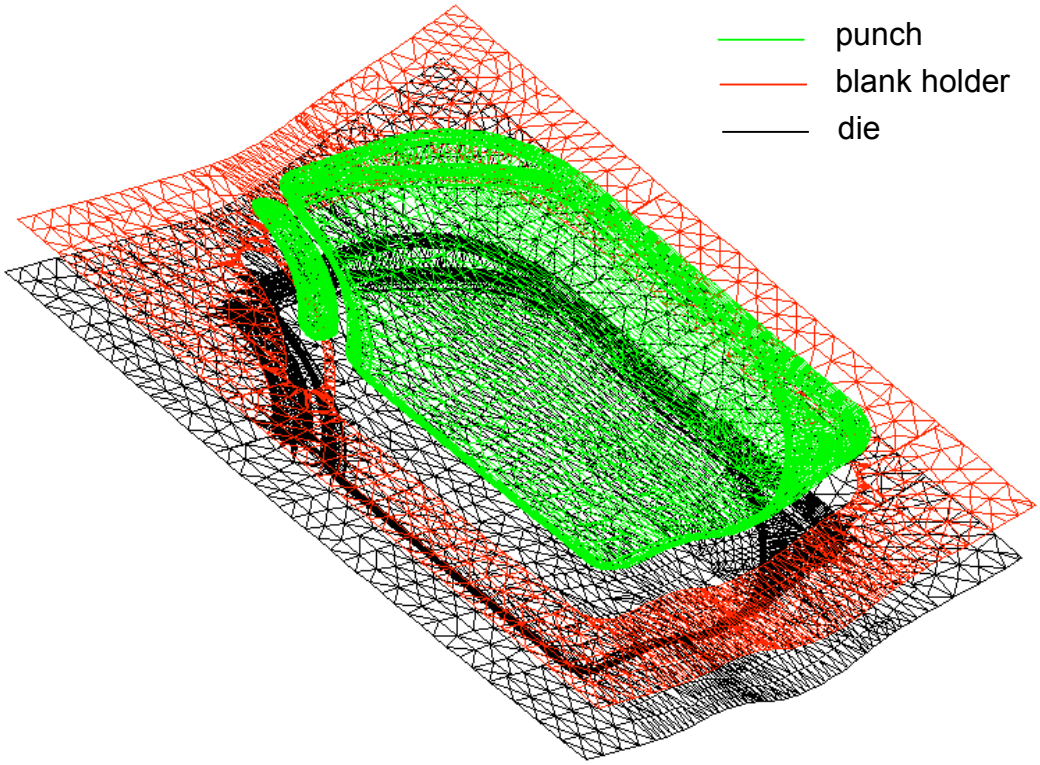

Figure 7-21 Simulation set-up

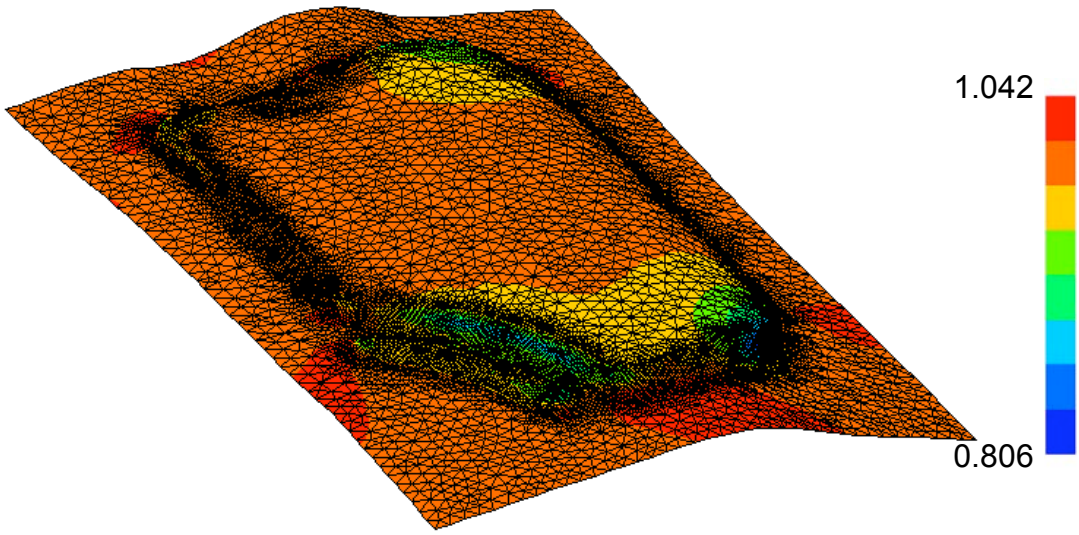

Figure 7-22 Deformed product shape with thickness distribution

Conclusions and recommendations

The Vegter yield function is implemented properly in a finite element code. The stress update procedure turns out difficult due to the definition in principal stresses, but a special numerical Euler backward scheme solves the difficulties. Also the possibility of defining the Vegter yield function directly in general stresses is investigated but further research is necessary to reveal the viability of this definition. The current yield function assumes 4 earing behaviour in deep drawing a cylindrical product, it should be extended to incorporate multiple earing behaviour. In deep draw validation cases the Vegter function provides significant better results than common anisotropic yield criteria. It can be applied conveniently to simulate the forming process of complex deep draw products.

The yield function is extended with two hardening models, a physically based isotropic hardening model and an anisotropic hardening model. The models are validated by cyclic and non-proportional experiments. A cyclic deformation pattern can be simulated properly but the material behaviour in a non-proportional deformation path is not simulated in a realistic way yet, hence more research is needed in this area.

A bi-axial test equipment is developed to obtain the data for the new material description. The test equipment is able to investigate a large variety of stress and deformation states. The current set-up is considered a prototype and can be improved with respect to steering and control of the (tensile) deformation and the optical strain measurement at large deformations. The horizontal movement of the equipment is performed with a Galil drive unit and the vertical movement is performed with a Zwick tensile tester. The horizontal movement is much more accurate (table 5-1) than the vertical movement, hence it is recommended that the Zwick equipment is also replaced by a Galil drive unit. The accuracy of the strain measurements is investigated roughly by the definition of a spread in the data and needs also a more thorough approach. The equipment uses a deformation analysis system which is based on the recognition of objects on the sheet metal. These objects exist of elastic sylicon kit and are placed on the sheet metal by hand. A more uniform and less time consuming method is preferred.

In the scope of this research the equipment is used to determine the plane strain and shear reference points of the Vegter yield function and the anisotropic hardening parameter. The equipment can be used appropriately for these purposes.

Appendix A Normal on the yield surface

This appendix elaborates the normal on the yield surface in the principal stress space σ_1-σ_2. This means that the derivative of the yield function to principal stresses is determined, which can be written as the derivative of the equivalent stress to the principal stresses:

$$\frac{\partial \phi}{\partial \sigma_1} = \frac{\partial \left(\sigma_{eq}(\sigma_1, \sigma_2, \theta) - \sigma_y \right)}{\partial \sigma_1} = \frac{\partial \sigma_{eq}(\sigma_1, \sigma_2, \theta)}{\partial \sigma_1}$$
$$\frac{\partial \phi}{\partial \sigma_2} = \frac{\partial \left(\sigma_{eq}(\sigma_1, \sigma_2, \theta) - \sigma_y \right)}{\partial \sigma_2} = \frac{\partial \sigma_{eq}(\sigma_1, \sigma_2, \theta)}{\partial \sigma_2} \qquad (1)$$

The change of the planar angle is handled separately (appendix C). In (1) the planar angle θ is considered constant, so the derivatives with respect to this angle are zero.

The starting point for the normal is equation (3.14):

$$\sigma_{eq} = \frac{\sigma_1}{f1(\mu, \theta)}$$
$$\sigma_{eq} = \frac{\sigma_2}{f2(\mu, \theta)} \qquad (2)$$

with

$$f1(\mu, \theta) = \frac{\sigma_{10}(\theta) + 2\mu \cdot \left(\sigma_{11}(\theta) - \sigma_{10}(\theta) \right) + \mu^2 \cdot \left(\sigma_{12}(\theta) + \sigma_{10}(\theta) - 2\sigma_{11}(\theta) \right)}{\sigma_y}$$
$$f2(\mu, \theta) = \frac{\sigma_{20}(\theta) + 2\mu \cdot \left(\sigma_{21}(\theta) - \sigma_{20}(\theta) \right) + \mu^2 \cdot \left(\sigma_{22}(\theta) + \sigma_{20}(\theta) - 2\sigma_{21}(\theta) \right)}{\sigma_y} \qquad (3)$$

From these equations follows:

$$\frac{\partial \sigma_1}{\partial \sigma_1} = \frac{\partial \sigma_{eq}}{\partial \sigma_1} \cdot f1(\mu, \theta) + \frac{\partial f1(\mu, \theta)}{\partial \sigma_1} \cdot \sigma_{eq} = \frac{\partial \sigma_{eq}}{\partial \sigma_1} \cdot f1(\mu, \theta) + \frac{\partial f1(\mu, \theta)}{\partial \mu} \cdot \frac{\partial \mu}{\partial \sigma_1} \sigma_{eq} = 1$$
$$\frac{\partial \sigma_2}{\partial \sigma_1} = \frac{\partial \sigma_{eq}}{\partial \sigma_1} \cdot f2(\mu, \theta) + \frac{\partial f2(\mu, \theta)}{\partial \sigma_1} \cdot \sigma_{eq} = \frac{\partial \sigma_{eq}}{\partial \sigma_1} \cdot f2(\mu, \theta) + \frac{\partial f2(\mu, \theta)}{\partial \mu} \cdot \frac{\partial \mu}{\partial \sigma_1} \sigma_{eq} = 0 \qquad (4)$$

From (4) an expression for the derivative of μ to the principal stress σ_1 is obtained:

$$\frac{\partial \mu}{\partial \sigma_1} = \frac{\frac{\partial \sigma_{eq}}{\partial \sigma_1} \cdot f2(\mu, \theta)}{\frac{\partial f2(\mu, \theta)}{\partial \mu} \cdot \sigma_{eq}} \qquad (5)$$

By substituting (5) in the first of (4) and substituting (2) in (1), the first component of the normal is obtained:

$$\frac{\partial \phi}{\partial \sigma_1} = \frac{\dfrac{\partial f2(\mu,\theta)}{\partial \mu}}{\dfrac{\partial f2(\mu,\theta)}{\partial \mu} \cdot f1(\mu,\theta) - \dfrac{\partial f1(\mu,\theta)}{\partial \mu} \cdot f2(\mu,\theta)} \qquad (6)$$

By interchanging the indices of the first and the second components the second component of the normal is also derived:

$$\frac{\partial \phi}{\partial \sigma_2} = \frac{\dfrac{\partial f1(\mu,\theta)}{\partial \mu}}{\dfrac{\partial f1(\mu,\theta)}{\partial \mu} \cdot f2(\mu,\theta) - \dfrac{\partial f2(\mu,\theta)}{\partial \mu} \cdot f1(\mu,\theta)} \qquad (7)$$

Appendix B Euler backward stress projection

The expression for the Euler-backward method for a plane stress situation is given by:

$$\begin{pmatrix}\sigma_{xx}\\ \sigma_{yy}\\ \tau_{xy}\end{pmatrix}_n = \begin{pmatrix}\sigma_{xx}\\ \sigma_{yy}\\ \tau_{xy}\end{pmatrix}_t - \Delta\lambda \begin{bmatrix} \frac{E}{1-\nu^2} & \nu\cdot\frac{E}{1-\nu^2} & 0 \\ \nu\cdot\frac{E}{1-\nu^2} & \frac{E}{1-\nu^2} & 0 \\ 0 & 0 & \frac{E}{2(1+\nu)} \end{bmatrix} \cdot \begin{pmatrix}\frac{\partial\phi}{\partial\sigma_{xx}}\\ \frac{\partial\phi}{\partial\sigma_{yy}}\\ \frac{\partial\phi}{\partial\tau_{xy}}\end{pmatrix}_n \qquad (1)$$

Here the derivatives of the yield function to the stress components are written as:

$$\begin{pmatrix}\frac{\partial\phi}{\partial\sigma_{xx}}\\ \frac{\partial\phi}{\partial\sigma_{yy}}\\ \frac{\partial\phi}{\partial\tau_{xy}}\end{pmatrix} = \frac{\partial\phi}{\partial\sigma_1}\begin{pmatrix}\frac{\partial\sigma_1}{\partial\sigma_{xx}}\\ \frac{\partial\sigma_1}{\partial\sigma_{yy}}\\ \frac{\partial\sigma_1}{\partial\tau_{xy}}\end{pmatrix} + \frac{\partial\phi}{\partial\sigma_2}\begin{pmatrix}\frac{\partial\sigma_2}{\partial\sigma_{xx}}\\ \frac{\partial\sigma_2}{\partial\sigma_{yy}}\\ \frac{\partial\sigma_2}{\partial\tau_{xy}}\end{pmatrix} + \frac{\partial\phi}{\partial\cos 2\theta}\begin{pmatrix}\frac{\partial\cos 2\theta}{\partial\sigma_{xx}}\\ \frac{\partial\cos 2\theta}{\partial\sigma_{yy}}\\ \frac{\partial\cos 2\theta}{\partial\tau_{xy}}\end{pmatrix} \qquad (2)$$

The derivatives of the yield function to the principal stresses can be written as

$$\frac{\partial\phi}{\partial\sigma_1} = \frac{\frac{\partial f2(\mu,\theta)}{\partial\mu}}{\frac{\partial f2(\mu,\theta)}{\partial\mu}\cdot f1(\mu,\theta) - \frac{\partial f1(\mu,\theta)}{\partial\mu}\cdot f2(\mu,\theta)} \qquad (3)$$

$$\frac{\partial\phi}{\partial\sigma_2} = -\frac{\frac{\partial f1(\mu,\theta)}{\partial\mu}}{\frac{\partial f2(\mu,\theta)}{\partial\mu}\cdot f1(\mu,\theta) - \frac{\partial f1(\mu,\theta)}{\partial\mu}\cdot f2(\mu,\theta)}$$

The derivatives of the first principal stress to the general stress components are determined using the rules of tensor transformation (3.9):

$$\begin{pmatrix} \frac{\partial \sigma_1}{\partial \sigma_{xx}} \\ \frac{\partial \sigma_1}{\partial \sigma_{yy}} \\ \frac{\partial \sigma_1}{\partial \tau_{xy}} \end{pmatrix} = \begin{pmatrix} \frac{1}{2} \\ \frac{1}{2} \\ 0 \end{pmatrix} + \begin{pmatrix} \frac{1}{2 \cdot \sqrt{(\sigma_{xx} - \sigma_{yy})^2 + 4 \cdot (\tau_{xy})^2}} & \frac{-1}{2 \cdot \sqrt{(\sigma_{xx} - \sigma_{yy})^2 + 4 \cdot (\tau_{xy})^2}} & 0 \\ \frac{-1}{2 \cdot \sqrt{(\sigma_{xx} - \sigma_{yy})^2 + 4 \cdot (\tau_{xy})^2}} & \frac{1}{2 \cdot \sqrt{(\sigma_{xx} - \sigma_{yy})^2 + 4 \cdot (\tau_{xy})^2}} & 0 \\ 0 & 0 & \frac{2}{\sqrt{(\sigma_{xx} - \sigma_{yy})^2 + 4 \cdot (\tau_{xy})^2}} \end{pmatrix} \cdot \begin{pmatrix} \sigma_{xx} \\ \sigma_{yy} \\ \tau_{xy} \end{pmatrix}$$

or

$$\begin{pmatrix} \frac{\partial \sigma_1}{\partial \sigma_{xx}} \\ \frac{\partial \sigma_1}{\partial \sigma_{yy}} \\ \frac{\partial \sigma_1}{\partial \tau_{xy}} \end{pmatrix} = \begin{pmatrix} \frac{1}{2} \\ \frac{1}{2} \\ 0 \end{pmatrix} + \begin{pmatrix} \frac{1}{2 \cdot (\sigma_1 - \sigma_2)} & \frac{-1}{2 \cdot (\sigma_1 - \sigma_2)} & 0 \\ \frac{-1}{2 \cdot (\sigma_1 - \sigma_2)} & \frac{1}{2 \cdot (\sigma_1 - \sigma_2)} & 0 \\ 0 & 0 & \frac{2}{(\sigma_1 - \sigma_2)} \end{pmatrix} \cdot \begin{pmatrix} \sigma_{xx} \\ \sigma_{yy} \\ \tau_{xy} \end{pmatrix} \tag{4}$$

In a similar way the derivatives of the second principal stress to the stress components are:

$$\begin{pmatrix} \frac{\partial \sigma_2}{\partial \sigma_{xx}} \\ \frac{\partial \sigma_2}{\partial \sigma_{yy}} \\ \frac{\partial \sigma_2}{\partial \tau_{xy}} \end{pmatrix} = \begin{pmatrix} \frac{1}{2} \\ \frac{1}{2} \\ 0 \end{pmatrix} + \begin{pmatrix} \frac{-1}{2 \cdot (\sigma_1 - \sigma_2)} & \frac{1}{2 \cdot (\sigma_1 - \sigma_2)} & 0 \\ \frac{1}{2 \cdot (\sigma_1 - \sigma_2)} & \frac{-1}{2 \cdot (\sigma_1 - \sigma_2)} & 0 \\ 0 & 0 & \frac{-2}{(\sigma_1 - \sigma_2)} \end{pmatrix} \cdot \begin{pmatrix} \sigma_{xx} \\ \sigma_{yy} \\ \tau_{xy} \end{pmatrix} \tag{5}$$

The derivative of the yield function to the term cos2θ is given by appendix C:

$$\frac{\partial \phi}{\partial \cos(2\theta)} = -\frac{\sigma_1}{(f1(\mu,\theta))^2} \left(\frac{\partial f1(\mu,\theta)}{\partial \cos(2\theta)} + \frac{\partial f1(\mu,\theta)}{\partial \mu} \cdot \frac{f2(\mu,\theta) \cdot \frac{\partial f1(\mu,\theta)}{\partial \cos(2\theta)} - f1(\mu,\theta) \cdot \frac{\partial f2(\mu,\theta)}{\partial \cos(2\theta)}}{\frac{\partial f2(\mu,\theta)}{\partial \mu} \cdot f1(\mu,\theta) - \frac{\partial f1(\mu,\theta)}{\partial \mu} \cdot f2(\mu,\theta)} \right) =$$

$$-\frac{\sigma 2}{(f2(\mu,\theta))^2} \left(\frac{\partial f2(\mu,\theta)}{\partial \cos(2\theta)} + \frac{\partial f2(\mu,\theta)}{\partial \mu} \cdot \frac{f2(\mu,\theta) \cdot \frac{\partial f1(\mu,\theta)}{\partial \cos(2\theta)} - f1(\mu,\theta) \cdot \frac{\partial f2(\mu,\theta)}{\partial \cos(2\theta)}}{\frac{\partial f2(\mu,\theta)}{\partial \mu} \cdot f1(\mu,\theta) - \frac{\partial f1(\mu,\theta)}{\partial \mu} \cdot f2(\mu,\theta)} \right) \tag{6}$$

The derivatives of the term cos2θ to the stress components are determined are determined using the rules of tensor transformation (3.9):

$$\cos 2\theta = \frac{\frac{\sigma_{xx} - \sigma_{yy}}{2}}{\sqrt{\left(\frac{\sigma_{xx} - \sigma_{yy}}{2}\right)^2 + \left(\tau_{xy}\right)^2}} \tag{7}$$

$$\frac{\partial \cos 2\theta}{\partial \sigma_{xx}} = \frac{\frac{1}{2}}{\sqrt{\left(\frac{\sigma_{xx} - \sigma_{yy}}{2}\right)^2 + \left(\tau_{xy}\right)^2}} - \frac{\frac{1}{2}\left(\frac{\sigma_{xx} - \sigma_{yy}}{2}\right)^2}{\left(\left(\frac{\sigma_{xx} - \sigma_{yy}}{2}\right)^2 + \left(\tau_{xy}\right)^2\right) \cdot \sqrt{\left(\frac{\sigma_{xx} - \sigma_{yy}}{2}\right)^2 + \left(\tau_{xy}\right)^2}} = \frac{1}{diamohr} - \frac{\left(\sigma_{xx} - \sigma_{yy}\right)^2}{diamohr^3} \tag{8}$$

$$\frac{\partial \cos 2\theta}{\partial \sigma_{yy}} = -\left(\frac{1}{diamohr} - \frac{\left(\sigma_{xx} - \sigma_{yy}\right)^2}{diamohr^3}\right) \tag{9}$$

$$\frac{\partial \cos 2\theta}{\partial \tau_{xy}} = -\frac{4 \cdot \tau_{xy}\left(\sigma_{xx} - \sigma_{yy}\right)}{diamohr^3} \tag{10}$$

with

$$diamohr = 2 * \sqrt{\left(\frac{\sigma_{xx} - \sigma_{yy}}{2}\right)^2 + \left(\tau_{xy}\right)^2}$$

The expressions (3) to (10) can be substituted into (2). Then expression (2) can be substituted back into (1). Because (6) is very extensive, this latter will not be substituted into (2) yet:

$$\begin{pmatrix}\sigma_{xx}\\ \sigma_{yy}\\ \tau_{xy}\end{pmatrix}_n = \begin{pmatrix}\sigma_{xx}\\ \sigma_{yy}\\ \tau_{xy}\end{pmatrix}_t - \Delta\lambda \begin{bmatrix} \frac{E}{1-\nu^2} & \nu\cdot\frac{E}{1-\nu^2} & 0 \\ \nu\cdot\frac{E}{1-\nu^2} & \frac{E}{1-\nu^2} & 0 \\ 0 & 0 & \frac{E}{2(1+\nu)} \end{bmatrix} \begin{bmatrix} \frac{\left[\frac{\partial f2(\mu,\theta)}{\partial\mu}\right]_n}{\left[\frac{\partial f2(\mu,\theta)}{\partial\mu}\cdot f1(\mu,\theta) - \frac{\partial f1(\mu,\theta)}{\partial\mu}\cdot f2(\mu,\theta)\right]_n} \left[\begin{pmatrix}\frac{1}{2}\\ \frac{1}{2}\\ 0\end{pmatrix} + \begin{bmatrix} \frac{1}{2\cdot(\sigma_1-\sigma_2)_n} & \frac{-1}{2\cdot(\sigma_1-\sigma_2)_n} & 0 \\ \frac{-1}{2\cdot(\sigma_1-\sigma_2)_n} & \frac{1}{2\cdot(\sigma_1-\sigma_2)_n} & 0 \\ 0 & 0 & \frac{2}{(\sigma_1-\sigma_2)_n} \end{bmatrix} \cdot \begin{pmatrix}\sigma_{xx}\\ \sigma_{yy}\\ \tau_{xy}\end{pmatrix}_n \right] - \\ \frac{\left[\frac{\partial f1(\mu,\theta)}{\partial\lambda}\right]_n}{\left[\frac{\partial f2(\mu,\theta)}{\partial\mu}\cdot f1(\mu,\theta) - \frac{\partial f1(\mu,\theta)}{\partial\mu}\cdot f2(\mu,\theta)\right]_n} \left[\begin{pmatrix}\frac{1}{2}\\ \frac{1}{2}\\ 0\end{pmatrix} + \begin{bmatrix} \frac{-1}{2\cdot(\sigma_1-\sigma_2)_n} & \frac{1}{2\cdot(\sigma_1-\sigma_2)_n} & 0 \\ \frac{1}{2\cdot(\sigma_1-\sigma_2)_n} & \frac{-1}{2\cdot(\sigma_1-\sigma_2)_n} & 0 \\ 0 & 0 & \frac{-2}{(\sigma_1-\sigma_2)_n} \end{bmatrix} \cdot \begin{pmatrix}\sigma_{xx}\\ \sigma_{yy}\\ \tau_{xy}\end{pmatrix}_n \right] + \\ \frac{\partial\phi}{\partial\cos 2\theta} \begin{pmatrix} \frac{\partial\cos 2\theta}{\partial\sigma_{xx}} \\ \frac{\partial\cos 2\theta}{\partial\sigma_{yy}} \\ \frac{\partial\cos 2\theta}{\partial\tau_{xy}} \end{pmatrix}_n \end{bmatrix} \quad (11)$$

Expression (11) is the general expression for the Euler backward method for the Vegter yield function. Because the last angle-dependent term between brackets in (11) is very extensive and appears to have only a small contribution compared to the other terms, it was decided to leave this term out in the first instance. This derivation is known as the Euler backward method with a constant planar angle. It is elaborated in the first part of this appendix. It appeared however, that, despite its small contribution, leaving out this term showed significant difference in anisotropic effects. For instance the shear behaviour in an uni-axial tensile test of section 3.5 was not present at all. Therefore the Euler backward is also derived including the latter term.

Euler backward method with a constant planar angle

The basis is expression (11) without the last term:

$$\begin{pmatrix}\sigma_{xx}\\ \sigma_{yy}\\ \tau_{xy}\end{pmatrix}_n = \begin{pmatrix}\sigma_{xx}\\ \sigma_{yy}\\ \tau_{xy}\end{pmatrix}_t - \Delta\lambda \begin{bmatrix} \frac{E}{1-\nu^2} & \nu\cdot\frac{E}{1-\nu^2} & 0 \\ \nu\cdot\frac{E}{1-\nu^2} & \frac{E}{1-\nu^2} & 0 \\ 0 & 0 & \frac{E}{2(1+\nu)} \end{bmatrix} \begin{bmatrix} \frac{\left[\frac{\partial f2(\mu,\theta)}{\partial\mu}\right]_n}{\left[\frac{\partial f2(\mu,\theta)}{\partial\mu}\cdot f1(\mu,\theta) - \frac{\partial f1(\mu,\theta)}{\partial\mu}\cdot f2(\mu,\theta)\right]_n} \left[\begin{pmatrix}\frac{1}{2}\\ \frac{1}{2}\\ 0\end{pmatrix} + \begin{bmatrix} \frac{1}{2\cdot(\sigma_1-\sigma_2)_n} & \frac{-1}{2\cdot(\sigma_1-\sigma_2)_n} & 0 \\ \frac{-1}{2\cdot(\sigma_1-\sigma_2)_n} & \frac{1}{2\cdot(\sigma_1-\sigma_2)_n} & 0 \\ 0 & 0 & \frac{2}{(\sigma_1-\sigma_2)_n} \end{bmatrix} \cdot \begin{pmatrix}\sigma_{xx}\\ \sigma_{yy}\\ \tau_{xy}\end{pmatrix}_n \right] - \\ \frac{\left[\frac{\partial f1(\mu,\theta)}{\partial\lambda}\right]_n}{\left[\frac{\partial f2(\mu,\theta)}{\partial\mu}\cdot f1(\mu,\theta) - \frac{\partial f1(\mu,\theta)}{\partial\mu}\cdot f2(\mu,\theta)\right]_n} \left[\begin{pmatrix}\frac{1}{2}\\ \frac{1}{2}\\ 0\end{pmatrix} + \begin{bmatrix} \frac{-1}{2\cdot(\sigma_1-\sigma_2)_n} & \frac{1}{2\cdot(\sigma_1-\sigma_2)_n} & 0 \\ \frac{1}{2\cdot(\sigma_1-\sigma_2)_n} & \frac{-1}{2\cdot(\sigma_1-\sigma_2)_n} & 0 \\ 0 & 0 & \frac{-2}{(\sigma_1-\sigma_2)_n} \end{bmatrix} \cdot \begin{pmatrix}\sigma_{xx}\\ \sigma_{yy}\\ \tau_{xy}\end{pmatrix}_n \right]_n \end{bmatrix} \quad (12)$$

By taking the stress terms with subscript ‘n’ to one side:

$$\left[\begin{pmatrix}1&0&0\\0&1&0\\0&0&1\end{pmatrix}+\Delta\lambda\begin{bmatrix}\frac{E}{1-v^2}&v\cdot\frac{E}{1-v^2}&0\\v\cdot\frac{E}{1-v^2}&\frac{E}{1-v^2}&0\\0&0&\frac{E}{2(1+v)}\end{bmatrix}\cdot\begin{bmatrix}\frac{\left[\frac{\partial f2(\mu,\theta)}{\partial\mu}\right]_n}{\left[\frac{\partial f2(\mu,\theta)}{\partial\mu}\cdot f1(\mu,\theta)-\frac{\partial f1(\mu,\theta)}{\partial\mu}\cdot f2(\mu,\theta)\right]_n}\begin{bmatrix}\frac{1}{2\cdot(\sigma_1-\sigma_2)_n}&\frac{-1}{2\cdot(\sigma_1-\sigma_2)_n}&0\\\frac{-1}{2\cdot(\sigma_1-\sigma_2)_n}&\frac{1}{2\cdot(\sigma_1-\sigma_2)_n}&0\\0&0&\frac{2}{(\sigma_1-\sigma_2)_n}\end{bmatrix}-\\\frac{\left[\frac{\partial f1(\mu,\theta)}{\partial\mu}\right]_n}{\left[\frac{\partial f2(\mu,\theta)}{\partial\mu}\cdot f1(\mu,\theta)-\frac{\partial f1(\mu,\theta)}{\partial\mu}\cdot f2(\mu,\theta)\right]_n}\begin{bmatrix}\frac{-1}{2\cdot(\sigma_1-\sigma_2)_n}&\frac{1}{2\cdot(\sigma_1-\sigma_2)_n}&0\\\frac{1}{2\cdot(\sigma_1-\sigma_2)_n}&\frac{-1}{2\cdot(\sigma_1-\sigma_2)_n}&0\\0&0&\frac{-2}{(\sigma_1-\sigma_2)_n}\end{bmatrix}+\end{bmatrix}\right]\cdot\begin{pmatrix}\sigma_{xx}\\\sigma_{yy}\\\tau_{xy}\end{pmatrix}_n=$$

$$\begin{pmatrix}\sigma_{xx}\\\sigma_{yy}\\\tau_{xy}\end{pmatrix}_t-\Delta\lambda\begin{bmatrix}\frac{E}{1-v^2}&v\cdot\frac{E}{1-v^2}&0\\v\cdot\frac{E}{1-v^2}&\frac{E}{1-v^2}&0\\0&0&\frac{E}{2(1+v)}\end{bmatrix}\cdot\left[\frac{\left[\frac{\partial f2(\mu,\theta)}{\partial\mu}\right]_n}{\left[\frac{\partial f2(\mu,\theta)}{\partial\mu}\cdot f1(\mu,\theta)-\frac{\partial f1(\mu,\theta)}{\partial\mu}\cdot f2(\mu,\theta)\right]_n}\begin{pmatrix}\frac{1}{2}\\\frac{1}{2}\\0\end{pmatrix}-\frac{\left[\frac{\partial f1(\mu,\theta)}{\partial\mu}\right]_n}{\left[\frac{\partial f2(\mu,\theta)}{\partial\mu}\cdot f1(\mu,\theta)-\frac{\partial f1(\mu,\theta)}{\partial\mu}\cdot f2(\mu,\theta)\right]_n}\begin{pmatrix}\frac{1}{2}\\\frac{1}{2}\\0\end{pmatrix}_n\right]\qquad(13)$$

Expression (12) can be simplified by defining the matrix A(μ,Δλ):

$$\begin{pmatrix}1&0&0\\0&1&0\\0&0&1\end{pmatrix}+\Delta\lambda\begin{bmatrix}\frac{E}{1-v^2}&v\cdot\frac{E}{1-v^2}&0\\v\cdot\frac{E}{1-v^2}&\frac{E}{1-v^2}&0\\0&0&\frac{E}{2(1+v)}\end{bmatrix}\cdot\begin{bmatrix}\frac{\left[\frac{\partial f2(\mu,\theta)}{\partial\mu}\right]_n}{\left[\frac{\partial f2(\mu,\theta)}{\partial\mu}\cdot f1(\mu,\theta)-\frac{\partial f1(\mu,\theta)}{\partial\mu}\cdot f2(\mu,\theta)\right]_n}\begin{bmatrix}\frac{1}{2\cdot(\sigma_1-\sigma_2)_n}&\frac{-1}{2\cdot(\sigma_1-\sigma_2)_n}&0\\\frac{-1}{2\cdot(\sigma_1-\sigma_2)_n}&\frac{1}{2\cdot(\sigma_1-\sigma_2)_n}&0\\0&0&\frac{2}{(\sigma_1-\sigma_2)_n}\end{bmatrix}-\\\frac{\left[\frac{\partial f1(\mu,\theta)}{\partial\mu}\right]_n}{\left[\frac{\partial f2(\mu,\theta)}{\partial\mu}\cdot f1(\mu,\theta)-\frac{\partial f1(\mu,\theta)}{\partial\mu}\cdot f2(\mu,\theta)\right]_n}\begin{bmatrix}\frac{-1}{2\cdot(\sigma_1-\sigma_2)_n}&\frac{1}{2\cdot(\sigma_1-\sigma_2)_n}&0\\\frac{1}{2\cdot(\sigma_1-\sigma_2)_n}&\frac{-1}{2\cdot(\sigma_1-\sigma_2)_n}&0\\0&0&\frac{-2}{(\sigma_1-\sigma_2)_n}\end{bmatrix}+\end{bmatrix}=A(\mu,\Delta\lambda)\qquad(14)$$

Then equation (12) changes into :

$$\cdot\begin{pmatrix}\sigma_{xx}\\\sigma_{yy}\\\tau_{xy}\end{pmatrix}_n=A(\mu,\Delta\lambda)^{-1}\cdot\begin{pmatrix}\sigma_{xx}\\\sigma_{yy}\\\tau_{xy}\end{pmatrix}_t-A(\mu,\Delta\lambda)^{-1}\cdot\Delta\lambda\begin{bmatrix}\frac{E}{1-v^2}&v\cdot\frac{E}{1-v^2}&0\\v\cdot\frac{E}{1-v^2}&\frac{E}{1-v^2}&0\\0&0&\frac{E}{2(1+v)}\end{bmatrix}\cdot\left[\frac{\left[\frac{\partial f2(\mu,\theta)}{\partial\mu}\right]_n-\left[\frac{\partial f1(\mu,\theta)}{\partial\mu}\right]_n}{\left[\frac{\partial f2(\mu,\theta)}{\partial\mu}\cdot f1(\mu,\theta)-\frac{\partial f1(\mu,\theta)}{\partial\mu}\cdot f2(\mu,\theta)\right]_n}\begin{pmatrix}\frac{1}{2}\\\frac{1}{2}\\0\end{pmatrix}_n\right]\qquad(15)$$

1 2

Parts 1 and 2 of equation (15) are written out separately. For this the inverted matrix $A(\mu,\Delta\lambda)^{-1}$ is written as:

$$A(\mu,\Delta\lambda)^{-1}=\begin{bmatrix}\frac{1+a}{1+2a} & \frac{a}{1+2a} & 0\\ \frac{a}{1+2a} & \frac{1+a}{1+2a} & 0\\ 0 & 0 & \frac{1}{1+2a}\end{bmatrix} \qquad (16)$$

where

$$a=\frac{\left(\frac{\partial f1(\mu,\theta)}{\partial\mu}+\frac{\partial f2(\mu,\theta)}{\partial\mu}\right)E\Delta\lambda}{2\sigma_v\left(f1(\mu,\theta)-f2(\mu,\theta)\right)\left(\frac{\partial f2(\mu,\theta)}{\partial\mu}\cdot f1(\mu,\theta)-\frac{\partial f1(\mu,\theta)}{\partial\mu}\cdot f2(\mu,\theta)\right)(1+v)}$$

The first part of (15) then gives:

$$\begin{aligned}(\sigma_{xx})_n&=\frac{a+1}{2a+1}(\sigma_{xx})_t+\frac{a}{2a+1}(\sigma_{yy})_t\\ (\sigma_{yy})_n&=\frac{a}{2a+1}(\sigma_{xx})_t+\frac{a+1}{2a+1}(\sigma_{yy})_t\\ (\tau_{xy})_n&=\frac{1}{2a+1}(\tau_{xy})_t\end{aligned} \qquad (17)$$

The second part:

$$\begin{aligned}\sigma_{xx_n}=&-A(\mu,\Delta\lambda)^{-1}\cdot\Delta\lambda\frac{\left[\frac{\partial f2(\mu,\theta)}{\partial\mu}\right]_n-\left[\frac{\partial f1(\mu,\theta)}{\partial\mu}\right]_n}{\left[\frac{\partial f2(\mu,\theta)}{\partial\mu}\cdot f1(\mu,\theta)-\frac{\partial f1(\mu,\theta)}{\partial\mu}\cdot f2(\mu,\theta)\right]_n}\begin{pmatrix}\frac{1}{2}(1+v)\frac{E}{1-v^2}\\ \frac{1}{2}(1+v)\frac{E}{1-v^2}\\ 0\end{pmatrix}=\\ &-\Delta\lambda\frac{\left[\frac{\partial f2(\mu,\theta)}{\partial\mu}\right]_n-\left[\frac{\partial f1(\mu,\theta)}{\partial\mu}\right]_n}{\left[\frac{\partial f2(\mu,\theta)}{\partial\mu}\cdot f1(\mu,\theta)-\frac{\partial f1(\mu,\theta)}{\partial\mu}\cdot f2(\mu,\theta)\right]_n}\cdot\left(\frac{1+2a}{1+2a}\right)\cdot\frac{1}{2}(1+v)\frac{E}{1-v^2}=\\ &-\Delta\lambda\frac{\left[\frac{\partial f2(\mu,\theta)}{\partial\mu}\right]_n-\left[\frac{\partial f1(\mu,\theta)}{\partial\mu}\right]_n}{\left[\frac{\partial f2(\mu,\theta)}{\partial\mu}\cdot f1(\mu,\theta)-\frac{\partial f1(\mu,\theta)}{\partial\mu}\cdot f2(\mu,\theta)\right]_n}\frac{1}{2}(1+v)\frac{E}{1-v^2}\end{aligned} \qquad (18)$$

$$\sigma_{yy_n}=-\Delta\lambda\frac{\left[\frac{\partial f2(\mu,\theta)}{\partial\mu}\right]_n-\left[\frac{\partial f1(\mu,\theta)}{\partial\mu}\right]_n}{\left[\frac{\partial f2(\mu,\theta)}{\partial\mu}\cdot f1(\mu,\theta)-\frac{\partial f1(\mu,\theta)}{\partial\mu}\cdot f2(\mu,\theta)\right]_n}\frac{1}{2}(1+v)\frac{E}{1-v^2}$$

$$\tau_{xy_n}=0$$

By adding the first (17) and the second (18) parts equation (15) becomes:

$$\sigma_{xx_n} = \frac{a+1}{2a+1}\cdot\sigma_{xx_t} + \frac{a}{2a+1}\cdot\sigma_{yy_t} - \frac{\Delta\lambda\left(\frac{\partial f2(\mu,\theta)}{\partial\mu} - \frac{\partial f1(\mu,\theta)}{\partial\mu}\right)_n}{\left(\frac{\partial f2(\mu,\theta)}{\partial\mu} f1(\mu,\theta) - \frac{\partial f1(\mu,\theta)}{\partial\mu} f2(\mu,\theta)\right)_n} \frac{1}{2}(1+\nu)\frac{E}{1-\nu^2}$$

$$\sigma_{yy_n} = \frac{a}{2a+1}\cdot\sigma_{xx_t} + \frac{a+1}{2a+1}\cdot\sigma_{yy_t} - \frac{\Delta\lambda\left(\frac{\partial f2(\mu,\theta)}{\partial\mu} - \frac{\partial f1(\mu,\theta)}{\partial\mu}\right)_n}{\left(\frac{\partial f2(\mu,\theta)}{\partial\mu} f1(\mu,\theta) - \frac{\partial f1(\mu,\theta)}{\partial\mu} f2(\mu,\theta)\right)_n} \frac{1}{2}(1+\nu)\frac{E}{1-\nu^2} \qquad (19)$$

$$\tau_{xy_n} = \frac{1}{2a+1}\cdot\tau_{xy_t}$$

Because the back-scaled situation is on the yield surface, another 2 equations apply:

$$\frac{\sigma_{1n}}{f1(\mu,\theta)} - \sigma_v = 0$$
$$\frac{\sigma_{2n}}{f2(\mu,\theta)} - \sigma_v = 0 \qquad (20)$$

These equations can be written in general stress components as:

$$\frac{\sigma_{xx_n} + \sigma_{yy_n}}{2} + \sqrt{\left(\frac{\sigma_{xx_n} - \sigma_{yy_n}}{2}\right)^2 + \tau_{xy}{}^2} = f1(\mu,\theta)\cdot\sigma_v$$
$$\frac{\sigma_{xx_n} + \sigma_{yy_n}}{2} - \sqrt{\left(\frac{\sigma_{xx_n} - \sigma_{yy_n}}{2}\right)^2 + \tau_{xy}{}^2} = f2(\mu,\theta)\cdot\sigma_v \qquad (21)$$

Adding and substracting equations (20) results in:

$$\sigma_{xx_n} + \sigma_{yy_n} = f1(\mu,\theta)\cdot\sigma_v + f2(\mu,\theta)\cdot\sigma_v \qquad (22)$$

$$2\sqrt{\left(\frac{\sigma_{xx_n} - \sigma_{yy_n}}{2}\right)^2 + \tau_{xy_n}{}^2} = f1(\mu,\theta)\cdot\sigma_v - f2(\mu,\theta)\cdot\sigma_v \qquad (23)$$

When equations (19) are substituted into (22):

$$\frac{a+1}{2a+1}\cdot\sigma_{xx_t}+\frac{a}{2a+1}\cdot\sigma_{yy_t}+\frac{a}{2a+1}\cdot\sigma_{xx_t}+\frac{a+1}{2a+1}\cdot\sigma_{yy_t}$$
$$-\frac{\Delta\lambda\left(\frac{\partial f2(\mu,\theta)}{\partial\mu}-\frac{\partial f1(\mu,\theta)}{\partial\mu}\right)_n}{\left(\frac{\partial f2(\mu,\theta)}{\partial\mu}f1(\mu,\theta)-\frac{\partial f1(\mu,\theta)}{\partial\mu}f2(\mu,\theta)\right)_n}\frac{1}{2}(1+\nu)\frac{E}{1-\nu^2}-\frac{\Delta\lambda\left(\frac{\partial f2(\mu,\theta)}{\partial\mu}-\frac{\partial f1(\mu,\theta)}{\partial\mu}\right)_n}{\left(\frac{\partial f2(\mu,\theta)}{\partial\mu}f1(\mu,\theta)-\frac{\partial f1(\mu,\theta)}{\partial\mu}f2(\mu,\theta)\right)_n}\frac{1}{2}(1+\nu)\frac{E}{1-\nu^2} \quad (24)$$
$$=$$
$$f1(\mu,\theta)\cdot\sigma_v+f2(\mu,\theta)\cdot\sigma_v$$

Or simplified:

$$\sigma_{xx_t}+\sigma_{yy_t}-\frac{\Delta\lambda\left(\frac{\partial f2(\mu,\theta)}{\partial\mu}-\frac{\partial f1(\mu,\theta)}{\partial\mu}\right)_n}{\left(\frac{\partial f2(\mu,\theta)}{\partial\mu}f1(\mu,\theta)-\frac{\partial f1(\mu,\theta)}{\partial\mu}f2(\mu,\theta)\right)_n}(1+\nu)\frac{E}{1-\nu^2} \quad (25)$$
$$=$$
$$f1(\mu,\theta)\cdot\sigma_v+f2(\mu,\theta)\cdot\sigma_v$$

This gives an expression for $\Delta\lambda$:

$$\Delta\lambda=\frac{\sigma_{xx_t}+\sigma_{yy_t}-f1(\mu,\theta)\cdot\sigma_v+f2(\mu,\theta)\cdot\sigma_v}{\left(\frac{E}{1-\nu}\right)\frac{\left(\frac{\partial f2(\mu,\theta)}{\partial\mu}-\frac{\partial f1(\mu,\theta)}{\partial\mu}\right)_n}{\left(\frac{\partial f2(\mu,\theta)}{\partial\mu}f1(\mu,\theta)-\frac{\partial f1(\mu,\theta)}{\partial\mu}f2(\mu,\theta)\right)_n}} \quad (26)$$

Substitution of equations (19) into (23) results in:

$$2\sqrt{\left(\frac{\frac{a+1}{2a+1}\sigma_{xx_t}+\frac{a}{2a+1}\sigma_{yy_t}-\frac{a}{2a+1}\sigma_{xx_t}-\frac{a+1}{2a+1}\sigma_{yy_t}}{2}\right)^2+\left(\frac{1}{2a+1}\tau_{xy_n}\right)_t^2}+$$
$$=f1(\mu,\theta)\cdot\sigma_v-f2(\mu,\theta)\cdot\sigma_v \quad (27)$$

By substituting the expression for (a) into (27):

$$2\sqrt{\left(\frac{\sigma_{xx_t}-\sigma_{yy_t}}{2}\right)^2+\left(\tau_{xy_n}\right)}-\left(f1(\mu,\theta)\cdot\sigma_v-f2(\mu,\theta)\cdot\sigma_v\right)=$$
$$\left(\frac{\left(\frac{\partial f1(\mu,\theta)}{\partial\mu}+\frac{\partial f2(\mu,\theta)}{\partial\mu}\right)_n\cdot E\cdot\Delta\lambda}{\sigma_v\cdot\left(f1(\mu,\theta)-f2(\mu,\theta)\right)\left(\frac{\partial f2(\mu,\theta)}{\partial\mu}-\frac{\partial f1(\mu,\theta)}{\partial\mu}\cdot\right)_n(1+\nu)}\cdot\sigma_v\cdot\left(f1(\mu,\theta)-f2(\mu,\theta)\right)\right) \quad (28)$$

By substituting the expression for $\Delta\lambda$ (26) into the right-hand side of (28):

$$2\sqrt{\left(\frac{\sigma_{xx_t}-\sigma_{yy_t}}{2}\right)^2+\left(\tau_{xy_t}\right)}-\left(f1(\mu,\theta)\cdot\sigma_v-f2(\mu,\theta)\cdot\sigma_v\right)=$$
$$\left(\frac{\left(\frac{\partial f1(\mu,\theta)}{\partial\mu}+\frac{\partial f2(\mu,\theta)}{\partial\mu}\right)_n(1-\nu)}{\left(\frac{\partial f2(\mu,\theta)}{\partial\mu}-\frac{\partial f1(\mu,\theta)}{\partial\mu}\cdot\right)_n(1+\nu)}\cdot\left(\sigma_{xx_t}+\sigma_{yy_t}\right)-\sigma_v\cdot\left(f1(\mu,\theta)+f2(\mu,\theta)\right)\right) \quad (29)$$

With (29) an equation for μ is obtained in which μ is the only unknown parameter, which can be solved with a Newton-Raphson method. This method is stable when the first guess of μ is close enough to the end solution. Therefore first a Bisection method is applied until an accuracy of 10 % in μ is reached before the Newton – Raphson method is used to compute the end solution. Subsequently the solution for μ can be substituted into (26), which provides the value of $\Delta\lambda$. By substituting μ and $\Delta\lambda$ in (14) and subsequently (14) in (15), the back-scaled stress $\underline{\sigma}_n$ is obtained.

Euler backward method with changing planar angle

The basis is expression (11). By taking the stress terms with subscript ‘n’ to one side:

$$\left[\begin{pmatrix}1&0&0\\0&1&0\\0&0&1\end{pmatrix}+\Delta\lambda\begin{bmatrix}\frac{E}{1-\nu^2}&\nu\cdot\frac{E}{1-\nu^2}&0\\ \nu\cdot\frac{E}{1-\nu^2}&\frac{E}{1-\nu^2}&0\\0&0&\frac{E}{2(1+\nu)}\end{bmatrix}\cdot\begin{bmatrix}\frac{\left[\frac{\partial f2(\mu,\theta)}{\partial\mu}\right]_n}{\left[\frac{\partial f2(\mu,\theta)}{\partial\mu}\cdot f1(\mu,\theta)-\frac{\partial f1(\mu,\theta)}{\partial\mu}\cdot f2(\mu,\theta)\right]_n}\begin{bmatrix}\frac{1}{2\cdot(\sigma_1-\sigma_2)_n}&\frac{-1}{2\cdot(\sigma_1-\sigma_2)_n}&0\\ \frac{-1}{2\cdot(\sigma_1-\sigma_2)_n}&\frac{1}{2\cdot(\sigma_1-\sigma_2)_n}&0\\0&0&\frac{2}{(\sigma_1-\sigma_2)_n}\end{bmatrix}-\\ \frac{\left[\frac{\partial f1(\mu,\theta)}{\partial\mu}\right]_n}{\left[\frac{\partial f2(\mu,\theta)}{\partial\mu}\cdot f1(\mu,\theta)-\frac{\partial f1(\mu,\theta)}{\partial\mu}\cdot f2(\mu,\theta)\right]_n}\begin{bmatrix}\frac{-1}{2\cdot(\sigma_1-\sigma_2)_n}&\frac{1}{2\cdot(\sigma_1-\sigma_2)_n}&0\\ \frac{1}{2\cdot(\sigma_1-\sigma_2)_n}&\frac{-1}{2\cdot(\sigma_1-\sigma_2)_n}&0\\0&0&\frac{-2}{(\sigma_1-\sigma_2)_n}\end{bmatrix}+\end{bmatrix}\right]\cdot\begin{pmatrix}\sigma_{xx}\\ \sigma_{yy}\\ \tau_{xy}\end{pmatrix}_n=$$

$$\begin{pmatrix}\sigma_{xx}\\ \sigma_{yy}\\ \tau_{xy}\end{pmatrix}_t-\Delta\lambda\begin{bmatrix}\frac{E}{1-\nu^2}&\nu\cdot\frac{E}{1-\nu^2}&0\\ \nu\cdot\frac{E}{1-\nu^2}&\frac{E}{1-\nu^2}&0\\0&0&\frac{E}{2(1+\nu)}\end{bmatrix}\cdot\left[\frac{\left[\frac{\partial f2(\mu,\theta)}{\partial\mu}\right]_n}{\left[\frac{\partial f2(\mu,\theta)}{\partial\mu}\cdot f1(\mu,\theta)-\frac{\partial f1(\mu,\theta)}{\partial\mu}\cdot f2(\mu,\theta)\right]_n}\begin{pmatrix}\frac{1}{2}\\ \frac{1}{2}\\0\end{pmatrix}-\frac{\left[\frac{\partial f1(\mu,\theta)}{\partial\mu}\right]_n}{\left[\frac{\partial f2(\mu,\theta)}{\partial\mu}\cdot f1(\mu,\theta)-\frac{\partial f1(\mu,\theta)}{\partial\mu}\cdot f2(\mu,\theta)\right]_n}\begin{pmatrix}\frac{1}{2}\\ \frac{1}{2}\\0\end{pmatrix}+\frac{\partial\phi}{\partial\cos 2\theta}\begin{pmatrix}\frac{\partial\cos 2\theta}{\partial\sigma_{xx}}\\ \frac{\partial\cos 2\theta}{\partial\sigma_{yy}}\\ \frac{\partial\cos 2\theta}{\partial\tau_{xy}}\end{pmatrix}_n\right] \qquad (30)$$

Expression (30) can be simplified by defining the matrix A(μ,Δλ), see (14). Then equation (30) changes into:

$$\cdot\begin{pmatrix}\sigma_{xx}\\ \sigma_{yy}\\ \tau_{xy}\end{pmatrix}_n=\underbrace{A(\mu,\Delta\lambda)^{-1}\cdot\begin{pmatrix}\sigma_{xx}\\ \sigma_{yy}\\ \tau_{xy}\end{pmatrix}_t}_{1}-\underbrace{A(\mu,\Delta\lambda)^{-1}\cdot\Delta\lambda\begin{bmatrix}\frac{E}{1-\nu^2}&\nu\cdot\frac{E}{1-\nu^2}&0\\ \nu\cdot\frac{E}{1-\nu^2}&\frac{E}{1-\nu^2}&0\\0&0&\frac{E}{2(1+\nu)}\end{bmatrix}\cdot\left[\frac{\left[\frac{\partial f2(\mu,\theta)}{\partial\mu}\right]_n-\left[\frac{\partial f1(\mu,\theta)}{\partial\mu}\right]_n}{\left[\frac{\partial f2(\mu,\theta)}{\partial\mu\lambda}\cdot f1(\mu,\theta)-\frac{\partial f1(\mu,\theta)}{\partial\mu}\cdot f2(\mu,\theta)\right]_n}\begin{pmatrix}\frac{1}{2}\\ \frac{1}{2}\\0\end{pmatrix}+\frac{\partial\phi}{\partial\cos 2\theta}\begin{pmatrix}\frac{\partial\cos 2\theta}{\partial\sigma_{xx}}\\ \frac{\partial\cos 2\theta}{\partial\sigma_{yy}}\\ \frac{\partial\cos 2\theta}{\partial\tau_{xy}}\end{pmatrix}_n\right]}_{2}\qquad(31)$$

Like the derivation with a constant planar angle, the parts 1, 2 and 3 of equation (31) are written out separately. The first parts (1) and (2) of (31) are given by (32) and (33):

$$\begin{aligned}(\sigma_{xx})_n&=\frac{a+1}{2a+1}(\sigma_{xx})_t+\frac{a}{2a+1}(\sigma_{yy})_t\\ (\sigma_{yy})_n&=\frac{a}{2a+1}(\sigma_{xx})_t+\frac{a+1}{2a+1}(\sigma_{yy})_t\\ (\tau_{xy})_n&=\frac{1}{2a+1}(\tau_{xy})_t\end{aligned}\qquad(32)$$

$$\sigma_{xx_n} = -A(\mu,\Delta\lambda)^{-1}\cdot\Delta\lambda\frac{\left[\frac{\partial f2(\mu,\theta)}{\partial\mu}\right]_n - \left[\frac{\partial f1(\mu,\theta)}{\partial\mu}\right]_n}{\left[\frac{\partial f2(\mu,\theta)}{\partial\mu}\cdot f1(\mu,\theta) - \frac{\partial f1(\mu,\theta)}{\partial\mu}\cdot f2(\mu,\theta)\right]_n}\begin{pmatrix}\frac{1}{2}(1+\nu)\frac{E}{1-\nu^2}\\ \frac{1}{2}(1+\nu)\frac{E}{1-\nu^2}\\ 0\end{pmatrix} =$$

$$-\Delta\lambda\frac{\left[\frac{\partial f2(\mu,\theta)}{\partial\mu}\right]_n - \left[\frac{\partial f1(\mu,\theta)}{\partial\mu}\right]_n}{\left[\frac{\partial f2(\mu,\theta)}{\partial\mu}\cdot f1(\mu,\theta) - \frac{\partial f1(\mu,\theta)}{\partial\mu}\cdot f2(\mu,\theta)\right]_n}\cdot\left(\frac{1+2a}{1+2a}\right)\cdot\frac{1}{2}(1+\nu)\frac{E}{1-\nu^2} =$$

$$-\Delta\lambda\frac{\left[\frac{\partial f2(\mu,\theta)}{\partial\mu}\right]_n - \left[\frac{\partial f1(\mu,\theta)}{\partial\mu}\right]_n}{\left[\frac{\partial f2(\mu,\theta)}{\partial\mu}\cdot f1(\mu,\theta) - \frac{\partial f1(\mu,\theta)}{\partial\mu}\cdot f2(\mu,\theta)\right]_n}\frac{1}{2}(1+\nu)\frac{E}{1-\nu^2} \qquad (33)$$

$$\sigma_{yy_n} = -\Delta\lambda\frac{\left[\frac{\partial f2(\mu,\theta)}{\partial\mu}\right]_n - \left[\frac{\partial f1(\mu,\theta)}{\partial\mu}\right]_n}{\left[\frac{\partial f2(\mu,\theta)}{\partial\mu}\cdot f1(\mu,\theta) - \frac{\partial f1(\mu,\theta)}{\partial\mu}\cdot f2(\mu,\theta)\right]_n}\frac{1}{2}(1+\nu)\frac{E}{1-\nu^2}$$

$$\tau_{xy_n} = 0$$

The third part (3):

$$\sigma_{xx_n} = -A(\mu,\Delta\lambda)^{-1}\cdot\Delta\lambda\begin{bmatrix}\frac{E}{1-\nu^2} & \nu\cdot\frac{E}{1-\nu^2} & 0\\ \nu\cdot\frac{E}{1-\nu^2} & \frac{E}{1-\nu^2} & 0\\ 0 & 0 & \frac{E}{2(1+\nu)}\end{bmatrix}\cdot\frac{\partial\phi}{\partial\cos 2\theta}\begin{pmatrix}\frac{\partial\cos 2\theta}{\partial\sigma_{xx}}\\ \frac{\partial\cos 2\theta}{\partial\sigma_{yy}}\\ \frac{\partial\cos 2\theta}{\partial\tau_{xy}}\end{pmatrix}_n =$$

$$-A(\mu,\Delta\lambda)^{-1}\cdot\Delta\lambda\cdot\begin{pmatrix}\frac{E}{1-\nu^2}\cdot\frac{\partial\phi}{\partial\cos 2\theta}\left(\frac{\partial\cos 2\theta}{\partial\sigma_{xx}}+\nu\cdot\frac{\partial\cos 2\theta}{\partial\sigma_{yy}}\right)_n\\ \frac{E}{1-\nu^2}\cdot\frac{\partial\phi}{\partial\cos 2\theta}\left(\nu\cdot\frac{\partial\cos 2\theta}{\partial\sigma_{xx}}+\frac{\partial\cos 2\theta}{\partial\sigma_{yy}}\right)_n\\ \frac{E}{2(1+\nu)}\frac{\partial\phi}{\partial\cos 2\theta}\left(\frac{\partial\cos 2\theta}{\partial\tau_{xy}}\right)_n\end{pmatrix} = \qquad (34)$$

$$-\Delta\lambda\frac{E}{1-\nu^2}\left(\frac{1+a}{1+2a}\frac{\partial\phi}{\partial\cos 2\theta}\left(\frac{\partial\cos 2\theta}{\partial\sigma_{xx}}+\nu\cdot\frac{\partial\cos 2\theta}{\partial\sigma_{yy}}\right)_n+\frac{a}{1+2a}\frac{\partial\phi}{\partial\cos 2\theta}\left(\nu\cdot\frac{\partial\cos 2\theta}{\partial\sigma_{xx}}+\frac{\partial\cos 2\theta}{\partial\sigma_{yy}}\right)_n\right)$$

$$\sigma_{yy_n} = -\Delta\lambda\frac{E}{1-\nu^2}\left(\frac{a}{1+2a}\frac{\partial\phi}{\partial\cos 2\theta}\left(\frac{\partial\cos 2\theta}{\partial\sigma_{xx}}+\nu\cdot\frac{\partial\cos 2\theta}{\partial\sigma_{yy}}\right)_n+\frac{1+a}{1+2a}\frac{\partial\phi}{\partial\cos 2\theta}\left(\nu\cdot\frac{\partial\cos 2\theta}{\partial\sigma_{xx}}+\frac{\partial\cos 2\theta}{\partial\sigma_{yy}}\right)_n\right)$$

$$\tau_{xy_n} = -\Delta\lambda\frac{E}{2\cdot(1+\nu)}\left(\frac{1}{1+2a}\frac{\partial\phi}{\partial\cos 2\theta}\frac{\partial\cos 2\theta}{\partial\tau_{xy}}\right)_n$$

.

By adding the first (1), second (2) and third parts (3), equation (31) becomes:

$$
\begin{aligned}
\sigma_{xx\,n} &= \frac{a+1}{2a+1}\cdot\sigma_{xx\,t} + \frac{a}{2a+1}\cdot\sigma_{yy\,t} \\
&\quad - \frac{\Delta\lambda\left(\dfrac{\partial f2(\mu,\theta)}{\partial\mu} - \dfrac{\partial f1(\mu,\theta)}{\partial\mu}\right)_n}{\left(\dfrac{\partial f2(\mu,\theta)}{\partial\mu} f1(\mu,\theta) - \dfrac{\partial f1(\mu,\theta)}{\partial\mu} f2(\mu,\theta)\right)_n} \frac{1}{2}(1+\nu)\frac{E}{1-\nu^2} \\
&\quad - \Delta\lambda\frac{E}{1-\nu^2}\left(\frac{1+a}{1+2a}\frac{\partial\phi}{\partial\cos 2\theta}\left(\frac{\partial\cos 2\theta}{\partial\sigma_{xx}} + \nu\cdot\frac{\partial\cos 2\theta}{\partial\sigma_{yy}}\right)_n + \frac{a}{1+2a}\frac{\partial\phi}{\partial\cos 2\theta}\left(\nu\cdot\frac{\partial\cos 2\theta}{\partial\sigma_{xx}} + \frac{\partial\cos 2\theta}{\partial\sigma_{yy}}\right)_n\right) \\
\sigma_{yy\,n} &= \frac{a}{2a+1}\cdot\sigma_{xx\,t} + \frac{a+1}{2a+1}\cdot\sigma_{yy\,t} \\
&\quad - \frac{\Delta\lambda\left(\dfrac{\partial f2(\mu,\theta)}{\partial\mu} - \dfrac{\partial f1(\mu,\theta)}{\partial\mu}\right)_n}{\left(\dfrac{\partial f2(\mu,\theta)}{\partial\mu} f1(\mu,\theta) - \dfrac{\partial f1(\mu,\theta)}{\partial\mu} f2(\mu,\theta)\right)_n} \frac{1}{2}(1+\nu)\frac{E}{1-\nu^2} \\
&\quad - \Delta\lambda\frac{E}{1-\nu^2}\left(\frac{a}{1+2a}\frac{\partial\phi}{\partial\cos 2\theta}\left(\frac{\partial\cos 2\theta}{\partial\sigma_{xx}} + \nu\cdot\frac{\partial\cos 2\theta}{\partial\sigma_{yy}}\right)_n + \frac{1+a}{1+2a}\frac{\partial\phi}{\partial\cos 2\theta}\left(\nu\cdot\frac{\partial\cos 2\theta}{\partial\sigma_{xx}} + \frac{\partial\cos 2\theta}{\partial\sigma_{yy}}\right)_n\right) \\
\tau_{xy\,n} &= \frac{1}{2a+1}\cdot\tau_{xy\,t} \\
&\quad - \Delta\lambda\frac{E}{2(1+\nu)}\frac{1}{1+2a}\frac{\partial\phi}{\partial\cos 2\theta}\left(\frac{\partial\cos 2\theta}{\partial\tau_{xy}}\right)_n
\end{aligned}
\tag{35}
$$

Because the back-scaled situation is on the yield surface, another 2 equations apply:

$$
\begin{aligned}
\frac{\sigma_{1n}}{f1(\mu,\theta)} - \sigma_v &= 0 \\
\frac{\sigma_{2n}}{f2(\mu,\theta)} - \sigma_v &= 0
\end{aligned}
\tag{36}
$$

These equations can be written in general stress components

$$
\begin{aligned}
\frac{\sigma_{xx\,n} + \sigma_{yy\,n}}{2} + \sqrt{\left(\frac{\sigma_{xx\,n} - \sigma_{yy\,n}}{2}\right)^2 + \tau_{xy}{}^2} &= f1(\mu,\theta)\cdot\sigma_v \\
\frac{\sigma_{xx\,n} + \sigma_{yy\,n}}{2} - \sqrt{\left(\frac{\sigma_{xx\,n} - \sigma_{yy\,n}}{2}\right)^2 + \tau_{xy}{}^2} &= f2(\mu,\theta)\cdot\sigma_v
\end{aligned}
\tag{37}
$$

Adding and substracting equations (37) results in:

$$\sigma_{xx\,n} + \sigma_{yy\,n} = f1(\mu,\theta)\cdot\sigma_v + f2(\mu,\theta)\cdot\sigma_v \qquad (38)$$

$$2\sqrt{\left(\frac{\sigma_{xx\,n} - \sigma_{yy\,n}}{2}\right)^2 + {\tau_{xy\,n}}^2} = f1(\mu,\theta)\cdot\sigma_v - f2(\mu,\theta)\cdot\sigma_v \qquad (39)$$

When equations (35) are substituted into (38):

$$\begin{aligned}
&\frac{a+1}{2a+1}\cdot\sigma_{xx\,t} + \frac{a}{2a+1}\cdot\sigma_{yy\,t} + \frac{a}{2a+1}\cdot\sigma_{xx\,t} + \frac{a+1}{2a+1}\cdot\sigma_{yy\,t} \\
&- \frac{\Delta\lambda\left(\frac{\partial f2(\mu,\theta)}{\partial\mu} - \frac{\partial f1(\mu,\theta)}{\partial\mu}\right)_n}{\left(\frac{\partial f2(\mu,\theta)}{\partial\mu} f1(\mu,\theta) - \frac{\partial f1(\mu,\theta)}{\partial\mu} f2(\mu,\theta)\right)_n}\frac{1}{2}(1+\nu)\frac{E}{1-\nu^2} - \frac{\Delta\lambda\left(\frac{\partial f2(\mu,\theta)}{\partial\mu} - \frac{\partial f1(\mu,\theta)}{\partial\mu}\right)_n}{\left(\frac{\partial f2(\mu,\theta)}{\partial\mu} f1(\mu,\theta) - \frac{\partial f1(\mu,\theta)}{\partial\mu} f2(\mu,\theta)\right)_n}\frac{1}{2}(1+\nu)\frac{E}{1-\nu^2} \\
&- \Delta\lambda\frac{E}{1-\nu^2}\left(\frac{1+a}{1+2a}\frac{\partial\phi}{\partial\cos 2\theta}\left(\frac{\partial\cos 2\theta}{\partial\sigma_{xx}} + \nu\cdot\frac{\partial\cos 2\theta}{\partial\sigma_{yy}}\right)_n + \frac{a}{1+2a}\frac{\partial\phi}{\partial\cos 2\theta}\left(\nu\cdot\frac{\partial\cos 2\theta}{\partial\sigma_{xx}} + \frac{\partial\cos 2\theta}{\partial\sigma_{yy}}\right)_n\right) \\
&- \Delta\lambda\frac{E}{1-\nu^2}\left(\frac{a}{1+2a}\frac{\partial\phi}{\partial\cos 2\theta}\left(\frac{\partial\cos 2\theta}{\partial\sigma_{xx}} + \nu\cdot\frac{\partial\cos 2\theta}{\partial\sigma_{yy}}\right)_n + \frac{1+a}{1+2a}\frac{\partial\phi}{\partial\cos 2\theta}\left(\nu\cdot\frac{\partial\cos 2\theta}{\partial\sigma_{xx}} + \frac{\partial\cos 2\theta}{\partial\sigma_{yy}}\right)_n\right) = \\
&f1(\mu,\theta)\cdot\sigma_v + f2(\mu,\theta)\cdot\sigma_v
\end{aligned} \qquad (40)$$

Or simplified, taking into account that $\partial\cos 2\theta/\partial\sigma_{xx} = -\partial\cos 2\theta/\partial\sigma_{yy}$

$$\sigma_{xx\,t} + \sigma_{yy\,t} - \frac{\Delta\lambda\left(\frac{\partial f2(\mu,\theta)}{\partial\mu} - \frac{\partial f1(\mu,\theta)}{\partial\mu}\right)_n}{\left(\frac{\partial f2(\mu,\theta)}{\partial\mu} f1(\mu,\theta) - \frac{\partial f1(\mu,\theta)}{\partial\mu} f2(\mu,\theta)\right)_n}(1+\nu)\frac{E}{1-\nu^2} \qquad (41)$$

$$= f1(\mu,\theta)\cdot\sigma_v + f2(\mu,\theta)\cdot\sigma_v$$

This gives an expression for $\Delta\lambda$:

$$\Delta\lambda = \frac{\sigma_{xx\,t} + \sigma_{yy\,t} - f1(\mu,\theta)\cdot\sigma_v + f2(\mu,\theta)\cdot\sigma_v}{\left(\frac{E}{1-\nu}\right)\frac{\left(\frac{\partial f2(\mu,\theta)}{\partial\mu} - \frac{\partial f1(\mu,\theta)}{\partial\mu}\right)_n}{\left(\frac{\partial f2(\mu,\theta)}{\partial\mu} f1(\lambda) - \frac{\partial f1(\mu,\theta)}{\partial\mu} f2(\mu,\theta)\right)_n}} \qquad (42)$$

When this expression is compared to expression (26), it can be concluded that taking into account the extra planar angle term does not influence the expression for $\Delta\lambda$.

When equations (35) are substituted in (39):

$$2\sqrt{\left(\frac{\begin{array}{l}\frac{a+1}{2a+1}\sigma_{xx\,t}+\frac{a}{2a+1}\sigma_{yy\,t}-\frac{a}{2a+1}\sigma_{xx\,t}-\frac{a+1}{2a+1}\sigma_{yy\,t}\\ -\Delta\lambda\frac{E}{1-\nu^2}\left(\frac{1+a}{1+2a}\frac{\partial\phi}{\partial\cos 2\theta}\left(\frac{\partial\cos 2\theta}{\partial\sigma_{xx}}+\nu\cdot\frac{\partial\cos 2\theta}{\partial\sigma_{yy}}\right)_n+\frac{a}{1+2a}\frac{\partial\phi}{\partial\cos 2\theta}\left(\nu\cdot\frac{\partial\cos 2\theta}{\partial\sigma_{xx}}+\frac{\partial\cos 2\theta}{\partial\sigma_{yy}}\right)_n\right)\\ +\Delta\lambda\frac{E}{1-\nu^2}\left(\frac{a}{1+2a}\frac{\partial\phi}{\partial\cos 2\theta}\left(\frac{\partial\cos 2\theta}{\partial\sigma_{xx}}+\nu\cdot\frac{\partial\cos 2\theta}{\partial\sigma_{yy}}\right)_n+\frac{1+a}{1+2a}\frac{\partial\phi}{\partial\cos 2\theta}\left(\nu\cdot\frac{\partial\cos 2\theta}{\partial\sigma_{xx}}+\frac{\partial\cos 2\theta}{\partial\sigma_{yy}}\right)_n\right)\end{array}}{2}\right)^2+\left(\left(\frac{1}{2a+1}\tau_{xy\,n}-\Delta\lambda\frac{E}{2(1+\nu)}\frac{1}{1+2a}\frac{\partial\phi}{\partial\cos 2\theta}\left(\frac{\partial\cos 2\theta}{\partial\tau_{xy}}\right)_n\right)_t\right)^2}$$

$$=f1(\mu,\theta)\cdot\sigma_v-f2(\mu,\theta)\cdot\sigma_v \qquad (43)$$

Or simplified, taking into account that $\partial\cos 2\theta/\partial\sigma_{xx} = -\partial\cos 2\theta/\partial\sigma_{yy}$ gives:

$$\frac{2}{1+2a}\sqrt{\left(\frac{\sigma_{xx\,t}-\sigma_{yy\,t}-\Delta\lambda\frac{E}{1-\nu^2}\left((1-\nu)\frac{\partial\phi}{\partial\cos 2\theta}\left(\frac{\partial\cos 2\theta}{\partial\sigma_{xx}}\right)_n-(1-\nu)\frac{\partial\phi}{\partial\cos 2\theta}\left(\frac{\partial\cos 2\theta}{\partial\sigma_{yy}}\right)_n\right)}{2}\right)^2+\left(\tau_{xy}-\Delta\lambda\frac{E}{2(1+\nu)}\frac{\partial\phi}{\partial\cos 2\theta}\left(\frac{\partial\cos 2\theta}{\partial\tau_{xy}}\right)_n\right)^2}$$

$$=f1(\mu,\theta)\cdot\sigma_v-f2(\mu,\theta)\cdot\sigma_v \qquad (44)$$

By substituting the expression for (a) into (44):

$$2\sqrt{\left(\frac{\sigma_{xx_t}-\sigma_{yy_t}-\Delta\lambda\frac{E}{1-\nu^2}\left((1-\nu)\frac{\partial\phi}{\partial\cos 2\theta}\left(\frac{\partial\cos 2\theta}{\partial\sigma_{xx}}\right)_n-(1-\nu)\frac{\partial\phi}{\partial\cos 2\theta}\left(\frac{\partial\cos 2\theta}{\partial\sigma_{yy}}\right)_n\right)}{2}\right)^2+\left(\tau_{xy_n}-\Delta\lambda\frac{E}{2(1+\nu)}\frac{\partial\phi}{\partial\cos 2\theta}\left(\frac{\partial\cos 2\theta}{\partial\tau_{xy}}\right)_n\right)^2}+ -\left(f1(\mu,\theta)\cdot\sigma_v-f2(\mu,\theta)\cdot\sigma_v\right)= \left(\frac{\left(\frac{\partial f1(\mu,\theta)}{\partial\mu}+\frac{\partial f2(\mu,\theta)}{\partial\mu}\right)_n\cdot E\cdot\Delta\lambda}{\sigma_v\cdot\left(f1(\mu,\theta)-f2(\mu,\theta)\right)\left(\frac{\partial f2(\mu,\theta)}{\partial\mu}-\frac{\partial f1(\mu,\theta)}{\partial\mu}\cdot\right)_n(1+\nu)}\cdot\sigma_v\cdot\left(f1(\mu,\theta)-f2(\mu,\theta)\right)\right) \quad (45)$$

By substituting the expression for $\Delta\lambda$ into the right-hand side of (45):

$$2\sqrt{\left(\frac{\sigma_{xxt}-\sigma_{yy_t}-\Delta\lambda\frac{E}{1-\nu^2}\left((1-\nu)\frac{\partial\phi}{\partial\cos 2\theta}\left(\frac{\partial\cos 2\theta}{\partial\sigma_{xx}}\right)_n-(1-\nu)\frac{\partial\phi}{\partial\cos 2\theta}\left(\frac{\partial\cos 2\theta}{\partial\sigma_{yy}}\right)_n\right)}{2}\right)^2+\left(\tau_{xy_t}-\Delta\lambda\frac{E}{2(1+\nu)}\frac{\partial\phi}{\partial\cos 2\theta}\left(\frac{\partial\cos 2\theta}{\partial\tau_{xy}}\right)_n\right)^2}+ -\left(f1(\mu,\theta)\cdot\sigma_v-f2(\mu,\theta)\cdot\sigma_v\right)= \left(\frac{\left(\frac{\partial f1(\mu,\theta)}{\partial\mu}+\frac{\partial f2(\mu,\theta)}{\partial\mu}\right)_n(1-\nu)}{\left(\frac{\partial f2(\mu,\theta)}{\partial\mu}-\frac{\partial f1(\mu,\theta)}{\partial\mu}\cdot\right)_n(1+\nu)}\cdot\left(\sigma_{xxt}+\sigma_{yy_t}\right)-\sigma_v\cdot\left(f1(\mu,\theta)+f2(\mu,\theta)\right)\right) \quad (46)$$

The expression for $\Delta\lambda$ can also be substituted into the left part of equation (45) or (46). When also the expressions (8) for $\partial\cos 2\theta/\partial\sigma_{xx}$, $\partial\cos 2\theta/\partial\sigma_{yy}$, $\partial\cos 2\theta/\partial\sigma_{yy}$ and (6) for $\partial\phi/\partial\cos 2\theta$ are substituted into (46), an equation for μ is obtained in which μ is the only unknown parameter. However, given the extensive expressions (6) and (8), the expression becomes to complicated to solve. Therefore the derivation of the Euler backward method with changing planar angle stops here. It is important to notice that the difference between (46) and the equation for μ of the Euler backward method with a constant planar angle (29) can be described as a deviation from the trial stress components:

- $\left(\sigma_{xx}\right)_t-\Delta\lambda\frac{E}{1-\nu^2}\left((1-\nu)\frac{\partial\phi}{\partial\cos 2\theta}\frac{\partial\cos 2\theta}{\partial\sigma_{xx}}\right)_n$ instead of $\left(\sigma_{xx}\right)_t$
- $\left(\sigma_{yy}\right)_t-\Delta\lambda\frac{E}{1-\nu^2}\left((1-\nu)\frac{\partial\phi}{\partial\cos 2\theta}\frac{\partial\cos 2\theta}{\partial\sigma_{yy}}\right)_n$ instead of $\left(\sigma_{yy}\right)_t$
- $\left(\tau_{xy}\right)_t-\Delta\lambda\frac{E}{2(1+\nu)}\left(\frac{\partial\phi}{\partial\cos 2\theta}\frac{\partial\cos 2\theta}{\partial\tau_{xy}}\right)_n$ instead of $\left(\tau_{xy}\right)_t$

(47)

Note that (46) are just the terms for the adaptation of the trial stress of section 3.4.

In finite element applications use is made of (47). First an estimate is made of the stress projection using the Euler backward method with a constant angle.

Subsequently the terms of (47) are determined with this first estimate. The trial stress is adapted from these terms, which leads to an adaptation of μ and $\Delta\lambda$. Then the projected stress is also adapted by using (30) instead of (13). Consequently the trial stress is adapted again on the basis of the new projected stress, which leads again to a new μ and $\Delta\lambda$ and so on. The procedure is repeated until convergence is reached. Scheme 3-1 illustrates the procedure.

Appendix C Derivative of the yield function with respect to the planar angle

In this appendix the derivative of the yield function with respect to the planar angle is elaborated. Because the yield function is defined as a direct function of the cosine of twice the planar angle, the derivative with respect to this term is found. It can be written as the derivative of the equivalent stress to the planar angle as follows:

$$\frac{\partial \phi}{\partial \cos(2\theta)} = \frac{\partial\left(\sigma_{eq}(\sigma_1,\sigma_2,\theta)-\sigma_y\right)}{\partial \cos(2\theta)} = \frac{\partial \sigma_{eq}(\sigma_1,\sigma_2,\theta)}{\cos(2\theta)}$$
$$\frac{\partial \phi}{\partial \cos(2\theta)} = \frac{\partial\left(\sigma_{eq}(\sigma_1,\sigma_2,\theta)-\sigma_y\right)}{\partial \cos(2\theta)} = \frac{\partial \sigma_{eq}(\sigma_1,\sigma_2,\theta)}{\partial \cos(2\theta)} \quad (1)$$

The starting point is equation 3.14:

$$\sigma_{eq} = \frac{\sigma_1}{f1(\mu,\theta)}$$
$$\sigma_{eq} = \frac{\sigma_2}{f2(\mu,\theta)} \quad (2)$$

with

$$f1(\mu,\theta) = \frac{\sigma_{10}(\theta) + 2\mu\cdot\left(\sigma_{11}(\theta)-\sigma_{10}(\theta)\right) + \mu^2\cdot\left(\sigma_{12}(\theta)+\sigma_{10}(\theta)-2\sigma_{11}(\theta)\right)}{\sigma_y} \quad (3)$$
$$f2(\mu,\theta) = \frac{\sigma_{20}(\theta) + 2\mu\cdot\left(\sigma_{21}(\theta)-\sigma_{20}(\theta)\right) + \mu^2\cdot\left(\sigma_{22}(\theta)+\sigma_{20}(\theta)-2\sigma_{21}(\theta)\right)}{\sigma_y}$$

The principal stresses are not dependent on the planar angle:

$$\frac{\partial \sigma_1}{\partial \cos(2\theta)} = \frac{\partial \sigma_{eq}}{\partial \cos(2\theta)}\cdot f1(\mu,\theta) + \frac{\partial f1(\mu,\theta)}{\partial \cos(2\theta)}\cdot\sigma_{eq} = 0$$
$$\frac{\partial \sigma_2}{\partial \cos(2\theta)} = \frac{\partial \sigma_{eq}}{\partial \cos(2\theta)}\cdot f2(\mu,\theta) + \frac{\partial f2(\mu,\theta)}{\partial \cos(2\theta)}\cdot\sigma_{eq} = 0 \quad (4)$$

From (4) two expressions for the derivative of the equivalent stress to cos(2θ) are obtained:

$$\frac{\partial \sigma_{eq}}{\partial \cos(2\theta)} = -\frac{\sigma_{eq}}{f1(\mu,\theta)}\cdot\frac{\partial f1(\mu,\theta)}{\partial \cos(2\theta)}$$
$$\frac{\partial \sigma_{eq}}{\partial \cos(2\theta)} = -\frac{\sigma_{eq}}{f2(\mu,\theta)}\cdot\frac{\partial f2(\mu,\theta)}{\partial \cos(2\theta)} \quad (5)$$

The two expressions (5) can be equalised:

$$\frac{1}{f1(\mu,\theta)}\cdot\frac{\partial f1(\mu,\theta)}{\partial\cos(2\theta)}=\frac{1}{f2(\mu,\theta)}\cdot\frac{\partial f2(\mu,\theta)}{\partial\cos(2\theta)} \tag{6}$$

In (6) the derivatives with respect to the term cos(2θ) are written as:

$$\begin{aligned}\frac{\partial f1(\mu,\theta)}{\partial\cos(2\theta)}&=\left(\frac{\partial f1(\mu,\theta)}{\partial\cos(2\theta)}\right)_{\mu\_const}+\left(\frac{\partial f1(\mu,\theta)}{\partial\mu}\right)_{\theta\_const}\cdot\frac{\partial\mu}{\partial\cos(2\theta)}\\ \frac{\partial f2(\mu,\theta)}{\partial\cos(2\theta)}&=\left(\frac{\partial f2(\mu,\theta)}{\partial\cos(2\theta)}\right)_{\mu\_const}+\left(\frac{\partial f2(\mu,\theta)}{\partial\mu}\right)_{\theta\_const}\cdot\frac{\partial\mu}{\partial\cos(2\theta)}\end{aligned} \tag{7}$$

By substituting (7) in (6) the derivative of μ with respect to cos(2θ) can be written:

$$\frac{\partial\mu}{\partial\cos(2\theta)}=\frac{f2(\mu,\theta)\cdot\left(\frac{\partial f1(\mu,\theta)}{\partial\cos(2\theta)}\right)_{\mu\_const}-f1(\mu,\theta)\cdot\left(\frac{\partial f2(\mu,\theta)}{\partial\cos(2\theta)}\right)_{\mu\_const}}{f1(\mu,\theta)\cdot\left(\frac{\partial f2(\mu,\theta)}{\partial\mu}\right)_{\theta\_const}-f2(\mu,\theta)\cdot\left(\frac{\partial f1(\mu,\theta)}{\partial\mu}\right)_{\theta\_const}} \tag{8}$$

Now (8) is substituted in (7). By substituting (7) in (5) and making use of (1) and (2), an expression for the derivative of the yield function with respect to cos(2θ) is obtained:

$$\begin{aligned}\frac{\partial\phi}{\partial\cos(2\theta)}=&-\frac{\sigma_1}{(f1(\mu,\theta))^2}\left(\frac{\partial f1(\mu,\theta)}{\partial\cos(2\theta)}+\frac{\partial f1(\mu,\theta)}{\partial\mu}\cdot\frac{f2(\mu,\theta)\cdot\frac{\partial f1(\mu,\theta)}{\partial\cos(2\theta)}-f1(\mu,\theta)\cdot\frac{\partial f2(\mu,\theta)}{\partial\cos(2\theta)}}{\frac{\partial f2(\mu,\theta)}{\partial\mu}\cdot f1(\mu,\theta)-\frac{\partial f1(\mu,\theta)}{\partial\mu}\cdot f2(\mu,\theta)}\right)=\\ &-\frac{\sigma2}{(f2(\mu,\theta))^2}\left(\frac{\partial f2(\mu,\theta)}{\partial\cos(2\theta)}+\frac{\partial f2(\mu,\theta)}{\partial\mu}\cdot\frac{f2(\mu,\theta)\cdot\frac{\partial f1(\mu,\theta)}{\partial\cos(2\theta)}-f1(\mu,\theta)\cdot\frac{\partial f2(\mu,\theta)}{\partial\cos(2\theta)}}{\frac{\partial f2(\mu,\theta)}{\partial\mu}\cdot f1(\mu,\theta)-\frac{\partial f1(\mu,\theta)}{\partial\mu}\cdot f2(\mu,\theta)}\right)\end{aligned} \tag{9}$$

Appendix D Isotropic hardening parameter (f)

When isotropic hardening is assumed, the tensor ($\underline{\beta}$) in (2.16) can be replaced by the yield stress (σ_y):

$$\dot{\phi} = \frac{\partial \phi}{\partial \underline{\sigma}} : \underline{\dot{\sigma}} + \frac{\partial \phi}{\partial \sigma_y} \dot{\sigma}_y = 0 \qquad (1)$$

Commonly the yield stress (σ_y) is related to the equivalent plastic strain (ε_p), so (1) can be written as:

$$\dot{\phi} = \frac{\partial \phi}{\partial \underline{\sigma}} : \underline{\dot{\sigma}} + \frac{\partial \phi}{\partial \sigma_y} \frac{d\sigma_y}{d\varepsilon_p} \dot{\varepsilon}_p = 0 \qquad (2)$$

The second term is proportional to the plastic multiplier rate:

$$\frac{\partial \phi}{\partial \sigma_y} \frac{d\sigma_y}{d\varepsilon_p} \dot{\varepsilon}_p = f\dot{\lambda} \qquad (3)$$

and consequently:

$$\dot{\phi} = \frac{\partial \phi}{\partial \underline{\sigma}} : \underline{\dot{\sigma}} + f\dot{\lambda} = 0 \qquad (4)$$

The plastic strain rate is connected to the plastic multiplier rate by the normality principle of Drucker:

$$\underline{\dot{\varepsilon}}^p = \dot{\lambda} \frac{\partial \phi}{\partial \underline{\sigma}} \qquad (5)$$

The equivalent plastic strain rate is related to the plastic strain rate by:

$$\sigma_y \dot{\varepsilon}_p = \underline{\sigma} : \underline{\dot{\varepsilon}}^p \qquad (6)$$

By the substitution of (5) into (6), the equivalent plastic strain rate is expressed as a function of the plastic multiplier rate:

$$\dot{\varepsilon}_p = \dot{\lambda} \frac{\underline{\sigma}}{\sigma_y} : \frac{\partial \phi}{\partial \underline{\sigma}} \qquad (7)$$

Subsequently (7) is substituted into (3) to derive an expression for (f) in the equivalent plastic strain rate:

$$\frac{\partial \phi}{\partial \sigma_y}\frac{\partial \sigma_y}{\partial \varepsilon_p}\dot{\lambda}\frac{\underline{\sigma}}{\sigma_y}:\frac{\partial \phi}{\partial \underline{\sigma}} = f\dot{\lambda} \qquad (8)$$

and consequently:

$$f = \frac{\partial \phi}{\partial \sigma_y}\frac{d\sigma_y}{d\varepsilon_p}\frac{\underline{\sigma}}{\sigma_y}:\frac{\partial \phi}{\partial \underline{\sigma}} \qquad (9)$$

The first term of (9) is obtained by equation (3.10):

$$\frac{\partial \phi}{\partial \sigma_y} = -1 \qquad (10)$$

The last part of (9) is elaborated for the Vegter yield function to:

$$\frac{\underline{\sigma}}{\sigma_y}:\frac{\partial \phi}{\partial \underline{\sigma}} = \frac{\sigma_{xx}}{\sigma_y}\frac{\partial \phi}{\partial \sigma_{xx}} + \frac{\sigma_{yy}}{\sigma_y}\frac{\partial \phi}{\partial \sigma_{yy}} + \frac{\tau_{xy}}{\sigma_y}\frac{\partial \phi}{\partial \tau_{xy}} = \frac{\sigma_1}{\sigma_y}\frac{\partial \phi}{\partial \sigma_1} + \frac{\sigma_2}{\sigma_y}\frac{\partial \phi}{\partial \sigma_2} =$$

$$f1(\mu,\theta)\frac{\dfrac{\partial f2(\mu,\theta)}{\partial \mu}}{\dfrac{\partial f2(\mu,\theta)}{\partial \mu}\cdot f1(\mu,\theta) - \dfrac{\partial f1(\mu,\theta)}{\partial \mu}\cdot f2(\mu,\theta)} + \qquad (11)$$

$$f2(\mu,\theta)\frac{\dfrac{\partial f1(\mu,\theta)}{\partial \mu}}{\dfrac{\partial f1(\mu,\theta)}{\partial \mu}\cdot f2(\mu,\theta) - \dfrac{\partial f2(\mu,\theta)}{\partial \mu}\cdot f1(\mu,\theta)} =$$

$$1$$

By substitution of (10) and (11) into (9), the hardening parameter (f) is defined by:

$$f = -\frac{d\sigma_y}{d\varepsilon_p} \qquad (12)$$

Appendix E Yield surface based on constant slope reference points

In order to simplify the calculation of the derivative of the yield function, a Bezier function based upon reference points with constant gradients is investigated. In the current Vegter function the positions and the gradients of the reference points vary with the planar angle. To determine the hinge points, first the positions of the reference points are interpolated and subsequently the gradients. Then the positions of the hinge points are defined by the intersection of the gradients in the reference points, see also section 3.2. The derivative of the yield function with respect to the planar angle depends on the derivative of the components of the Bezier curve (f1 and f2) with respect to the planar angle, see also appendix C:

$$\frac{\partial \phi}{\partial \cos(2\theta)} = \frac{\partial \phi}{\partial \cos(2\theta)} \left(\frac{\partial f1(\mu,\theta)}{\partial \cos(2\theta)}, \frac{\partial f2(\mu,\theta)}{\partial \cos(2\theta)} \right) \tag{1}$$

With the current definition of the hinge points this expression becomes very extensive. When the reference points are chosen with constant gradients, only the positions of the reference points vary with the planar angle. Then the hinge points can be determined more easily by interpolated positions without the interpolation of the gradients. This could provide a more easy derivation.

So the gain of this procedure is a simplified calculation of the individual components of the derivative of the yield function with respect to the stress. Because both the interpolation of the reference points and that of the hinge points comes down to the interpolation of positions, the partial derivatives of the components of the Bezier curve can be written in a matrix form:

$$\begin{aligned} fi(\mu,\theta) &= \{\mu\} \cdot [Q_i] \cdot \{c\} \\ \left.\frac{\partial fi}{\partial \mu}\right|_{\theta\_const} &= \{d\mu\} \cdot [Q_i] \cdot \{c\} \\ \left.\frac{\partial fi}{\partial \cos(2\theta)}\right|_{\mu\_const} &= \{\mu\} \cdot [Q_i] \cdot \{dc\} \end{aligned} \tag{2}$$

where

f_i is given by (3.13)

$$\{\mu\} = \{1 \quad \mu \quad \mu^2\}$$
$$\{d\mu\} = \{0 \quad 1 \quad 2\mu\}$$
$$\{c\} = \begin{Bmatrix} 1 \\ \cos(2\theta) \\ \cos(2\theta)^2 \end{Bmatrix} \qquad \{dc\} = \begin{Bmatrix} 0 \\ 1 \\ 2\cos(2\theta) \end{Bmatrix}$$

$[Q_i]$ represents a 3×3 matrix consisting of constants.

To formulate reference points with constant gradients, the current reference points have to be shifted. For instance the uni-axial reference point will not be situated on the first principal axis for each planar angle, see figure E-1. In fact the uni-axial reference point no longer represents a real uni-axial stress state. So the relation with the uni-axial experiment is less straightforward. This is also the case with the other reference points.

At this moment no real judgement of the viability of the alternative reference points can be given. The adaptation provides a faster calculation of the partial derivatives and more orderly expressions in a finite element code. The disadvantage of the method is that the positions of the reference points have to be shifted and therefore have a less straightforward relation with measured data. Because the method is not appropriate to directly solve all complications in the Euler backward method (section 3.4), it has not been elaborated further yet.

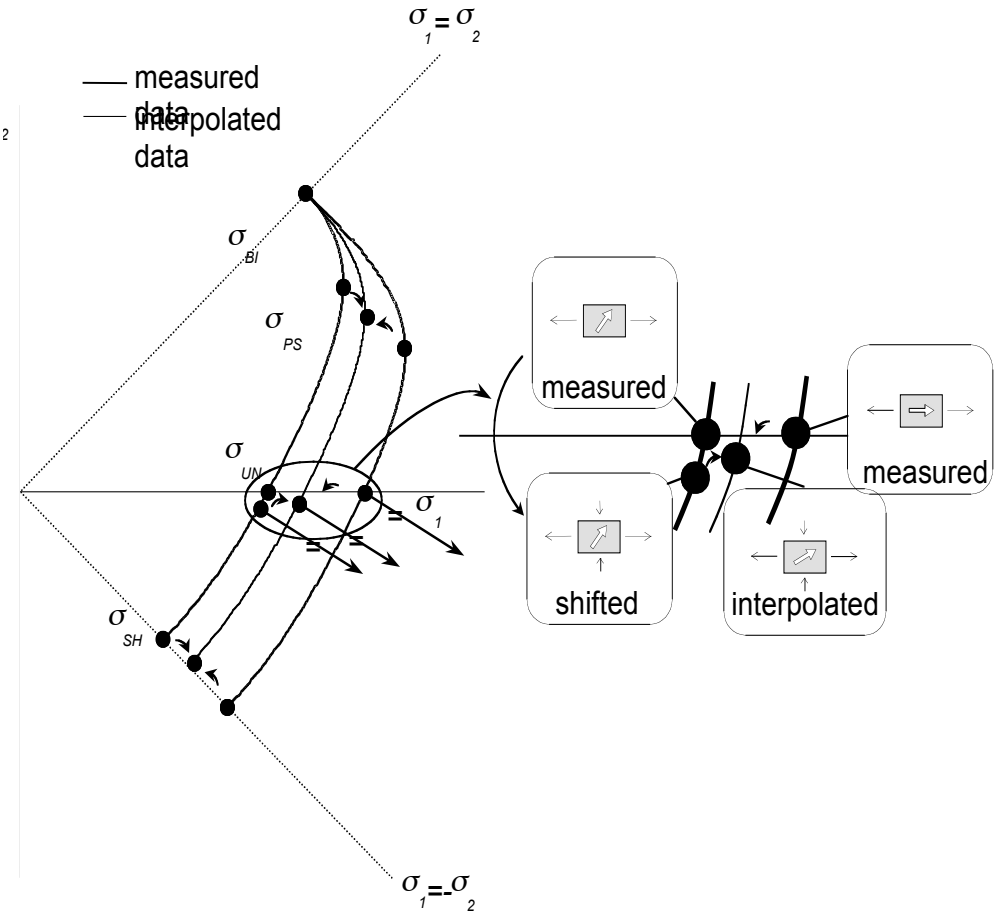

Figure E-1 Shift of the uni-axial reference point in order to obtain a constant strain vector for different planar angles

Appendix F Design of clamping equipment

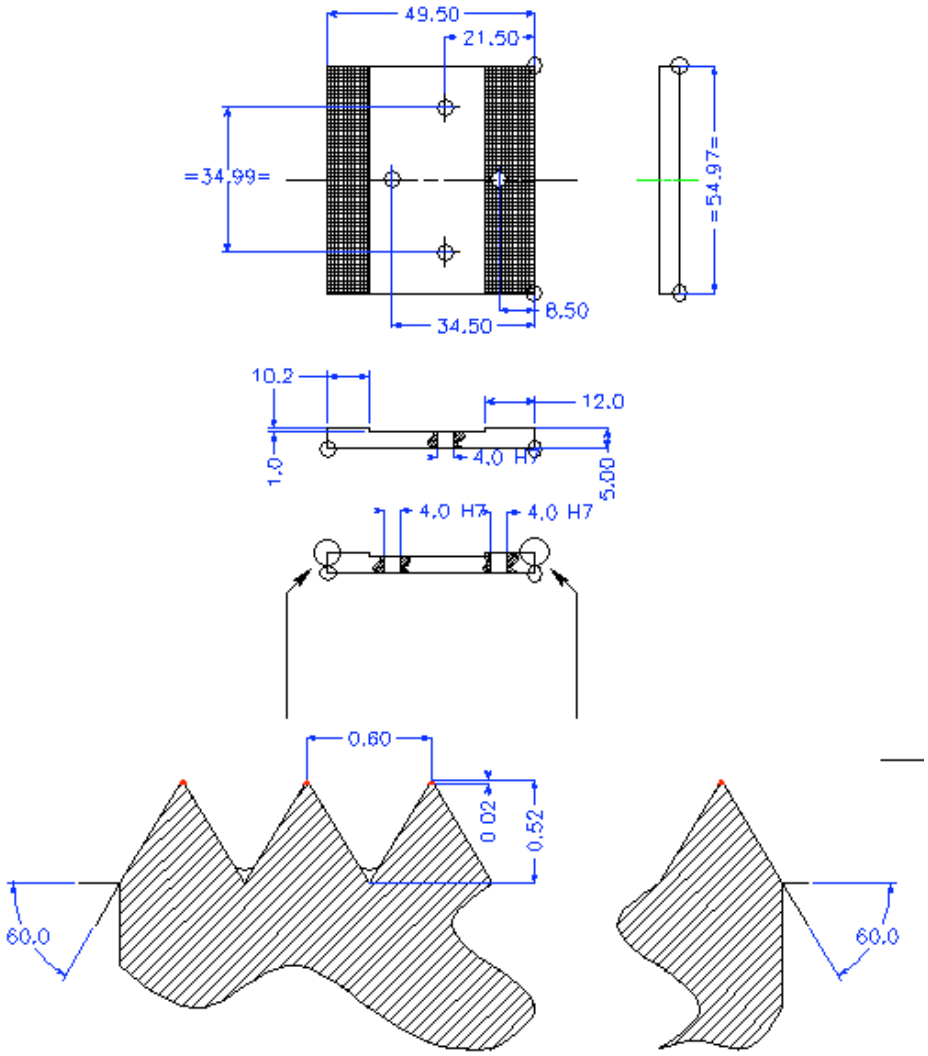

*Aantal:4
*Materiaal:UHB ARNE AISI 01–
UDDEHOLMS AKTIEBOLAG SCHWEDEN
*Harden en ontlaten:
–825 graden harden
–200 graden ontlaten
zie aangehechte copie

Opm. 1

*De aangegeven hoeken
0.5*45 afschuinen d.m.v.
vlakslijpen

OPm.2

*Gearceerde oppervlak frictieblok
in 2 loodrechte richtingen
bewerken als aangegeven
*Aanzet beitel 0.60 mm
*Beitel indringdiepte vanaf scherpe
punt 0.52 mm
*0.02 mm naslijpen oppervlakte
ter verwijdering bramen
*Afronding beitel naar eigen inzicht
*Na bewerken gaten vonken

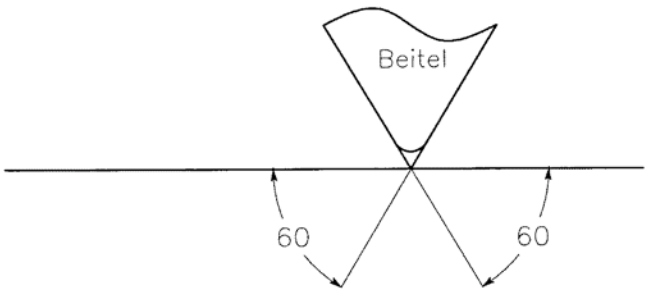

Frictieblok		Schaal: 1:1 Datum:29–4–99
		Getekend: H.H. Pijlman
	Universiteit Twente Werktuigbouwkunde	
		Behoort bij Multi–ax tester
		Aantal: 4

Appendix G Design of bearing blocks

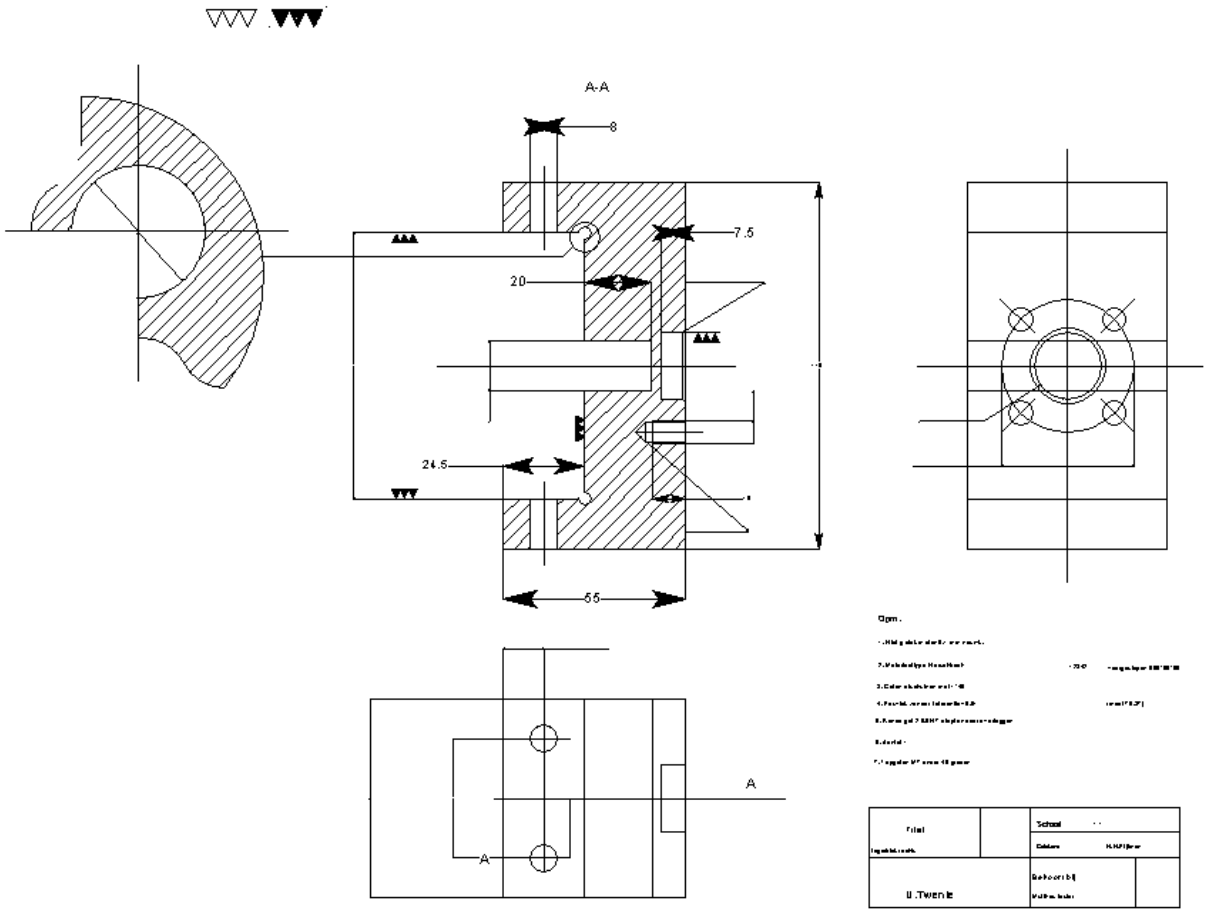

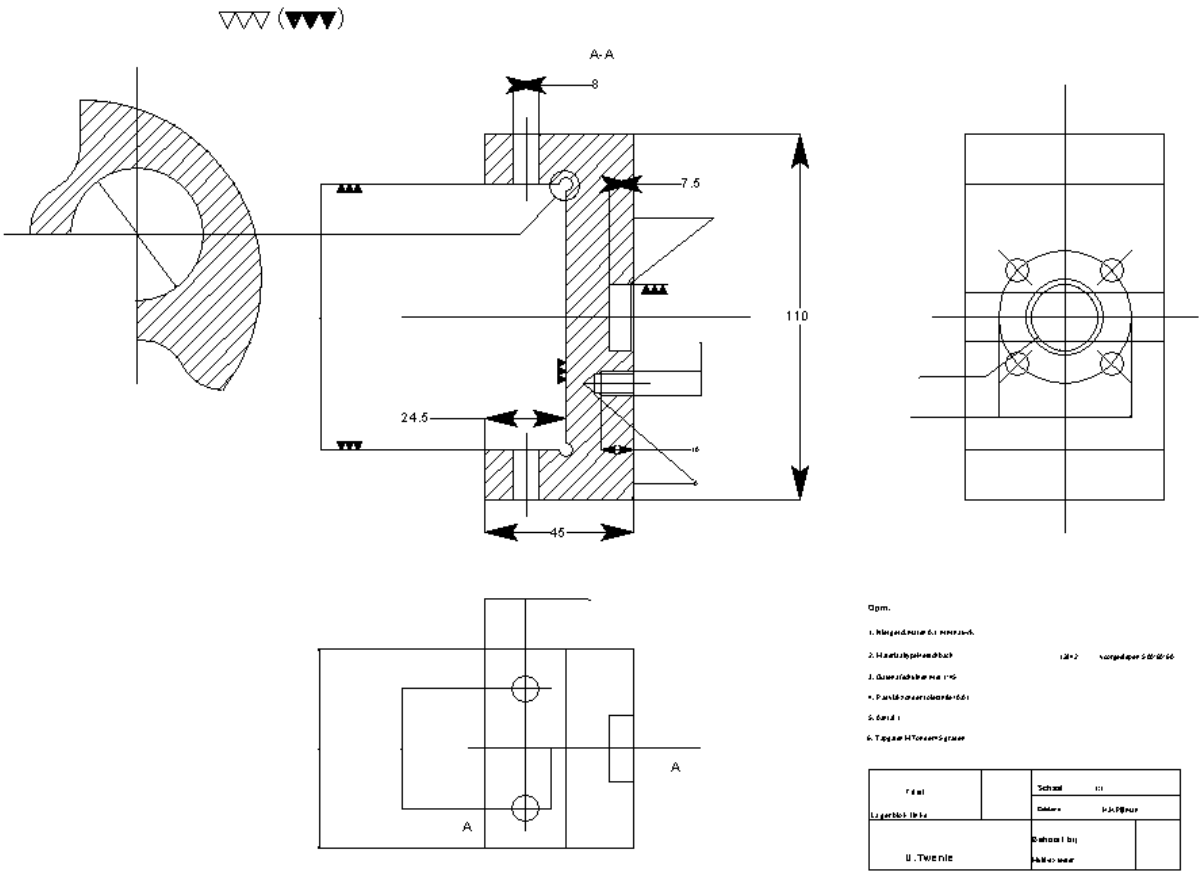

Opm.

1. [illegible]

2. [illegible] 12H7 vorgedraaid 58/62/66

3. [illegible]

4. [illegible]

5. [illegible]

6. [illegible]

Titel Liggerblok links		School Docent	
U.Twente		Datum Schaal 1:1	

Opm:

1. Niet getol. maten 0.1 mm nauwk.

2. Materiaaltype Herschbach 12842 voorgeslepen 500*60*60

3. Gaten afschuinen met 1*45

4. Pasvlak zonder tolerantie +0.01 (maat 79.87)

5. Ronde gat 20.0 H7 diepte nader overleggen

6. Aantal 1

7. Tapgaten M7 onder 45 graden

Titel Lagerblok rechts		Schaal 1:1 Getekend H.H.Pijlman
U.Twente	Behoort bij Multi-ax tester	

Appendix H Accuracy of test equipment measurements

In order to obtain the accuracy of the results of the shear and plane strain factor, the dispersion in the individual measured data is investigated. Then the combination of the individual dispersions provides the dispersion of the two factors. This gives an idea of the accuracy of the measurements. In many cases no exact values can be given of certain data. For instance in one test the initial distance between dots could be 50 pixels, whereas the other test could begin with a pixel distance of 60. This initial pixel distance does not influence the interpretation of the data, but has an influence on the accuracy. Therefore in the determination of the accuracy worst cases are taken. In the case of the initial pixel distance 50 pixels are taken. A precise statistical procedure which provides the standard deviation of the data has not been carried out.

Data measured during the test are:

- Measured force in horizontal direction on the upper clamp
  The accuracy of the horizontal force is ± 20 N
- Measured force in vertical direction on the lower clamp
  The accuracy of the vertical force is ± 50 N
- Measured horizontal displacement on the upper clamp
  The accuracy of the horizontal displacement is not known. The displacement is not used in the interpretation of the results, so it is neglected.
- Measured vertical displacement on the lower clamp
  The accuracy of the horizontal displacement is not known. The displacement is not used in the interpretation of the results, so it is also neglected.
- Measured deformation by the vision system
  The accuracy of determining the centre of a dot is 0.4 pixel
- Measured thickness of the sheet
  The thickness is measured to an accuracy of 0.005 mm

Plane strain parameter (fps) accuracy

The accuracy of the plane strain factor is determined by first determining the dispersion of the strain measurement and subsequently the dispersion of the stress determination. On the basis of this analysis the worst and best cases for the plane strain factor is determined.

Strain measurement

The strain ε_{ps} is measured by dividing the vertical distance between the centre of the dots by the initial vertical distance. The initial distance is about 60 pixels, worst case 50 pixels. The dispersion is 0.4 pixel. Therefore the accuracy of the measured strain can be determined as follows.

In the initial configuration of the test the nominal strain is 0 %. The maximum possible strain calculated by the vision system is equal to:

$$\varepsilon_{ps} = \ln\left(\frac{50 + 0.4}{50 - 0.4}\right) = 1.6\%$$

The minimum strain is equal to:

$$\varepsilon_{ps} = \ln\left(\frac{50 - 0.4}{50 + 0.4}\right) = -1.6\%$$

When a plane strain test is finished, the distance between the dots has changed to at least 70 pixels. Then the nominal strain is 33.6 %. The maximum strain is equal to:

$$\varepsilon_{ps} = \ln\left(\frac{70 + 0.4}{50 - 0.4}\right) = 35.0\%$$

The minimum strain is equal to:

$$\varepsilon_{ps} = \ln\left(\frac{70 - 0.4}{50 + 0.4}\right) = 32.3\%$$

So in general the strain in the test can be calculated to an absolute accuracy of 1.6%. Because the time is assumed to be absolute, the strain rate accuracy is related directly to the accuracy of the strain.

Stress measurement

The stress is determined by the force on the clamps, the initial thickness of the sheet and the thickness strain, corrected with a correction factor determined by a finite element simulation:

$$\sigma_{ps} = \frac{Fy}{45 \cdot \left[d_{ini} \cdot e^{(-\varepsilon_{ps})}\right]} Corr(\varepsilon_{ps})$$

where

σ_{ps}	is the plane strain stress
Fy	is the force on the clamp in vertical direction
d_{ini}	is the initial thickness of the sheet
ε_{ps}	is the strain in tensile direction
Corr(ε_{ps})	is a correction factor determined by the finite element calculation

Note that the dispersion of the stress also depends on the dispersion of the strain measurement. The correction factor will be left out in the rest of the determination of the accuracy. The plane strain factor is fitted for strains ranging from 8 to 18 %. Therefore the accuracy of the stress at a strain of 8 % and at a strain of 18 % is determined:

εps= 8 %:

The nominal stress in this case is:

$$\sigma_{ps} = \frac{12670}{45 \cdot \left[(0.80 \cdot e^{(-0.08)}\right]} = 381.3\,Mpa$$

The maximum stress in this case is equal to:

$$\sigma_{ps} = \frac{12670 + 50}{45 \cdot \left[(0.80 - 0.005) \cdot e^{(-0.08-0.016)}\right]} = 391.4\,Mpa = 102.6\% \cdot \sigma_{ps,no\min al}$$

The minimum stress is equal to:

$$\sigma_{ps} = \frac{12670 - 50}{45 \cdot \left[(0.80 + 0.005) \cdot e^{(-0.08+0.016)}\right]} = 371.4\,Mpa = 97.4\% \cdot \sigma_{ps,no\min al}$$

εps= 18 %:

The nominal stress in this case is:

$$\sigma_{ps} = \frac{13860}{45 \cdot \left[(0.80 \cdot e^{(-0.18)}\right]} = 460.9\,Mpa$$

The maximum stress in this case is equal to:

$$\sigma_{ps} = \frac{13860 + 50}{45 \cdot \left[(0.80 - 0.005) \cdot e^{(-0.18-0.016)}\right]} = 473.0\,Mpa = 102.6\% \cdot \sigma_{ps,no\min al}$$

The minimum stress is equal to:

$$\sigma_{ps} = \frac{13860 - 50}{45 \cdot \left[(0.80 + 0.005) \cdot e^{(-0.18+0.016)}\right]} = 449.2\,Mpa = 97.5\% \cdot \sigma_{ps,no\min al}$$

So the stress is calculated to an accuracy of 2.6 %.

Results summarized

The strain measurement is accurate to an absolute strain of 0.016.
The strain rate is accurate to an absolute value of $0.016/t_{test}$.
The stress measurement is accurate to a relative value of 2.6 %.

Now the influence on the plane strain factor fps can be investigated by varying the data with their inaccuracy. The first option is to vary the strain data with +0.016 and –0.016 and the stress data with +2.6 % and –2.6 %. Subsequently the influence on the resulting plane strain parameter can be obtained by the least squares method. However, the accuracy of the stress is dependent on the accuracy of the strain measurement. Therefore the stress cannot be varied independently from the strain. The second option is to vary all independent data with their inaccuracy. For instance the thickness can be taken 0.005 mm greater than the measured thickness. Subsequently the difference in the factors fps due to the variation in thickness can be obtained by the least squares method. In a similar way the difference in the plane strain factor by a variation in the strain data can be investigated. Also the difference by the variation of the thickness, measured force and the strain data can be obtained in the same way.

It appears that the largest plane strain factor is obtained by:

- a variation of the measured force by +50 N
- a variation of the measured thickness by –0.005 mm
- a variation of the strain by - 0.016

The smallest plane strain factor is obtained by:

- a variation of the measured force by -50 N
- a variation of the measured thickness by +0.005 mm
- a variation of the strain by + 0.016

Based upon these results, the variation in the factor fps is equal to + 0.03 or –0.03. Hence the absolute accuracy of the plane strain factor is ±0.03

Shear parameter (fsh) accuracy

The accuracy of the shear factor is determined by first determining the accuracy of the strain measurement and subsequently the accuracy of the stress determination. On the basis of this analysis the worst and best cases for the shear factor are determined.

Strain measurement

The shear strain γ_{sh} is measured by dividing the relative horizontal displacement of the centre of dots by the vertical distance. The vertical distance is about 60 pixels, worst case 50 pixels. The dispersion is 0.4 pixel. Therefore the accuracy of the measured shear strain can be determined as follows.

In the initial configuration of the test the nominal strain is 0 %. The maximum possible strain calculated by the vision system is equal to:

$$\gamma_{sh} = \left(\frac{0.4}{50 - 0.4} \right) = 0.8\%$$

The minimum strain is equal to:

$$\gamma_{sh} = \left(\frac{-0.4}{50 - 0.4} \right) = -0.8\%$$

At the end of a shear test has been finished, the relative horizontal distance has changed to at least 20 pixels. Then the nominal strain is 40 %. The maximum strain is equal to:

$$\gamma_{sh} = \left(\frac{20 + 0.4}{50 - 0.4} \right) = 41.1\%$$

The minimum strain is equal to:

$$\gamma_{sh} = \left(\frac{20 - 0.4}{50 + 0.4} \right) = 38.9\%$$

So in general the strain in the test can be calculated to an absolute accuracy of 1.1%. Because the time is assumed to be absolute the strain rate accuracy is related directly to the accuracy of the strain.

Stress measurement

The stress is determined by the force on the clamps, the initial thickness of the sheet, corrected with a correction factor determined by a finite element simulation:

$$\sigma_{sh} = \frac{Fx}{45 \cdot [d_{ini}]} \cdot Corr(\gamma_{sh})$$

where

σ_{sh}	is the shear stress
Fx	is the force on the clamp in horizontal direction
d_{ini}	is the initial thickness of the sheet
Corr(γ_{sh})	is a correction factor determined by the finite element calculation

Note that, in contrast to the plane strain stress, the accuracy of the shear stress is not dependent on the accuracy of the strain measurement. The correction factor will be left out in the rest of the determination of the accuracy. The shear factor is fitted for strains ranging from 8 to 18 %. Therefore the accuracy of the stress at the strain of 8% and at the strain of 18 % is determined:

γ_{sh}= 8 %:

The nominal stress in this case is:

$$\sigma_{sh} = \frac{5133}{45 \cdot \left[(0.80\right]} = 142.6\,Mpa$$

The maximum stress in this case is equal to:

$$\sigma_{sh} = \frac{5133 + 20}{45 \cdot \left[(0.80 - 0.005)\right]} = 144.0\,Mpa = 101.0\% \cdot \sigma_{sh,nominal}$$

The minimum stress is equal to:

$$\sigma_{sh} = \frac{5133 - 20}{45 \cdot \left[(0.80 + 0.005)\right]} = 141.1\,Mpa = 99.0\% \cdot \sigma_{sh,nominal}$$

γ_{sh}= 18 %:

The nominal stress in this case is:

$$\sigma_{sh} = \frac{6363}{45 \cdot \left[(0.80\right]} = 176.8\,Mpa$$

The maximum stress in this case is equal to:

$$\sigma_{sh} = \frac{6363 + 20}{45 \cdot \left[(0.80 - 0.005)\right]} = 178.4\,Mpa = 100.9\% \cdot \sigma_{sh,nominal}$$

The minimum stress is equal to:

$$\sigma_{sh} = \frac{6363 - 20}{45 \cdot \left[(0.80 + 0.005)\right]} = 175.1\,Mpa = 99.0\% \cdot \sigma_{sh,nominal}$$

So the stress is calculated to an accuracy of 1 %.

Results summarized

The strain measurement is accurate to an absolute strain of 0.011.
The strain rate is accurate to an absolute value of $0.011/t_{test}$.
The stress measurement is accurate to a relative value of 1 %.

Now the influence on the shear factor f_{sh} can be investigated by varying the data with their inaccuracy. This influence can be obtained in the same way as for the plane strain parameter f_{ps}.

It appears that the largest shear factor is obtained by:

- a variation of the measured force by +20 N
- a variation of the measured thickness by –0.005 mm
- a variation of the strain by - 0.011

The smallest plane strain factor is obtained by:

- a variation of the measured force by -20 N
- a variation of the measured thickness by +0.005 mm
- a variation of the strain by + 0.011

Based upon these results, the variation in the factor f_{sh} is equal to + 0.015 or –0.015. So the absolute accuracy of the shear factor is ±0.015.

Appendix I Extension of the Vegter yield function with (τ_{xz}) and (τ_{yz})

Mindlin sheet elements also take into account a shear deformation (γ_{xz} and γ_{yz}) normal to the sheet. An option is to incorporate the shear stresses (τ_{xz} and τ_{yz}) similar to the von Mises yield function. The Von Mises function without these shear stresses is given by:

$$\sqrt{(\sigma_{xx}-\sigma_{yy})^2+(\sigma_{yy})^2+(\sigma_{xx})^2+6\cdot(\tau_{xy})^2}-\sqrt{2}\cdot\sigma_{yield}=0 \qquad (1)$$

Formula (1) shows the von Mises function with implemented shear stresses normal to the sheet:

$$\sqrt{(\sigma_{xx}-\sigma_{yy})^2+(\sigma_{yy})^2+(\sigma_{xx})^2+6\cdot(\tau_{xy})^2+6\cdot(\tau_{xz})^2+6\cdot(\tau_{yz})}-\sqrt{2}\cdot\sigma_{yield}=0 \qquad (2)$$

Following the same procedure in the Vegter yield function, this function changes from

$$\phi=\frac{\sigma_1}{f1(\mu,\theta)}-\sigma_y \quad or \quad \phi=\frac{\sigma_2}{f2(\mu,\theta)}-\sigma_y \qquad (3)$$

to

$$\phi=\sqrt{\left(\frac{\sigma_1}{f1(\mu,\theta)}\right)^2+\frac{6}{2}\cdot\tau_{xz}{}^2+\frac{6}{2}\cdot\tau_{yz}{}^2}-\sigma_y \quad or \quad \phi=\sqrt{\left(\frac{\sigma_2}{f2(\mu,\theta)}\right)^2+\frac{6}{2}\cdot\tau_{xz}{}^2+\frac{6}{2}\cdot\tau_{yz}{}^2}-\sigma_y \qquad (4)$$

Equation (4) defines the Vegter yield function with the shear stresses in normal direction.

References

An, Y. (2001), *Strain path change effects on stretch formability of 6082 aluminium alloy*, Materials Science and Technology 17, p. 258-263

Barlat, F. (1990*), A six component yield function for anisotropic materials,* International Journal of Plasticity 7, p.693-712

Bergström, Y. (1969), *A dislocation model for the stress-strain behaviour of polycrystalline α-Fe with special emphasis on the variation of the densities of mobile and immobile dislocations*, Materials Science. Eng. 5, p.179-192

Borst, R. , *Computational strategies for strongly curved and non-smooth yield-criteria with applications to localisation of deformation*, Proceedings of Second International Conference on Computational Plasticity, Swansea, p.237-261

Carleer, B.D. (1997), *Finite element analysis of deep drawing*, ISBN 90-9010358-9

Corus RD&T, (2001), *The Phast way of strain measurement*, workshop Geodelta and Corus RD&T, Delft

Dewie, B.R. (1988), *Computer graphics for Engineers*, Harper & Row, New York

DVS, (1999), *Dottracker user manual*, Internal Report University of Twente, confidential, 1988

Gere, J.M. (1991), *Mechanics of Materials*, third edition, PWS-KENT Publishing Company, Boston

G'Sell, (1983), *Application of the plane simple shear test for determination of the plastic behaviour of solid polymers at large strains*, Journal of Material Science 18, p. 903-918

Hill , R. (1950), *Mathematical theory of plasticity*, Clarendon Press, Oxford

Hoogenboom, S. (1995), *The pure bending of sheet*, Journal of Materials Processing Technology 51, p. 274-295

Hoverlin, E. (1998), *Biaxial tests on cruciform specimens for the validation of crystallographic yield loci*, Journal of Materials Processing Technology 80-81, p. 545-550

Houtte, P. van (1997), *Modelling of anisotropy based texture and dislocation structure*, Elsevier Science 9, p. 274-284

Huetink, J. (1991), *Extension of Anisotropic hardening elastic-plastic theory to finite strains based on visco-elastic finite strain theory* – Proceedings of IUTAM symposium, Hannover

Inpro, (1989), *Durchführung von Versuchen zur Ermittlung von Fliesskurven für Tiefziehstahl der Güte ZStE 340*, internal report Inpro, confidential

Kevie, C. van de (1999), *Deep drawing simulation with PamStamp*, Hoogovens R&D internal report, confidential

Knockaert, R. (2001),*Experimental and numerical determination of texture evolution during deep drawing tests*, Journal of Materials Processing Technology 110, p. 300-311

Kuwabara, T. (1995), *Elastic-Plastic Behavior of Sheet Metal Subjected to In-plane Reverse loading*, Proceedings of Plasticity '95, Dynamic Plasticity and Structural Behaviors, p. 841-844

Kuwabara, T. (1998), *Measurement and analysis of different work hardening in cold-rolled steel sheet under bi-axial tension*, Journal of Material Processing Technology 80-81, p. 517-523

Liempt, P. van (1988), *A model of the deformation resistance and substructure of steel for large strains*, Internal Report Hoogovens Ijmuiden R&D, confidential

Meinders, T. (2000), *Developments in numerical simulations of the real-life deep drawing process*, ISBN 90-36514002

Meinders, T. (2001), *Improvement of implicit finite element code performance in deep drawing simulations*, Journal of Materials Processing Technology, to be published

Miyauchi, K. (1987), *On Simple Shear Deformation*, Scientific papers of the Institute of Physical and Chemical Research 81, p. 57-67

Numiform (1998), proceedings Numiform '98, Enschede

Numisheet (1999), *p*roceedings Numisheet '99, Besançon

Paulus, (1999), *Multi-axial testing and strain measurements by optical method*, Proceedings of Video Controlled Materials Testing, Nancy, p. 40-43

Salmon, R. (1987), *Computer Graphics; Systems and Concepts*, Addison-Wesley, 1987

Vegter H. (1991), *On the plastic behaviour of steel during sheet forming*, ISBN 90-9004373-X

Vegter, H. (1995), *A planar isotropic yield criterion based on mechanical testing at multi-axial stress states*, proceedings Numiform '95

Vegter, H. (1996), *Auxiliary Benchmarks AB2.1 and AB2.2,* proceedings Numisheet'96, Dearborn, p. 807-809, p. 826-833

Vegter, H. (1998), *Advanced material models in simulation of sheet forming processes and prediction of forming limits,* proceedings Esaform 1, Sophia Antipolis, p. 499-502

Vegter, H (1999), *Different Approaches to Describe the Plastic Material Behaviour of Steel and Aluminium-Alloys in Sheet Forming,* proceedings 2nd Esaform, Guimarães, p. 127-132

Vegter, H. (1999), *Advanced Mechanical Testing on Aluminium Alloys and Low Carbon Steels for Sheet Forming, p*roceedings Numisheet '99, Besançon

Vreede, P. (1992), *A finite Element method for simulations of 3-dimensional sheet metal forming*, ISBN 90-9004754-9

List of Symbols

Letters

f	hardening factor
v	poisson's ratio
x,y,z	carthesian coordinates

Capitals

E	elastic modulus
F,G,H	anisotropy factors for the Hill yield-criterion
R	R-value
R0, R45, R90	R-values in 0°, 45° and 90°

Greek symbols

δ	infinite small increment
Δ	increment
ε	normal strain component
γ	shear strain component
σ	normal stress component
τ	shear stress component
θ	planar angle
λ	plastic multiplier

Tensors/vectors

$\underline{\sigma}$	stress tensor
$\underline{\varepsilon}$	strain tensor
$\underline{\varepsilon}^{p}$	plastic strain tensor
$\underline{\varepsilon}^{el}$	elastic strain tensor
$\underline{\alpha}$	back stress tensor
$\underline{\beta}$	hardening tensor
$\underline{\dot{\sigma}}$	stress rate tensor
$\underline{\dot{\varepsilon}}$	strain rate tensor
$\underline{\dot{\varepsilon}}^{p}$	plastic strain rate tensor
$\underline{\dot{\varepsilon}}^{el}$	elastic strain rate tensor
$\underline{\dot{\alpha}}$	back stress rate tensor
$\underline{\dot{\beta}}$	hardening rate tensor
$\underline{\underline{E}}$	elasticity tensor
$\underline{\underline{Y}}$	plasticity tensor

Subscripts

i,j	vector/tensor component
t	trial situation
n	back scaled situation
x,y,z	vector/tensor component in x,y,z direction

Hardening function symbols

$\underline{\beta}$	hardening tensor
f	hardening factor
σ_y	yield stress, equal to the average uni-axial yield stress
σ_{eq}	equivalent yield stress
σ_{y0}	initial yield stress
σ_0	static yield stress
σ^*	dynamic yield stress
ε_p	equivalent plastic strain
ε_0	initial equivalent plastic strain
$\Delta\sigma_m$	stress increase constant for strain hardening
β	strain hardening constant
Ω	strain hardening constant
n'	strain hardening exponent
k	Boltzman number, $8.617 \cdot 10^{-5}$ eV
T	temperature
$\dot{\varepsilon}_p$	equivalent plastic strain rate
$\dot{\varepsilon}_0$	limit strain rate
σ^*_0	limit dynamic flow stress
m'	dynamic stress exponent
ΔG_0	maximum activation enthalpy
$\Delta\varepsilon_p$	equivalent plastic strain increment
Δt	time increment
σ_{wh}	work hardening part of yield stress
σ_{dyn}	dynamic part of yield stress
f_{ini}	initial hardening rate in a load reversal
f_{iso}	hardening rate at isotropic yielding
α_{eq}	equivalent back stress
α_{lim}	maximum equivalent back stress
q	anisotropic hardening parameter

Yield function symbols

ϕ	yield function
σ_1	first principal stress
σ_2	second principal stress
θ	planar angle
σ_{SH}	shear yield stress
σ_{UN}	uni-axial yield stress
σ_{PS}	plane strain yield stress
σ_{BI}	equi-bi-axial yield stress
α_{ps}	factor for second component of the plane strain point
$\begin{pmatrix}\sigma_1\\ \sigma_2\end{pmatrix}_0$	first reference point
$\begin{pmatrix}\sigma_1\\ \sigma_2\end{pmatrix}_1$	hinge point
$\begin{pmatrix}\sigma_1\\ \sigma_2\end{pmatrix}_2$	second reference point
$\begin{pmatrix}\sigma_1\\ \sigma_2\end{pmatrix}_i(\theta)$	reference/hinge point positions for the planar angle θ (i=0,1 or 2)
$\begin{pmatrix}\sigma_1\\ \sigma_2\end{pmatrix}_{i_n}(\theta)$	normalized reference/hinge point positions (i=0,1 or 2)
$g_1(\theta)$	gradient in first reference point for the planar angle θ
$g_2(\theta)$	gradient in second reference point for the planar angle θ
$\begin{pmatrix}\sigma fac_1\\ \sigma fac_2\end{pmatrix}_{i,j}$	vectors dependent on measured positions of reference points
$gfac_{i,j}$	factors dependent on measured gradients of reference points
μ	situation on Bezier-curve between two reference points
σ_y	yield stress, equal to the average uni-axial yield stress
σ_{eq}	equivalent yield stress
α_{ps}	factor for the second component of the plane-strain point
$f1(\mu,\theta)$ and $f2(\mu,\theta)$	normalized components of the situation on the Bezier curve
$\Delta\varepsilon_1^*$ and $\Delta\varepsilon_2^*$	normal strain increment components in the directions of the first and second principal stress respectively.
$\frac{\partial\phi}{\partial\underline{\sigma}}$	yield function derivative, defines the normal on the yield surface
$\underline{\alpha}$	back stress tensor
α_{eq}	equivalent back stress
α_{lim}	maximum equivalent back stress
θ_α	planar angle of the back stress
α_1	first principal back stress
α_2	second principal back stress

Symbols in experiments

Δu_{clamp}	clamp displacement
h_D	height of the deformation zone
FX	horizontal clamp force
L	length of the test piece
FY	vertical clamp force
a	initial sheet thickness
a_c	current sheet thickness
M	bending moment
b	width of sheet
t	thickness of sheet
ρ	curvature radius

Bedankt

Aan het tot stand komen van dit proefschrift hebben een groot aantal mensen meegewerkt. Ik denk daarbij niet alleen aan de steun die rechtstreeks heeft bijgedragen aan resultaten van het onderzoek maar ook aan de morele steun en de gezelligheid die misschien wel veel belangrijker zijn. Tijdens mijn werk hebben een zeer groot aantal mensen mij geholpen en ik wil hun bij deze bedanken. Ik wil beginnen met Joop, die grotendeels heeft gezorgd voor het tot stand komen van de twee-assige tester in dit proefschrift. Joop, je was naast degene die veel werk aan de tester heeft verricht iemand die gezellig was en aardig wat flauwekul kon tentoonspreiden. Bedankt voor de goede samenwerking. Ik wil mijn promotoren Han en Henk danken voor de leuke en ongedwongen manier van samenwerken en overleggen tijdens het onderzoek. Zonder jullie bijdrage was dit werk met zekerheid niet tot stand gekomen.

Nynke, sûnder dyn steun op het thùsfront soe dit wurk miskien wol onmoglik foar my west wêze. Do hast my faaks in hert under de riem stutsen en ik wol dy tige tanke foar al dyn soarch, ek doe it lestich of dreech wie op it wurk. Ek myn heit en mem fertsjinje hjirfoar seker een bedankje. Nêst dat ik altyt mei alles by jimme an komme koe hawwe jimme der foar soarge dat ik ek nog es my de bealch oan it wurk koe, dat hâld dy lichamelik en yn de kop in bytsje yn balans. Jan en Andor, jimme binne een sear balancerend factor wist yn de lêste tiit. Het ùtgean, de gesellichhyt en it flauwe praat sil ik net ferjitte en woe ik greach sa trochsette.

Annette, Gerrit en Timo (in chronologische volgorde), jullie wil ik bedanken voor je gezelligheid als kamergenoot. Ik denk dat ik het met jullie alle drie zeer goed heb kunnen vinden, niet iedereen heeft een zo relaxte en sociale manier van omgaan met elkaar als jullie. Ik wil in dit verband Timo extra bedanken. Timo, je hebt me in de laatste tijd naast het corrigeren van mijn proefschrift erg geholpen met het voor elkaar krijgen van gecompliceerde berekeningen, bij het laatste hoofdstuk had ik je niet kunnen missen. Yuguo, thanks for your great contribution in the validation by the experiments and simulations on the cylindrical cup drawing. It added a lot to the value of the developed model. Matthijs en Pawel wil ik danken voor hun bijdrage aan dit proefschrift. Jullie hebben met je afstudeerwerk bijgedragen aan het tot stand komen van een goede wiskundige beschrijving en a good validation of the developed material description. Naast Han, Timo en Henk hebben Ton en Marianna mij geholpen met de correktie van dit proefschrift, dank voor de kritische rectificaties en thanks for the fast corrections in the last days.

Met het uitvoeren van experimenten bij Corus hebben Leo en Frank mij zeer geholpen, bedankt voor jullie enthousiaste inzet hierbij. Stan heeft voor mij de buigexperimenten van hoofdstuk 6 uitgevoerd, het was prettig met je samen te werken. Voor het maken van benodigde gereedschappen ter uitvoering van de proeven met de twee-assige tester hebben Henk en Paul van het IMC veel moeite gedaan, ik wil jullie danken voor de flexibele manier van overleggen.

Met regel-activiteiten op de vakgroep zijn Annemarie en Debbie mij altijd zeer ter wille geweest. Zeer bedankt voor jullie flexibele inzet en natuurlijk ook voor de ‘shots’ salmiak. Als laatste wil ik de vakgroep in het algemeen bedanken. Vooral de laatste tijd heb ik de koffiepauzes zeer relaxt en gezellig gevonden, dit heeft erg geholpen in het voltooien van dit werk.

Samenvatting

Een geavanceerd materiaal model is ontwikkeld dat toepasbaar is in eindige elementen simulaties van het dieptrek proces. Tijdens dieptrekken wordt de initiele vlakke plaat plastisch vervormd tot een gewenste vorm. Om een product zonder gebreken te verkrijgen moeten de materiaal en proces parameters zorgvuldig gekozen worden. Met eindige elemente simulaties kunnen de invloed van materiaal en de proces parameters worden onderzocht voordat het werkelijke dieptrekken wordt uitgevoerd. Op deze manier kan een langdurig trial en error proces worden voorkomen.

De vloeifunctie is het eerste aandachtspunt. De vloeifunctie bepaalt of een spanningstoestand in het plaatmateriaal elastisch of plastisch is en hangt samen met het vloeioppervlak. Gewoonlijk worden de materiaal parameters voor de vloeifunctie bepaalt aan de hand van een-assige experimenten. Het blijkt dat resulaten van eindige elementen simulaties erg gevoelig zijn voor variaties in de vloeifunctie onder multi-axial condities. Vegter (1996) heeft een nieuwe vloeifunctie voorgesteld die gebaseerd is op metingen van de afschuif spanning (σ_{SH}), de een-assige spanning (σ_{UN}), de vlakke vervormings spanning (σ_{PS}) en de twee-assige spanning (σ_{BI}). Deze metingen definieren de referentie punten van het vloeioppervlak in de hoofdspannings ruimte. Het vloeioppervlak tussen de referentie punten wordt geconstrueerd met tweede orde Bezier interpolatie functies. Elke Bezier functie is relevant voor een bepaald gedeelte van de hoofd spanningsruimte. Het Vegter vloeioppervlak wordt geillustreerd op de volgende pagina.

Anisotropie wordt in acht genomen door de metingen in verschillende richtingen in de plaat uit te voeren. Hiermee worden referentie punten voor elke gemeten richting gedefinieerd. Voor tussenliggende richtingen worden de referentie punten geinterpoleerd door een Fourier functie. Op deze manier kan een vloeioppervlak voor elke willekeurige richting worden verkregen. Vervolgens wordt de vloeifunctie als volgt bepaald:

- De spaningstoestand wordt omgezet in een hoofdspanningstoestand
- De richting van de hoofd spanningen in de plaat worden bepaald
- De referentie punten behorend tot de bepaalde richting worden gedefinieerd
- De relevante Bezier interpolatie functie wordt gedefinieerd
- De vloei functie wordt afgeleid van de hoofd spanningen en de relevante Bezier functie

De eindige elementen implementatie van de Vegter vloeifuntie is gecontroleerd en blijkt correct te zijn.

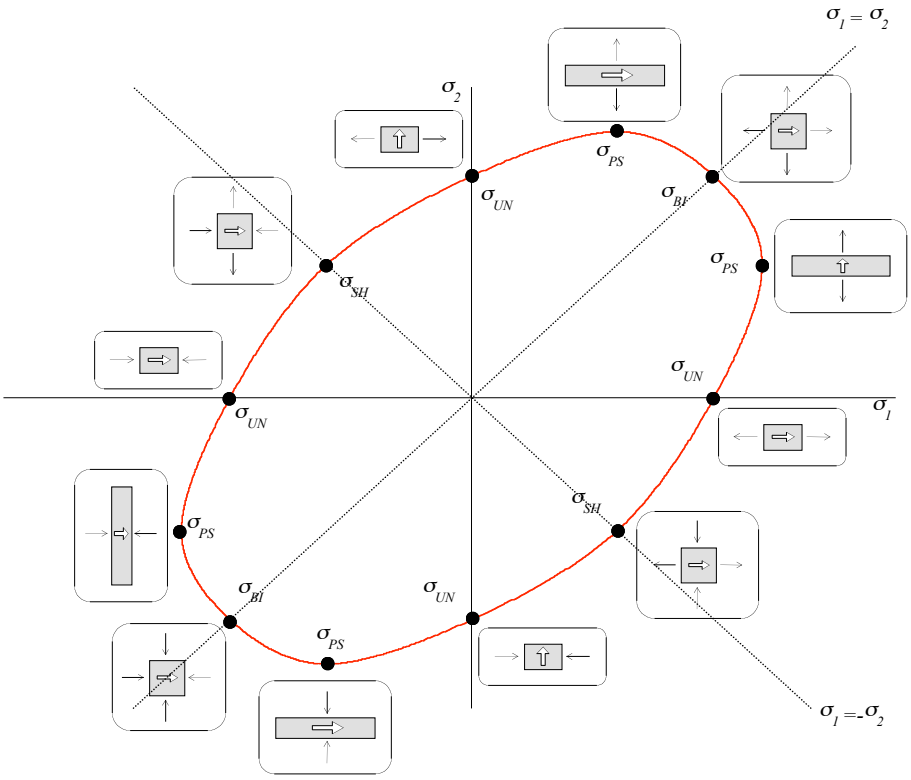

Vegter vloei oppervlak

De vloeifunctie wordt uitgebreid met 2 verstevigings modellen. Het eerste model is het fysische model van v. Liempt (v. Liempt, 1988) en Vegter (Vegter, 1991). Dit verstevigingsmodel kan de vloeispanning voor een grote deformatie range nauwkeurig voorspellen en houdt rekening met de invloed van de deformatie snelheid. Het model gaat uit van isotroop verstevigingsgedrag, wat inhoudt dat elke (meer-assige) vloeispanning met de zelfde factor toeneemt na plastische deformatie. Uit experimenten blijkt dat dit gedrag alleen geldig is bij proportionele rekpaden. Daarom is een tweede verstevigingsmodel ontwikkeld, dat het materiaal gedrag bij een cyclisch rekpad kan beschrijven. Dit model is gebaseerd op het model van Vreede (Vreede, 1992). Omdat de vloeifunctie is gedefinieerd in hoofdspanningen, wordt het model aangepast om het te combineren met de Vegter vloeifunctie. Een begin is gemaakt met de extensie van het verstevigings model naar algemene niet-proportionele rekpaden, maar deze extensie geeft nog geen realistische resultaten en vergt meer onderzoek.

Om de data voor de nieuwe materiaalbeschrijving te meten is een twee-assige tester ontwikkeld. De tester is in staat een afschuif deformatie en een vlakke vervormings deformatie te testen. De afschuif deformatie kan in 2 richtingen worden opgelegd en de vlakke vervormings deformatie kan in trek en druk worden opgelegd. Op deze manier kan het materiaal gedrag onder een grote verscheidenheid aan deformaties en spanningen worden onderzocht. In dit proefschrift wordt de tester gebruikt voor de volgende doelen:

- De bepaling van het afschuif en vlakke vervormings referentie punt
- De parameter bepaling van het anisotrope verstevigings model

Tijdens de experimenten wordt een plaatstalen proefstuk tussen 2 klemblokken gemonteerd. Tussen de klemblokken en aan de vrije randen van het proefstuk wijkt de deformatie en de spanning af van de opgelegde en gemeten waarden. De spanning kan hiervoor kwantitatief gecorrigeerd worden met behulp van een eindige elementen model van een gedeelte van het proefstuk. De deformatie kan niet kwantitatief voorspeld worden met het model, daarom is een deformatie analyse systeem aangeschaft dat de deformatie direct op het proefstuk meet.

Het materiaal model wordt gevalideerd aan 3 test cases. De eerste case is een buig experiment, uitgevoerd in samenwerking met de Technische Universiteit in Eindhoven. Deze case valideert de Vegter vloeifunctie bij de vlakke vervormings toestand. De tweede case betreft het dieptrekken van een cylindrisch produkt, uitgevoerd in samenwerking met Corus RD&T. Deze case valideert de Vegter functie aan de hand van het oor profiel, waarvan bekend is dat het gevoelig is voor meer-assige spannings toestanden. De derde case is het dieptrekken van een trapezium vormig produkt. Het materiaal model wordt gevalideert aan een kritisch product, hetgene inhoudt dat het produkt net kan worden diep getrokken zonder dat het materiaal breekt. Het blijkt dat in elke test case de Vegter vloeifunctie betere resultaten geeft dan de veel gebruikte Hill vloeifunctie, dus de nieuwe materiaal beschrijving kan als erg zinvol worden beschouwd.

Ten slotte worden 2 applicaties van complexe dieptrek produkten onderzocht. De eerste applicatie betreft het diep trekken van een Volvo pedaal bak. Corus RD&T beschikt over enige ervaring met het dieptrekken van dit produkt en simulaties van dit produkt kunnen kunnen worden vergeleken met experimenten. Het blijkt echter dat de proces condities niet erg nauwkeurig kunnen worden vastgesteld vanwege slijtage aan de gereedschappen, wat als consequentie heeft dat de experimentele resultaten met voorzichtigheid moeten worden geinterpreteerd. De tweede applicatie is het dieptrekken van een Audi spatbord, gebruikt als Benchmark op de Numisheet ’99 conferentie. De vereiste rekentijd voor deze applicatie blijkt positief waardoor geconcludeerd kan worden dat het ontwikkelde materiaal model geschikt kan worden gebruikt in realistische dieptrek applicaties.